TECHNISCHE UNIVERSITÄT MÜNCHEN

Department Chemie

Lehrstuhl Biotechnologie

Conformational analysis of proteins of biopharmaceutical interest

Marco Georg Dehling

Vollständiger Abdruck der von der Fakultät für Chemie der Technischen Universität München zur Erlangung des akademischen Grades eines Doktors der Naturwissenschaften (Dr. rer. nat.) genehmigten Dissertation.

Vorsitzender: Prof. Dr. Aymelt Itzen

Prüfer der Dissertation:

1. Prof. Dr. Johannes Buchner
2. Prof. Dr. Matthias Feige

Die Dissertation wurde am 04.12.2017 bei der Technischen Universität München eingereicht und durch die Fakultät für Chemie am 22.01.2018 angenommen.

Table of content

List of figures

List of tables

1. Introduction **1**

1. 1. Diversity of biopharmaceuticals **1**

1. 2. Antibody structure and folding **2**

1. 3. Heterogeneity in biopharmaceuticals – assessing critical quality attributes **4**

1. 4. Protein folding and protein dynamics **6**

1. 4. 1. Antibody folding 8

1. 5. Mass spectrometry in protein analysis **9**

1. 5. 1. Electrospray ionization technique 10
1. 5. 2. Mass analyzers 11
1. 5. 2. 1. Time-of-flight (ToF) detector 11
1. 5. 2. 2. Orbitrap mass analyzer 12
1. 5. 3. Fragmentation techniques 14
1. 5. 4. Determination of structural alterations and protein dynamics by H/DX-MS... 15
1. 5. 4. 1. Theoretical background 15
1. 5. 4. 2. Experimental set-up of an H/DX-MS analysis 20
1. 5. 4. 3. H/DX-MS data processing and evaluation 22

1. 6. Study objectives **23**

1. 6. 1. Unravelling the structure-function relationship of IgG2 disulfide isoforms.... 23
1. 6. 2. Dimeric structures and the major dimerization pathway of an IgG1 24
1. 6. 3. Phosphorylation caused structural rearrangement of c-Src kinase during activation 24

2. Experimental procedures **25**

2. 1. Material **25**

2. 1. 1. Chemicals 25
2. 1. 2. Proteins, enzymes and standard peptides 27
2. 1. 3. Chromatographic columns 28
2. 1. 4. Instrumentation 29
2. 1. 5. Computer software 30
2. 1. 6. Miscellaneous material and laboratory equipment 31

2. 2. Methods **32**

2. 2. 1. General protein preparation procedures 32
2. 2. 1. 1. IgG2 disulfide isoform enrichment / isolation 32
2. 2. 1. 2. IdeS digestion of immunoglobulins 33
2. 2. 1. 3. Limited Lys-C digestion of immunoglobulins 34
2. 2. 1. 4. Reduction of immunoglobulins 34
2. 2. 1. 5. De-N-glycosylation of immunoglobulins 34
2. 2. 2. Biophysical methods [in cooperation with Dr. E. Boczek] 35
2. 2. 2. 1. Kinase activity measurements 35
2. 2. 2. 2. CD Spectroscopy and Thermal Transition 35
2. 2. 2. 3. ANS Binding Assay 36
2. 2. 2. 4. Tryptophan Quenching 36
2. 2. 2. 5. Aggregation Assay 36
2. 2. 2. 6. Nano differential scanning fluorimetry (DSF) 36
2. 2. 2. 7. Surface plasmon resonance (SPR) 37
2. 2. 3. Chromatographic methods 37
2. 2. 3. 1. Size-exclusion chromatography (SEC) 37
2. 2. 3. 2 Strong cation exchange chromatography (SCX) 38
2. 2. 3. 3. Weak cation exchange chromatography (WCX) 39
2. 2. 3. 4. Protein A chromatography 39
2. 2. 4. Mass spectrometric methods 40
2. 2. 4. 1. Mass analysis of intact protein samples 40
2. 2. 4. 2. Middle-down mass spectrometry 41
2. 2. 4. 3. Reduced peptide mapping 42
2. 2. 4. 4. Non-reduced peptide mapping 42
2. 2. 4. 5. Hydrogen/deuterium exchange mass spectrometry (H/DX-MS) 43
2. 2. 5. Small angle X-ray scattering [in cooperation with Dr. R. Stehle] 46
2. 2. 6. Analytical ultracentrifugation 47
2. 2. 7. *In-silico* methodologies 48
2. 2. 7. 1. Homology model construction 48
2. 2. 7. 2. Molecular Dynamics Simulations [in cooperation with Prof. Dr. Kaila & Florian Kandzia] 48
2. 2. 8. Bioactivity assays 50
2. 2. 8. 1. Cell-based bioactivity assay 50
2. 2. 8. 2. ELISA based bioactivity assay 50

3. Unravelling the structure-function relationship of IgG2 disulfide isoforms **52**

3. 1. Introduction **52**

3. 2. Results **55**

3. 2. 1. *In vivo* conversion of IgG2 disulfide isoforms 55
3. 2. 2. Isolation of disulfide isoforms 56
3. 2. 3. Confirmation and identity verification of generated isoforms 57
3. 2. 4. Structural characterization of isolated IgG2 isoforms 66
3. 2. 5. Small angle X-ray scattering analysis and homology modeling of the IgG2 disulfide variants 70
3. 2. 6. Functional characterization 73

3. 3. Discussion **76**

3. 3. 1. Isolation and verification of the three most dominant disulfide isoforms 76
3. 3. 2. Structural characterization of isolated isoforms 77
3. 3. 3. Functional characterization and bioactivity estimation 79

4. Dimeric structures and the major dimerization pathway of an IgG1 ..... **82**

4. 1. Introduction **82**

4. 2. Results **85**

4. 2. 1. Isolation and purity of dimeric aggregates 85
4. 2. 2. Global structural arrangement of dimeric species 88
4. 2. 3. Potency estimation of isolated size variants 95
4. 2. 4. Identification and localization of intermolecular interaction-sites 95
4. 2. 5. Analysis of post-translational modifications that trigger the aggregation processes 110
4. 2. 6. *In silico* investigation of the conformational impact of the isomerization in the CDR2 117

4. 3. Discussion **122**

4. 3. 1. Investigated IgG1 forms two predominant structural dimer variants 122
4. 3. 2. Analysis of intermolecular interaction-sites within dimeric variants 123
4. 3. 3. The crucial role of the heavy chain CDRs in aggregation process 125

5. Phosphorylation caused structural rearrangement of c-Src kinase during activation **127**

5. 1. Introduction **127**

5. 2. Results **130**

5. 2. 1. Y416-phosphorylation increases the activity of c-Src 130
5. 2. 2. Y416-phosphorylation traps c-Src in the active state 131

5. 2. 3. Intramolecular interactions in the kinase domain are strengthened upon Y416-phosphorylation..... 136
5. 2. 4. Y416 phosphorylation of c-Src globally alters its intramolecular interactions 139
5. 2. 5. ATP differently affects the unphosphorylated and the pY416 state..... 146

5. 3. Discussion..... 150

6. Summary..... 154

7. Abbreviations..... 156

8. References..... 160

9. Acknowledgements..... 183

Declaration

List of figures

Fig. 1: Crystal structures of different marketed biopharmaceuticals.

Fig. 2: Structural arrangement of the polypeptide chains in an IgG molecule.

Fig. 3: Degrees of freedom within the protein backbone and the most important secondary structure motifs.

Fig. 4: Representation of the protein folding funnel and illustration of protein dynamics in the native state.

Fig. 5: Schematic overview of *in vivo* antibody folding and assembly.

Fig. 6: Schematic overview of an ESI source set-up.

Fig. 7: Schematic view of an orbitrap mass analyzer.

Fig. 8: Fragmentation pattern of protein backbone showing a series of a- and x- ions, b- and y- ions, and c- and z- ions.

Fig. 9: Different types of hydrogen hydrogens within a peptide sequence.

Fig. 10: pH dependency of exchange rates of different hydrogens in proteins.

Fig. 11: Isotopic distribution characteristic for EX2 and EX1 kinetics.

Fig. 12: Schematic illustration of an H/DX-MS experiment.

Fig. 13: Schematic representation of disulfide connectivity of the main isoform variants observed in IgG2 biotherapeutics.

Fig. 14: *In vivo* composition of disulfide isoforms as determined by reversed phase chromatography after affinity purification from preclinical serum samples.

Fig. 15: Strong-cation exchange chromatogram of re-injected isolated isoforms of the IgG2 antibody.

Fig. 16: Stacked chromatograms of reduced LC-MS/MS peptide mapping.

Fig. 17: Stacked chromatograms of non-reduced LC-MS/MS peptide mapping.

Fig. 18: Baseline and binding adjusted SPR target binding sensorgrams of the different isoforms and their target.

Fig. 19: H/DX-MS comparison of redox-enriched and non-redox-enriched isoform B.

Fig. 20: Strong-cation exchange chromatograms of the isolated isoforms after stress induction.

Fig. 21: Size-exclusion chromatograms of the degradation time-courses of the investigated isoforms and the WSTD.

Fig. 22: Deconvoluted intact mass spectra of the four weeks stressed samples of the isolated isoforms and the WSTD.

Fig. 23: UV chromatograms of IdeS digested and reduced isoforms and the WSTD (time-point 0d).

Fig. 24: UV chromatograms of IdeS digested and reduced samples incubated for four weeks.

Fig. 25: Distribution of sedimentation coefficients of the different analyzed IgG2 isoforms.

Fig. 26: Overlay of SEC chromatograms of the different analyzed IgG2 samples.

Fig. 27: Overlay of thermograms of the different analyzed IgG2 samples.

Fig. 28: Comparison of H/DX-MS results for isoform A versus isoform B and isoform A versus isoformA/B comparison.

Fig. 29: Sum of difference plots for hydrogen exchange comparison of isoform B and isoform A/B compared to isoform A.

Fig. 30: Scattering intensity plots in depence of the scattering vector of the different analyzed IgG2 samples.

Fig. 31: Pair distribution function p(r) derived by fourir transformation of the scattering data.

Fig. 32: Structural models of the investigated IgG2 isoforms obtained by SAXS and rigid body modeling.

Fig. 33: Bar plots illustrating the results of potency determination.

Fig. 34: Sedimentation coefficient distribution of the formed complexes by either an excess of target or an excess of antibody in the equilibrium state.

Fig. 35: Structural representation of the target molecule.

Fig. 36: Schematic representation of formed IgG2/target complexes.

Fig. 37: Simplified representation of the complexity of protein aggregation.

Fig. 38: SEC chromatograms of unstressed and differently stressed IgG1 samples.

Fig. 39: Analysis of isolated size variants by SEC.

Fig. 40: Sedimentation coefficient distribution of the isolated fractions in the presence of SDS.

Fig. 41: Sedimentation coefficient distributions of monomer and stress induced dimer species analyzed by AUC.

Fig. 42: Exemplary scattering raw data.

Fig. 43: Exemplary pair distribution function s of ML and D2L.

Fig. 44: Homology model of the investigated IgG1 molecule.

Fig. 45: Monomer structures of the differently stressed IgG1 molecules revealed by rigid-body modeling.

Fig. 46: Best-fit calculated models of the isolated dimer species obtained by rigid-body modeling.

Fig. 47: Total ion chromatograms of IdeS digested monomer and dimer samples.

Fig. 48: Schematic illustration of limited Lys-C digested dimer aggregates.

Fig. 49: SEC chromatogram of limited Lys-C digested samples.

Fig. 50: Final Lys-C fragments derived from of the temperature stressed fractions.

Fig. 51: H/DX-MS comparison of D1T Fab:Fab and MT Fab heavy and light chain.

Fig. 52: Crystal structure for H/DX-MS comparison of D1T Fab:Fab and MT Fab.

Fig. 53: H/DX-MS comparison of D1T Fab:Fc and MT Fab heavy and light chain.

Fig. 54: H/DX-MS comparison of D1T Fab:Fc and MT Fab heavy and light chain.

Fig. 55: H/DX-MS comparison of D1T Fab:Fc and MT Fc.

Fig. 56: H/DX-MS comparison of D2T Fab:Fab and MT Fab heavy and light chain.

Fig. 57: Crystal structure for H/DX-MS comparison of D2T Fab:Fab and MT Fab.

Fig. 58: H/DX-MS comparison of D2T Fab:Fc and MT Fab heavy and light chain.

Fig. 59: Crystal structure for H/DX-MS comparison of D2T Fab:Fc and MT Fab.

Fig. 60: H/DX-MS comparison of D2T Fab:Fc and MT Fc.

Fig. 61: Dimer models derived by rigid body modeling including color coded H/D exchange differences and docked antigen for temperature stress induced variants.

Fig. 62: Reduced Lys-C peptide mapping chromatograms of isolated interacting domains (Fab:Fab) of D1T and D2T and Fab of MT.

Fig. 63: Reduced Lys-C peptide mapping chromatograms of isolated interacting domains (Fab:Fc) of D1T and D2T and Fab and Fc of MT.

Fig. 64: Extracted ion chromatograms of isomerized and unmodified peptide AA[44-65].

Fig. 65: Extracted ion chromatograms of the oxidized peptide AA[44-65].

Fig. 66: Extracted ion chromatograms of oxidized peptide AA[66-76].

Fig. 67: MS/MS spectrum of AA[44-65] obtained by ETD fragmentation for N52 verification.

Fig. 68: MS/MS spectrum of AA[44-65] obtained by ETD fragmentation for isoAsp52 verification.

Fig. 69: MS/MS spectrum of AA[44-65] obtained by ETD fragmentation for isoAsp63 verification.

Fig. 70: Representation of the observed differences in D1T Fab:Fab and D2T Fab:Fab.

Fig. 71: Structural arrangement of the CDR2 in the Asn52 variant.

Fig. 72: Sampled hydrogen bond donor-acceptor distances and angles of Asn52.

Fig. 73: Structural arrangement of the CDR2 in the isoAsp52 variant.

Fig. 74: Sampled hydrogen bond donor-acceptor distances and angels of isoAsp52.

Fig. 75: Structural arrangement of c-Src and phosphorylation dependent kinase activity.

Fig. 76: Annotated MS/MS spectra of the phosphorylated and unphosphorylated peptide AA [411-424] obtained by protease digestion.

Fig. 77: A-loop and E310-K295 sampling of c-Src in different ligand states.

Fig. 78: Molecular dynamics simulations of c-Src in different ligand states.

Fig. 79: Detailed analysis of the KER and HRD motif with regard to solvent accessible surface area.

Fig. 80: Molecular dynamics simulations of the KER- and HRD motif of the unphosphorylated (KDU) and the phosphorylated (KDP) version of the kinase domain.

Fig. 81: Structural comparison of the different states of c-Src and the kinase domain.

Fig. 82: Free energy landscape of FLU and FLP.

Fig. 83: Bioanalytical characterization of different c-Src constructs (CD-spectroscopy and T_M determination).

Fig. 84: Bioanalytical characterization of different c-Src constructs (ANS binding; Trp quenching; aggregation).

Fig. 85: H/DX-MS results for the comparison of exchange kinetics between FLU and FLP.

Fig. 86: Annotated MS/MS spectra of the mutated peptide AA [293-306] and unmutated peptide AA [293-307] obtained by protease digestion.

Fig. 87: H/DX-MS results for the comparison of exchange kinetics between FLU-K295R and FLU.

Fig. 88: H/DX-MS results for the comparison of exchange kinetics between FLP and KDP.

Fig. 89: H/DX-MS results for the comparison of exchange kinetics between KDU and KDP.

Fig. 90: Annotated MS/MS spectra of the phosphorylated and unphosphorylated peptide AA [520-533] obtained by protease digestion.

Fig. 91: H/DX-MS results for the comparison of exchange kinetics between FLU and FLU-pY527.

Fig. 92: H/DX-MS results for the comparison of exchange kinetics between FLU and FLU+AMP-PNP.

Fig. 93: H/DX-MS results for the comparison of exchange kinetics between FLP and FLU-pY527.

Fig. 94: The influence of nucleotide binding to different c-Src states.

List of tables

Tab. 1: Post-translational modifications and their impact on IgG drug molecules.

Tab. 2: Gradient for SCX chromatography analysis.

Tab. 3: Gradient for WCX chromatography analysis

Tab. 4: Gradient for Protein A chromatography analysis

Tab. 5: Gradient for intact LC-MS analysis.

Tab. 6: Gradient for middle-down analysis.

Tab. 7: Analytical gradient for IgG2 H/DX-MS.

Tab. 8: Analytical gradient for IgG1 H/DX-MS.

Tab. 9: Analytical gradient for c-Src H/DX-MS.

Tab. 10: Affinity constant values.

Tab. 11: Observed masses of the IdeS digested and reduced samples.

Tab. 12: Parameters derived by AUC, SEC and DSF.

Tab. 13: Derived parameters describing structural properties of the samples obtained by SAXS.

Tab. 14: Complex formation in the equilibrium state of the different IgG2 samples by adding an excess of the target.

Tab. 15: Complex formation in the equilibrium state of the different IgG2 samples by adding an excess of the antibody.

Tab. 16: Purity and elution time of the isolated fractions.

Tab. 17: Hydrodynamic data obtained by AUC analysis.

Tab. 18: Summary of R_G and D_{max} values obtained by SAXS.

Tab. 19: Parameters used to assess accuracy of calculated models.

Tab. 20: Relative potency values of isolated fractions.

Tab. 21: Summary of differences revealed by H/DX-MS for temperature stress induced dimers.

Tab. 22: Significantly increased post-translational modifications in D1T.

Tab. 23: Significantly increased post-translational modifications in D2T.

1. INTRODUCTION

1. 1. Diversity of biopharmaceuticals

Biopharmaceuticals are drug molecules produced using biotechnology; including genetic engineering, hybridoma technology, and recombinant expression [Chadd & Chamow, 2001; Dingermann, 2008]. They are large and highly complex therapeutic drug molecules composed of proteins, carbohydrates, peptides and in the case of antibody drug conjugates specific toxins [Chauhan & Sood, 2016]. The first biologic drug, recombinant human insulin, was approved in the 1980s with recombinant human insulin [Johnson, 1983]. From there on, a huge variety of biopharmaceuticals such as cytokines, interferons, interleukins, candidates of the tumor necrosis factor (TNF) family, granulocyte colony stimulating factor, hematopoietins, hormones and different enzymes [Chauhan & Sood, 2016] were approved to treat various diseases like hematologic malignancies and solid tumors, as well as systemic immune-mediated diseases, such as rheumatoid arthritis, inflammatory diseases and psoriasis [Pinada *et al*., 2016].

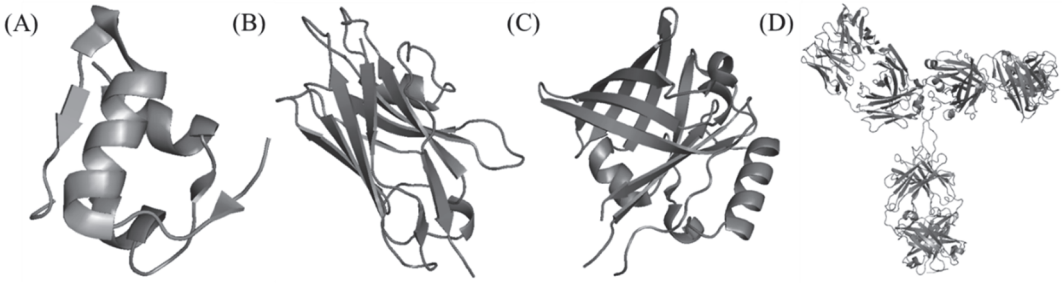

Fig. 1: Crystal structures of different marketed biopharmaceuticals. (A) Structure of the first biopharmaceutical – the peptide hormone insulin [PDB ID: 4EY9; Favero-Retto *et al.*, 2013]; (B) Structure of a nanobody (camel single-domain V_H antibody fragment) [PDB ID: 1MEL; Desmyter *et al.*, 1996]; (C) Structural arrangement of a digoxigenin-binding anticalin [PDB ID: 1LNM; Korndoerfer *et al.*, 2003]; (D) Crystal structure of an IgG1 antibody [PDB ID: bpj1831mmc3; Brandt *et al.*, 2010]. Not drawn to scale.

The biggest class of biopharmaceuticals are monoclonal antibodies. These are of great interest regarding different indications due to their highly specific binding to target molecules and their ability to activate effector functions and initiate immune responses. In 2013, global sales for therapeutic monoclonal antibody biologicals were nearly $75

billion, which totals approximately half of the sales of all biopharmaceutical products with more than 300 different new biological entities currently in development for the treatment of multiple indications [Ecker *et al*., 2015].

With the expiry of patents securing originator products more and more biosimilars have entered the market over the past years. These are highly similar in structure, function, efficacy and safety to the original drug product. The rise of biosimilars increases patient´s access to expensive biologicals facilitating treatment of different diseases and in addition yield savings for national healthcare systems [Ecker *et al*., 2015].

1. 2. Antibody structure and folding

Antibodies of the IgG class share the same basic structure comprising two heavy polypeptide chains (approx. 50 kDa) and two light polypeptide chains (approx. 25 kDa), connected to a Y-shaped structure by disulfide bonds [Edelmann *et al.*, 1969, Crisp *et al*., 2016; Schroeder *et al*., 2010]. Figure 2 illustrates the structural arrangement of an IgG1 molecule.

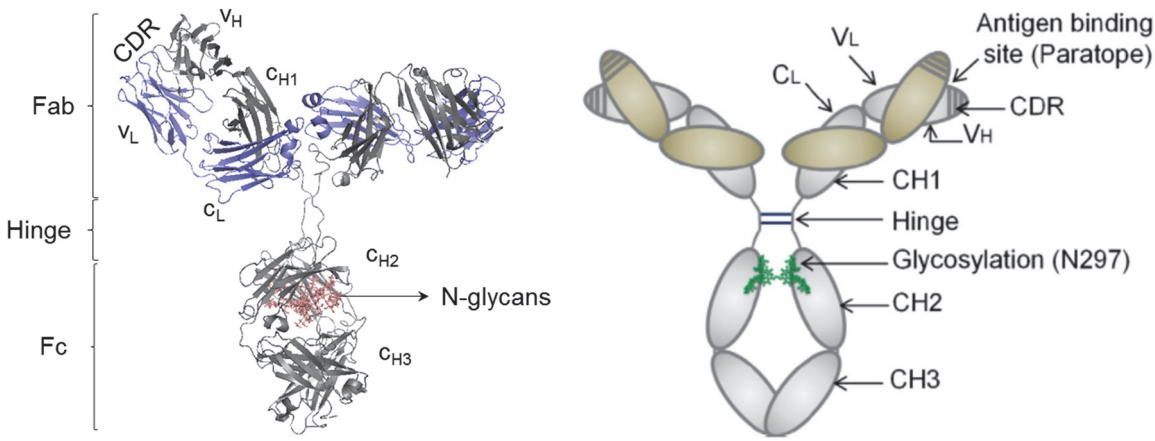

Fig. 2: Structural arrangement of the polypeptide chains in an IgG molecule. An IgG molecule can be divided into two Fab and one Fc segment that are connected by the hinge region. The heavy chains (grey) are part of the Fab as well as the Fc part. The light chains (blue) are located in the Fab parts. The N-glycosylation-site within the Fc is an asparagine at approximately amino acid position 297 of the heavy chain. The C_L and C_H domains represent constant regions whereas V_H and V_L are variable bearing the complementary determining regions (CDRs) that are responsible for antigen binding. A schematic representation is depicted on the left. Figures taken from: Irani *et al*., 2015 & Brandt *et al*., 2010; PDB ID: bpj_1831_mmc3].

The architecture of antibodies can be divided into three regions – two antigen binding fragments (Fab) and one crystallizable fragment (Fc). Both consist of *β*-sheet-rich domains exhibiting the immunoglobulin fold very rigid domains that are linked by a flexible hinge region. The Fab fragments contain the complementary determining regions (CDR1-3) which are responsible for antigen binding. These are defined as hypervariable regions since the amino acid composition depends on the target and thus provides its high specifity. They are located in flexible loops in the V_H and V_L domains. The Fc part is connected to the Fab segments via the disulfide-bridge stabilized hinge region. It contains the conserved N-glycosylation-site linked to an asparagine residue at approximately position 297 and consists of the C_H2 and C_H3 domains. The Fc of IgG is responsible for effector functions and interacts with the different cellular Fc gamma receptors (FcγRs), C1q and the neonatal Fc receptor (FcRn) to stimulate and regulate effector mechanisms like antibody-dependent cellular cytotoxicity (ADCC), complement-dependent cytotoxicity whereby FcRn plays an important role in transcytosis and the recycling pathway of IgGs in serum [Guilliams *et al*., 2014; Roopenian, D. C. & S. Akilesh, 2007]. There are five different activating Fcγ receptors, categorized as FγRI (CD64), FcγRIIa (CD32a), FcγRIIc (CD32c), FcγRIIIa (CD16a) and FcγRIIIb(CD16b), and one inhibitory receptor FcγRIIb (CD32b) [Guilliams *et al*., 2014; Hogarthand, P. M. & G. A. Pietersz, 2012; Pincetic *et al*., 2014, Irani *et al*., 2015]. Fcγ receptor and C1q binding-sites are located close to the lower hinge region involving the C_H2 segment and the glycans attached to N-297 [Irani *et al*. 2015; Higel *et al*., 2016]. From this fact, glycosylation plays an important role in FcγR binding and consequently in activating effector functions [Abes & Teillaud, 2010]. In addition, glycosylation stabilizes the IgG structure by interacting with a hydrophobic pocket in the Fc part [Liu *et al*., 2006; Schroeder *et al*., 2010; Feige *et al*., 2009].

The heavy chains can be categorized in different types γ_1, γ_2, γ_3 and γ_4 which defines the subclasses IgG1, IgG2, IgG3 and IgG4. Since differences between the heavy chain types exist, the IgG subclasses further differ by the amount of stabilizing intra- and interchain disulfide bridges [Vidarsson *et al*., 2014]. Additionally, also the light chains display variability and can be divided into the κ-type and λ-type with the differences located in the constant region C_L [Higel *et al*., 2016].

1. 3. Heterogeneity in biopharmaceuticals – assessing critical quality attributes

In contrast to synthetic small molecule drugs, biopharmaceuticals contain post-translational modifications that result in an increase in complexity and heterogeneity of the protein. These heterogeneities are either already introduced within the cell or during downstream processing and storage of the formulated drug-product. The diversity of heterogeneity is illustrated on monoclonal antibody therapeutics in the following.

The most common modification of recombinant proteins that are produced in eukaryotic cells is N-linked glycosylation [Zhong & Wright, 2013]. N-glycosylation occurs in the endoplasmatic reticulum and the Golgi apparatus [Bieberich, 2014; Higel *et al.,* 2016]. Both heavy chains contain a glycosylation-site in the C_H2 domain. Glycans attached to this domain can be categorized in three types: high-mannose, complex and hybrid whereas the last two can appear fucosylated or afucosylated as well as sialylated [Jefferis, 2009; Higel *et al*., 2016]. The glycan types affect the antibody structure, stability, clearance, immunogenicity and potency of effector functions [Abes & Teillaud, 2010; Higel *et al.*, 2016; Kurogochi *et al.*, 2015; Thoman *et al*., 2015; Zheng *et al*., 2011; Arnold *et al*., 2007].

Another modification in which carbohydrates are involved is non-enzymatic glycation. This phenomenon originates from the reaction of a carbonyl group on reducing sugars with N-terminal primary amine or lysine side chains [Neglia *et al*., 1983]. Glycation can occur during cell culture as well as storage of the product, where it strongly depends on the reducing carbohydrate content of the formulation [Andya *et al*., 1999]. It can affect the binding affinity to the antigen when that glycation occurs within the strongly solvent-exposed CDRs where it could lead to steric hindrance. Furthermore, every glycation event reduces the overall charge by one positive charge making the molecule more acidic which can reduce immunoreactivity of the protein as demonstrated by loss of complement-fixing activity [Dolhofer *et al*., 1985; Zhong *et al.,* 2013].

The N-terminus of heavy and light chains are also modification-prone regions in therapeutic antibodies. Heavy chains generally start with either glutamine or glutamate, while λ light chains begin with glutamine, occasionally with serine, arginine, or leucine and κ light chains with glutamate or aspartate [Zhong *et al*., 2013]. Terminal glutamine

or glutamate can cyclize spontaneously to pyroglutamate *in vitro* and *in vivo*; pyroglutamate formation occurs faster than cyclization of glutamine. These transformations impact the overall charge state and is supposed to have stabilizing effects since it protects the protein from protease digestion [Rink *et al*., 2010]. Recent studies revealed that this N-terminal modification does not affect the clearance of the biotherapeutic and is strongly dependent on the structural arrangement of the monoclonal antibody [Liu *et al*., 2011].

Also deamidation of asparagine and glutamine residues is non-enzymatic and thus formation also occurs during as well as after the production process. Deamidation is a hydrolytic reaction which results in the formation of aspartate or glutamate *via* succinimide intermediates, respectively and shows strong dependency on pH value, temperature, ionic strength and the adjacent amino acid sequence [Wright, 1991; Bischoff & Kolbe, 1994; Geiger & Clarke, 1987]. It results in a change of the net-charge state by conversion of a positively to a negatively charged residue. The succinimide intermediate can also convert to isoaspartate or isoglutamate in an alternative reaction resulting in a lengthening of the protein backbone by one methylene group in addition to charge conversion. These modifications are particularly critical in the CDR regions of a monoclonal antibody because they could impact structural stability as well as binding affinity [Yan *et al.,* 2016].

Another factor introducing product heterogeneity is the oxidation of amino acid residues. The most susceptible residue for oxidation is methionine, which can be oxidized to methionine sulfoxide. Subsequently, the proteins polarity is increased by this kind of modification [Zhong & Wright, 2013]. The most critical ones for monoclonal antibodies are located in the Fc part (Met-255 and Meth-431) close to the C_H2 and C_H3 interface [Zhong *et al.*, 2013]. Modifications in this region might impact FcRn binding and thus pharmacokinetics [Shields *et al*., 2001]. Besides methionine also tryptophan and cysteine were found to oxidize in antibody-based biotherapeutics which is critical for stability and target affinity when it occurs in the CDRs [Yang *et al*., 2007].

From the factors presented in Table 1 influencing heterogeneity in monoclonal antibodies it becomes obvious that the combination of these present in a large molecule

like an antibody results in a complex drug product. All possible modifications have to be considered to derive the intended attributes of the final drug product.

Tab. 1: Post-translational modifications and their impact on IgG drug molecules.

Modification	Impact	Origin
N-glycosylation	Alteration of structure, function & clearance	Biosynthesis
Glycation	Influence on net charge Functional alterations	During cultivation; Post-cultivation/storage
N-terminal Gln/Glu cyclization	Influence on net charge	During cultivation
Asn/Gln deamidation	Influence on net charge	During cultivation; Post-cultivation/storage
Isomerization	Influence on net charge and structural alteration of protein backbone	During cultivation; Post-cultivation/storage
Oxidation	Increase of polarity	Post-cultivation/storage
C-terminal Lys	Influence on net charge	Biosynthesis

1. 4. Protein folding and protein dynamics

The native folded state of a protein is essential for its activity. This state is defined as the small ensemble of three-dimensional conformations in which the protein is thermodynamically stable and exhibits its active nature [Anfinsen, 1973]. Reaching this state is a complex process since polypeptide chains exhibit an enormous amount of degrees of freedom [Levintal, 1986]. The major ones are the highly flexible dihedral angles (ϕ, ψ) of the two σ bonds of each amino acid linked together, while the dihedral angle ω is generally fixed due to the mesomeric effect but can be found in a cis/trans isomeric states. The (ϕ, ψ) configuration space shows two characteristic free-energy minima, that are taken by the two most important secondary structure motifs (Fig. 3): α-helices (approx. ϕ = -60° and ψ = -45°) and β-sheets (approx. ϕ = -140° and ψ = 135° in antiparallel and ϕ = –120° and ψ = 115° in parallel sheets) [Boyle & Woolfson, 2011; Woutersen *et al*., 2002]. Giving a large number of connected amino acids in a naturally occurring protein this results in an amazing huge number of conformations a protein

has to sample to find its native, low-energy state only when taking the angles located in the polypeptide backbone into account [Dill *et al.*, 2008].

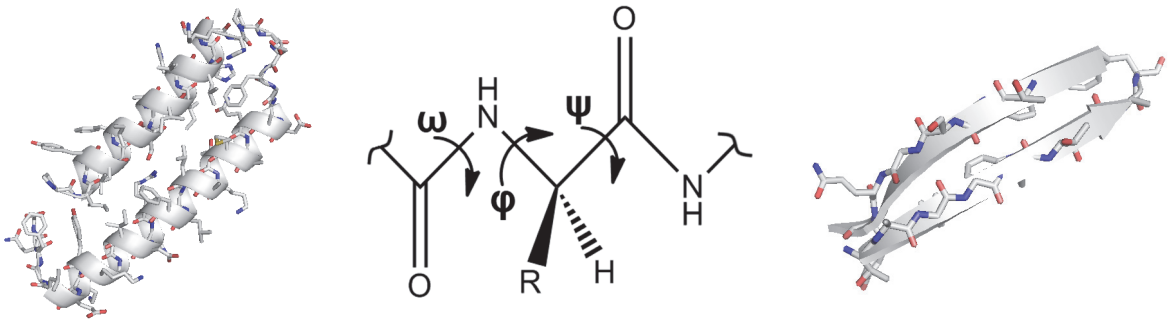

Fig. 3: Degrees of freedom within the protein backbone and the most important secondary structure motifs. Despite the high degrees of freedom originating from the two σ bonds of each amino acid (middle), proteins exhibit well-defined structural motifs like *α*-helices (left) and *β*-sheets (right) with distinctive amino acid orientations due to side-chain interactions. Middle figure taken from https://www.quora.com/.

Interestingly, many proteins fold within milliseconds to seconds which is in contrast to the theoretical amount of random conformations. This, generally known as the Levinthal´s paradox (Levinthal, 1968), can be explained by intermediates that direct further events during folding progress. The folding process can be illustrated as the motion of the polypeptide chain on a complex energy landscape [Buchner *et al.*, 2011; Dill *et al.*, 2008]. The way to the native state is controlled by the thermodynamic stability of partially folded intermediates, the sampling of these conformations by dynamic motions of the polypeptide chain and the interactions of amino acid side chains that arise (hydrophobic interactions, van der Waals interaction, hydrogen-bond bridges or ionic interactions) [Buchner *et al.*, 2011]. The free-energy surface of the polypeptide depicted in Figure 4 is the major determinant. It is the sum of potential energy within the protein, which gradually decreases on the proteins way to the native state. This process favors folding whereas the entropy of the molecule decreases [Henzler-Wildmann & Kern, 2007]. The balance between the two determinants leads to free energy barriers [Karplus, 2011].

The increased use of crystal-structures to visualize natively folded protein structures lead to the suggestion that the native state is one rigid conformation. But these are solely snapshots of the protein trapped in a crystal lattice. In aqueous solution, however,

proteins are highly dynamic entities exhibiting motions and fluctuations in time-scales ranging from 10^{-15} sec to 10^{3} sec within the native folded state [Brooks *et al.*, 1990]. With regard to the time-scale, dynamics can be divided into "slow" or "fast". Dynamics that are considered to be slow occur within microseconds and milliseconds, indicated in Figure 4 as tier 0 dynamics that defines fluctuations between two states such as large collective motions.

Tier 1 dynamics describe fluctuations of high frequencies on a timescale of ns to allow fast transition between tier 1 sub-states (i.e. loop motions) [Yang *et al.*, 2013]. In contrast, tier 2 describes even faster fluctuations at higher frequencies than tier 1 dynamics. Here, motions occur on timescales of ps in which a large number of closely related sub-states located within tier 1 wells are taken (such as side chain rotations) [Sang *et al.*, 2016; Henzler-Wildmann & Kern, 2007; Yang *et al.*, 2014].

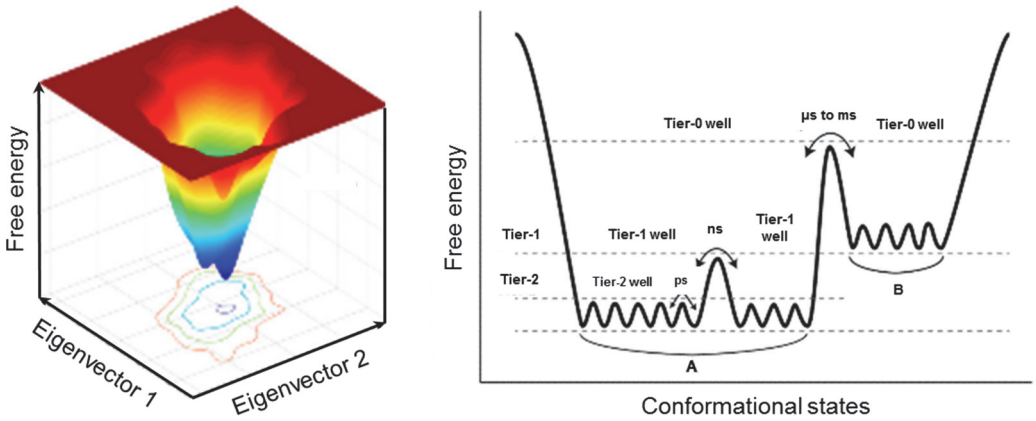

Fig. 4: Representation of the protein folding funnel (left) and illustration of protein dynamics in the native state (right). The width of the funnel represents the dependence of conformational entropy when a protein reaches the native folding state. The depth of the funnel illustrates the change in total Gibbs free energy between the denatured and native states by forming intermediate states that direct the process towards the native state. These intermediates show compact folding states exhibiting secondary structure elements but few ordered tertiary structure elements. The right illustration describes the energy barriers present in protein dynamics. Tier 0 is defined by large conformational changes on global level in a microsecond to millisecond timescale in which the conversion between two states takes place. Tiers 1 and 2 represent finer motions of loops and side-chains chains [Henzler-Wildmann & Kern, 2007]. Figures adapted from: Sang *et al.*, 2016.

1. 4. 1. Antibody folding

Antibody folding and polypeptide assembly occurs in the endoplasmatic reticulum (ER). The heavy and light chains are co-translationally translocated into the ER [Feige

et al., 2009] whereas folding of C_L and C_H2/C_H3 occurs very fast when entering the ER [Bergman & Kuehl, 1979]. In contrast, folding of C_H1 and V_L is timely delayed since they are associated in a first step with the chaperone BiP. The interaction of BiP with C_H1 is of special importance as it prevents premature secretion of the heavy chains. It recognizes hydrophobic residues in C_H1 and V_L [Vanhove *et al.*, 2001]. The folding of the single domains is catalyzed by a PPIase which is responsible for proline cis-trans isomerization of the conserved proline residues located in the loops between the *β*-sheets of the different domains [Lilie *et al.,* 1995; Thies *et al.*, 1999]. BiP is released from C_H1 and the light chain takes over its position. C_H1 is unfolded and the interaction with C_L is required for C_H1 folding. In a last step, the folding process is finalized with the aid of peptidyl-prolyl isomerases (PPIases) and the protein disulfide isomerase (PDI) which catalyzes interchain disulfide bridging which subsequently allows the secretion out of the ER [Feige *et al.*, 2009].

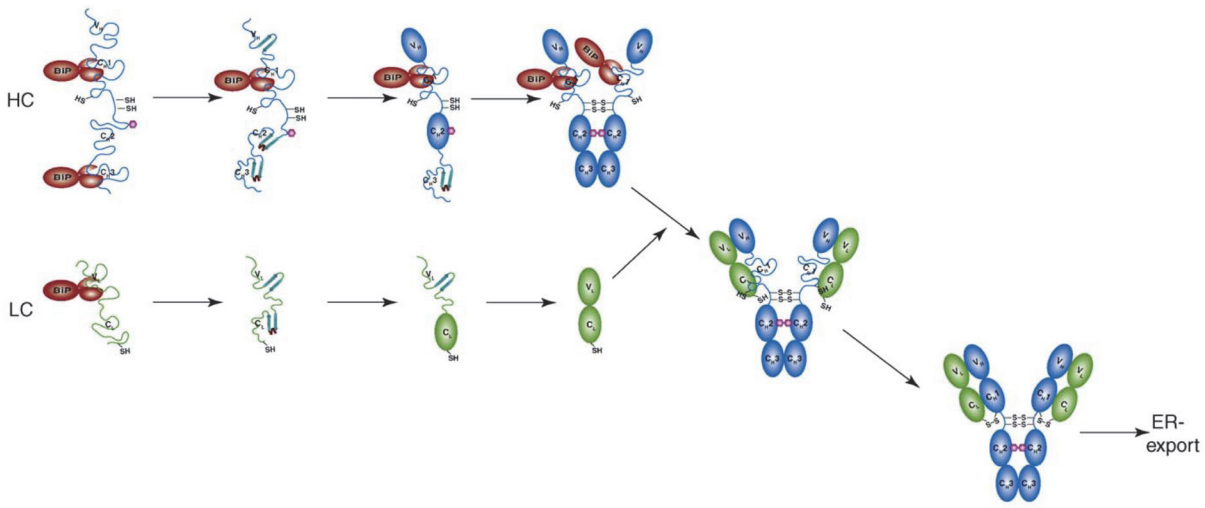

Fig. 5: Schematic overview of *in vivo* antibody folding and assembly. Already during translocation into the ER the light and the heavy chains start to fold. BiP associates rapidly with the unfolded states of the C_H1 and V_H domains. Dimerization and disulfide bridging in the hinge occurs as soon as C_H3 folding is finished. After displacement of BiP by the light chain the C_L domain functions as template for correct C_H1 folding and disulfide connectivity which is supported by different chaperones like PPIase and PDI. Figure taken from: Feige *et al.*, 2009.

1. 5. Mass spectrometry in protein analysis

Mass spectrometry (MS) has become a major tool in protein and peptide identification and characterization as well as complex determination over the past years [Jonsson, 2001; Wysocki *et al.*, 2005] because of its analytical sensitivity, selectivity and specificity. MS determines the mass-to-charge ratio (*m/z*) of gas phase ions – for proteins and peptides generally positive charged - which enables to estimate the accurate mass of the molecules of interest. In addition, MS/MS (or tandem MS or MS^2) fragmentation offers the opportunity to determine the amino acid sequence of peptides using different kinds of activation techniques like collision induced dissociation (CID) and electron transfer dissociation (ETD) for unambiguous analyte identification [Quan *et al*., 2013; Sobott *et al*., 2009]. A typical mass spectrometer comprises an ion source, a mass analyzer, and a detector.

1. 5. 1. Electrospray ionization technique

Electrospray ionization (ESI) is, besides matrix-assisted laser desorption ionization (MALDI) the most common used technique to bring protein and peptide ions into the gas phase. The ESI process can be divided into three steps: (1) formation of charged droplets in the emitter tip, (2) shrinking of the generated droplets caused by solvent evaporation and repeated fission, (3) generation of gas-phase ions due to the advancing shrinking process.

In the first step, the positive charged analyte ions are repelled from the emitter walls since high voltages are applied whereas the emitter needle represents the anode and the sampling aperture the cathode [Cech & Enke, 2001]. Thus, the analyte is accumulated in the center of the capillary and drifts towards the emitter outlet [Banerjee & Mazumdar, 2012]. Under the influence of the applied electric field the fluid is drawn out and forms the so-called Taylor cone [Kebarle & Tang, 1993]. Due to the formation of the cone, the charge density is drastically increased in the center of the cone and subsequently coulombic repulsion within the tip increases. As the repulsive forces exceed the surface tension of the solvent, the Taylor cone, consequently, produces a

fine jet towards the cathode which disperses into small droplets that contain the positive charged analyte ions [Wysocki *et al*., 2005]. Under the influence of elevated temperature within the source and the continuous nitrogen gas flow the solvent constantly evaporates which causes increasing charge density within the shrinking droplets. As soon as the repulsion exceeds the surface tension of the droplet, Coulomb explosion takes place resulting in the formation of multiple smaller droplets – this also happens repeatedly to the offspring droplets.

In this way, all solvent molecules depart from the droplets and solely analyte ions remain. For this process two theories are proposed – the ion evaporation model (IEM) and the charged residue model (CRM). IEM is characterized by the release of nanodroplets ($r < 10$ nm) from the surface of the primary formed droplet as soon as the electrostatic repulsion exceeds the Rayleigh limit [Konermann *et al.,* 2012]. Subsequently, small gas-phase clusters are formed that contain one single analyte ion and a few solvent molecules. While travelling of this cluster to the mass spectrometer inlet the remaining few solvent molecules get lost due to collisions with the background gas, and subsequently the solvent free gas-phase analyte enters the inlet [Konermann *et al*., 2012; Daub & Cann, 2011].

For proteins, CRM is the model of choice to describe the generation of gas-phase ions during electrospray ionization. This theory states that the neutral analyte protein – can be more than one - remains in the droplet. While the last solvent molecules evaporate during the transfer into the mass spectrometer, all the present charge is transferred on the protein [Kebarle & Verkerk, 2009].

The generated solvent free gas-phase ions are then pulled into the mass spectrometer by ultrahigh vacuum and the applied electric fields [Wilm, 2011; Banerjee *et al.*, 2011].

The ions formed during electrospray ionization can carry multiple charges. Due to this, one and the same peptide/protein can give multiple signals after detection since the mass analyzers detect *m/z* values (actually $(M + z)/z$), where M is the uncharged mass of analyte). Figure 6 schematically displays an electrospray ionization source.

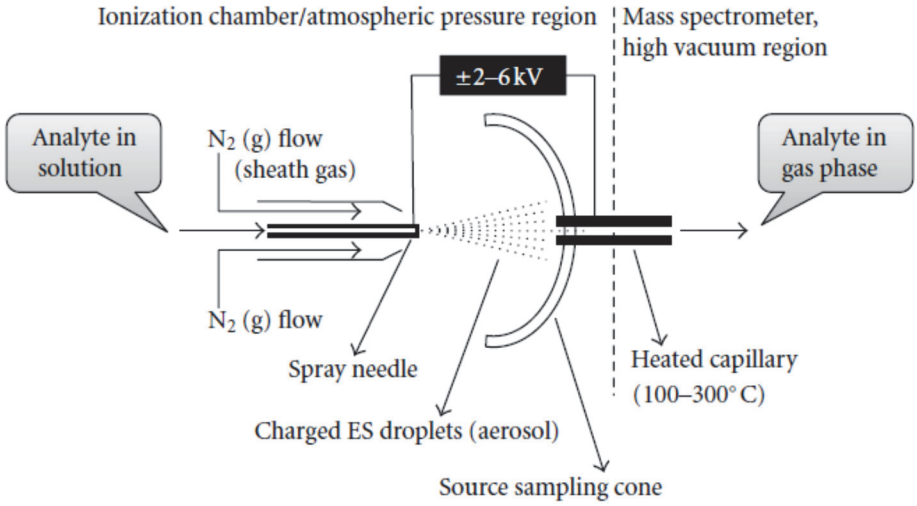

Fig. 6: Schematic overview of an ESI source set-up. The solution that contains the components to be analyzed pass the spray needle emitter. The electric field induces ionization and directs the charged droplets to the MS inlet. Desolvation occurs due to the influence of heated nitrogen and collision with the background gas. The generated gas-phase ions enter the high vacuum region of the mass spectrometer after passing the heated capillary. Figure taken from: Banerjee *et al.*, 2011.

1. 5. 2. Mass analyzers

Once the ions are in the gas-phase and have entered the ultrahigh vacuum they might pass one or more multipoles – depending on the mass spectrometer – for focusing and isolation of proteins/peptides of special interest prior to introduction into the detector for *m/z* determination. The analyzers used in this work are time-of-flight and orbitrap detectors.

1. 5. 2. 1. Time-of-flight (ToF) detector

Time-of-Flight (ToF) analyzers accelerate the entering gas-phase ions by applying a voltage gradient and measure the time that they take to traverse a field-free flight tube with defined length [Wysocki *et al.*, 2005]. The dependence of the kinetic energy of the ions from their net charge can be described by:

$$(ze)\Delta U = \frac{1}{2}mv^2 \qquad \text{[Eq. 1].}$$

With *ze* as the net charge, ΔU the applied potential field, *m* the mass and *v* the velocity of the gas-phase ion. By using equation 1 the velocity can be expressed as:

$$v = \sqrt{\frac{2ze\Delta U}{m}} \qquad \text{[Eq. 2].}$$

The flight time of the accelerated ions within the field-free flight tube is proportional to the length of the flight distance *L* and to the square root of the *m/z*-value of the analyte,

$$t = \frac{L}{v} = \frac{L}{\sqrt{2e\Delta U}}\left(\frac{m}{z}\right)^{1/2} \qquad \text{[Eq. 3].}$$

The ions are separated and form packets of ions while travelling through the flight tube. The focused ions packages hit the ion detector – usually a secondary electron multiplier - and are detected.

1. 5. 2. 2. Orbitrap mass analyzer

The orbitrap mass analyzer is an alternative detector to the ToF technique. It is an ion trap consisting of an inner and outer electrode (Fig. 7) that create an electric field. The entering ion bundles compensate the electrostatic attraction from the central electrode by the centrifugal force that origins from the initial tangential velocity [Hu *et al*., 2005]. The electric field forces the ions to oscillate in complex spiral patterns around the central electrode [Hardman & Makarov, 2003]:

$$U(r,z) = \frac{k}{2}\left(z^2 - \frac{r^2}{2}\right) + \frac{k}{2}(R_m)^2 ln\left(\frac{r}{R_m}\right) + C \qquad \text{[Eq. 4]}$$

with r and z as cylindrical coordinates, C is the constant, k the field curvature, and R_m as the characteristic radius [Hardman & Makarov, 2003]. The frequency of axial oscillation movement around the z-axis is directly related to the *m/z* ratios of the ions [Hardman & Makarov, 2003]:

$$\omega = \sqrt{(^{q}/_{m})k} \qquad \text{[Eq. 5].}$$

A Fourier transformation converts the time-dependent oscillation frequencies of the ions, which are detected at the equatorial positions, to accurate reading of the *m/z* values of the circulating bundles [Scigelova *et al*., 2006; Makarov, 2000].

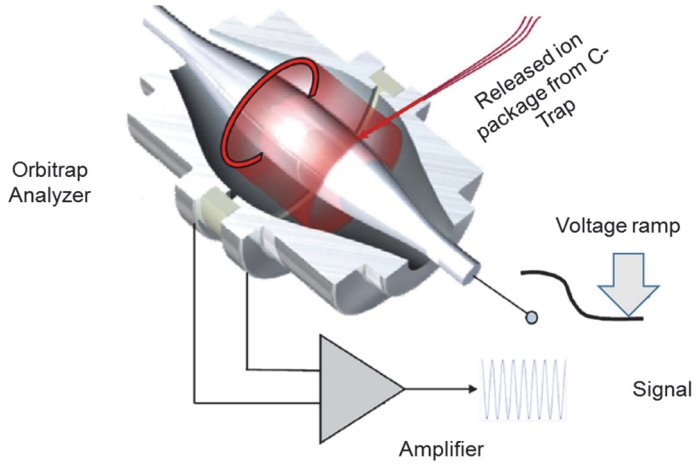

Fig. 7: Schematic view of an orbitrap mass analyzer. From C-trap Injected ions are oscillating around the central electrode. The outer electrode is interrupted by an insulating ceramic ring. The current induced by passing ions (indicated in red) is detected by electrodes in equatorial positions. The signal is amplified prior acquisition by a downstreamed amplifier. Figure adapted with permission from: Zubarev, R. A. & Makarov, A, 2013].

1. 5. 3. Fragmentation techniques

A widely used technique in MS/MS mass spectrometry to fragment peptides or proteins is collision induced dissociation (CID). The gas-phase ions are activated by collision with an inert gas, like argon or nitrogen, in the collision cell. This leads to conversion of the kinetic energy of the ions into intramolecular vibrational energy that is distributed all within entire ion. As the vibrational energy exceeds a certain threshold, covalent peptide bonds break and fragments of the precursor are generated. In the case of CID the weakest bond, the amide bond within the backbone of a protein, is broken resulting in b- and y- ion series.

Electron transfer dissociation (ETD) is an alternative method to fragment peptides and proteins. ETD is considered as "soft" fragmentation technique that does not destroy post-translational modifications. The general process is that an electron is transferred from a radical anion to a protonated peptide bond. This transfer induces fragmentation of the peptide backbone, causing cleavage of the Cα-N bond that generates a series of c- and z- ions [Coon *et al*., 2005]. The cleavage sites of a peptide are shown in Figure 8.

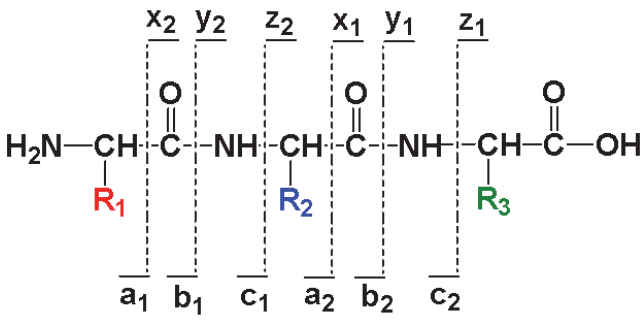

Fig. 8: Fragmentation pattern of protein backbone showing a series of a- and x- ions, b- and y- ions, and c- and z- ions.

1. 5. 4. Determination of structural alterations and protein dynamics by H/DX-MS

1. 5. 4. 1. Theoretical background

Hydrogen–deuterium exchange mass spectrometry is increasingly being recognized over the past two decades as an analytical tool for studying protein structure and dynamics in solution [Kim *et al.*, 1993, Zhang *et al*., 1993, Katta *et al.*, 1991] and has found its way from academia to industry due to automated workflow solutions and consequent improved reproducibility as well as increased sample throughput [Bobst *et al.*, 2008, Kaltashov *et al*., 2012, Houde *et al*., 2009, Berkowitz *et al.*, 2012].

This methodology relies on reversible isotopic labeling using the phenomenon that hydrogen-atoms of a protein exchange with heavy hydrogen isotopes of the surrounding solvent. This leads to H/D replacements that increase the mass of the protein by one Dalton (1.007 Da) per exchange event. In general, hydrogen atoms are covalently but labile bound to carbon, sulfur, phosphor, nitrogen or oxygen. All of these bound

hydrogens show characteristic exchange kinetics with the surrounding solvent. Carbon-bonded hydrogens (i.e. in alkyl residues) essentially do not exchange and, therefore, are not taken into account. In contrast, hydrogens in polar functional groups like sulfhydryl-(-R-SH) or hydroxy groups (-R-OH) exchange very fast ($\geq 10^{-3}$ sec) [Maier & Deinzer, 2005] and, thus, exchange rates of these cannot be tracked by LC-MS since the back-exchange immediately occurs during the chromatographic step. Amide hydrogens in the peptide backbone exchange in rates (seconds to hours) that can be experimentally observed in real time by LC-MS analysis [Bai *et al.*, 1993].

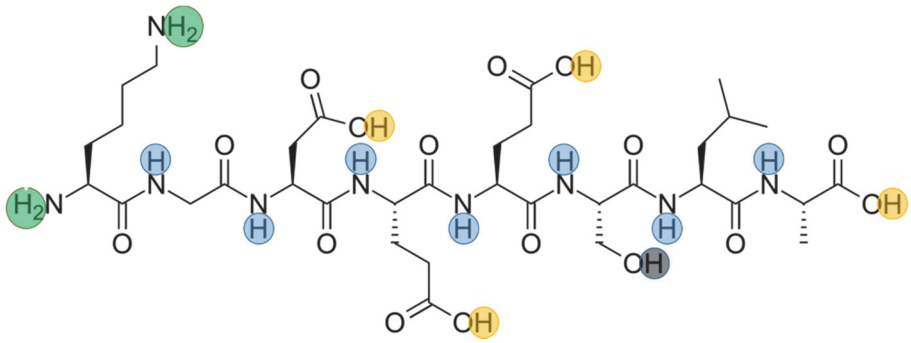

Fig. 9: Different types of hydrogen within a peptide sequence. Blue: Backbone amide hydrogens (trackable in terms of H/D exchange); not highlighted: Alkyl hydrogens (not trackable; exchange too slow); black: Hydroxyl hydrogens (not trackable; exchange too fast); orange: Carboxyl hydrogens (not trackable; exchange too fast).

Amide hydrogen exchange of proteins in aqueous solutions is catalyzed by hydroxide ions down to pH 3 and below that by hydronium ions. Thus, the exchange kinetics can be described as follows [Englander, 2006]:

$$k_{ch} = k_{int,A}\,[H^+] + k_{int,B}\,[OH^-] + k_{int,W}\,[H_2O] \qquad \text{[Eq. 6].}$$

Where k_{ch} describes the chemical exchange rate, k_{int} the intrinsic second order exchange rate constants for $[H^+]$, $[OH^-]$ and $[H_2O]$ as illustrated for the acid-catalyzed A, the base catalyzed B and the water catalyzed reaction C [Morgan *et al.,* 2009; Englander, 2006]. The individual exchange kinetics of each amide hydrogen depends on extrinsic factors like pH-value and temperature as well as intrinsic factors like local inductive effects of adjacent side chains, steric hindrance, solvent accessibility and structural arrangement [Englander *et al.*, 1983; Bai *et al.*, 1993].

Chemical exchange rates of amide hydrogens have a minimum at pH 2-3 [Walters *et al.*, 2012] as illustrated in the schematic log k_{ex} versus pH plot in Figure 10 and described by Thévenon-Emeric and co-workers [Thévenon-Emeric *et al.*, 1992]. The high pH sensitivity is described to show a tenfold increase of k_{ex} for each pH unit [Molday *et al.,* 1972, Englander *et al.*, 1983, Hvidt, 1964] for the backbone amide hydrogens.

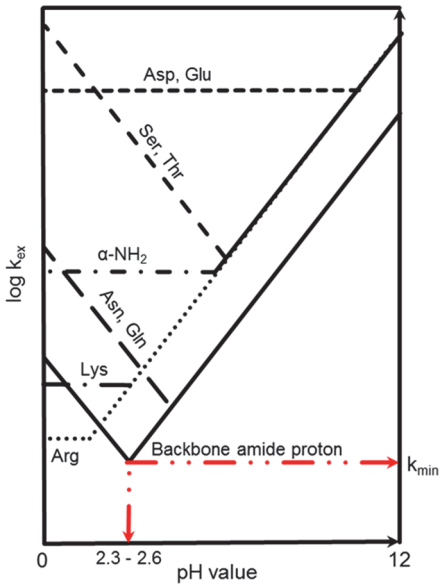

Fig. 10: Schematic pH dependency of exchange rates of different hydrogens located in the protein backbone and amino acid side chains.

Another extrinsic factor drastically influencing the hydrogen exchange rate is the temperature drastically increasing k_{ex} by elevation [Bai et al., 1993]. The temperature dependency follows the Arrhenius equation:

$$k_{exTi} = k_{exTex} e^{\left(E_a\left[\frac{1}{T_i} - \frac{1}{T_{ex}}\right]/R\right)} \qquad \text{[Eq. 7]}$$

Where k_{exTi} is the rate of exchange at any desired temperature, k_{exTex} the exchange rate at the initial temperature, E_a the activation energy for the exchange reaction and R is the gas constant [Bai *et al.*, 1993]. Walters and co-workers also describe ionic strength as significantly influencing k_{ex} and as a very important parameter that has to be considered when setting-up an H/DX experiment e. g. regarding formulation or quench buffers [Walters *et al.*, 2012].

By applying constant extrinsic parameters, backbone amide H/D exchange is exclusively affected by structural and dynamic attributes of the protein since the intrinsic factors that influence k_{ex} are limited to structural and dynamical features like local inductive effects of adjacent side chains, steric hindrance, solvent accessibility and structural arrangement [Englander *et al.*, 1983; Bai *et al.*, 1993]. Thus, exchange rates are directly related to conformational dynamics of structural elements and the conformational arrangement of the entire molecule [Kim *et al.*, 1993; Yong-Sung *et al.*, 2003; Xuguang *et al.*, 2004].

Amide hydrogens play a key role in the formation of secondary and tertiary structure elements. Subsequently, folding and refolding of these elements is essential for exchange events because the backbone amide hydrogen bonds must be broken to get replaced by deuterium. The exchange reaction can be described, as:

$$N - H_{folded} \overset{k_0}{\leftrightarrow} N - H_{unfolded} \overset{k_i}{\leftrightarrow} N - D_{unfolded} \overset{k_c}{\leftrightarrow} N - D_{folded} \qquad \text{[Eq. 8]}$$

with k_o, k_c and k_i as opening, closing and intrinsic exchange rate constants. The resulting rate of exchange (k_{ex}) is given by equation:

$$k_{ex} = \frac{k_0 k_i}{k_0 + k_i + k_c} \qquad \text{[Eq. 9].}$$

This mechanism was first postulated by Linderstrøm-Lang and implicates that when unfolding occurs, a kinetic competition is initialized between the chemical exchange rate and structural refolding. In cases where $k_0 >> k_i$, frequent unfolding of structural elements is necessary for any H/D exchange event. Regions that experience this mechanism are called EX2 regimes [Englander *et al.*, 1983; Hvidt *et al.*, 1966]. In this case equation 9 can be described as followed:

$$k_{ex} = \frac{k_o * k_i}{k_c} \qquad \text{[Eq. 10].}$$

Revealing the equilibrium constant (K_U) for local structural fluctuations:

$$\frac{k_{ex}}{k_i} = \frac{k_o}{k_c} = K_u \qquad \text{[Eq. 11].}$$

Using these postulations it is possible to calculate the protection factor (P_f) for every amide hydrogen in the backbone. Here, the inverse ratio of k_i and k_{ex} is considered:

$$P_f = \frac{k_i}{k_{ex}} = \frac{1}{K_u} \qquad \text{[Eq. 12].}$$

Consequently the inverse equilibrium constant can be used to calculate the thermodynamic stability of each amide hydrogen [Jaswal *et al.,* 2013]:

$$\Delta G_u = -RTlnK_u = RTlnP_f \qquad \text{[Eq. 13].}$$

In case, $k_0 << k_i$ the refolding process is slower than the exchange reaction and therefore H/D exchange is solely limited to the structural unfolding of protein segments. At every unfolding event all the amide hydrogens are exchanged. These are referred to EX1 regimes [Englander *et al*., 2006] and can be described by the following equation:

$$k_{ex} = k_o \qquad \text{[Eq. 14].}$$

EX2 and EX1 show characteristic signatures in an H/DX experiment. EX1 regimes reveal bimodal pattern implicating two different populations in the sample – a less deuterated and a highly deuterated population. The EX2 regime displays binomial distribution of isotope pattern that describes random exchange [Maier & Deinzer, 2005]. Figure 11 illustrates the occurrence of the different kinetic mechanisms in H/DX-MS raw spectra.

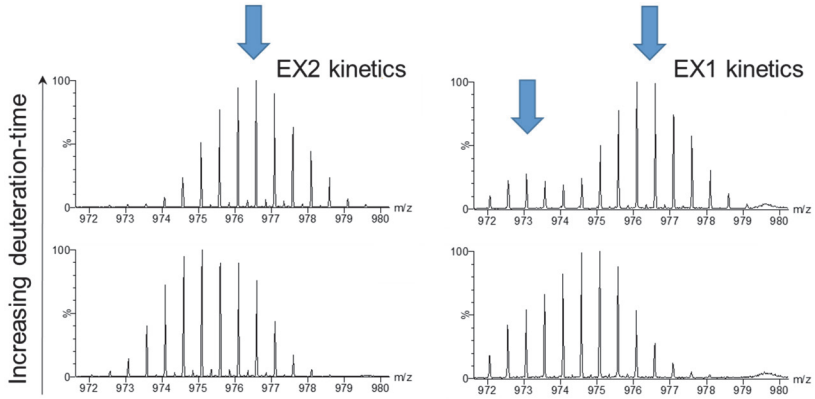

Fig. 11: Isotopic distribution characteristic for EX2 and EX1 kinetics. Peptides showing EX2 kinetics gradually incorporate the deuterium over time, giving binomial distribution of isotopic peaks. EX1 peptides reveal bimodal distribution implicating different populations with high dynamic behavior (highlighted with blue arrows).

1. 5. 4. 2. Experimental set-up of an H/DX-MS analysis

The procedure of an H/DX-MS experiment can be roughly divided into five main stages:

(1) Incubation of the protein in deuterium buffer, (2) quenching of the exchange reaction, (3) proteolytic digestion, (4) separation of peptides using reversed-phase liquid chromatography, (5) identification and mass determination of generated peptides (Fig. 12).

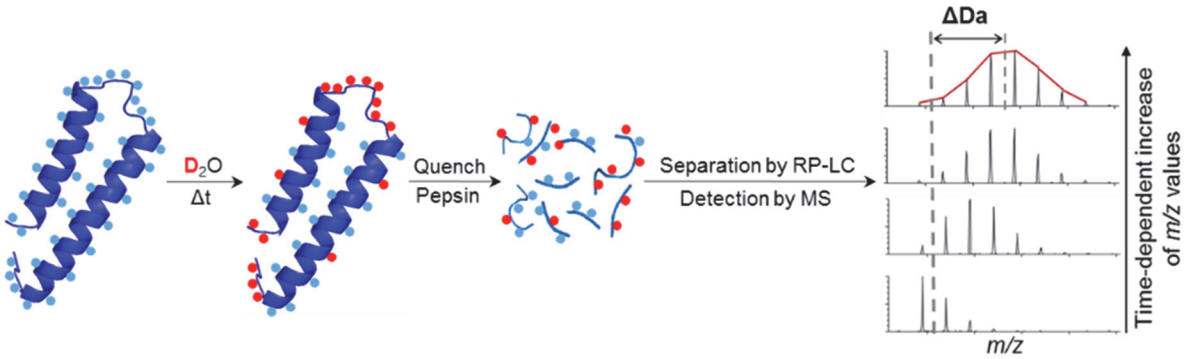

Fig. 12: Schematic illustration of an H/DX-MS experiment. First, the protein is incubated for pre-defined times in D_2O buffer. Afterwards, the exchange reaction is quenched at low temperature and low pH and the sample is subjected to proteolytic digestion. The generated peptides are separated by reversed-phase liquid chromatography and introduced into a coupled mass spectrometer for identification and mass determination.

Deuterium incubation generally occurs in a 10-100 fold excess of deuterium buffer depending on the initial protein concentration at 20-25°C for pre-defined incubation-times at near neutral pH value in order to favor the exchange reaction. Afterwards, the sample is transferred into pre-chilled (0 °C) quench buffer in a ratio of 1:1 to quickly slow down the exchange rates of the amide hydrogens. The quench buffer contains a strong buffer system to retain its acidic pH-value – generally pH 2.35 to 2.5 – also after mixing with the deuterated sample. By decreasing the pH value k_{ex} is pushed to the minimum as already mentioned in section 1. 5. 4. 1. In addition, the quench buffer also includes certain amounts of chaotropic salts (e.g. guanidinium hydrochloride) and reductive agents (e.g. TCEP) to denature the analyzed protein sample. The labeled and denatured sample is afterwards subjected to on-line pepsin digestion. During this step the sample is non-specifically dissected into small peptides at constant temperature (usually 20 °C). It is crucial to use pepsin since this protease has its highest activity under acidic conditions. The resulting peptides are trapped on a C18 column to collect them from the pepsin column flow-through and to remove the high amounts of salts. In the next step, the deuterated peptides are eluted from the trapping column and separated on a reversed-phase analytical column and consequently introduced into an ESI mass spectrometer. The chromatographic step solely results in spatially separated peaks since this step occurs at 0 °C and with steep and fast gradients to decrease the level of deuterium back-exchange. In order to increase peak capacity and to avoid overlapping mass spectra during mass acquisition the eluting peptides can additionally be separated by ion-mobility (IM) within the mass spectrometer.

IM is a separation technique that separates ion mixtures depending on the time each specie takes to travel in contrary to the direction of an inert gas-flow (usually N_2) through a pressurized cell under the influence of a weak electric field. Thus, emigration time depends on size, shape, mass and charge of the analyte ion. Following ion-mobility separation, the pepsin cleaved peptide ions are unambiguously identified by accurate mass and tandem MS using MS^E fragmentation. MS^E is based on collision-induced fragmentation resulting in *b*- and *y*-ion fragments. It uses a data independent acquisition (DIA) approach in which parallel alternating scans are acquired at either low collision in the collision cell to obtain precursor ion information, or high collision energy to

obtain accurate masses of generated fragments (*b*- and *y*-ion series), precursor ions and neutral loss information without isolating one single precursor [Plumb *et al*., 2006].
The by MS^E identified fragments are assigned to their precursor mass, drift-time and LC-retention time. This is performed by using data bank search algorithms (e.g. PLGS).

1. 5. 4. 3 H/DX-MS data processing and evaluation

Due to the high sensitivity and strong dependence on various parameters, hydrogen-deuterium exchange analyses are always performed in head-to-head measurements of two states [Burkitt & O´Connor, 2008]. Consequently H/DX-MS reveals relative results instead of absolute by assessing differences in folding, binding or dynamics.
Within an analysis, time-dependence of deuterium uptake is always measured relative to the non-deuterated sample along with the labeled samples.
In a first step, the eluting peptides are identified by using MS^E fragmentation and subsequent databank search and assignment to their characteristic retention- and drift-time. These data are then exported into an H/DX evaluation software (e.g. DynamX® or HX-Express) in parallel with the raw data of the deuterated samples. Within this, time-dependent deuterium incorporation is calculated. First, peak detection within the retention-time and drift-time of the non-deuterated sample, including isotope peak detection is performed and the different charge-states of the peptides are clustered. In a second step, mass increase of the labeled peptides is calculated and compared to the unlabeled ones. For this, the width ($\Delta m/z$) of the isotopic distribution is determined at a specified percentage of peak intensity (typically 20 %) and an empirical peak-to-peak envelope is laid over the isotopic peaks [Weis & Engen, 2006]. In cases where isotopic peaks do not exceed the base peak intensity threshold, linear interpolation is performed [Weis & Engen, 2006]. For isotopic peak distribution where isotopic peaks below the threshold are solely on one side of the pattern, direct linear extrapolation at the monoisotopic peak is performed to define the minimum *m/z* value. The search algorithm searches from low *m/z* to higher *m/z* values to make sure that also bimodal distributions (EX1 regime) are detected [Weis & Engen, 2006].
Using these envelopes the centroid – geometric center on the z-axis - is calculated:

$$Centroid = \frac{\sum(^{m}/_{z})_i * I_i}{\sum I_i} \quad \text{[Eq. 15]}$$

With *I* as spectral intensity at each *m/z* value, which is subsequently used to determine the mass of the peptide at this specific incubation time-point in the center of the envelope:

$$M = z * centroid - M(H^+) * (z - 1) \quad \text{[Eq. 16]}$$

This result obtained in Eq. 16 is now independent from the charge-state and can be used to calculate the mass increase (*D(t)*) relative to the undeuterated peptide *M (t = 0)*:

$$D(t) = M(t) - M(t = 0) \quad \text{[Eq. 17]}$$

The mass increase of every peptide is considered for all detected charge-states which are merged and averaged for final mass determination [Weis & Engen, 2006].

1. 6. Study objectives

1. 6. 1. Unravelling the structure-function relationship of IgG2 disulfide isoforms

Disulfide isoform heterogeneity of IgG2 antibodies enabled by the close proximity of cysteines in the upper hinge and Fab regions is a well-known phenomenon. This shuffling was described to influence the global structure of the distinct isoforms and to impact bioactivity in some cases [Dillon *et al.*, 2008; Liu *et al.*, 2014; Zhang *et al.*, 2015 & Wang *et al.*, 2011]. It is of high relevance for IgG2 biopharmaceutical development to understand the correlations between isoform pattern and structure/bioactivity in detail since they can provide insight into the criticality of the isoform ratio in the final product. In this study, the structure-function relationship of the single main isoforms A, A/B and B had to be investigated to rate the criticality of isoform ratio present in the administered drug product.

1. 6. 2. Dimeric structures and the major dimerization pathway of an IgG1

Aggregation esp. dimer formation of biopharmaceutical products is described to be a complex mechanism [Philo *et al*., 2008] in which besides native present molecules also post-translational modifications on the surface might play an important role [Wang *et al*., 2009; Wu *et al.*, 2010; Li *et al.*, 2016]. Due to the complexity it is challenging to unambiguously to determine the reasons for self-assembly as well as the resulting dimer structures esp. in IgG drug products [Plath *et al.,* 2016; Paul *et al.,* 2012 & Deperalta *et al*., 2013]. Since aggregates in biopharmaceuticals are supposed to potentially influence biological functions [Paul *et al.*, 2012], reduce potency, induce/enhance immune responses by initiating anti-drug antibody production [Rosenberg, 2006; Sauerborn *et al*., 2010; van Beers *et al.,* 2010] it is of high relevance to get detailed insights into the dimerization process and identify aggregation prone regions. For this reason, the structure-function of different dimeric species of an IgG1 drug molecule should be investigated. Furthermore, aggregation triggering mechanisms within the dimer should be determined to assess the reason for this IgG1 showing enhanced aggregation propensity.

1. 6. 3. Phosphorylation caused structural rearrangement of c-Src kinase during activation

c-Src kinase plays an important role in numerous signal transduction pathways and its activity is tightly regulated by a sophisticated mechanism involving one dephosphorylation- and one phosphorylation-step. While the first part during activation is well understood, the details of the final conformational switching mechanism caused by a phosphorylation on Tyr416 still remains elusive. Here, a comprehensive investigation of the structural transitions within c-Src upon autophosphorylation on Tyr416 was performed by a combined approach using molecular dynamics simulations, various biophysical techniques and H/DX-MS. This case study demonstrates the general power of the combination of bioanalytics, H/DX-MS and MD simulations to reveal the dynamics of protein conformational states in a detailed manner.

2. Experimental procedures

2. 1. Material

2. 1. 1. Chemicals

1-Anilino-8-Naphthalene Sulfonate	Sigma-Aldrich Corp., St. Louis, USA
2,2'-azino-di-(3-ethylbenzthiazoline-6-sulfonate)	Sigma-Aldrich Corp., St. Louis, USA
Acetic acid – D1 deuterated	Merck KGaA, Darmstadt, Germany
Acetic acid (glacial)	Merck KGaA, Darmstadt, Germany
Acetonitrile	Merck KGaA, Darmstadt, Germany
Adenosyl-imidodiphosphate	Roche, Mannheim, Germany
Acrylamide	Carl Roth GmbH, Karlsruhe, Germany
Ammonium acetate	Sigma-Aldrich Corp., St. Louis, USA
Cystamine dihydrochloride	Sigma-Aldrich Corp., St. Louis, USA
Cysteine	Sigma-Aldrich Corp., St. Louis, USA
Deuterium chloride	Sigma-Aldrich Corp., St. Louis, USA
Deuterium oxide (99.9 %)	Sigma-Aldrich Corp., St. Louis, USA
Di-sodium-hydrogenphosphate dihydrate	Merck KGaA, Darmstadt, Germany
Dithiothreitol	Sigma-Aldrich Corp., St. Louis, USA
D-Sorbitol	Sigma-Aldrich Corp., St. Louis, USA
ESI-L Low Concentration Tuning Mix	Agilent Tech. Inc., Santa Clara, USA
Ethylen-diamintetraacetate (0.5 M)	Sigma-Aldrich Corp., St. Louis, USA
Formic acid	Thermo Scientific Inc., Massachusetts, USA
Glycine	Sigma-Aldrich Corp., St. Louis, USA
Guanidinium hydrochloride (8 M)	Sigma-Aldrich Corp., St. Louis, USA
HBS P+	GE Healthcare, Freiburg, Germany
Hydrochloric acid	Merck KGaA, Darmstadt, Germany

Iodacetamide	Sigma-Aldrich Corp., St. Louis, USA
Isopropanole	Merck KGaA, Darmstadt, Germany
Magnesium chloride	Sigma-Aldrich Corp., St. Louis, USA
Methanol	Merck KGaA, Darmstadt, Germany
Ortho-phosphoric acid (85%)	Merck KGaA, Darmstadt, Germany
Phosphate buffered saline	Thermo Scientific Inc., Massachusetts, USA
Polysorbate 20	Sigma-Aldrich Corp., St. Louis, USA
Polysorbate 80	Sigma-Aldrich Corp., St. Louis, USA
Potassium chloride	Sigma-Aldrich Corp., St. Louis, USA
Potassium hydroxide	Merck KGaA, Darmstadt, Germany
Potassium phosphate dibasic	Merck KGaA, Darmstadt, Germany
Potassium phosphate monobasic	Merck KGaA, Darmstadt, Germany
Pierce™ LTQ Velos ESI Positive Ion Calibration Solution	Thermo Scientific Inc., Massachusetts, USA
Silver behenate	TCI Deutschland GmbH, Eschborn, Germany
Sodium acetate	Sigma-Aldrich Corp., St. Louis, USA
Sodium chloride	Merck KGaA, Darmstadt, Germany
Sodium citrate tribasic dihydrate	Sigma-Aldrich Corp., St. Louis, USA
Sodium deuteroxide (40 %)	Sigma-Aldrich Corp., St. Louis, USA
Sodium-di-hydrogenphosphate dihydrate	Merck KGaA, Darmstadt, Germany
Sodium hydroxide (1M)	Merck KGaA, Darmstadt, Germany
Tris-HCl (1M)	Thermo Scientific Inc., Massachusetts, USA
Tris(2-carboxyethyl)phosphin (TCEP)	Thermo Scientific Inc., Massachusetts, USA
Trifluoracetic acid	Merck KGaA, Darmstadt, Germany

2. 1. 2. Proteins, enzymes and standard peptides

Leucine enkephaline	Waters Corp., Milford, USA
Lysyl endopeptidase	Wako Chemicals GmbH, Neuss, Germany
Trypsin	Promega Corp., Madison, USA
Poroszyme™ (immobilized pepsin)	Applied Biosystems Inc., Foster City, USA
Fabricator™ (IdeS)	Genovis AB, Lund, Sweden
IgG1 for dimer studies	Sandoz AG, Holzkirchen, Germany
IgG2κ	Sandoz AG, Holzkirchen, Germany
IgG2 antigen	Peprotech Inc., Rocky Hill, USA
c-Src (chicken)	E. E. Boczek (plasmid: pFastBacHTA)
c-SrcK295R	E. E. Boczek (plasmid: pFastBacHTA)
c-SrcY416F	E. E. Boczek (plasmid: pFastBacHTA)
Alkaline phosphatase	Roche AG, Mannheim, Germany
Aprotinin	Sigma-Aldrich Corp., St. Louis, USA
Carbonic anhydrase	Sigma-Aldrich Corp., St. Louis, USA
Holo-transferrin	Sigma-Aldrich Corp., St. Louis, USA
IgG1	Novartis generic reference substance
Ovalbumin	Sigma-Aldrich Corp., St. Louis, USA
Thyroglobulin	Sigma-Aldrich Corp., St. Louis, USA
Rapid PNGase F	New England Biolabs GmbH, Frankfurt/Main, Germany

2. 1. 3. Chromatographic columns

CSH™ C18 (1.7 µm; 1.0 x 100 mm)	Waters Corp., Milford, USA
MabPac® WCX-10 (4 x 250 mm)	Thermo Scientific Inc., Massachusetts, USA
MabPac® SCX-10 (4 x 250 mm)	Thermo Scientific Inc., Massachusetts, USA
MabPac® WCX-10 (9 x 250 mm)	Thermo Scientific Inc., Massachusetts, USA
MabPac® SCX-10 (9 x 250 mm)	Thermo Scientific Inc., Massachusetts, USA
BEH C8 (1.7 µm, 2.1 x 100 mm)	Waters Corp., Milford, USA
BEH200® SEC (1.7 µm, 4.6 x 300 mm)	Waters Corp., Milford, USA
Acclaim® PepMap100 C18 (75 µm x 2 mm, 3 µm, 100 Å)	Thermo Scientific Inc., Massachusetts, USA
Acclaim® PepMapC18 (75 µm x 250 mm, 2 µm, 100 Å)	Thermo Scientific Inc., Massachusetts, USA
Acclaim® PepMapRSLC-C18 (75 µm x 150 mm, 2 µm, 100 Å)	Thermo Scientific Inc., Massachusetts, USA
TSKgel G3000SWXL (7.8 mm x 300 mm)	Tosoh Corp., Tokyo, Japan
BEH® C8 (2.1 x 100 mm 1.7µm)	Waters Corp., Milford, MA, USA
MabPacRP® (1 x 50 mm, 4 µm)	Thermo Scientific Inc., Massachusetts, USA
PA ID sensor cartridge (2.1 mm x 30 mm, 2 µm)	Applied Biosystems, Foster City, USA
MassPrep™ micro desalting column (2.1 x 5 mm, 20 µm, 100 Å)	Waters Corp., Milford, USA
BEH130 C18 (2.1x100mm, 1.7µm)	Waters Corp., Milford, USA
Yarra® SEC 30000 (300 x 4.6 mm; 3 µm)	Phenomenex Inc., Torrance, USA

2. 1. 4. Instrumentation

Biacore® T100	GE Healthcare GmbH, Freiburg, Germany
Biacore® 3000	GE Healthcare GmbH, Freiburg, Germany
Leap® robot	Leap Technologies, Carrboro, NC
nanoAcquity® UPLC	Waters Corp., Milford, USA
Synapt® G2-S qToF	Waters Corp., Milford, USA
H/DX manager®	Waters Corp., Milford, USA
UltiMate™ 3000 RSLCnano	Thermo Scientific Inc., Massachusetts, USA
QExactive® Plus orbitrap	Thermo Scientific Inc., Massachusetts, USA
NanoDSF Prometheus® NT.48	NanoTemper Technologies, Munich, Germany
BioSAXS-1000 (HF007 Cu-target)	Rigaku Corp., Tokyo, Japan
1260 series HPLC	Agilent Tech. Inc., Santa Clara, USA
1200 series HPLC	Agilent Tech. Inc., Santa Clara, USA
1290 series HPLC	Agilent Tech. Inc., Santa Clara, USA
FluoroMax-3 fluorescence spectrometer with tempering cuvette holder	Spex Forensics, Edison, USA
Cary 100 Bio UV-VIS-spectrophotometer	Varian Inc., Palo Alto, USA
Cary 50 Bio UV-VIS-spectrophotometer	Varian Inc., Palo Alto, USA
Analytical ultracentrifuge ProteomeLab XL-I	Beckmann Coulter Corp., Brea, USA
Amazon ETD ion trap	Bruker Corp., Billerica, USA
Impact HD QqTOF	Bruker Corp., Billerica, USA
Compact QqTOF	Bruker Corp., Billerica, USA
J-720 spectropolarimeter	Jasco GmbH, Grossumstadt, Germany

Typhoon 9200 phosphoimager	GE Healthcare GmbH, Freiburg, Germany

2. 1. 5. Computer software

MassLynx®	Waters Corp., Milford, USA
LeapShell ®	Leap Technologies, Carrboro, NC
Chromeleon® 6.8	Thermo Scientific Inc., Massachusetts, USA
Chromeleon® 7.0	Thermo Scientific Inc., Massachusetts, USA
DynamX® 3.0	Waters Corp., Milford, USA
GeneData® 10.5	Genedata GmbH, Munich, Germany
HyStar®	Bruker Corp., Billerica, USA
Bruker Data Analysis	Bruker Corp., Billerica, USA
PyMol® 1.8.4.2	Delano Scientific LLC, Schrödinger
Origin™ 7	OriginLab Corp., Northampton, USA
ProteinLynx Global Server (PLGS®) 2.5.3	Waters Corp., Milford, USA
PR.Control®	NanoTemper Technologies, Munich, Germany
SAXS Lab software 3.0	Rigaku Corp., Tokyo, Japan
Coral	Petoukhov & Svergun, 2005
ATSAS package 2.7.0	Petoukhov *et al.,* 2012
NAMD	Philips *et al.,* 2005
VMD	Humphrey *et al.,* 1996
CHARMM27 force field	MacKerell *et al.*, 1998
ExPASy bioinformatics resource portal	Kuznetsov *et al*., 2012
NCBI blast	National Center for Biotechnology Information (NCBI), Bethesda, USA

Microsoft Office® 2013	Microsoft, Unterschleißheim, Germany
Adobe Reader 8.0	Adobe Inc., San Jose, USA
CDNN®	Bohm *et al*., 1992
Sedfit 15.01b	Schuck, 2000
Sedphat 12.1c	Schuck, 2003
Gussi 1.1.0	C. Brautigam, 2015
ImageQuant®	GE Healthcare GmbH, Munich, Germany

2. 1. 6. Miscellaneous material and laboratory equipment

Slide a lyzer® dialysis	Thermo Scientific Inc., Massachusetts, USA
Quartz cuvettes (0.5 mm)	Starna Optiglass Ltd., Hainault, UK
CM 5 chip	GE Healthcare GmbH, Freiburg, Germany
Centricon® 30kDa spin filter	Amicon GmbH, Witten, Germany
Protein A sensor chip	GE Healthcare GmbH, Freiburg, Germany
PathHunter®/ProLabel®/ProLink™ detection kit	DiscoverX Corp., Fremont, USA
Assay complete U2OS cell culture kit 14	DiscoverX Corp., Fremont, USA
Assay complete cell plating 22 reagent	DiscoverX Corp., Fremont, USA
Balance LP6200S	Sartorius, Göttingen, Germany
SpeedVac RVC 2-18	Martin Christ, Osterode, Germany
WTW pH540 GLP pH meter	WTW GmbH & Co. KG, Weilheim, Germany
Lyophilisator Alpha 1-2 / LD Plus	Martin Christ, Osterode, Germany
Centrifuge 5415D	Eppendorf, Hamburg Germany

Magnetic stirrer MR3001	Heidolph, Kelheim, Germany
Vortexer Ika MS3 basic	Ika, Staufen im Breisgau, Germany
Thermomixer comfort	Eppendorf, Hamburg, Germany
Rotilabo® Centrifuge	Carl Roth, Karlsruhe, Germany
Pipette tips (10 – 1000 µl)	StarLab GmbH, Hamburg, Germany
PE tubes (50/15 ml)	Greiner & Söhne GmbH & Co. KG, Nürtingen, Germany
Safe-lock tubes (0.5 – 2.0 ml)	Eppendorf AG, Hamburg, Germany
HPLC vials (250 µl / 1.0 ml)	Agilent Tech. Inc., Santa Clara, USA
PD-10 column	GE Healthcare GmbH, Freiburg, Germany
Prometheus NT.48 Series nanoDSF Grade High Sensitivity Capillaries	NanoTemper Technologies, Munich, Germany
Water purification system MilliQ® Integral	Merck Millipore, Billerica, USA

2. 2. Methods

2. 2. 1. General protein preparation procedures

2. 2. 1. 1. IgG2 disulfide isoform enrichment / isolation

The IgG2 drug substance (WSTD) consisted of a mixture of IgG2 disulfide isoforms (A, A/B and B). To obtain higher levels of either isoform A or isoform B, redox enrichment was performed by using two different kinds of redox conditions [Dillon *et al.*, 2008]. In this way rearrangement of disulfide bonds was initialized to form either isoform A or isoform B.

For this, two separate stock-solutions were prepared with 50 mM cysteine and 50 mM cystamine dissolved in 200 mM Tris-HCl (pH 8.0). To generate isoform A, 26.65 µl of 200 mM Tris-HCl (pH 8.0), 50 µl cysteine stock-solution, 10 µl cysteine stock-solution,

56.25 µl GdmCl (8 M) and 357.1 µl WSTD (70 µg/µl) were mixed ending-up in final concentrations of 5 mM cysteine, 1 mM cystamine, 0.9 M GdmCl and 50 µg IgG2 with a final volume of 500 µl. The mixture was mixed and incubated for 48 h at 2 - 8 °C.
To generate isoform B 133.0 µl 200 mM Tris-HCl (pH 8.0), 1.7 µl cystamine stock-solution, 8.3 µl cysteine stock-solution and 357.1 µl WSTD were mixed resulting in concentrations of 0.83 mM cysteine, 0.17 mM cystamine and 50 µg/µl IgG2 in a final volume of 500 µl. The mixture was subsequently incubated for 48 h at 2 - 8 °C.
The enriched samples were subsequently fractionated by cation exchange chromatography. Strong cation exchange chromatography (SCX; see chapter 2.2.3.2) was used to isolate isoform B and weak cation exchange chromatography (WCX; see chapter 2.2.3.3.) to separate isoform A. Since isoform A/B cannot be enriched this isoform was directly fractionated out of the starting material (WSTD) using the above described strong cation exchange chromatographic method as described in chapter 2.2.3.2.

Pooled fractions were subsequently concentrated and buffer exchanged in 18 mM acetate, 4.6% sorbitol (pH 5.2) using Centricon® 30 kDa filter (Amicon GmbH, Witten, Germany) and analyzed by SCX for purity estimation (see Fig. 18).
For forced degradation study the isolated fractions and the starting isoform mixture were diluted in 18 mM acetate, 4.6% sorbitol (pH 5.2) to a final concentration of 1 mg/ml to a final volume of 200 µl and subjected to 40°C incubation for pre-defined time-points 0 d, 2 d, 4 d, 1 w, 2 w and 4 w. Afterwards, the samples were flash-frozen in liquid nitrogen and stored at -80°C until analysis.

2. 2. 1. 2. IdeS digestion of immunoglobulins

Antibody samples were diluted using 50 mM Na-phosphate, pH 7.2 to a final concentration of 1 µg/µl. 50 units of IdeS lyophilisate (Genovis AB, Lund, Sweden) was reconstituted in 100 µl 50 mM Na-phosphate (pH 7.2). 50 µl IdeS solution were added to 50 µL IgG solution. The samples were mixed and centrifuged. Afterwards they were incubated at 37°C for 60 min. No inactivation of the enzyme was performed sine no over-digestion

takes place by using this enzyme. Storage of digested samples occurred at 2-8°C until analysis.

2. 2. 1. 3. Limited Lys-C digestion of immunoglobulins

To obtain Fab and Fc fragments for domain-specific analysis limited Lys-C (Wako Chemicals GmbH, Neuss, Germany) digestion was performed. In the native folded state, Lys-C cleaves the IgG right above the hinge region to release the single fragments.
100 µg IgG in 100 mM Tris buffer pH 7.3 with a volume of 100 µl was prepared. Subsequently, 1 µl of 0.5 µg/µl Lys-C in H_2O was added and gently mixed. Digestion occurred at 37°C for 15 minutes. The reaction was stopped by adding 25 µl of a 25% acetonitrile (ACN) / 0.75% formic acid (FA) solution. The sample was stored at 2-8°C until analysis.

2. 2. 1. 4. Reduction of immunoglobulins

Reduction of IgG molecules was performed to create free light and heavy chains. The sample was diluted to 0.5 mg/ml in 50 mM phosphate buffer pH 7.2. 12.5 µl TCEP solution (51 µg/µl; in 50 mM phosphate buffer pH 7.2) were added to 100 µl IgG solution. The sample was mixed and incubated for 15 min at 70°C. The sample was stored at 2-8°C until analysis.

2. 2. 1. 5. De-N-glycosylation of immunoglobulins

The IgG sample was diluted to a final concentration of 1 mg/ml using 50 mM phosphate buffer (50 mM Na-phosphate, pH 7.2) to a final volume 50 µl. 1.5 µl rapid PNGase F (New England Biolabs GmbH, Frankfurt/Main, Germany) were added to the sample [Tarentino *et al.*, 1985]. The sample was gently mixed and spinned down. De-N-glycosylation occurred at 50°C for 30 min. The sample was stored at 2-8°C until analysis.

2. 2. 2. Biophysical methods [in cooperation with Dr. E. Boczek]

2. 2. 2. 1. Kinase activity measurements

c-Src full length, its Y416F mutant and the c-Src kinase domain were expressed and purified as described (Boczek *et al.*, 2015, Seeliger *et al.*, 2005). To achieve full Y416-phosphorylation, the kinases were incubated with 10 mM ATP and 5 mM $MgCl_2$ overnight and subsequently purified using a PD-10 column (GE Healthcare GmbH, Freiburg, Germany). For activity measurements of c-Src variants, 320 nM of the respective kinase were incubated at 30 °C for 30 minutes in Src-buffer (40 mM Tris-HCl, 150 mM NaCl, 5 % Glycerine, 5 mM DTT, 10 mM $MgCl_2$, 1 mM $MnCl_2$, pH 7.5) supplemented with 40 µM [γ-^{32}P]-ATP with an activity of 0.5 µCi. A tenfold molar excess of acid-denatured enolase (Sigma-Aldrich Corp., St. Louis, USA) was used as a substrate. The reaction was stopped by adding Laemmli buffer and boiling the sample. The samples were separated by SDS-PAGE and transphosphorylation was detected by applying a phosphor image screen onto the gel. The screen was subsequently analyzed using a Typhoon 9200 phosphoimager and the program Image Quant (GE Healthcare GmbH, Freiburg, Germany). For K_M-determination, the kinase activity was measured in the presence of increasing amounts of [γ-^{32}P]-ATP.

2. 2. 2. 2. CD Spectroscopy and Thermal Transition

CD measurements were performed using a Jasco J-720 spectropolarimeter (Jasco GmbH, Grossumstadt, Germany) equipped with a Peltier element. Far-UV CD spectra were measured using 5 µM protein in Src-buffer (40 mM Tris pH 7.5, 150 mM NaCl, 5 % Glycerin, 5 mM DTT) in a 0.1-mm quartz cuvette between 260 and 200 nm. The thermal unfolding of the proteins was monitored at 207 nm measuring changes of the CD signal between 20 and 80 °C, at a heating rate of 20 °C per h. The curves were fitted to a sigmoidal transition.

2. 2. 2. 3. ANS Binding Assay

A concentration of 1.6 µM of the respective kinase variant was incubated with 30 µM ANS in Src buffer for 20 min at room temperature and subsequently analyzed in a FluoroMax-3 fluorescence spectrometer (Spex Forensics, Edison, USA) with an excitation wavelength of 380 nm and an emission wavelength of 470 nm. The obtained emission spectra of the proteins were normalized against the Src buffer blank.

2. 2. 2. 4. Tryptophan Quenching

Acrylamide (5 M) was titrated to a 500 nM Src kinase in Src buffer at 25 °C. Tryptophan fluorescence emission quenching upon excitation at 295 nm was recorded using a FluoroMax-3 fluorescence spectrometer (Spex Forensics, Edison, USA). The slit widths were set to 3 and 5 nm for excitation and emission, respectively.

2. 2. 2. 5. Aggregation Assay

Protein aggregation was monitored using a Varian Cary 50 UV/Vis spectrophotometer (Varian Inc., Palo Alto, USA) equipped with a temperature-adjustable cuvette holder. Aggregation of 2 µM c-Src was initiated by heat at 42 °C. The aggregation reaction was monitored at 350 nm over time as an increase in signal caused by turbidity.

2. 2. 2. 6. Nano differential scanning fluorimetry (DSF)

NanoDSF was performed on a Prometheus NT.48 fluorimeter (NanoTemper Technologies, Munich, Germany). Isolated isoforms were diluted in PBS to a concentration of 0.1 µg/µL and subsequently subjected to dialysis at room temperature overnight using Slide-A-Lyzer (Thermo Scientific Inc., Massachusetts, USA) 10 kD dialysis cassettes. Heating-rate during analysis was set to 1 K/min. During unfolding the intrinsic tryptophan fluorescence was tracked. Data analysis was performed using PR.Control.

2. 2. 2. 7. Surface plasmon resonance (SPR)

SPR measurements were performed on a BIACore 3000 (GE Healthcare GmbH, Freiburg, Germany) as capture assays. All injected samples were diluted in ready-to-use HBS-P+ buffer (0.01 M HEPES pH 7.4, 0.15 M NaCl, 0.005% v/v Polysorbate 20; GE Healthcare GmbH, Freiburg, Germany).

For capturing of IgG2, a series S sensor chip Protein A (immobilized with Protein A; GE Healthcare GmbH, Freiburg, Germany) was used. The flow-rate was set to 20 µL/min and the final capture level amounted to 300 - 400 RU. The target molecule was injected in the concentrations of 20 nM, 10 nM, 5 nM, 0 nM. For each cycle the target molecule was allowed to associate for 600 sec and dissociate for 1200 sec. Regeneration occurred using 10 mM Glycine-HCl pH 1.5 for 30 sec. For data evaluation kinetic fit (ka [1/Ms], kd [1/s], KD [M]) was applied.

2. 2. 3. Chromatographic methods

2. 2. 3. 1. Size-exclusion chromatography (SEC)

Size-exclusion chromatography as performed in chapter 3

Size exclusion chromatography for analysis of degradation products of different IgG2 disulfide isoforms was performed on an Agilent 1200 SL series HPLC (Agilent Tech. Inc., Santa Clara, USA) using a Waters BEH200 SEC column (4.6 x 300 mm; 1.7 µm). Elution occurred during an isocratic gradient with 150 mM potassium phosphate (pH 6.5) with a flow-rate of 0.3 ml/min. The column temperature was set to 30 °C. Absorbance at 206, 214 and 280 nm was tracked during acquisition.

Size-exclusion chromatography as performed in chapter 4

SEC experiments and IgG1 size variant fractionation were performed with an Agilent 1260 chromatography system (Agilent Tech. Inc., Santa Clara, USA) at a flow rate of 0.4 ml/min

at 30°C. Separation occurred on a Tosoh TSKgel G3000SWXL (7.8 mm x 300 mm; 3 µm) or Phenomenex Yarra SEC3000 column (4.6 x 300 mm; 3 µm) using a mobile phase containing 150 mM potassium phosphate, pH 6.5 under isocratic condition. Absorbance at 206, 214 and 280 nm was tracked during acquisition.

2. 2. 3. 2. Strong cation exchange chromatography (SCX)

Strong cation exchange chromatography performed on a 1260 series chromatography system (Agilent Tech. Inc., Santa Clara, USA) was used to separate IgG2 disulfide isoforms on a MAbPac SCX-10 column (4 x 250 mm; Thermo Scientific Inc., Massachusetts, USA). Mobile phase A consisted of 20 mM sodium acetate (pH 5.2) and mobile phase B of 20 mM sodium acetate + 300 mM sodium chloride (pH 4.5). The column temperature was set to 15 °C. The loaded protein sample was eluted during a linear gradient from 30% to 100% mobile phase B with a flow rate of 1 ml/min on a 1260 series chromatography system (Agilent Tech. Inc., Santa Clara, USA) in a time-range of 31 min (Tab. 2). For preparative purposes, chromatographic separation occurred on a MAbPac SCX-10 (9 x 250 mm; Thermo Scientific Inc., Massachusetts, USA) column with a flow-rate of 3 ml/min. All other parameter remained unchanged. Absorbance at 206, 214 and 280 nm was tracked during separation.

Tab. 2: Gradient for SCX chromatography analysis.

Time [min]	% eluent B
0.00	30
3.00	30
33.00	90
35.00	100
38.00	100
40.00	30
45.00	off

2. 2. 3. 3. Weak cation exchange chromatography (WCX)

IgG2 disulfide isoforms were separated using weak cation exchange chromatography on a ProPac WCX-10 column (4 x 250 mm; Thermo Scientific Inc., Massachusetts, USA) on a 1260 series chromatography system (Agilent Tech. Inc., Santa Clara, USA). Mobile phase A consisted of 20 mM sodium acetate (pH 5.2) and mobile phase B of 20 mM sodium acetate + 400 mM sodium chloride (pH 4.5). In both methods, a linear gradient with a flow-rate of 1 ml/min was applied and the column temperature was 15 °C to increase resolution of separated isoforms. A 31 min linear gradient 30 % - 100 % mobile phase B with a flow-rate of 1 ml/min was applied for isoform separation (Tab. 3).
For preparative purposes, chromatographic separation occurred on a MAbPac WCX-10 (9 x 250 mm; Thermo Scientific Inc., Massachusetts, USA) column with a flow-rate of 3 ml/min. All other parameter remained unchanged. Absorbance at 206, 214 and 280 nm was tracked during separation.

Tab. 3: Gradient for WCX chromatography analysis.

Time [min]	% eluent B
0.00	30
3.00	30
33.00	90
35.00	100
38.00	100
40.00	30
45.00	off

2. 2. 3. 4. Protein A chromatography

Protein A chromatography was performed on a 1200 series HPLC system (Agilent Tech. Inc., Santa Clara, USA) using a PA ID sensor cartridge (2.1 mm x 30 mm, 2 µm; Applied Biosystems, Foster City, USA) which contained immobilized protein A. The IgG1 sample was loaded in 50 mM phosphate/150 mM NaCl buffer (pH = 7.0) at 25 °C column

temperature. The flow-rate was set to 1 ml/min. Elution was achieved by a gradient from 0 - 80% (Tab. 4) of 100 mM phosphate buffer (pH = 2.5). Absorbance was tracked at 206, 214 and 280 nm.

Tab. 4: Gradient for Protein A chromatography analysis.

Time [min]	Mobile phase B [%]
0.00	0
1.00	5
3.00	100
5.00	10
6.00	100
7.50	100
9.00	0
9.50	0

2. 2. 4. Mass spectrometric methods

2. 2. 4. 1. Mass analysis of intact protein samples

IgG samples were diluted in pure water to a concentration of 1 µg/µl. Using an Agilent 1260 series HPLC (Agilent Tech. Inc., Santa Clara, USA), 4 µg were injected onto a MabPacRP® column (1 x 50 mm, 4 µm; Thermo Scientific Inc., Massachusetts, USA). Desalting occurred using H_2O + 0.1 % FA (eluent A) and ACN + 0.1 % FA (eluent B) at a flow-rate of 0.6 ml/min. The protein was eluted using a steep gradient from 0.5 to 3.0 min (Tab. 5). The IgG was directly sprayed into a Q Exactive® Plus hybrid quadrupole-orbitrap mass spectrometer (Thermo Scientific Inc., Massachusetts, USA). Data analysis was performed using the evaluation software GeneData Refiner Version 10.5.

Tab. 5: Gradient for intact LC-MS analysis.

Time [min]	Mobile phase B [%]
0.0	1.0
0.5	1.0
3.0	99.0
3.5	99.0
4.5	1.0
8.0	End

2. 2. 4. 2. Middle-down mass spectrometry

IdeS digestion and reduction of IgG samples was performed according to 2. 2. 1. 2. and 2. 2. 1. 4.

For middle-down LC-MS/MS analysis 5 µg of resulting fragments [Ayoub *et al*., 2013] were separated on a BEH C8 column (2.1 x 100 mm; Waters Corp., Milford, USA) using an Agilent 1260 series HPLC (Agilent Tech. Inc., Santa Clara, USA). Eluent A contained H_2O + 0.1 % TFA, eluent B ACN + 0.1 % TFA. The flow rate was set to 0.3 ml/min. Separation took place at 60°C and a linear gradient from 5-50 % eluent B within 20 min (Tab. 6). Eluting fragments were sprayed into a Q Exactive Plus hybrid quadrupole-orbitrap mass spectrometer (Thermo Scientific Inc., Massachusetts, USA). Data analysis was performed using the evaluation software GeneData Version 10.5.

Tab. 6: Gradient for middle-down analysis.

Time [min]	Mobile phase B [%]
0.0	5.0
2.0	5.0
4.0	32.0
5.0	32.0
17.0	41.0
17.5	100
18.5	100
19.0	5.0
25.0	5.0

2. 2. 4. 3. Reduced peptide mapping

For reduced peptide mapping, 10 µg of IgG sample was lyophilized and re-suspended in 15 µl denaturation solution (6.0 M GdmCl, 50 mM Tris-HCl and 5 mM EDTA). Afterwards, 1.5 µl TCEP solution (50 µg/µl in 100 mM Tris-HCl) was added and incubated at 37°C for 15 min. 1 µl iodacetamide (IAA) solution (0.5 M) was added for alkylation and consequently incubated for 30 min at 25°C.

80.2 µl digestion buffer (50 mM sodium citrate, pH 7.0) and 0.1 µg Lys-C were added. The digestion reaction took place at 37°C for four hours. The reaction was stopped by adding 0.8 µl TFA.

For LC-MS/MS analysis, an UltiMate™ 3000 RSLCnano System (Thermo Scientific Inc., Massachusetts, USA) coupled to a Q Exactive Plus hybrid quadrupole-Orbitrap mass spectrometer equipped with a nano-spray source (Thermo Scientific Inc., Massachusetts, USA) was used. Peptide separation occurred on an Acclaim® PepMap100 C18 column (Thermo Scientific Inc., Massachusetts, USA) using a linear gradient (2% - 40% within 80 min) of H_2O + 0.1% FA and ACN + 0.1% FA at 70 °C after trapping on an Acclaim® PepMap100 nano-trap column (Thermo Scientific Inc., Massachusetts, USA). The flow rate was set to 0.3 µl/min.

Data analysis was performed using the evaluation software GeneData Version 10.5.

2. 2. 4. 4. Non-reduced peptide mapping

10 µg of the respective IgG sample was used for preparation of non-reduced peptide mapping. After lyophilization the sample was re-suspended in 15 µl denaturation solution (6.0 M GdmCl, 50 mM Tris HCl and 5 mM EDTA) and incubated at 37°C for 15 min. 80.2 µl digestion buffer (50 mM sodium citrate buffer, pH 7.0) was added ending-up in final concentrations of 0.95 M GdmCl and 0.78 mM EDTA. Subsequently, 0.1 µg Lys-C was added. The digestion reaction took place at 37 °C for four hours. The reaction was stopped by adding 0.8 µl TFA to each sample.

For LC-MS/MS analysis, an Agilent HPLC 1260 series coupled to a Q Exactive Plus hybrid quadrupole-Orbitrap mass spectrometer (Thermo Scientific Inc., Massachusetts, USA) was used. Peptide separation occurred on an BEH C8 column (Waters Corp., Milford, USA) using a linear gradient ranging from 2 – 50 % within 65 min of H_2O + 0.1% FA and ACN + 0.1% FA at 60 °C. The flow-rate was set to 0.35 ml/min. Peptide identification occurred used Top 5 CID fragmentation. Data analysis was performed with the evaluation software GeneData Refiner Version 10.5.

2. 2. 4. 5. Hydrogen/deuterium exchange mass spectrometry (H/DX-MS)

Hydrogen/deuterium exchange mass spectrometry (H/DX-MS) experiments were performed on a fully automated system equipped with a Leap® robot (CTC Leap Technologies, Carrboro, NC), a Waters nanoAcquity UPLC® (Waters Corp., Milford, USA), a H/DX manager® (Waters Corp., Milford, USA) and the Synapt® G2-S qToF mass spectrometer (Waters Corp., Milford, USA). Mass calibration was performed using sodium formate calibrant (5 mM NaOH, H_2O/isopropanol (50:50), 1% formic acid) in the *m/z*-range of 100-1700. Leucine enkephaline (0.2 mg/l, H_2O/ACN (50/50), 0.01% formic acid) was used as lock mass during H/DX-MS measurements.

Digestion was performed on-line by a Poroszyme™ immobilized pepsin column (Applied Biosystems Inc., Foster City, USA). Resulting peptides were trapped on a MassPrep® micro desalting column (2.1 x 5 mm, 20 µm, 100 Å; Waters Corp., Milford, USA) and subsequently separated on a Waters UPLC® CSH or BEH C18 column (1.7 µm; 1.0 x 100 mm; Waters Corp., Milford, USA) with a H_2O + 0.1% FA (v/v) and ACN + 0.1 % FA (v/v) linear gradient. Trapping and chromatographic separations were carried out at 0°C to minimize back-exchange. Eluting peptides were directly subjected to the time-of-flight mass spectrometer by electrospray ionization. Prior to fragmentation by MS^E and mass detection in resolution mode, the peptide ions were additionally separated by drift-time within the mobility cell. Data processing was performed using the Waters Protein Lynx

Global Server PLGS (Version 2.5.3.) and DynamX (Version 3.0). Data were not corrected for back-exchange since all measurements were performed in head-to-head comparisons.

H/DX-MS as performed in chapter 3

IgG2 samples were incubated for pre-defined increasing periods of time in buffer solutions prepared with deuterium oxide (18 mM acetate, 4.6 % sorbitol, pD 5.2). The exchange reaction was then rapidly stopped by cooling the solution down (to 4 °C) and decreasing the pH value of the protein solution by adding an equal volume of acidic quench buffer (pH = 2.35). During this exchange quench step, the protein was reduced and denatured by adding 4 M (final concentration 2 M) GdmCl and 0.5 M TCEP-HCl (final concentration 0.25 M). After pepsin digestion resulting peptides were trapped with a flow-rate of 65 µl/min on a MassPrep™ micro desalting column (Waters Corp., Milford, USA) at 0°C. Afterwards, the peptides were spatially separated on a reversed-phase C18 column using a 8 min linear gradient (Tab. 7) by using H_2O + 0.1% FA (eluent A) and ACN + 0.1% FA (eluent B) at a flow-rate of 40 µl/min and low temperature (0°C). Eluting peptides were directly sprayed into the time-of-flight mass spectrometer (Waters Corp., Milford, USA).

Tab. 7: Analytical gradient for IgG2 H/DX-MS.

Time [min]	Mobile phase B [%]
0.0	5
1.0	5
9.0	40
9.5	40
10.0	95
11.0	5
15.0	5
17.0	End

H/DX-MS as performed in chapter 4

Isolated IgG1 domains (50.4 mM sodium phosphate in H_2O; pH 6.2) were diluted in a 10-fold excess of labeling buffer (50.4 mM sodium phosphate in D_2O; pD 6.2). Labeling

occurred for 0 s, 20 s, 1 min, 10 min, 60 min and 120 min at 25°C. Each labeling time-point was measured twice. After the labeling reaction, the exchange was stopped by mixing the sample 1:1 with pre-cooled (0 °C) quenching buffer (200 mM sodium phosphate, 0.5 M TCEP-HCl, 4 M GdmCl; pH 2.35). Trapping and separation was carried out on a MassPrep® (Waters Corp., Milford, USA) and a BEH C18 column (1.7 µm; 1.0 x 100 mm; Waters Corp., Milford, USA) at flow-rates of 60 ml/min and 35 ml/min, respectively. The linear analytical gradient ranged from 5% to 50% eluent B within 6 min (Tab. 8).

Tab. 8: Analytical gradient for IgG1 H/DX-MS.

Time [min]	Mobile phase B [%]
0.0	5
1.0	5
8.0	50
9.0	50
10.0	95
11.0	5
13.0	5
15.0	End

H/DX-MS as performed in chapter 5

Different c-Src samples were diluted in a ratio of 1:10 with deuterium oxide-containing Src buffer (40 mM Tris, pH 7.1, 150 mM NaCl, 5 % (v/v) glycerine, 5 mM DTT) and incubated at 25 °C for 0 s, 20 s, 1 min, 10 min, 60 min, and 120 min. After the labeling reaction, the protein was denatured and the exchange was stopped by diluting the labeled protein 1:1 in quenching buffer (100 mM $Na_2HPO_4 \times 2\ H_2O$, 100 mM $NaH_2PO_4 \times 2\ H_2O$; 0.5 M TCEP-HCl, 4 M GdmCl, pH 2.6, 0 °C). Peptides were trapped and subsequently separated on a Waters UPLC CSH C18 column (1.7 µm, 1.0 × 100 mm; Waters Corp., Milford, USA) with a H_2O + 0.1% FA (v/v) and ACN + 0.1% FA (v/v) gradient (Tab. 9). Trapping and chromatographic separation were carried out at 0 °C. Peptide identification was performed in the IM-MS^E mode of the mass spectrometer.

Tab. 9: Analytical gradient for c-Src H/DX-MS.

Time [min]	Mobile phase B [%]
0.0	5
1.0	5
9.0	40
9.5	40
10.0	95
11.0	5
15.0	5
17.0	End

2. 2. 5. Small angle X-ray scattering [in cooperation with Dr. R. Stehle]

SAXS experiments were performed on a Rigaku BioSAXS-1000 instrument with a HF007 microfocus generator equipped with a Cu-target at 40 kV and 30 mA. Ag-behenate was used for q-calibration and beam center determination. Measurements were performed in multiple 900-s frames checked for beam damage and averaged. Circular averaging and background subtraction was done using the Rigaku SAXS Lab software v 3.0.2. Rigid body models were calculated with the program coral [Petoukhov & Svergun, 2012]. Although the molecule had a two-fold symmetry, no symmetry was included as a constraint to test whether the resulting structures would be symmetric. For each sample ten models were calculated and compared to each other.

D_{max}, Porod volumes and distance distribution were calculated with GNOM, all part of the ATSAS package V 2. 7. 0 [Petoukhov & Svergun, 2012].

SAXS analysis as performed in chapter 3

IgG2 isoforms and the unfractionated sample were measured at 20 °C with concentrations of 1.25 mg/ml, 2.5 mg/ml and 5.0 mg/ml in PBS. For background subtraction a blank sample containing solely PBS was measured.

SAXS analysis as performed in chapter 4

IgG1 monomer and dimer samples diluted in 50.4 mM sodium phosphate in H_2O (pH = 6.2) to 1.25 mg/ml, 2.5 mg/ml and 5.0 mg/ml were analyzed at 20 °C. In addition, the dilution buffer was analyzed for background subtraction.

2. 2. 6. Analytical ultracentrifugation

Analytical ultracentrifugation was carried out on a ProteomLab XL-I (Beckman, Krefeld, Germany) device supplied with absorbance and interference optics. Temperature during analysis was set to 20 °C. In total, 486 µl sample and as reference the corresponding buffer were loaded into separate cells with sapphire windows and 12-mm path length charcoal-filled Epon double sector centerpieces. The cells were inserted into an AnTi-50 8-hole rotor and analyzed at 50 000 rpm unless indicated otherwise. Data analysis was performed using Sedfit 15.01b [Schuck, 2000], Sedphat 12.1c [Schuck, 2003] and Gussi 1.1.0 [Brautigam, 2015].

Analytical ultracentrifugation analysis as performed in chapter 3

For complex analysis, the concentration of investigated IgG2 isoforms was set to 0.12 µg/µl and its antigen was added in the ratios of 1:3 and 3:1 and subsequently mixed by inverting (end-volume 600 µL in PBS). AUC analysis was performed in the equilibrium state after one week incubation at room temperature. Analysis was performed at 35 000 rpm and 20 °C. Absorbance optics were set to 280 nm and a total number of 150 scans were acquired.

Analytical ultracentrifugation analysis as performed in chapter 4

Sedimentation experiments on IgG1 dimer and monomer samples, were performed at 50 000 rpm, 280 nm and 20°C. The samples were diluted to a final concentration of 0.3 µg/µl using 50.4 mM sodium phosphate (pH 6.2).

2. 2. 7. *In-silico* methodologies

2. 2. 7. 1. Homology model construction

To set up a homology model of the investigated IgG1 the published simulated energy minimized structure of the IgG1 trastuzumab (PDB: bpj_1831_mmc3; Brandt *et al.*, 2010) was used as a template. Differing amino acids were exchanged and adapted using the mutagenesis function within PyMol 1.5.0.5.

For hydrogen deuterium exchange mass spectrometry, data visualization and small-angle X-ray scattering data evaluation including model set-up of investigated isoforms a homology model of the IgG2 was constructed using the published crystal structure of Li33 IgG2 di-Fab (PDB code: 3KYM) and the Fc-part of trastuzumab (PDB code: bpj_1831_mmc3). The hinge region was built-up from scratch. Amino acid mutation and hinge region construction was performed using PyMol 1.5.0.5.

2. 2. 7. 2. Molecular Dynamics Simulations

Molecular Dynamics Simulations as performed in chapter 4 [in cooperation with F. Kandzia]

For the simulation of the Asn52 to isoAsp52 conversion in IgG1, the in-house crystal structure of the Fab fragment functioned as starting model. Asn52 was replaced by isoaspartate. Necessary Amber [Case *et al*., 2017] parameters (.lib, .frcmod and .prep) were generated using gaussian09 [Frisch *et al*., 2009] for geometry optimization and RESP calculation and residuegen to create a compatible residue unit. The systems were converted from Amber to Gromacs format using acpype [Soussa Da Silva & Vranken, 2012]. The two separated copies of both states (dual-topologies) [Li *et al*., 2003] were manually created.

The systems were solved using TIP3P water in a cubic box with 1 nm distance to the boundaries and neutralized with counter ions (Na^+, Cl^-), if necessary. The dual-topology files were not neutralized.

All systems were simulated using the same protocol. First, each system was energy minimized in 15000 steps using steepest descent with a maximum tolerance (emtol) of 0.001 for the first 5000 steps which was increased to 0.01 for the last 10000 steps. Consecutively, the systems were heated up to 298 K in 200 ps using a time step of 1 fs and keeping all heavy-atoms fixed with a restraint barrier energy of 10000 kJ/(nm² x mol). This restraint was reduced in a step-wise manner over the next 350 ps of simulation and the systems were equilibrated for another 100 ps without any restraints. The production run was performed for 5 ns with a 2 fs time step. For all simulations the sd integrator and the v-rescale thermostat were used. The production was performed using Replica Exchange.
For free energy calculations, a thermodynamic cycle was set-up consisting of isoAsp (charged) – isoAsp (uncharged) – isoAps/Asn (uncharged) – Asn (uncharged) and Asn (charged). Free energy calculations were performed using gmx bar.

Molecular Dynamics Simulations as performed in chapter 5 [in cooperation with Prof. Dr. V. Kaila]

Full atomistic molecular models of c-Src with and without bound ATP and Y419 modeled in a phosphorylated state were constructed based on the X-ray structure of c-Src obtained from the Protein Databank (PDB ID: 1Y57). Each model was solvated in a water box with 34 Na^+/30 Cl^- ions, mimicking a 100 mM NaCl concentration. The molecular systems comprised *ca*. 100 000 atoms, and were simulated in an NPT ensemble at T=310 K and p=101.3 kPa for 1 µs, with an integration time-step of 2 fs using the CHARMM27 force field, and treating long-range electrostatics with the Particle Mesh Ewald approach. The extent of the A-loop was calculated using the average distance backbone oxygen and nitrogen distances between D413 and T417; N414 and A418; and, E415 and R419, as suggested by Meng & Roux [Meng & Roux, 2014]. All simulations were performed using NAMD 2.9 and Visual Molecular Dynamics was used for analysis.

2. 2. 8. Bioactivity assays

2. 2. 8. 1. Cell-based bioactivity assay

This assay is designed to assess the potency of the investigated IgG2. It is based on a PathHunter® pathway assay [Lamerdin *et al.*, 2016]. U2OS cells, genetically modified to express the fusion protein IκBα-ED (IκBα fusioned to the small β-galactosidase fragment as enzyme donor, ED), were stably transfected with the target receptor. Addition of a constant dose of target leads to the activation of the target-receptor which triggers the activation of the NF-κB pathway via the degradation of the inhibitory protein IκBα-ED. IgG2 was titrated into this system and neutralizes the activity of target. As a consequence, the NF-κB pathway is inhibited in a dose-dependent manner and the intact IκBα-ED complex can recombine with the exogenously added large β-galactosidase protein fragment (enzyme acceptor, EA) to form the active enzyme. The active β-galactosidase enzyme hydrolyzes the added substrate and produces a chemiluminescent signal. The activity of the IgG2 test samples was determined by comparison to a reference standard. The samples and the standard were normalized on the basis of protein content. Relative potency was calculated as parallel line assay in which the measured response is evaluated as a linear function of the logarithm of the administered dose [Djira, 2010]. The final result was expressed as relative potency of a sample (in percent) compared to the reference standard.

2. 2. 8. 2. ELISA based bioactivity assay

The potency and specificity of the IgG2 samples was determined in an ELISA assay that measures binding of IgG2 to the target which was immobilized on a microtiter plate. Bound IgG2 was quantified using an anti-human IgG-specific antibody coupled to horseradish peroxidase followed by addition of the substrate 2,2'-azino-di-(3-ethylbenzthiazoline-6-sulfonate) (ABTS).

The functional activity of IgG2 test samples was determined by comparison to a reference standard. The samples and the standard were normalized on the basis of protein content. Relative potency was then calculated using a parallel line assay [Djira, 2010]. The final

result is expressed as relative potency of a sample (in percent) compared to the reference standard.

3. Unravelling the structure-function relationship of IgG2 disulfide isoforms

3. 1. Introduction

Monoclonal antibodies represent a growing segment of the biopharmaceutical market with more than 40 therapeutic antibodies approved for clinical use [Niwa et *al.*, 2015] out of which five were in the top ten selling biologics of 2013.

These antibody-based drugs can be divided e.g. in terms of their main mode of action [Labrijn *et al*., 2008]. There are blocking antibodies [Kyi & Postow, 2014], designed to bind to cell-surface receptors or to capture endogenous ligands, respectively, in order to prevent mutual interaction. There are agonistic antibodies mimicking the action of endogenous ligands [Peng *et al.*, 2011; Labrijn *et al.*, 2008] and antibody-drug-conjugates. Here antibodies act as carriers of specific toxins that are transported to defined target sites and taken up into the cell where the toxins are released [Labrijn *et al*., 2008; Diamantis & Banerji, 2016]. And then there are activating antibodies which activate effector functions and initiate immune responses. For several indications specific binding of the antibody to the target is sufficient for the intended mode of action and no effector function is desired. For these therapeutic approaches IgG2 molecules are of special interest since this antibody isotype lacks the ability of activating immune response through Fc receptor binding.

Besides the usual IgG post-translational modifications (e.g. oxidation, aggregation, Asp/Glu isomerization and deamidation) IgG2 molecules exhibit an additional level of heterogeneity and complexity due to the presence of considerable amounts of disulfide isoforms [Martinez *et al.*, 2008; Wypych *et al*., 2008; Zhang *et al.,* 2010]. IgG2 molecules contain 12 intra-chain disulfide bonds, one in each domain and six inter-chain disulfide linkages of which four are found in the hinge region [Liu *et al.,* 2012] and two connecting the heavy and light chains (Fig. 13).

Recent reports described at least three major IgG2 disulfide isoforms named IgG2-A, IgG2-A/B and IgG2-B [Martinez *et al.*, 2008; Wypych *et al*., 2008; Dillon *et al.,* 2008]. Isoform IgG2-A represents the canonical form which is characterized by four disulfide bridges in the hinge region and a LC C-terminal/C_H1 linkage. The IgG2-B isoform is

defined by a disulfide bond between the C-terminal Cys of the light chain and the upper hinge Cys as well as a C_H1/upper hinge connectivity (Fig. 13).

Molecular dynamics simulations have shown considerable IgG2 disulfide scrambling in contrast to a lack of comparable scrambling in IgG1 molecules [Wang *et al.*, 2011]. Calculations revealed that the two Fab-domains repeatedly move towards the Fc-part resulting in close proximity of the carboxy-terminal Cys of the LC and C_H1-Cys of the HC with Cys residues in the upper hinge region that makes disulfide shuffling including the Fab domain feasible. In addition, the hinge region Cys residues seem to be highly dynamic, which further facilitates disulfide scrambling of inter- and intra- heavy chain disulfide linkages in the hinge region [Wang *et al.*, 2011]. Previous studies showed that the shuffling does not originate from the presence of a high content of free sulfhydryl groups since statistically only one out of five IgG2 molecules showed one single free sulfhydryl group [Franey *et al.*, 2010].

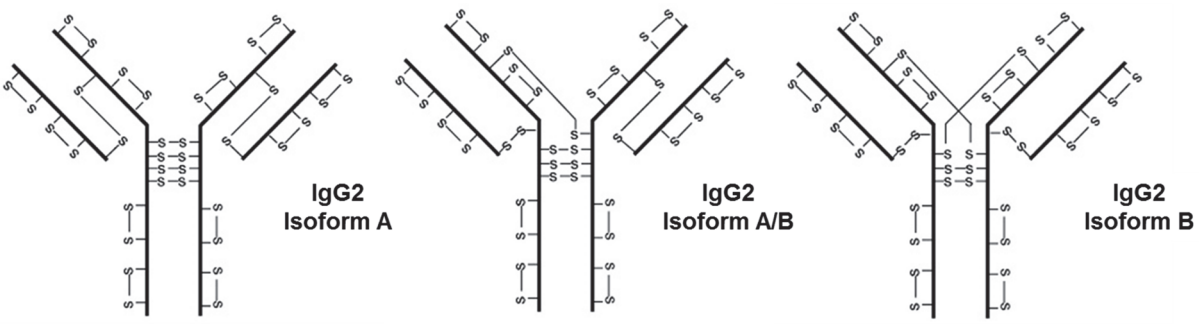

Fig. 13: Schematic representation of disulfide connectivity of the main isoform variants observed in IgG2 biotherapeutics. Close proximity of the involved cysteine residues facilitate disulfide scrambling in IgG2 molecules. Figure taken from: Liu & May; 2012.

While isoform A and B are symmetrical with respect to their disulfide bonding, isoform A/B is asymmetrical being a hybrid between isoform A and isoform B. Investigations performed on IgG2-A and IgG2-B isoforms by Dillon and co-workers [Dillon *et al.*, 2008] revealed that, in every IgG2 investigated, IgG2-B is consistently more compact than IgG2-A. However, differences in potency were observed between IgG2-A and IgG2-B only in a few cases, with IgG2-A being more active than IgG2-B, but not for every investigated IgG2 biopharmaceutical [Dillon *et al.*, 2008]. Since in previous investigations only a subset of therapeutic IgG2s show differences in bioactivity of the respective isoforms [Dillon *et al.*, 2008], it is necessary to expand the investigations to assess a correlation between structure-function of the IgG2 isoforms, complex formation and resulting bioactivity.

IgG2 A/B is a hybrid of the two isoforms A and B which was assumed to be more compact than IgG2-A, but more expanded than IgG2-B [Zhang *et al.*, 2015]. Cysteine to serine mutants in the upper-hinge region and within C_H1 domain if the antibodies were shown to reduce heterogeneity caused by directed disulfide patterns and led to homogenous IgG2-A- or IgG2-B-like molecules [Allen *et al*., 2009]. Investigations on these mutants resulted in similar C1q and Fcγ-receptor binding [Lightle *et al*., 2009] but, as expected, different migration in non-reducing SDS-capillary gel electrophoresis (CGE-SDS). Besides mutation, redox enrichment is another possibility to increase disulfide pattern homogeneity [Dillon *et al.,* 2008]. Redox conditions allowing to induce and direct disulfide shuffling *in vitro* to either enrichment of isoform B or isoform A by addition of low concentrations of chaotropic reagents. The chaotropic reagents disrupt intramolecular Fab-Fab interactions which favors in the canonical isoform A isoform when incubated in redox environment [Zhang *et al.*, 2015]. Analogous to the *in vitro* conversion, also *in vivo* conversion was observed due to the blood´s redox potential. Accordingly, interconversion to IgG2B takes place during circulation of the biopharmaceutical in the blood stream [Liu *et al*., 2008]. IgG2κ and IgG2λ show different conversion kinetics [Liu *et al.,* 2012].

Further studies investigating isoform heterogeneity of IgG2 molecules in more detail describe also the minor isoforms A_2 and A/B_2 [Martinez *et al*., 2008; Liu *et al.*, 2014]. IgG2-A_2 exhibits disulfide connectivity and structural characteristics similar to that of IgG2-A, but exhibits more flexibility of the Fab domains and lacks the ability to interconvert in a redox environment [Liu *et al*., 2014; Zhang *et al.,* 2015].

Forced degradation studies using enriched isoforms A and B investigated the temperature and pH dependency of the respective IgG2 with regard to clipping (P100 and P50 fragmentation) and aggregation [Perico *et al*., 2008]. Elevated temperatures lead to increased unique fragmentation and subsequent aggregation of IgG2-A, whereas in IgG2-B the respective clipping-site is supposed to be protected due to steric hindrance.

In this report we performed an *in vivo* study and followed the disulfide isoforms over time of an IgG2κ therapeutic. To understand the potential impact on efficacy due to the observed *in vivo* isoform conversion we generated the three major disulfide isoforms A, A/B and B with high purity, characterized them and performed detailed structural analyses using mass spectrometric methods, analytical ultracentrifugation and small

angle X-ray scattering in combination with homology and rigid-body modeling. Furthermore, the isoforms were compared with respect to binding affinity (surface plasmon resonance) and biological activity as well as complex formation with the target molecule. Taken together, the results reveal a detailed picture on the correlation of structural variation, complex formation and biological activity of an IgG2 therapeutic.

3. 2. Results

3. 2. 1. *In vivo* conversion of IgG2 disulfide isoforms

The time-course of disulfide distribution of an IgG2 biopharmaceutical was determined from samples of an *in vivo* study in cynomolgus monkeys in a previously conducted company internal pre-clinical study. The IgG2 antibody was affinity-purified from serum and subsequently subjected to C8 reversed-phase chromatography to track the change in disulfide composition. The time-dependent isoform distribution is depicted in Figure 14. Already after 8 hours of drug administration isoform conversion is observed. Isoform A constantly decreased in this short time range whereas A/B and B showed slightly increasing amounts which implicates that the conversion from isoform A to isoform B occurred over A/B as an intermediate state. With increasing time periods, the kinetics demonstrate that the relative amount of isoform B increased over time whereas isoform A/B and A constantly decreased compared to the pre-dose levels (depicted as dashed lines). In contrast to the three major isoforms, the minor isoform A2 kept the pre-dose level in this study which is in-line with previous published data that described A2 as stable with regard to disulfide scrambling under mild redox conditions [Liu *et al.*, 2014]. The observed slow conversion of the disulfide isoforms leads to a high portion of IgG2-B therapeutic after administration, which might have an influence on pharmacodynamics and was therefore investigated in-depth using purified isoforms.

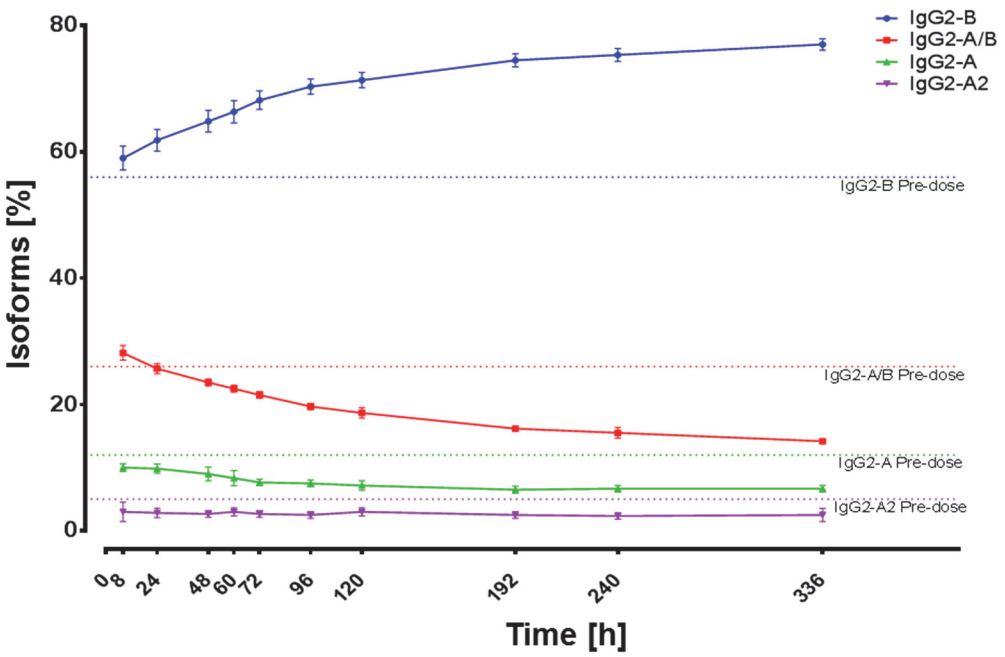

Fig. 14: *In vivo* composition of disulfide isoforms as determined by reversed phase chromatography after affinity purification from preclinical serum samples. Dashed lines represent disulfide composition before administration (pre-dose).

3. 2. 2. Isolation of disulfide isoforms

Disulfide isoforms A and B were redox-enriched by using a cysteine/cystamine redox system as described in 2. 2. 1. 1. and subsequently fractionated by cation exchange chromatography. For the fractionation of isoform A WCX and for isoform B SCX was used since both methods slightly differ in separation efficiency of the two variants. Isoform A/B was directly fractionated from starting material without redox treatment using SCX. Fractions of each isolated isoform were pooled and subsequently transferred in drug product buffer. The isolated disulfide isoform samples were re-injected using strong cation exchange chromatography (Fig. 15) to verify the purity of the derived samples. Figure 15 shows an overlay of the samples that were used for further characterization. The red chromatogram shows the CEX profile of isoform B, the green one results from re-injection of isoform A/B and blue indicates the isolated A isoform – for comparison also the unfractionated starting material (WSTD) is shown in the insert. These samples were flash-frozen and stored at -80 °C until further analysis.

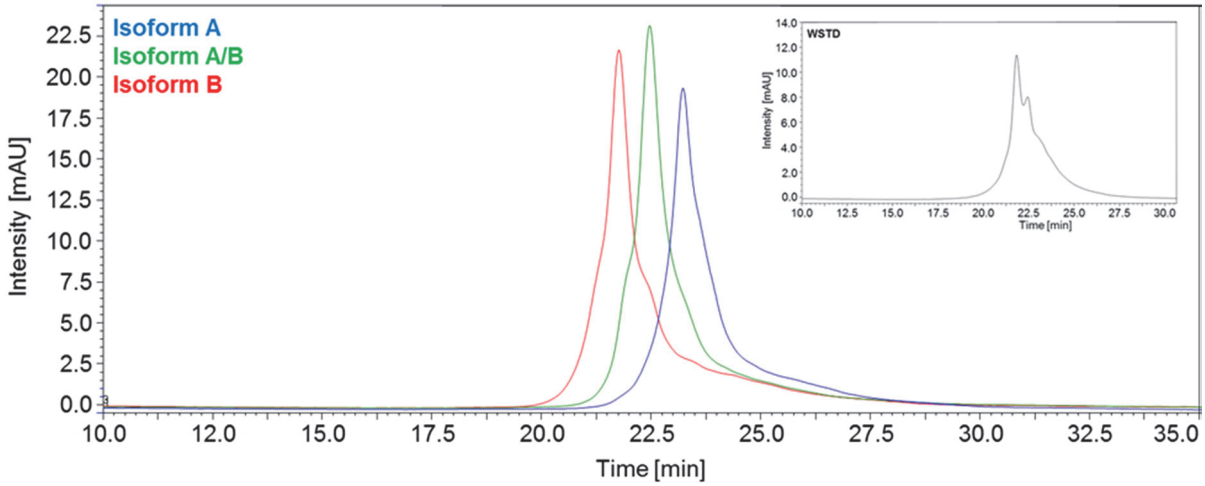

Fig. 15: Strong-cation exchange chromatogram of re-injected isolated isoforms of the IgG2 antibody. Isoform B is colored in red, isoform A/B in green and isoform A in blue. The untreated starting material is depicted in the upper right inset unravelling composition ratio of isoforms in the starting material (WSTD) as well as the characteristic elution time.

3. 2. 3. Confirmation and identity verification of generated isoforms

To minimize the risk and to confirm that redox treatment and fractionation has no influence on the primary structure, post-translational modifications (PTMs), secondary structure, and target binding, a head to head comparison between purified isoforms and the WSTD material was performed. In addition, the identity of isoforms was confirmed by peptide mapping, target binding and higher order structure investigations between purified isoforms and non-redox treated material to avoid misinterpretation.

Identification and quantification of post-translational modifications (PTM) was done by LC-MS/MS reduced peptide mappings. Figure 16 shows stacked chromatograms of tryptic digests of the WSTD and the three isolated isoforms A, A/B and B, indicating similarity with regard to PTMs such as e.g. oxidation, isomerization and deamidation. Consequently, neither the redox-enrichment nor the subsequent CEX fractionation enriched or induced any unwanted modifications or isoform that could possibly influence further investigations.

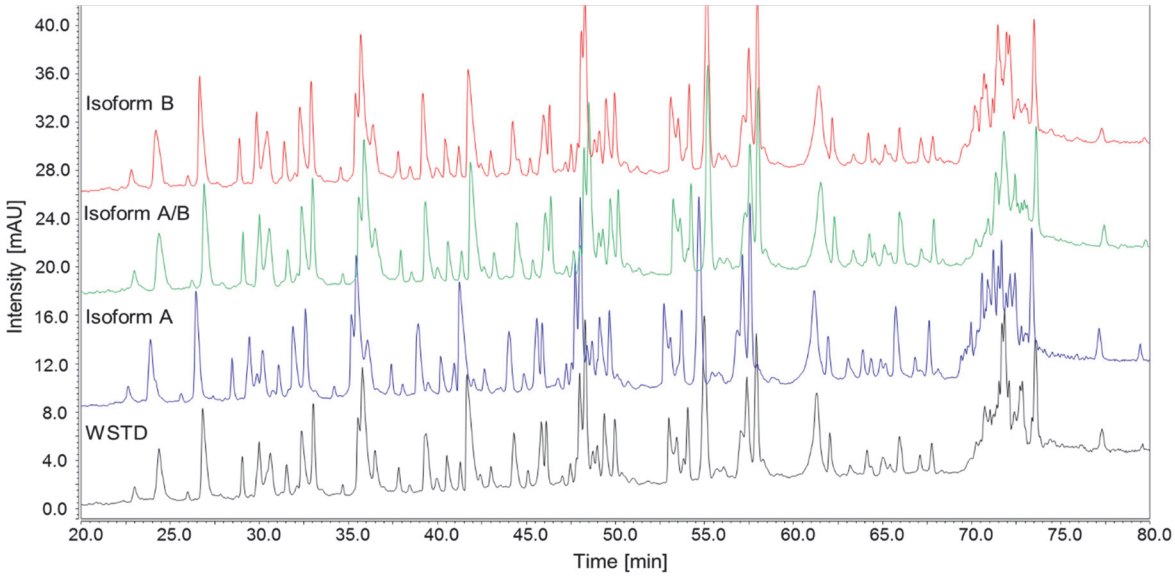

Fig. 16: Stacked chromatograms of reduced LC-MS/MS peptide mapping. Traces are colored according to the digested isoforms: WSTD in black, isoform A in blue, isoform A/B in green and isoform B in red. The chromatograms show the UV traces at 214 nm.

To confirm the identity of the final IgG2 isoform samples non-reduced peptide mapping using Lys-C was performed (Fig. 17). The reporter fragments resulting from peptides connected by disulfide bonds confirmed each isoform. Redox treatment of the IgG2 antibodies did not introduce new disulfide forms but successfully shifted the equilibrium of the isoform ratio either to the A or the B as previously described [Wypych *et al.*, 2008].

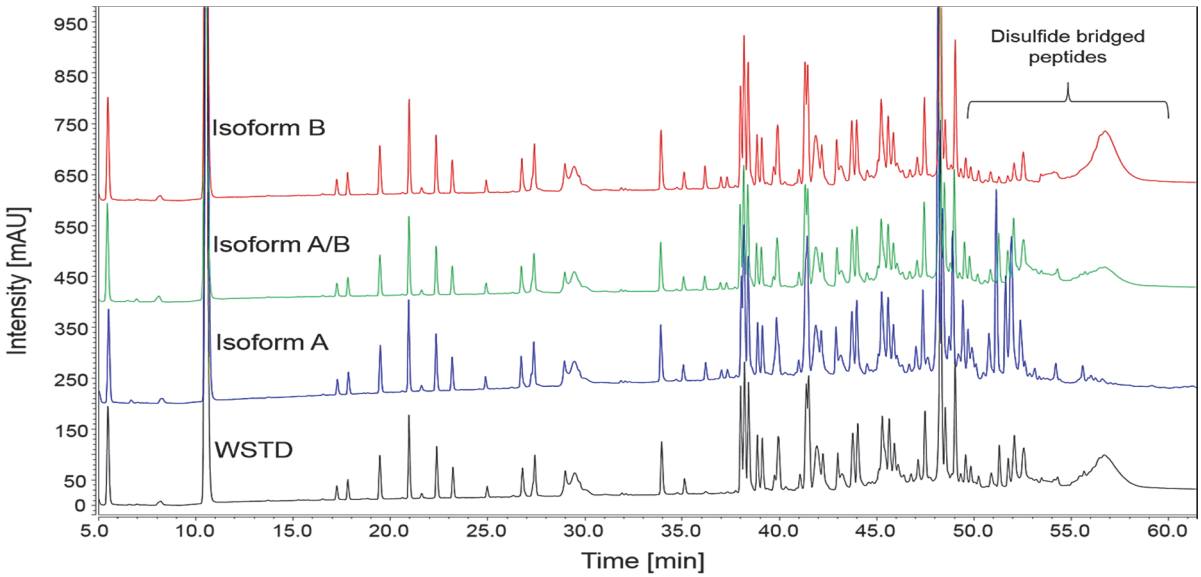

Fig. 17: Stacked chromatograms of non-reduced LC-MS/MS peptide mapping. Chromatograms are colored according to the digested isoform: isoform A in green, isoform A/B in light-green and isoform B in blue.

Following disulfide bond characterization and tracking of possible modifications, target binding of each isoform and the WSTD was tested by surface plasmon resonance (SPR) to confirm biological activity. Figure 18 shows the comparison of the sensorgrams concerning association and dissociation of the target molecule to the immobilized IgG2 samples.

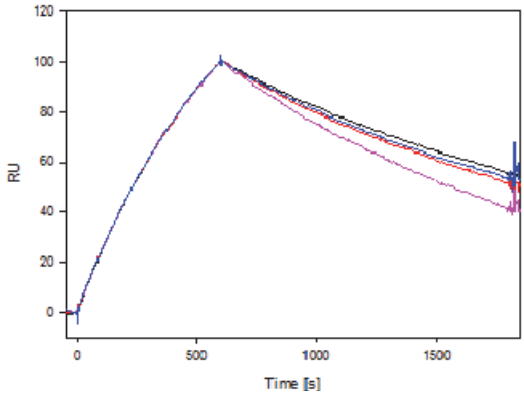

Tab. 10: Affinity constant values.

Sample	ka [1/Ms]	kd [1/s]	K_D [nM]	S_D [nM]
Isoform A	6.35E+4	5.05E-4	7.96	0.11
Isoform A/B	6.28E+4	4.34E-4	6.91	0.22
Isoform B	6.15E+4	4.34E-4	7.05	0.16
WSTD	5.82E+4	4.94E-4	8.49	0.31

Fig. 18: Baseline and binding adjusted SPR target binding sensorgrams of the different isoforms and their target (black: WSTD; red: isoform B; pink: isoform A/B; blue: isoform A). Table 10 shows the on- and off-rates as well as the binding affinity constant with the corresponding standard deviations. Each sample was analyzed in triplicates.

This analysis revealed that the generated and isolated samples are able to bind the target and that no biological inactive material was generated. The investigated samples showed similar dissociation/association rates and binding constants.

To test for structural integrity between the isoforms present in the untreated starting material and the redox-enriched/purified fractions, H/DX-MS was applied on non-treated and redox-treated isoform B derived after purification as described above. This isoform was chosen since it was more homogeneous than the A form (see Fig. 15) and has been previously described in the literature [Liu *et al.*, 2014]. Non-redox treated isoform B was directly fractionated from starting material using SCX. Both samples were buffer exchanged into the final product buffer (18 mM acetate, 4.6 % sorbitol, pH 5.2) and subjected to a head-to-head HDX-MS analysis. The analysis was set-up with three different deuterium incubation time-points (20 s, 10 min, 60 min). Each time point was measured in triplicates. In sum, 89.5% of the heavy chain (100 peptides) could be covered and identified by on-line pepsin digestion and MS^E. The light chain yielded 38 peptides encompassing 96.3% of its sequence. The sum of difference plots (Fig. 19) for the heavy and the light chain visualize the mass difference of every single peptide over the incubation time. Both isolated isoform B variants showed similar solvent exposure

of each investigated peptide since the sum of differences did not exceed the limit of significant differences (± 1 Da). Thus, the differently obtained isoform B variants were considered to have identical structure.

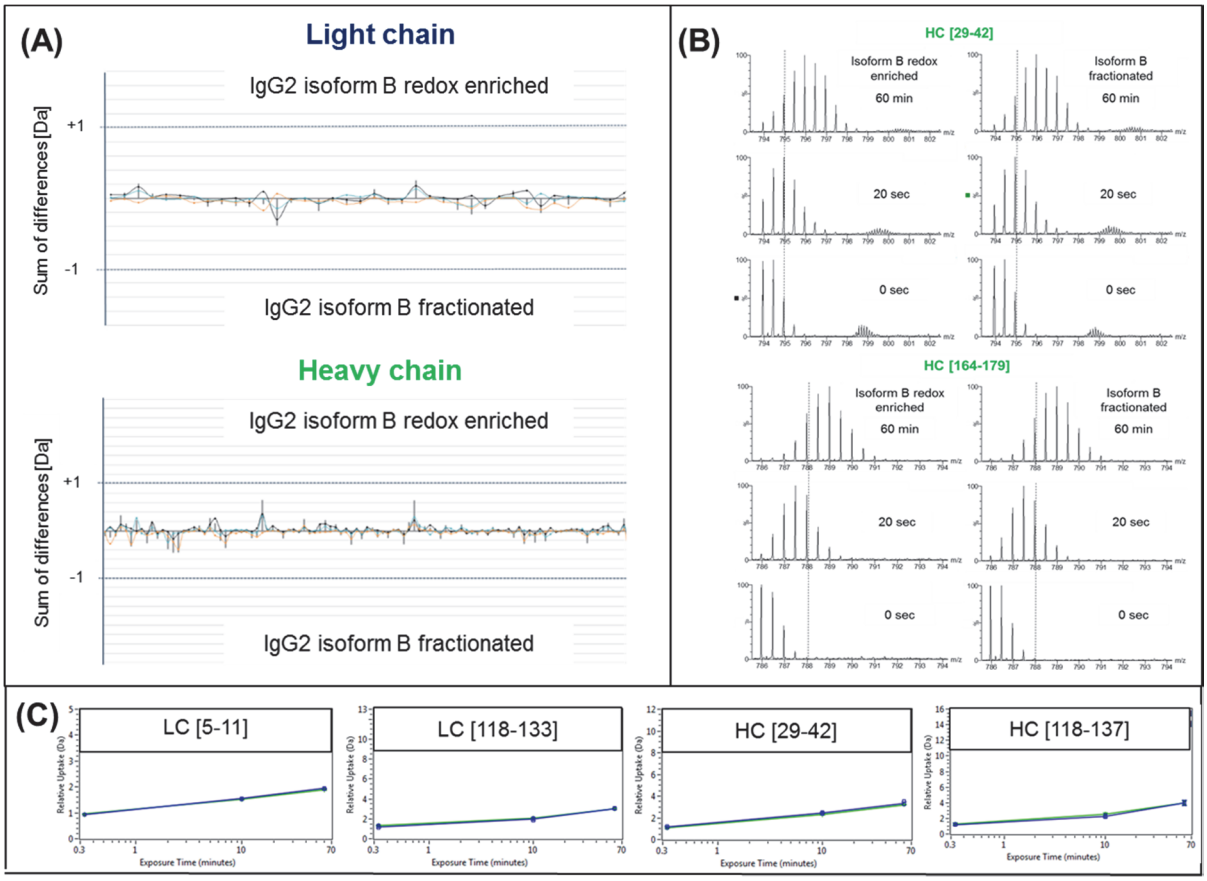

Fig. 19: H/DX-MS comparison of redox-enriched and non-redox-enriched isoform B. (A) Sum of difference plots of mass uptake for every peptide derived from the IgG2 heavy chain (upper plot) and light chain (lower plot). (B) Exemplary raw spectra of peptide [29-42] and [164-179] describing similar *m/z* increase in dependence of incubation time. (C) Exemplary uptake plots of evaluated peptides illustrating comparable absolute mass increase and thus structural identity.

Taken together, the results show that the isoform purification led to structurally and functionally identical molecules and that the isolated fractions can be used for further investigations.

Next, a forced degradation study was performed to make sure that the isoforms are stable and do not experience modifications or degradation and can be stored before further analysis. The samples were diluted to a final concentration of 1 µg/µl in drug product buffer and subjected to 40°C. Incubation occurred for 2 d, 4 d, 1 w, 2 w and 4 w. After incubation, the samples were flash-frozen in liquid nitrogen and stored at -80°C until analysis. The different species were investigated with regard to disulfide scrambling

using SCX, post-translational modifications (LC-MS/MS peptide mapping) and clipping/aggregation by SEC.

Prior to characterization of the stressed IgG2 isoforms the samples were subjected to SCX chromatography to provide a first glance at the integrity of the disulfide isoforms. Figure 20 shows the SCX chromatograms of the WSTD and the isoforms after different incubation times.

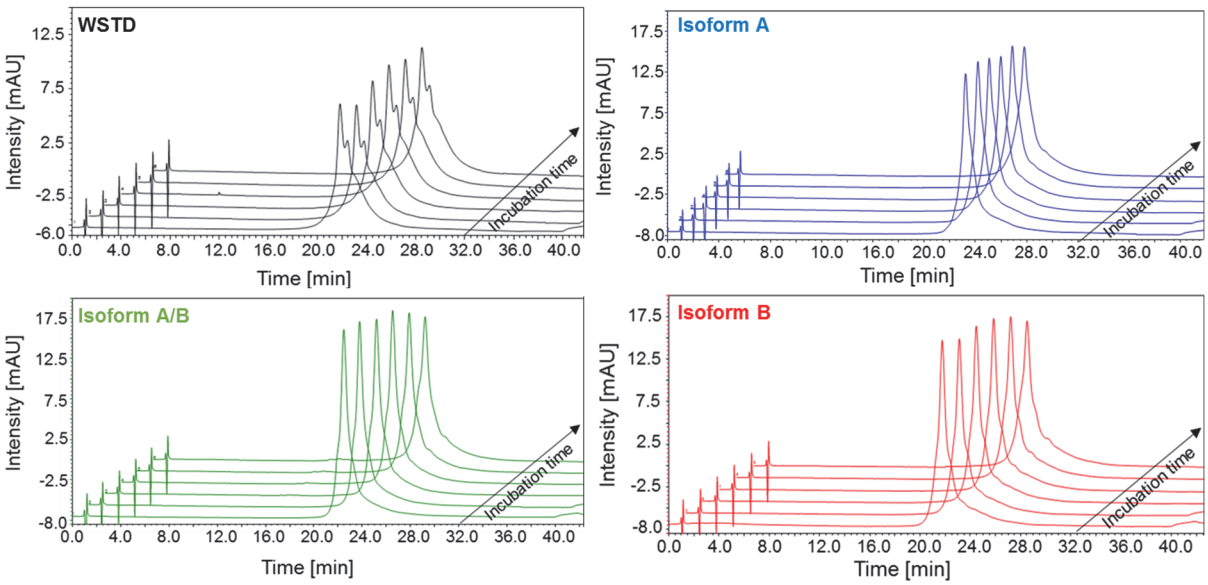

Fig. 20: Strong-cation exchange chromatograms of the isolated isoforms after stress induction. The stacked chromatograms show the isolated isoforms at increasing incubation times (0 d, 2 d, 4 d, 1 w, 2 w and 4 w). The WSTD is colored black; isoform A colored blue; isoform A/B colored green and isoform B is depicted in red.

The control of disulfide shuffling revealed stability of disulfide connectivity within the isoforms during incubation at elevated temperatures. Thus, further investigations of the samples were justified.

Degradation and aggregation are two of the critical quality attributes of biopharmaceuticals. Therefore, the temperature stressed (40 °C) samples were investigated by SEC to obtain information on size variants formed during this simulated ageing process. Figure 21 depicts the size-exclusion chromatograms of the different samples with the incubation time-points shown as stacked overlays.

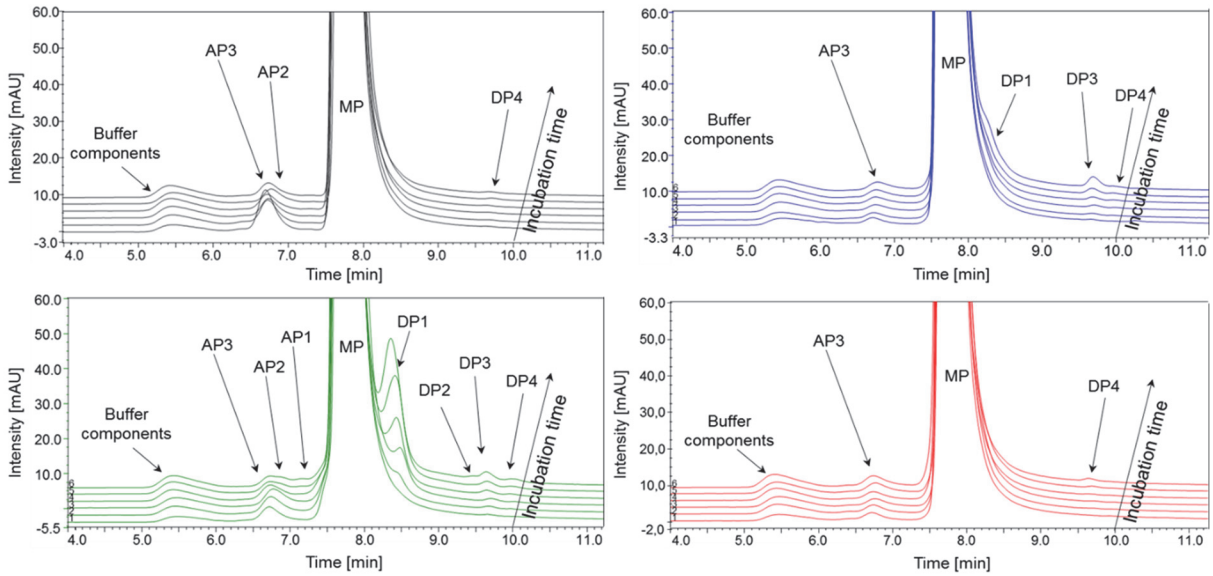

Fig. 21: Size-exclusion chromatograms of the degradation time-courses of the investigated isoforms and the WSTD. The color codes describe the different isoforms. The WSTD is shown in black; isoform A is shown in blue; isoform A/B is depicted in green and isoform B in red. The stacked overlays show the corresponding isoforms at increasing incubation-times (0 d, 2 d, 4 d, 1 w, 2 w and 4 w). Peak labels describe the main peak (MP), aggregate peaks (AP1-3) and fragments formed by degradation (DP1-4)

Isoform A showed little tendency to aggregate but formed degradation products during increased incubation time (DP1 and DP3) in measurable amounts. Isoform B and WSTD contained almost no degradation products even at the longest incubation time giving evidence of high stability with regard to clipping. As can be seen from the WSTD time-course (upper left), AP3 decreases over time, which is most likely caused by dissociation of non-covalently linked dimers upon dilution and subsequent incubation. Like isoform A, isoform B showed almost no propensity for aggregation under the applied stress condition. The most instable isoform identified in this study was isoform A/B which formed considerable amounts of different aggregate peaks (AP1, AP2 and AP3) as well as different degradation products (DP2, DP3 and DP4). AP2 and AP3 resulted most likely from the aggregation of the different DP fragments. The most abundant product formed by isoform A/B under heat-stress condition was DP1, which was also found in isoform A but in smaller amounts (isoform A after four weeks: 2.4%; isoform A/B after four weeks: 4.3% relative to the main peak).

For assessment of post-translational modifications on the intact protein level and degradation products, intact protein LC-MS was performed of the samples that were incubated for four weeks. The deconvoluted spectra revealed no differences in mass

distribution indicating no significant increase of post-translational modifications on intact protein level due to the applied stress condition. Figure 22 shows an overlay of the deconvoluted sprectra of the analyzed samples.

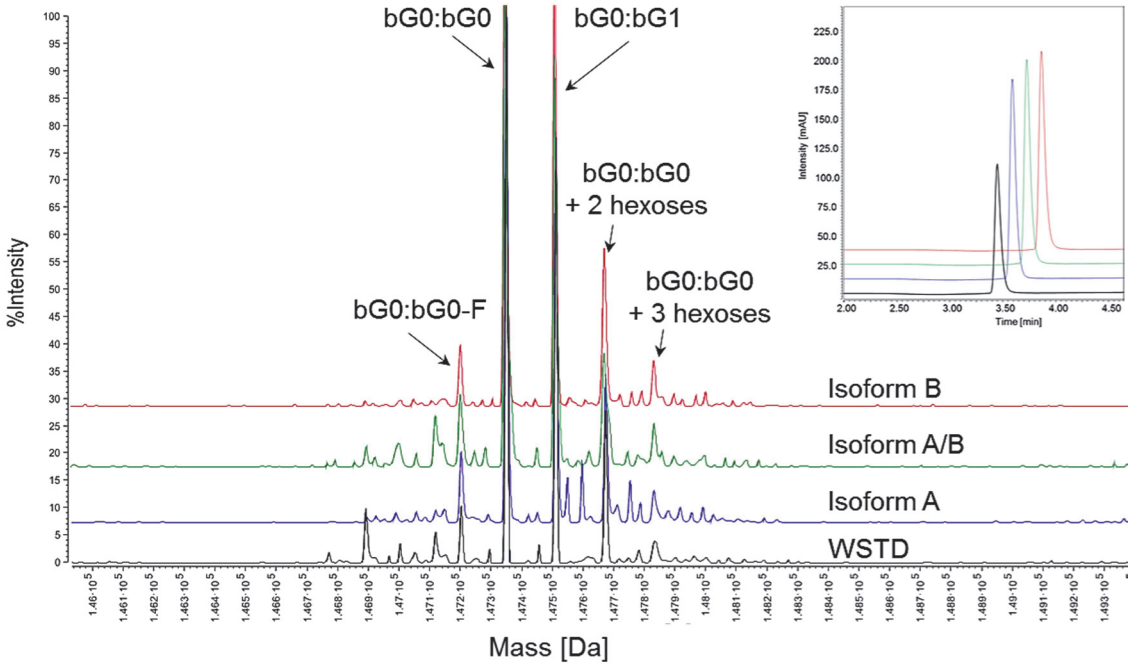

Fig. 22: Deconvoluted intact mass spectra of the four weeks stressed samples of the isolated isoforms and the WSTD. WSTD is depicted in black, isoform A in blue, isoform A/B in green and isoform B in red. The peak pattern shows the main glycoforms present in the IgG2 product. The inset (upper right) shows the elution profile during RP-HPLC of the investigated samples.

For a more detailed look into post-translational modifications and degradation products LC-MS was performed on IdeS digested and reduced samples. IdeS is a protease that specifically digests below the hinge region (...^{228}CPPCPAPP‖VAGPSVF^{242}...), yielding in two Fc/2 (formed by one single heavy chain ^{236}Val to ^{446}Gly) and F(ab)$_2$ fragments. Subsequent reduction results in formation of the light chains, Fc/2 and Fd fragments. The fragments identified by mass spectrometry are depicted in Figure 23 and listed in Table 11.

Besides the main fragments that resulted from the sample preparation procedure LC, Fc/2 and Fd also minor amounts of oxidized variants as well as glycated Fc/2 were identified. The WSTD showed almost no oxidized fragments as can be seen in UV chromatogram. This is supposed to originate from the isolation procedure of the isoforms by redox-enrichment in the case of isoform A and B as well as fractionation

by CEX. The corresponding average masses of the eluting fragments are listed in Table 11 for each sample.

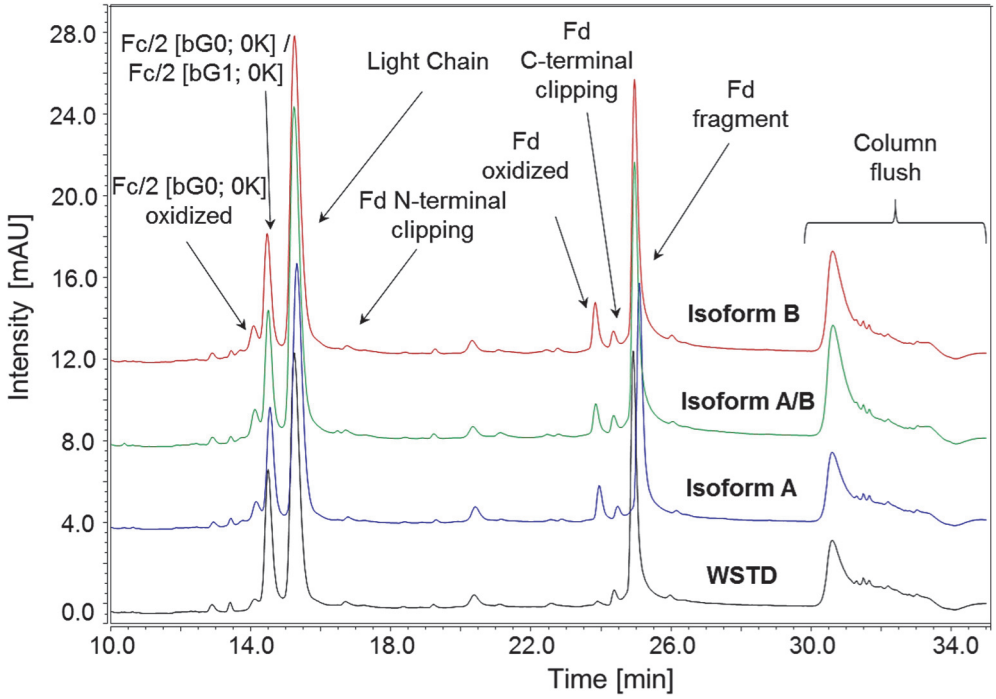

Fig. 23: UV chromatograms of IdeS digested and reduced isoforms and the WSTD (time-point 0d). The color code describes isoform A (blue), isoform A/B (green), isoform B (red) and the WSTD (black). Peak assignment occurred according to the deconvoluted average mass.

The amount of fragments and variants identified in the 0 d samples did not increase over incubation time in all the investigated samples. This implies that the isoforms and untreated material are very stable in this simulated ageing process. Figure 24 displays the overlays of UV chromatograms of the samples incubated for four weeks of the different isoforms and the WSTD sample.

The results obtained in the stability study show on the one hand that the isolated isoforms do not contain differing variants except for disulfide variation and on the other hand that these are very stable over time so that possible differences in structure and function can be solely attributed to the scrambled disulfide pattern.

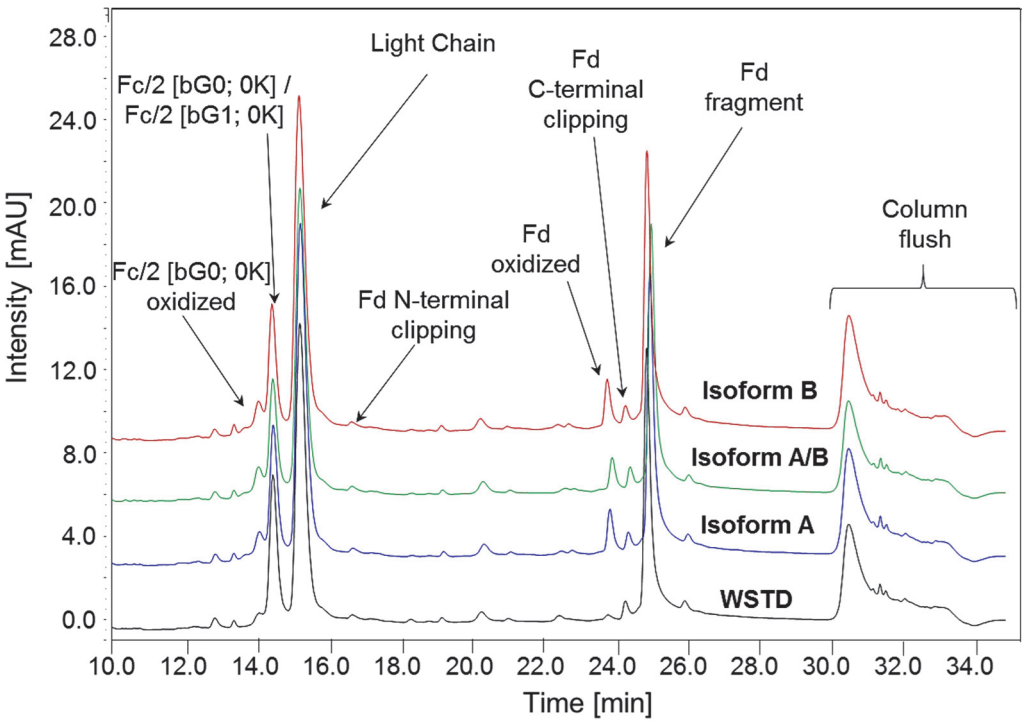

Fig. 24: UV chromatograms of IdeS digested and reduced samples incubated for four weeks. Isoform A is colored in blue, isoform A/B in green, isoform B in red and the WSTD is displayed in black.

Tab. 11: Observed masses of the IdeS digested and reduced samples.

Retention Time [min]	Isoform A Mass [Da]	Isoform B Mass [Da]	Isoform A/B Mass [Da]	WSTD Mass [Da]	Fragment
14.35	25253.0	25253.0	25252.8	-	Fc/2 [bG0; 0K] oxidized
14.59	25400.0	25401.0	25401.0	25400.0	Fc/2 [bG0; 0K] glycated
14.76	25238.0	25238.0	25237.8	25238.1	Fc/2 [bG0; 0K]
15.46	23486.4	23486.2	23486.2	23486.2	LC
16.94	10575.6	10575.6	10575.6	10575.6	Clipping Fd N-terminus
24.16	25002.6	25002.6	25002.6	-	Fd oxidized
24.62	14430.1	14430.1	14430.1	14430.1	Clipping Fd C-terminus
25.31	24987.6	24987.9	24987.8	24987.8	Fd

.

3. 2. 4. Structural characterization of isolated IgG2 isoforms

Low-resolution global structural information such as hydrodynamic properties and melting-temperature were derived by SEC, AUC and DSF analysis.

From size-exclusion chromatography measurements different elution times were obtained for the isoforms. The first to elute was isoform A followed by isoform A/B and isoform B suggesting the highest hydrodynamic radius for A and the lowest for B (Tab. 12). To verify the SEC data, AUC was performed in addition as an orthogonal method capable to reveal hydrodynamic properties. The s-values were 6.20 S for isoform A, 6.25 S for isoform A/ B, 6.30 S for isoform B and 6.30 S for the WSTD. Extrapolation of the s-values to zero concentration gave $s_{20,w}$ values of 6.45 S (isoform A), 6.49 S (isoform A/B), 6.55 S (isoform B) and 6.55 S (WSTD) as depicted in Figure 25. The lowest value was observed for isoform A, the highest for isoform B and the one of isoform A/B was in between, which confirmed the observed hydrodynamic properties as seen by SEC (Tab. 12). The untreated control material resulted in a $s_{20,w}$-value identical to isoform B, which was expected as the WSTD is mainly composed of this particular isoform (Fig. 15).

From SEC and AUC it can be concluded that isoform A has the most extended and isoform B the most compact structure. Since obvious structural differences exist between the different investigated isoforms, DSF was applied in addition to determine whether the observed global structural differences were reflected in differences in stability. The melting-temperatures of the isoforms were measured in triplicates ranged from 69.7°C to 71.6°C (Fig. 27). The differences between the samples were significant as can be seen from the standard deviations listed in Table 12. Isoform A showed the lowest, isoform B the highest transition point. The values of isoform A/B and the WSTD were in between A and B. Due to the fact that the profiles of the thermograms were identical, similar structure elements of the isoforms can be concluded. The difference in T_M most likely originates from additional interaction sites between the single domains in isoform B and A/B compared to A. A summary of the values derived from these low-resolution techniques is listed in Table 12.

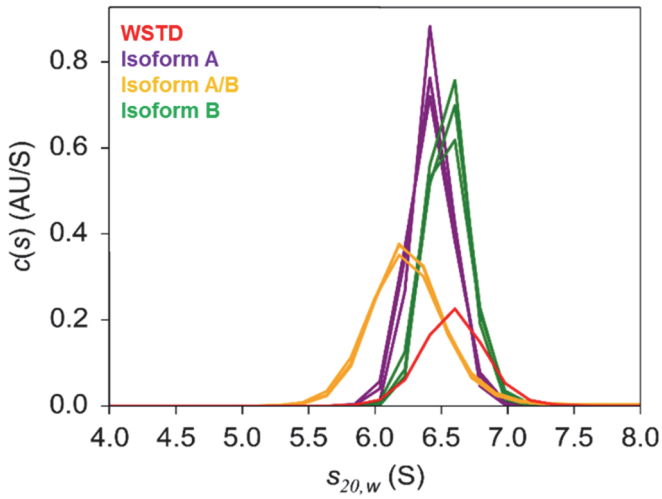

Fig. 25: Distribution of sedimentation coefficients of the different analyzed IgG2 isoforms. Each measurement was performed in triplicates. Isoform A is shown in violet, isoform B in green, isoform A/B in orange and the WSTD in red.

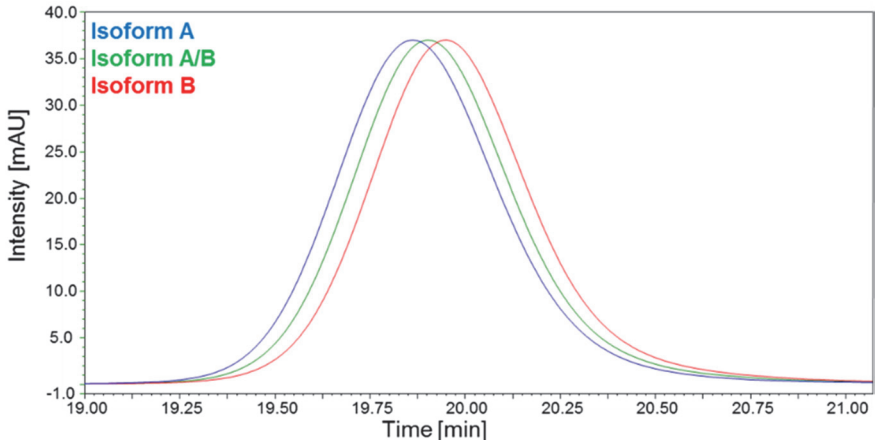

Fig. 26: Overlay of SEC chromatograms of the different analyzed IgG2 samples. Each measurement was performed in triplicates.

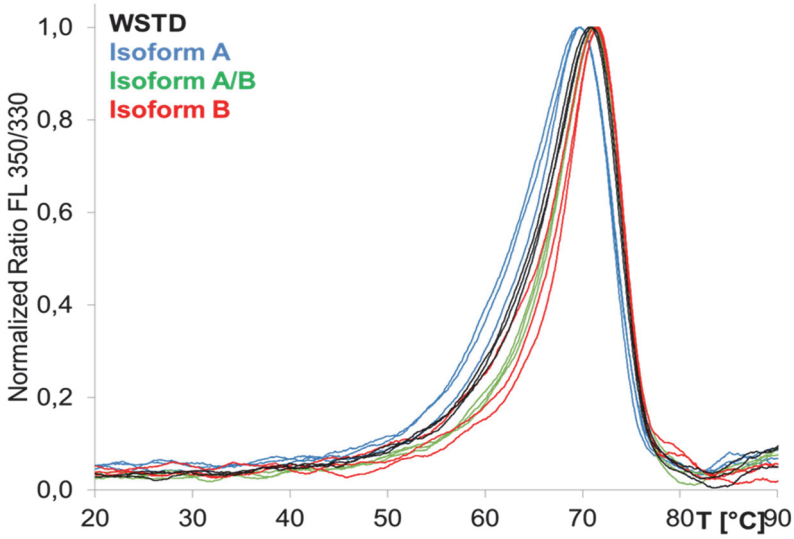

Fig. 27: Overlay of thermograms of the different analyzed IgG2 samples. Each measurement was performed in triplicates. The WSTD is shown in black, isoform A in blue, isoform A/B in green and isoform B in red.

Tab. 12: Parameters derived by AUC, SEC and DSF.

Method	AUC	SEC	DSF
Sample	$S_{20,w}$ [S]	RT [min]	T_M [°C]
Isoform A	6.45	19.85	69.7 (± 0.1)
Isoform A/B	6.49	19.92	71.3 (± 0.2)
Isoform B	6.55	19.98	71.6 (± 0.1)
WSTD	6.55	19.87	70.9 (± 0.2)

To gain a more detailed picture on the location of the structural differences, the three isoforms were investigated by H/DX-MS. Using this technique, the differences could be attributed to specific sequences within the molecule.

In sum, 94.4% of the heavy and 97.7% of the light chain could be compared with regard to hydrogen/deuterium exchange kinetics. Figure 31 shows the sum of difference plots for the comparison of isoform A and isoform B, revealing that differences were detected exclusively in the Fab domain of the antibody or more specific in the C_L,-V_L-, C_H1- as well as in the V_H-domain. In particular, differences in uptake kinetics were detected in the following sequences: AA [1-15], AA [37-57], AA [59-79], AA [161-164], AA [190-216] in the heavy chain and AA [1-10], AA [22-33], AA [55-72], AA [123-136], AA [145-163] and AA[197-215] in the light chain. Here, the exchange kinetics of isoform B were lower compared to isoform A suggesting either higher solvent protection or decreased dynamics of these regions. Similar results were obtained for the comparison of isoform A and isoform A/B but to a smaller extent. The differences in uptake were restricted to the Fab domain including significant differences found analogous to the isoform A/isoform B comparison in the sequences AA[1-15], AA [47-57], AA [161-164], AA [203-221] in the heavy chain and AA[55-72], AA [118-136] and AA [197-215] in the light chain. The results revealed by H/DX-MS strengthen the suggestion that isoform A/B is a hybrid form since identical sequences with significant uptake-differences were detected but with exchange kinetics in between isoform A and B as can be seen in the exemplary uptake-plots (Fig. 28). The reason for the detection of less sequences that showed significantly slower exchange kinetics in isoform A/B is that the asymmetrical structure decreased the effect below a threshold for differences defined as significant. Supporting the results listed above, also the H/DX-MS analysis identified isoform B as the most compact or rigid and isoform A as the most extended or flexible structure with the differences located in the Fab domain (Fig. 29).

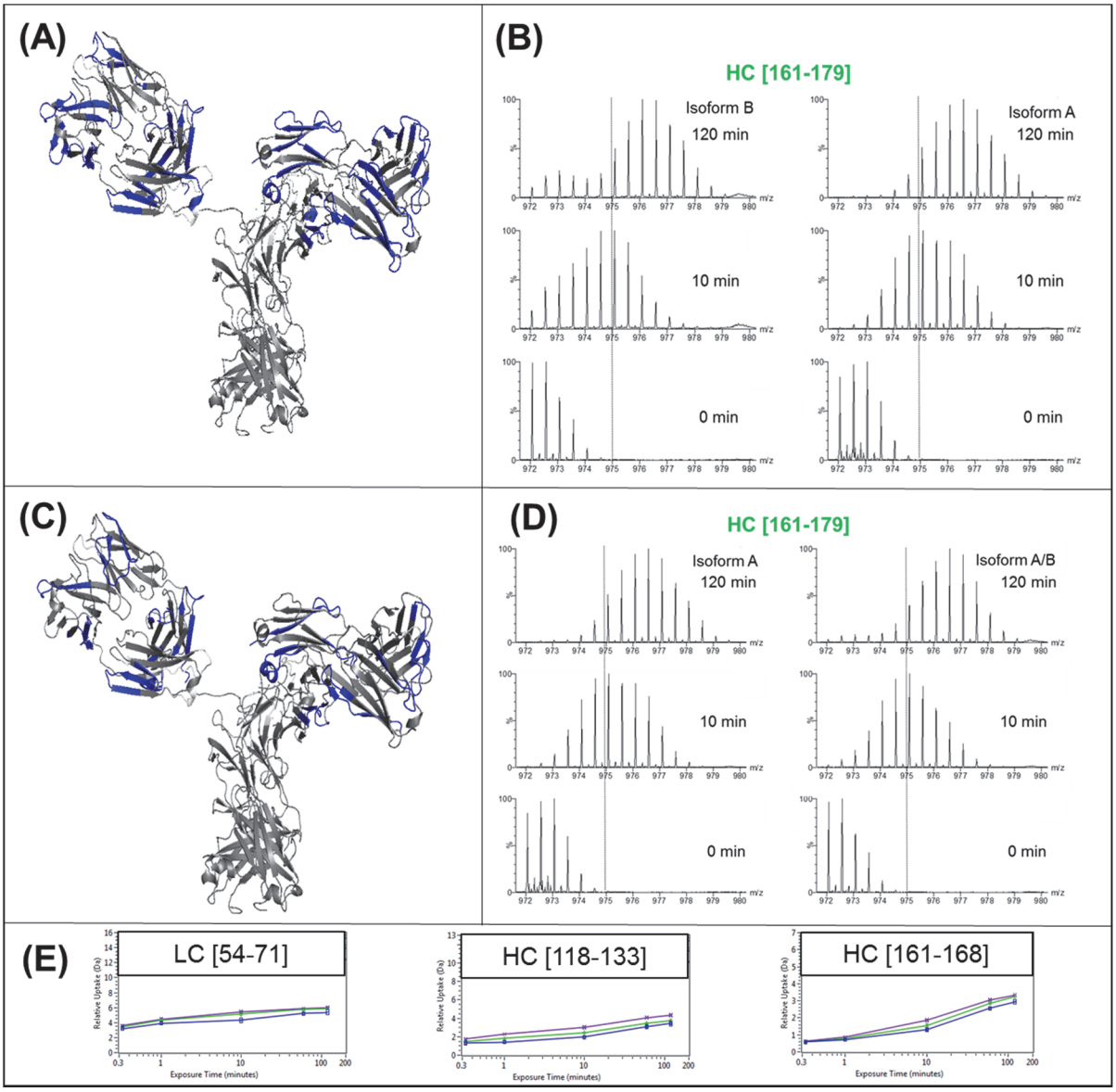

Fig. 28: Comparison of H/DX-MS results for isoform A versus isoform B and isoform A versus isoformA/B comparison.

(A) + (C): Crystal-structure with indicated differences in deuterium uptake. Blue marks sequences where isoform B (A) and isoform A/B (C) showed slower exchange kinetics compared to isoform A. Grey indicates no difference in uptake and white areas could not be identified.

(B) + (D): Exemplary raw spectra of peptide HC [161-179] at increasing incubation time-points. Isoform B shows remarkably bimodal spectra indicating slow dynamics for this isoform.

(E): Exemplary uptake plots of different peptides for all three investigated isoforms.

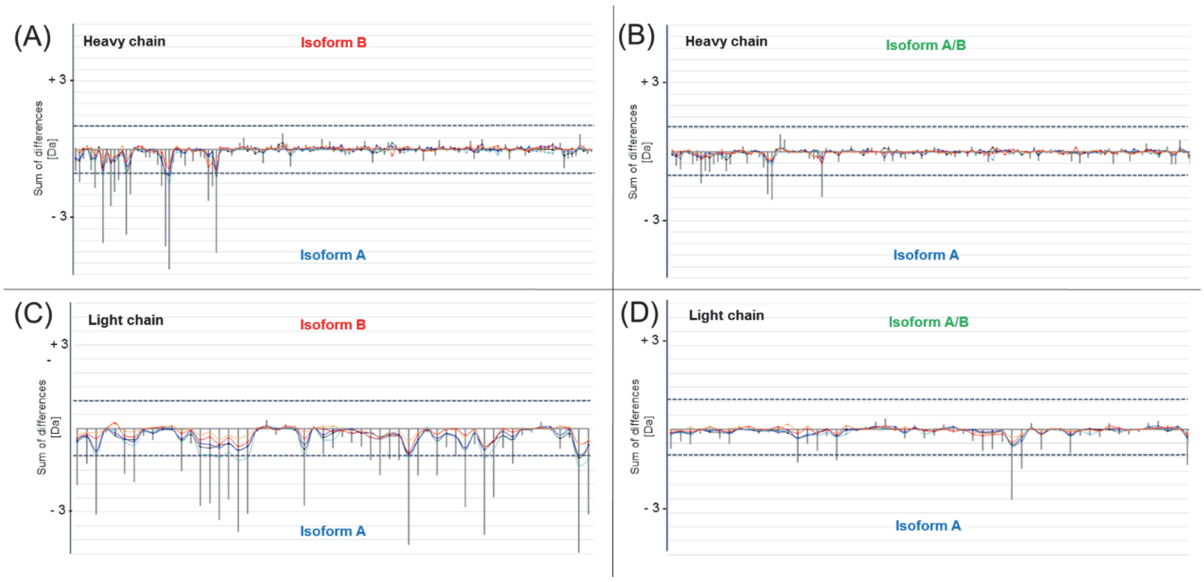

Fig. 29: Sum of difference plots for hydrogen exchange comparison of isoform B and isoform A/B compared to isoform A. (A) + (C): Sum of difference plots for isoform B heavy chain (A) and light chain (C) compared to A. (B) + (D): Sum of difference plots for isoform A/B heavy chain (A) and light chain (C) compared to A.

3. 2. 5. Small angle X-ray scattering analysis and homology modeling of the IgG2 disulfide variants

SAXS experiments were performed to obtain global size and shape information of the examined isolated isoforms. Moreover, the relative average solution arrangement of the Fab domains and the Fc could be derived by combining experimental scattering data and homology modeling.

The IgG2 samples were measured in a dilution series to eliminate effects originating from concentration-dependent intermolecular interactions. Guinier analyses were performed to obtain insight into the degree of elongation of the IgG2 isoforms. The higher R_G value for isoform A indicates an elongated conformation compared to isoform B and A/B which have similar R_G values (Tab. 13). The pair-distribution functions (p(r)) were calculated by indirect Fourier Transformation of the scattering profiles (Fig. 31) and revealed the distribution of pairwise distances of scattering centers within the molecule. Two maxima in the p(r) function correspond to two sets of frequently occurring interatomic distances within the structure. Furthermore, D_{max} was extracted demonstrating the longest interatomic distance within isoform A which is consistent with results of found derived by AUC. The D_{max} of isoform B indicates the most compact structure of all three isoforms. This information was used to calculate low resolution

bead-models (Fig. 32) in order to get an idea of the overall shape of the different IgG2 samples. The R_G, D_{max} and the biggest Porod volume of all three samples indicate that isoform A has the most extended structure. In contrast, isoform B showed the lowest value in all of the derived parameter which underpinned the results derived by AUC, SEC, DSF and H/DX-MS.

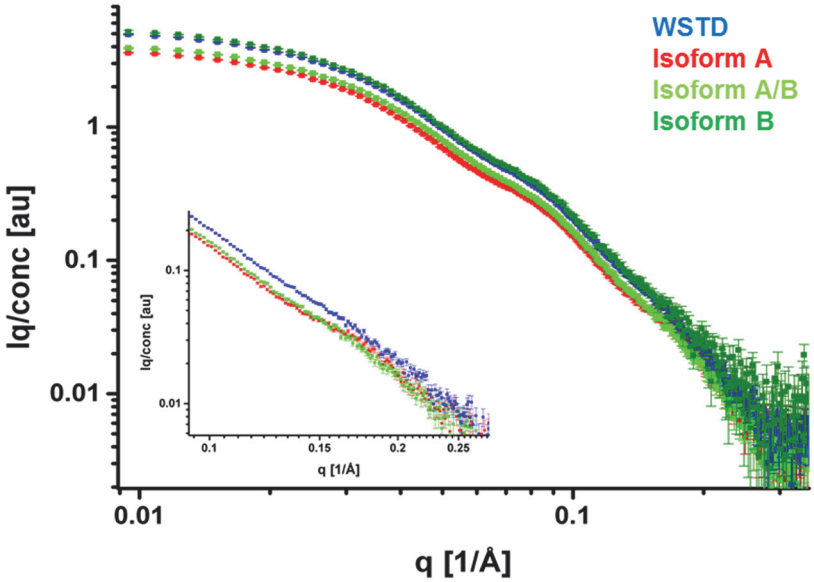

Fig. 30: Scattering intensity plots in depence of the scattering vector of the different analyzed IgG2 samples (left). A zommed view is depicted on the right to illustrate the differences observed in the raw data. Isoform A (red), isoform B (light-green), isoform A/B (dark-green) and the WSTD (blue).

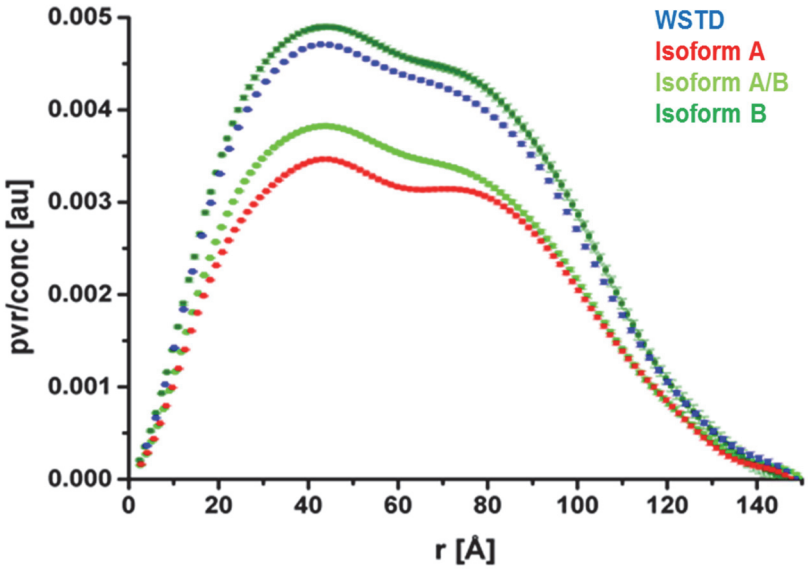

Fig. 31: Pair distribution function p(r) derived by fourir transformation of the scattering data. Isoform A (red), isoform B (light-green), isoform A/B (dark-green) and the WSTD (blue).

Tab. 13: Derived parameters describing structural properties of the samples obtained by SAXS.

Sample	R_G [Å]	D_{Max} [Å]	Porod volume [Å^3]
Isoform A	52.9 ± 0.9	150	252810
Isoform A/B	50.9 ± 0.6	146	246770
Isoform B	50.7 ± 0.4	143	246360
WSTD	50.8 ± 0.4	144	247550

The acquired scattering data were used to calculate homology models of the different isoforms resulting in an atomic-resolution model of the structural diversity of IgG2 molecules. Due to the fact that no single IgG2 crystal structure was solved until now, the homology model was built-up using the public accessible PDB Li33 IgG2 di-Fab (PDB ID accession code: 3KYM; Pepinsky *et al.*, 2010) and the Fc-part of an IgG1 (PDB ID accession code: bpj_1831_mmc3; Brandt *et al.*, 2010) since a very high identity level for these fragments were found in comparison to the examined IgG2 (Fd: 90% incl. 3 gaps; LC: 89% incl. 2 gaps; Fc: 96% incl. 0 gaps). The differences are mainly restricted to the complementary determining regions in the Fab that are characteristically placed in flexible loops. No insertions or deletions were performed in the template structures, and the main *β*-strand structures and locations of the highly conserved Cys residues were retained. Differing amino acids were exchanged using the *mutation* function within PyMol. The generated fragments were subjected to rigid body modeling in which the domains were iteratively coordinated according to the experimentally derived scattering data. The sequence section ^{224}CCVECPPCPAPPVA^{237} in the hinge was omitted in the simulation process to ensure unlimited degrees of freedom during approximation of the domains. For this reason, a maximal distance of 30 Å between C(α)-^{223}Lys and C(α)-^{238}Gly was defined as a placeholder for the missing amino acids. The hinge ^{224}CCVECPPCPAPPVA^{237} was inserted into the final model after the modeling process. In sum, ten models were calculated for each sample and ranked concerning their χ^2-value comparing the experimental scattering curve with the one derived for each calculated model. The best-fit models are depicted in Figure 32. In addition, the comparative scattering plots of experimental and calculated datasets and the derived calculated bead-models are shown. Cross-validation by sedimentation coefficient modelling of the final isoform structures using HydroPro resulted in $s_{20,w}$-values of 6.82 S (isoform A), 6.85 S (isoform A/B) and 6.90 S (isoform B).

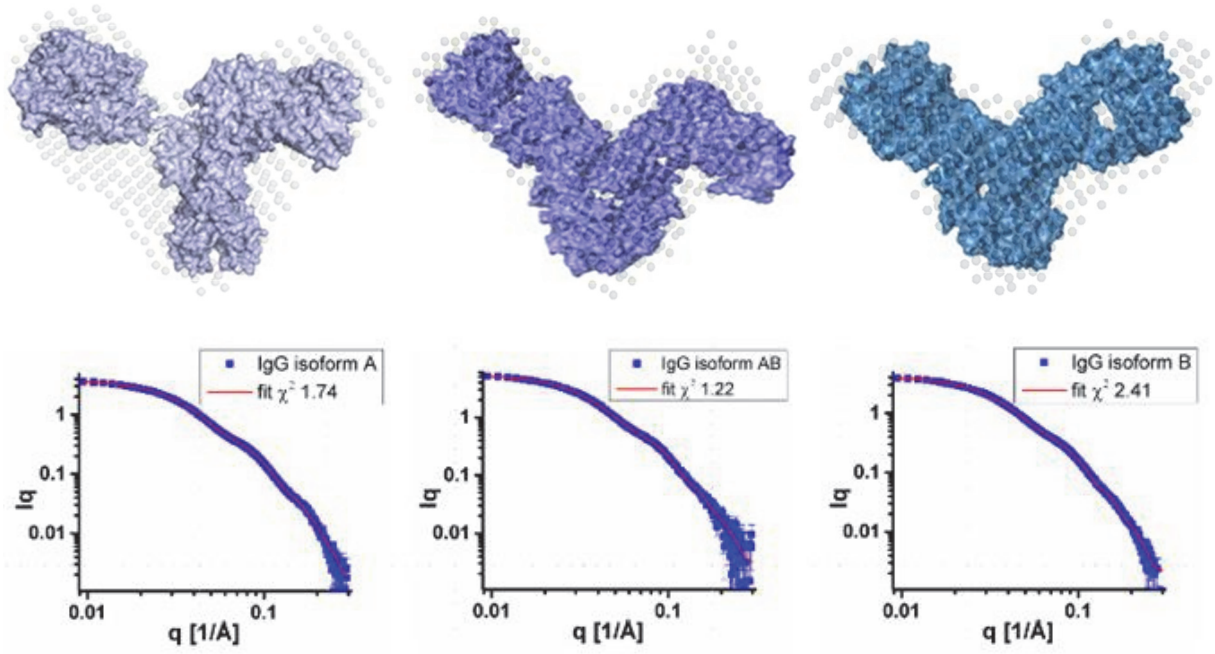

Fig. 32: Structural models of the investigated IgG2 isoforms obtained by SAXS and rigid body modeling. The *ab initio* calculated bead models are shown in the background of each structure. The lower panel shows the experimentally derived scattering data and the fits of the rigid body modeling.

3. 2. 6. Functional characterization

The above described methods revealed structural differences for the different isolated IgG2 isoforms. In the next step, the potency and specificity of the samples were determined in an ELISA assay that measures binding of the antibody to the target. Bound IgG2 molecules were quantified using an anti-human IgG-specific antibody coupled to horseradish peroxidase followed by addition of the substrate 2,2'-azino-di-(3-ethylbenzthiazoline-6-sulfonate) (ABTS). The isolated isoforms A and B were tested relative to the WSTD with its potency set to a value of 100 %.

The measurements were performed in two independent set-ups and resulted on average in a 29 % higher potency for isoform A (129 % ± 17 %) compared to the unfractionated material and 8 % less activity (92 % ± 10 %) for isoform B (Fig. 33). To verify the differences observed by ELISA, the samples were also tested in a cell-based potency experiments based on the PathHunter® assay. The assay uses the U20S cell line expressing the antigen and a reporter protein that is tagged with one fragment of a split β-galactosidase system [Lamerdin *et al.*, 2016]. When the tagged reporter protein is exposed to the other half of the split β-galactosidase protein, active β-galactosidase is

formed which hydrolyses the substrate and produces a chemiluminescent signal. In the assay, the antigen binds to its receptor on the cell surface resulting in signaling and reporter protein degradation, leading to a decrease in chemiluminescent signal. The antibody inhibits antigen-based activation leading to an increase in chemiluminescence that was tracked during analysis. In this assay, again, the two isolated isoforms were tested for their bioactivity relative to the starting material in two independent measurements. This analysis revealed on average a potency of 149 % (± 6 %) for isoform A and 93 % (± 1 %) for isoform B which supported the observation from the ELISA based potency determination.

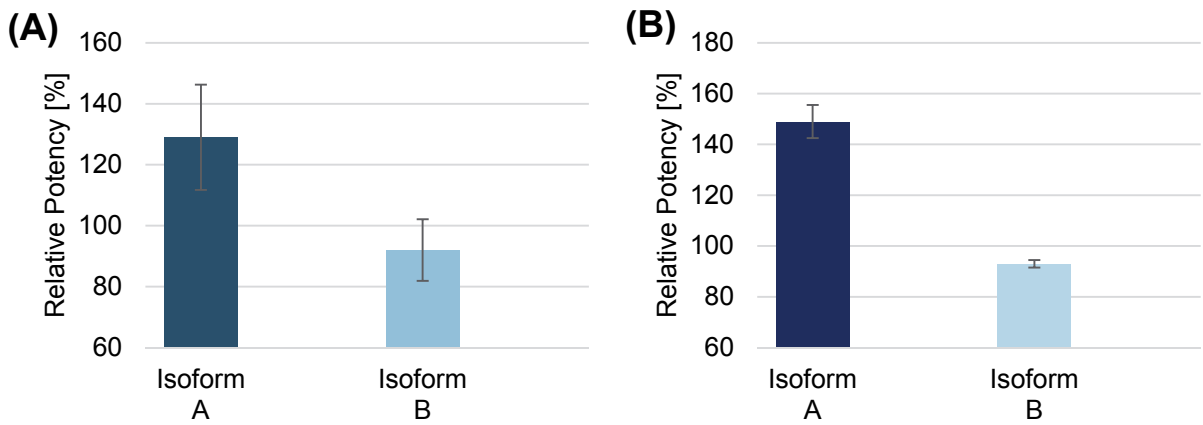

Fig. 33: Bar plots illustrating the results of potency determination. Bioactivity for isoform A and isoform B was analyzed by an ELISA-based assay (A) and additionally by a cell-based bioassay (B). The results describe the relative potency compared to the unfractionated starting material.

Next, the single isoforms were analyzed with regard to their complex formation with its antigen/target to unravel the cause for the discrepancies in biological activity. Since analytical ultracentrifugation provides high resolution also for higher order complexes, AUC was the method of choice for this analysis. The IgG2 isoforms and the unfractionated WSTD was mixed with the target molecule in an antibody to target ratio of 1:3 and 3:1 and subjected to AUC analysis after reaching the equilibrium state. The target of this investigated IgG2 appears as a trimer whereas every subunit contains one paratope (^{233}Thr-^{236}Leu) [Schieferdecker *et al*., 2014] for this IgG2. Since both proteins are multivalent (IgG2: divalent; target: trivalent) there is the possibility that the components do not bind in a simple 1:1 stoichiometry, but rather combine to form more complex assemblies. The formation of different complexes by the investigated isoforms

influence the potency of the drug molecule. Tables 14 and 15 summarize the $s_{20,w}$-values corresponding to the observed components and complexes.

Besides higher order complexes, the preferentially formed complexes in the presence of an excess of the target molecule yielded in the case of isoform A complexes with an antibody/target ratio of 1:1, 1:2 and 3:2, in the case of isoform A/B 1:1, 1:2, for isoform B 1:1, 2:1/2:2 and in the case of the WSTD 1:1, 1:2 and 3:2.

Adding different IgG2 samples in an excess relative to the target resulted in an antibody/target ratio complex of 3:2 for isoform A and 3:1 complexes for the other three investigated IgG2 isoforms.

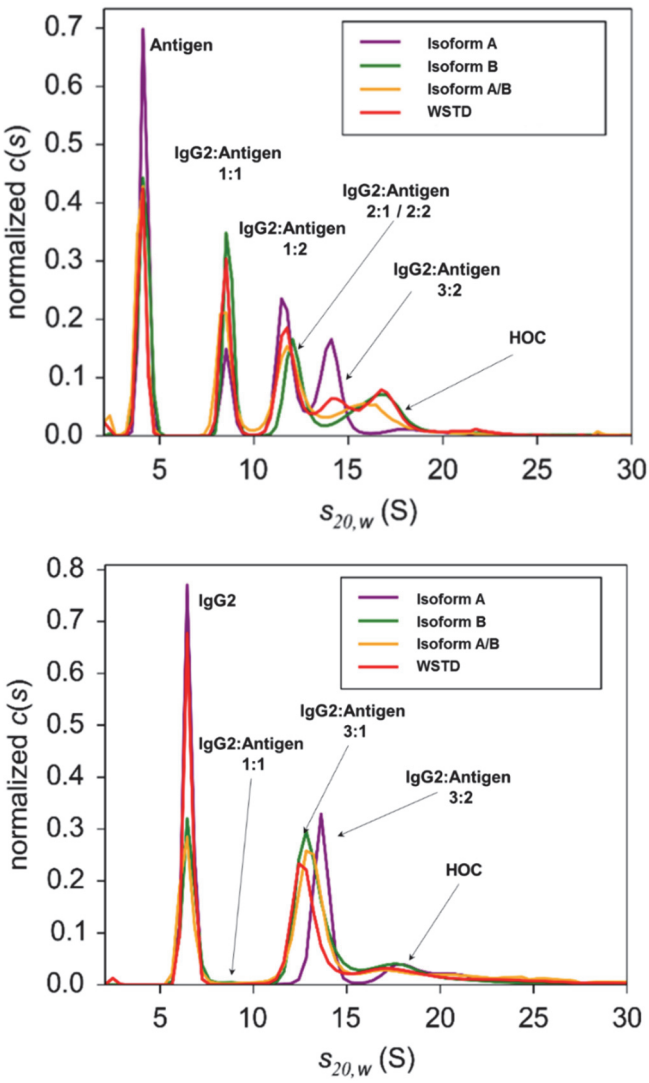

Fig. 34: Sedimentation coefficient distribution of the formed complexes by either an excess of target (upper plot) or an excess of antibody (lower plot) in the equilibrium state. The traces describe the sedimentation coefficient distribution of the isolated isoforms in the presence of the target molecule. The isoform A sample is depicted in violet, isoform B in green, isoform A/B in yellow and the WSTD in red.

Tab. 14: Complex formation in the equilibrium state of the different IgG2 samples by adding an excess of the target.

Sample	Target	Antibody	1:1	1:2	2:1/2:2	3:1	3:2	4:3 and HOC*
Isoform A	37.2	-	10.2	27.3	-	-	21.9	4.2
Isoform A/B	29.1	-	21.7	27.7	-	-	-	12.1
Isoform B	31.7	-	22.9	-	20.2	-	-	24.4
WSTD	23.3	-	20.3	25.0	-	-	13.7	16.0

*HOC: Higher order complexes

Tab. 15: Complex formation in the equilibrium state of the different IgG2 samples by adding an excess of the antibody.

Sample	Target	Antibody	1:1	1:2	2:1/2:2	3:1	3:2	4:3 and HOC*
Isoform A	-	45.7	0.5	-	-	-	34.2	11.2
Isoform A/B		25.8	-	-	-	49.3	-	10.4
Isoform B	-	26.7	0.6	-	-	54.1	-	18.3
WSTD		39.7	-	-	-	39.4	-	18.9

*HOC: Higher order complexes

3. 3. Discussion

3. 3. 1. Isolation and verification of the three most dominant disulfide isoforms

Recent studies described human IgG2 molecules to be a mixture of disulfide mediated structural isoforms [Wypych *et al.,* 2008; Allen *et al*., 2009] originating from redox environment during protein expression and downstream processing as well as *in vivo* caused by blood´s redox condition . The observed disulfide scrambling originates from close proximity of cysteines in the upper hinge region and those located in the C_L and C_H1 domain of the Fab [Wang *et al.*, 2011]. Reversed phase and cation exchange chromatographic investigations have shown to be suitable for separation of these three main variants isoform A, isoform A/B and isoform B [Zhang *et al.,* 2010; Wypych *et al*., 2008]. The extreme isoform A and isoform B can be interconverted by application of mild redox conditions with and without the addition of low concentrations of chaotropic agents [Liu *et al*., 2008].

In this study, the three main disulfide isoforms that occur in an IgG2 drug product were successfully isolated and consequently characterized to reveal the disulfide mediated structure-function relationship.

The enrichment and isolation procedure was tested to not alter the three dimensional structure of the molecule as well as to not induce any post-translational modifications in the primary structure of the isoforms. From these investigations it was concluded that the purification/isolation process was suitable to obtain pure isoform samples which could be characterized in more detail.

3. 3. 2. Structural characterization of isolated isoforms

Due to the high abundance of the different isoforms in native IgG2κ based biotherapeutics [Wypych *et al.*, 2008], it is of high interest to understand the structure-function relationship of these isoforms in detail. These results can provide insight into the impact of isoform distribution on the efficacy of the final product.

Studies that aimed to elucidate disulfide-mediated structural alterations of IgG2 molecules [Dillon *et al*., 2008; Zhang *et al.,* 2015; Tian *et al.*, 2014] have shown that isoform A exhibits a more extended structure than isoform B. This was revealed by size exclusion chromatography, analytical ultracentrifugation, reversed-phase liquid chromatography and intact mass spectrometry. These observations were confirmed by H/DX-MS studies that identified isoform B as the more rigid one displaying slower exchange kinetics in some regions [Zhang *et al*., 2015]. Ensemble optimization method (EOM) calculations using small-angle X-ray scattering data of an analysis of isoform mixtures gave insight into the conformational ensemble and an idea of the overall structure of the different isoforms in the IgG2 sample [Tian *et al.*, 2014].

In this study, the previous investigations performed on structural differences of IgG2 isoforms could be confirmed using low-resolution technics such as size-exclusion chromatography, analytical ultracentrifugation and differential scanning fluorimetry. In conclusion, isoform B is the most compact while isoform A the most extended variant, which is in-line with previous investigations. Isoform A/B showed values in between isoform A and B for every analytical method applied leading to the suspicion that A/B is a structural mixture of A and B. To locate the differences in structural arrangement between the isoforms and to compare structural dynamics and solvent accessibility on the peptide level, H/DX-MS was performed. Hydrogen deuterium exchange kinetics

were similar in the Fc-region for all analyzed isoforms whereas differences were detected in the Fab fragment. Here, all doamins, C_H1, V_H, C_L and V_L were affected with isoform B revealing less solvent exposure and slower hydrogen exchange compared to isoform A. H/D exchange for isoform A/B versus isoform A comparison showed that the same sequences as in isoform A versus isoform B comparison were affected by decreased exchange kinetics. Exchange kinetics of isoform A/B were constantly in between those of isoform A and isoform B. This can be attributed to the asymmetric disulfide distribution leading to an asymmetrical orientation and differing flexibility of the two Fab domains. In other words, for A/B one Fab is comparable to isoform A and the other Fab to isoform B regarding H/D exchange kinetics.

Since structural differences on the protein and peptide level were detected by the respective analytical methods, small-angle X-ray scattering combined with homology and rigid body modeling was performed to obtain a complete structural picture of the investigated isoforms. From the scattering raw data hydrodynamic parameters such as R_G -, D_{Max} and V_{porod} values were obtained which are in-line with the measurements done on the global (SEC, AUC, DSF) and peptide level (H/DX-MS). A homology model was built and fitted to the experimental scattering data. The final models were cross-validated by comparing the theoretical sedimentation coefficients to the experimental ones. Best-fitted structures show differences in compactness and proximity of the Fab domains to the Fc part. The resulting structure for isoform A is the most extended one with the largest distances between the Fab and the upper hinge region. One Fab arm is supposed to be bent down towards to the Fc which is also comparable to a calculated IgG1 structure in aqueous solution [Brandt *et al.*, 2010]. In contrast, the structural representation of isoform B is supposed to be very compact and rigid with both Fab fragments in very close proximity to the Fc-part revealing drastically decreased flexibility in the hinge region. The same picture was obtained for isoform A/B but just for one of the Fab domains while the other one is bent down. This indicates flexibility for one Fab domain, which additionally illustrates A/B as an intermediate of A and B resulting in an asymmetric structure. Inspecting the structural models, one has to keep in mind that they represent an averaged geometry in aqueous solution so that the flexible domains of A and A/B might be just a snapshot of multiple orientations.

Taken all the structural investigations together, from protein level to atomic structural models, it can be concluded that isoform A is the most extended variant in IgG2 antibody samples, containing Fab domains that are flexible due to the hinge region. Isoform B is the most compact form with Fab domains very close to the Fc part, which results in increased rigidity, restricted degrees of freedom and decreased dynamics. Isoform A/B exhibits both characteristics originating from asymmetric disulfide connectivity – one flexible Fab and one rigid very close to the Fc part which can be attributed to the asymmetric disulfide connectivity and unambiguously shown by H/DX-MS analysis.

3. 3. 3. Functional characterization and bioactivity estimation

Since the structural comparison of the three main isoforms revealed significant differences, they were investigated with regard to their biological activity. Recent published data showed differences in bioactivity with some isoforms of specific IgG2 therapeutics differing in potency while other do not show this effect [Dillon *et al.*, 2008]. For this reason, the isolated isoforms A and B of this IgG2 were tested in cell-based and ELISA-based bioassays. Both analyses revealed that isoform A is 56% more active in the cell-based and 29% more active in the ELISA-based bioassay than isoform B. From the SPR target binding analysis both isoforms have similar dissociation- and association rates which implies that binding strength was not the reason for the differences detected in bioactivity analysis.

To shed light on the origin for differences in activity of the investigated isoforms, they were analyzed with regard to the complexes they form with the target molecule. The target is a trimeric complex bearing three potential binding-sites for the IgG2 antibody as shown in Figure 35 [Schieferdecker *et al.*, 2014].

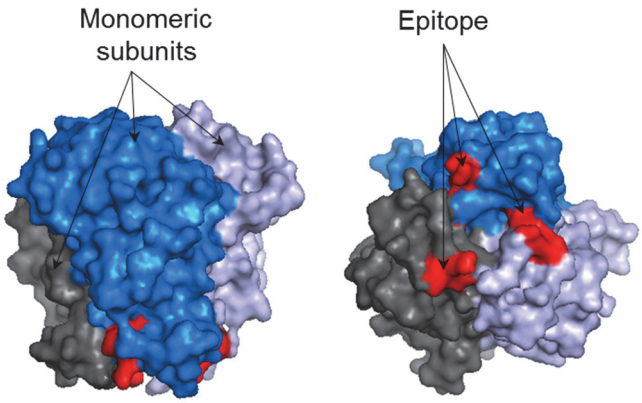

Fig. 35: Structural representation of the target molecule [adapted from PDB ID: 1JTZ]. The target molecule consists of three monomeric subunits – indicated in grey, blue and light blue. Each subunit exposes one IgG2 binding-site (shown in red).

To unravel complex stochiometry in the equilibrium state, target and antibody were mixed on the one hand with an excess of target and on the other hand with an excess of antibody isoform since this therapeutic is administered in an excess compared to the target molecule circulating in the patient´s body.

Analyzed by analytical ultracentrifugation solely isoform A is able to form the reported 3:2 (antibody:target) complex [Arthur *et al.*, 2012] whereas isoform B and A/B form complexes that lack one target molecule – three antibody molecules with one target molecule. This observation revealed that isoform A is able to capture more target molecules than compared to B and A/B and thus explains the differences in biological activity which origins from disulfide mediated structural alteration and increased rigidity of the non-canonical forms.

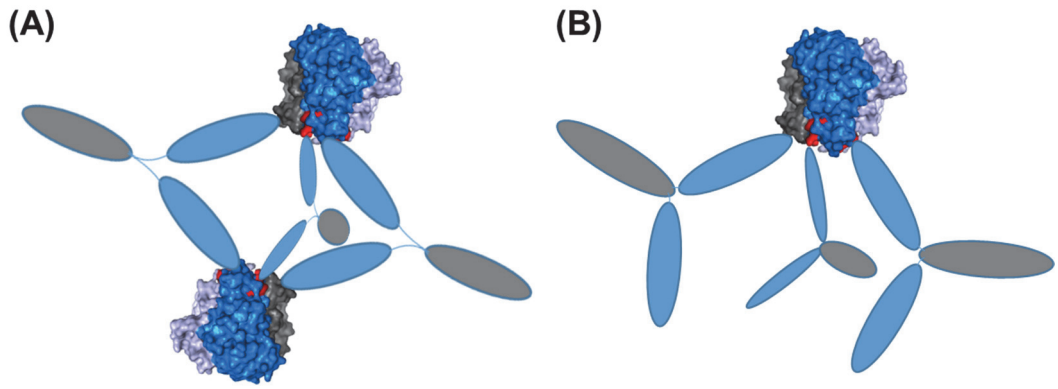

Fig. 36: Schematic representation of formed IgG2/target complexes. (A) Thermodynamically most stable complex formed by isoform A in a ratio of 3:2. (B) Complex formed by isoform B and isoform A/B with the target molecule in a ratio of 3:1. Fc fragments are colored grey and Fab fragments are shown in light blue. The target molecule is shown in surface representation of the crystal structure [adapted from PDB ID: 1JTZ].

Figure 36 schematically illustrates the complexes formed by the different disulfide isoforms. Due to the flexibility resulting from the hinge region in isoform A, the Fab domains are able to orientate in the way that the single IgG molecules can bind two target molecules to form the thermodynamically most stable complex (Fig. 36 A) [Arthur *et al*., 2012]. In contrast, due to the rigidity of the Fab domains in isoform B and one Fab in isoform A/B the degrees of freedom are restricted which results in a steric hindrance for these two isoforms to capture two target molecules (Fig. 36 B). These findings explain the differences for A and B in the bioactivity investigations since more target can be bound by isoform A than by isoform B. Investigations performed by Dillon and co-workers showed that isoform A and isoform B obtained from different IgG2s [Dillon *et al.,* 2008] do not always show differences in potency assays. Regarding the findings in this study this phenomenon can be explained by dependency of the IgG2´s avidity.

It was also shown that isoform A and A/B are converted to isoform B when circulating in blood, as revealed in the *in vivo* study in cynomolgus monkeys [company internal pre-clinical study]. Consequently, the isoform characterization results imply that the potency of the IgG2 therapeutic is steadily decreased after administration due to the interconversion from isoform A to isoform B. Complex investigations with the target showed that isoform A/B and isoform B form identical complexes (3:1) which means that both exhibit comparable bioactivity. Consequently, the interconversion from isoform A/B to isoform B is not critical – but the one of isoform A.

In sum, it can be concluded that the disulfide isoform distribution of isoform A and isoform B in the drug product is very critical – in the first days after administration isoform A is interconverted to isoform B. In contrast, the initial isoform A/B content in comparison to isoform B content is uncritical from a structure-function point of view since B and A/B show similar complex formation with the target.

Consequently, to obtain a more potent drug product it would be beneficial to engineer an isoform A structure-like drug molecule that is not prone to disulfide scrambling under mild redox conditions to retain a highly potent drug while circulating in patient´s blood.

4. Dimeric structures and the major dimerization pathway of an IgG1

4. 1. Introduction

Heterogeneity is a common and known property of biopharmaceutical products and is in focus of further development since the risk of unwanted side effects caused by variants has to be minimized. A subset of these modifications already arise during expression within the cell (e.g. glycosylation, C-terminal lysine truncation, ubiquitination) and additional ones occur in the culture medium as well as during subsequent harvesting and *in vitro* manipulations of the expressed proteins like purification, formulation and storage. Among modifications are glycosylation, asparagine/glutamine deamidation and isomerization, clipping, oxidation and self-association (Cholewinski *et al*., 1996; Manning *et al.*, 1989; Li *et al.*, 1995). The latter designation involves various forms differing in size, visibility, nature of intermolecular interaction, covalent or non-covalent linkages, ordered or disordered in structure, soluble or insoluble and reversible or irreversible association [Iwura *et al.*, 2014; Joubert *et al.*, 2011; Narhi *et al*., 2012]. The association can originate from various initializing conditions [Mahler *et al.*, 2008]. According to Philo and coworkers, the aggregation process can be divided into five mechanisms: reversible association of the native monomer, aggregation of conformational-altered monomer, aggregation of chemically-modified proteins, nucleation-controlled aggregation and surface-induced aggregation [Philo *et al*., 2009]. The complexity of aggregation is depicted in Figure 37.

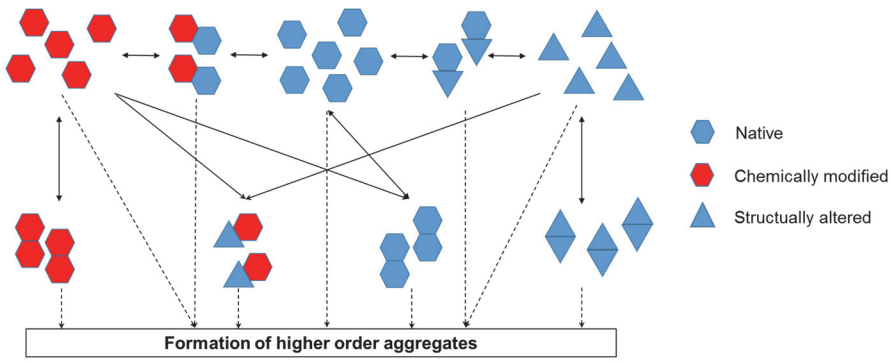

Fig. 37: Simplified representation of the complexity of protein aggregation. The native protein is drawn as blue colored hexagon; chemically modified protein is represented as red hexagon and structurally altered monomers as drawn as blue triangles. Surface-induced aggregation is feasible by subsequent structural or chemical alteration caused by surface contact.

This classification is supported by several studies on stress-induced and naturally occurring dimer formation and substantiate the complexity of protein aggregation implicated in this classification. Investigations on naturally formed dimers of the two different IgG1 drug molecules epratuzumab and palivizumab [Remmele *et al*., 2006; Iwura *et al*., 2014] revealed a mixture of covalent and non-covalent interacting dimers. Structural heterogeneity due to Fab:Fab, Fab:Fc and Fc:Fc interaction was observed. In contrast, in studies on other IgG1 therapeutics higher homogeneity with regard to the structure of the dimer species - exclusively linked by Fab:Fab interactions - and concerning the mode of interactions was detected [Plath *et al.*, 2016; Deperalta *et al.*, 2013; Moore *et al*., 1999]. Another IgG1 showed specific functional regions in the C_H2 domain and the hinge region between C_H1 and C_H2 domains to be directly involved in the association mechanism [Iacob *et al.*, 2013].

Besides investigations on naturally occurring aggregates and dimers, also studies characterizing modified and stress-induced IgG1 molecules are published. Kayser *et al*. demonstrated the need of glycosylation to dynamically stabilize the molecule and prevent self-association by shielding hydrophobic residues from being exposed to the solvent [Kayser *et al.*, 2011]. Stress conditions that promote aggregation include temperature-, mechanical-, freeze/thaw-, oxidative- and pH - stress. The resulting chemical modifications that are supposed to trigger the aggregation process were identified to be Asn deamidation and His/Trp/Met oxidation of solvent accessible residues [Luo *et al*., 2011; Iwura *et al*., 2014]. Indeed, depending on the applied stress conditions, Paul and coworkers demonstrated different and specific dimer structures of one IgG1 [Paul *et al.*, 2011].

In addition to the investigation of dimers and aggregates present in drug products, several algorithms were developed to predict *in silico* aggregation-prone regions (APR) in order to decrease the self-association propensity and to obtain better insight into the nature of dimerization or even improve the quality by amino acid exchange of APRs using directed mutagenesis [Courtois *et al*., 2016; Chennamsetty *et al*., 2010]. The *in silico* investigations are based on ranking aggregation propensity of single amino acids depending on their physicochemical properties and their accessible surface to facilitate engineering of stable drug molecules.

Generally speaking, the accelerated aggregation propensity of IgG1 molecules arises from the extensive hydrophobic patches on the surfaces of IgGs, especially on the Fc. In addition, the complementarity determining regions (CDRs) of IgGs, that are responsible for antigen binding, exhibit frequent occurrences of hydrophobic and electrostatic residues that are inserted intentionally for proper and strong antigen binding. Furthermore, stress-induced structural and chemical modifications on the surface of the protein are considered to trigger the aggregation process [Wang *et al*., 2009; Wu *et al.*, 2010; Li *et al.*, 2016].

From the multitude of studies conducted it can be seen that aggregation is of major concern in biopharmaceutical development. This is due to the fact that aggregates potentially influence biological functions [Paul *et al.*, 2012], reduce potency, induce/enhance immune responses by initiating anti-drug antibody production [Rosenberg, 2006; Sauerborn *et al*., 2010; van Beers *et al.,* 2010] and influence the antibody clearance machinery *in vivo* [Hotzel *et al.*, 2012; Li *et al*., 2016].

Here we describe an in-depth characterization study of thermal- and light-stress induced dimer species of an IgG1 molecule with regard to structure, function and dimerization triggering modifications using a broad range of physicochemical and biophysical methods. Thermal stress was chosen since this procedure is an established approach to simulate the ageing process of biopharmaceuticals. The applied methods comprise size-exclusion chromatography, analytical ultracentrifugation, mass spectrometry, small-angle X-ray scattering, partial hydrolysis, hydrogen/deuterium exchange mass spectrometry, *in silico* methodologies and potency assays. The combination of the derived results reveal novel insight in the structures of the species, the localization of intermolecular interaction-sites, the nature of interaction, aggregation initializing factors and the complexity of antibody aggregation.

4. 2. Results

4. 2. 1. Isolation and purity of dimeric aggregates

The investigated IgG1 shows remarkably increased aggregation propensity upon temperature and light stress exposure. Figure 38 shows a stacked overlay of size exclusion chromatograms (SEC) corresponding to unstressed, light stressed and temperature stressed material. The percentage of total dimer found in the analyzed samples was 1.8 % for the unstressed, 3.3 % for the temperature stressed and 11.9 % for the light stressed IgG1 relative to the monomer peak as measured by SEC. The dimer peak in the unstressed and temperature stressed sample contains local minima at 17.0 min (marked as dashed line in Fig. 38), indicating at least two different dimer species that differ in their hydrodynamic radii. Due to the dramatic increase of dimer content in the light stressed sample, the resolution of the two species observed in the other ones got lost and a single peak centered at the retention-time of the dimer 2 (D2) peak resulted.

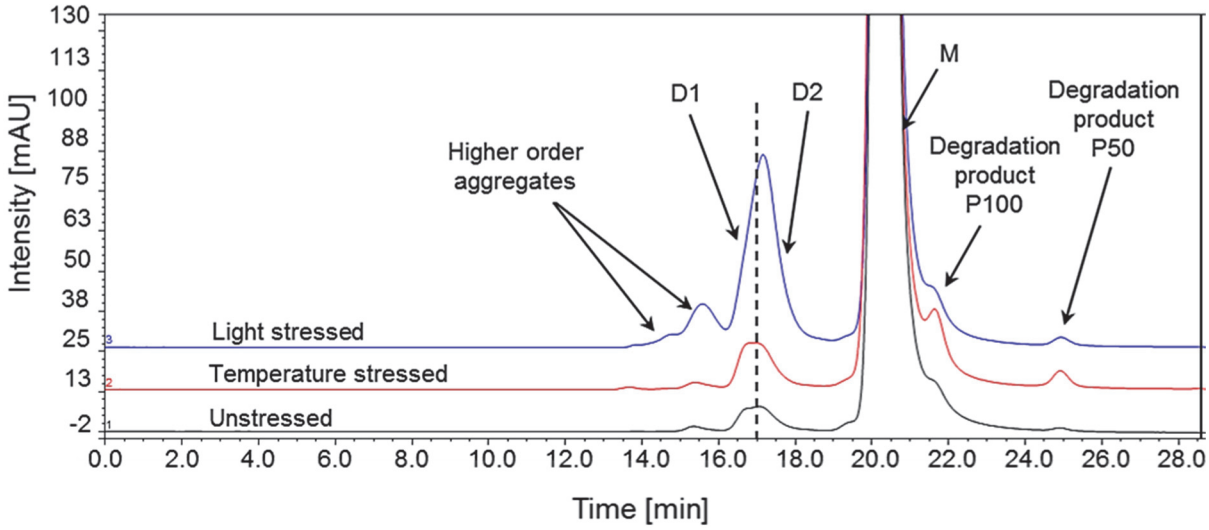

Fig. 38: SEC chromatograms of unstressed and differently stressed IgG1 samples. The black signal corresponds to the unstressed sample, the blue trace to light and the red one to temperature stressed material. Acquisition occurred at 214 nm. Peak designations mark eluting size variants in the chromatograms whereas dimer species (D1 and D2) are denoted according to their elution order. The rough separation of D1 and D2 is marked with a vertical dashed line. M corresponds to the monomer peak.

The two species and the monomers in each sample were isolated in a two-step fractionation workflow using two different SEC columns to obtain the highest possible purity of each specie. In the first step, dimer 1 (D1), dimer 2 (D2) - designation

according to their elution order - and monomer (M) were roughly fractionated using a Tosoh G3000SWXL column, concentrated and re-injected on a Phenomenex Yarra SEC-3000 column for a more precise fractionation of the aggregates. Afterwards, the samples were concentrated, buffer exchanged in drug substance buffer, flash-frozen and stored at -80 °C until usage. SEC chromatograms of the isolated size variants of the temperature-stressed (MT, D1T & D2T) and the light-stressed (ML, D1L & D2L) samples are shown in Figure 39. Unchanged elution profiles in periodic re-analysis of the separated species by SEC indicated stability of the samples.

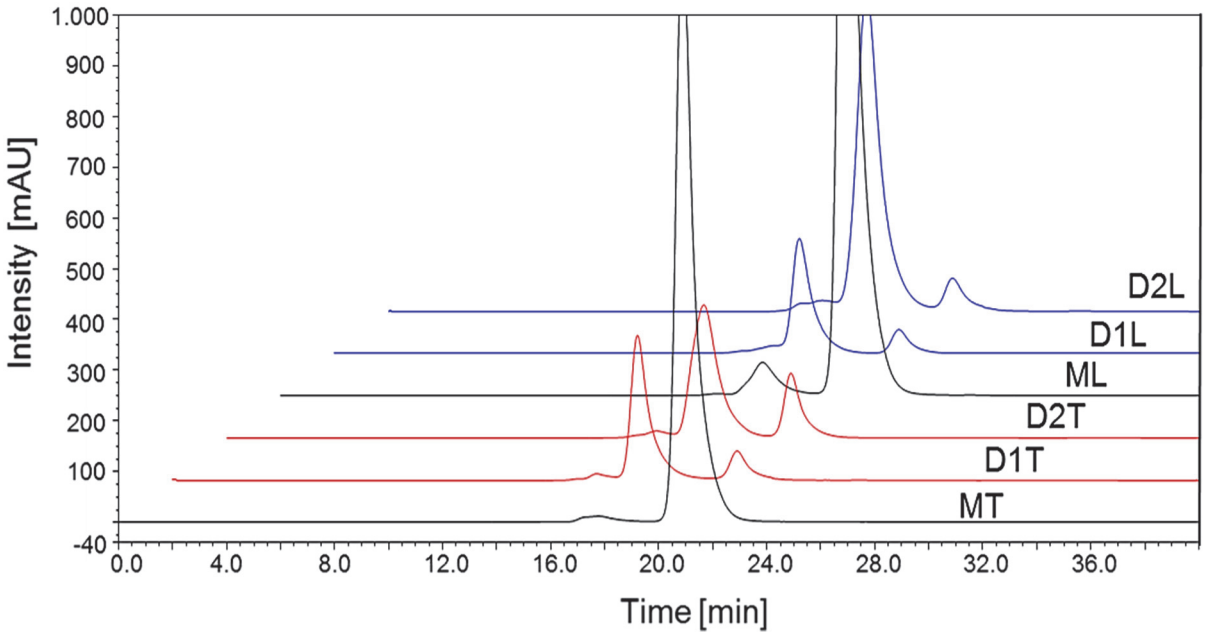

Fig. 39: Analysis of isolated size variants by SEC. The stacked chromatograms show the isolated isoforms after final buffer exchange. Designations correspond to the pre-treatment (T: temperature stress; L: light stress) and size variant (M: monomer; D1: dimer 1; D2: dimer 2). The purities range from 95.0% to 98.2% for the monomer (MT & ML) and from 76.6 % to 88.5 % (D1T, D2T, D1L & D2L) for the dimer variants. For analysis of the isolated variants the Tosoh G3000SWXL column was used according to chapter 2. 2. 3. 1.

From the reinjections of the samples in SEC the purities were estimated – the values are summarized in Table 16.

Tab. 16: Purity and elution time of the isolated fractions.

Sample	Retention time [min]	Purity [%]
MT	20.9	98.2
D1T	17.2	80.9
D2T	17.7	76.6
ML	20.9	95.0
D1L	17.2	84.2
D2L	17.7	88.5

Although the final fractions still contain monomer in the dimer samples – despite of multiple fractionation steps all dimer species contain transient, non-covalently linked dimers that dissociate upon dilution. This was verified by analyzing the samples in the presence of 0.3 % sodium dodecylsulfate (SDS). By addition of SDS, non-covalent linkages are disrupted and thus dissociation of the aggregate samples was enforced. Here, analysis occurred by analytical ultracentri-fugation (AUC) since SEC columns are not compatible with SDS. The s-value distribution is depicted in Figure 40.

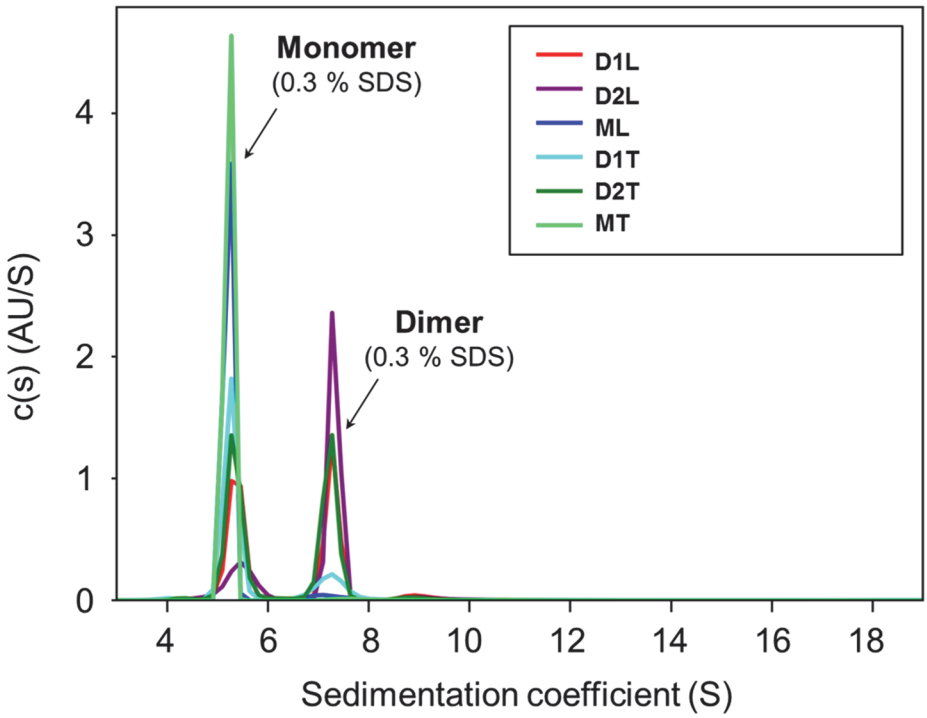

Fig. 40: Sedimentation coefficient distribution of the isolated fractions in the presence of SDS. AUC analysis revealed that the isolated dimer species contain non-covalent as well as covalent linked dimers by enforced dissociation in the presence of SDS.

Quantification of the covalent dimers present in the different samples resulted in a content of 26 % (D1T), 71 % (D2T), 64 % (D1L) and 89 % for D2L. By dilution of the

samples prior reinjection in SEC an equilibrium between non-covalent linked dimers and monomers arose. For this reason, obtaining 100 % pure dimer samples was not feasible.

Nevertheless, the samples showed sufficient purity for the following structural and functional analysis.

4. 2. 2. Global structural arrangement of dimeric species

The elution properties in SEC analysis revealed a higher hydrodynamic radius for D1T and D1L compared to D2T and D2L indicating a more extended complex structure for the dimer 1 species. In order to verify these observations, the collected samples were subsequently subjected to analytical ultracentrifugation (AUC). Furthermore, hydrodynamic data like R_G and $s_{20,w}$ were obtained to support homology modeling of the size variants and to get insight into the shape of the complex as well as orientation of the single domains of the interacting monomers. The extrapolated $s_{20,w}$-values of the in two independent analysis performed measurements amount to 6.54 S ± 0.01 S (ML), 9.12 S ± 0.02 S (D1L), 9.49 S ± 0.12 S (D2L) , 6.52 S ± 0.01 S (MT) , 9.08 S ± 0.08 S (D1T) and 9.39 S ± 0.10 S (D2T). Figure 44 displays the sedimentation coefficient distribution of the different size variants. These results strengthened the observations made by SEC and exclude possible differences in elution order attributed to different strong interaction of the species with the stationary phase of the SEC columns. Consequently, the elution order is solely caused by differing shapes of the variants since AUC exclusively reports on the sedimentation velocity of the molecules.

The frictional coefficient ratio f/f_0 calculated from the analysis compares the frictional coefficient f for the molecule with the the one for an ideal sphere f_0 of the same volume in order to estimate the compactness/extension of the investigated sample. Starting from the experimentally derived $s_{20,w}$-values the f/f_0 ratios were calculated to 1.52 (ML), 1.76 (D1L), 1.68 (D2L), 1.52 (MT), 1.77 (D1T) and 1,66 (D2T). The plotted sedimentation coefficient distributions and a summary of the hydrodynamic parameters of the measurements are presented in Figure 41 and Table 17.

SEC and AUC analysis indicated different size and shape of the D1 and D2 variants whereas the two D1 species displayed a more extended overall shape than D2.

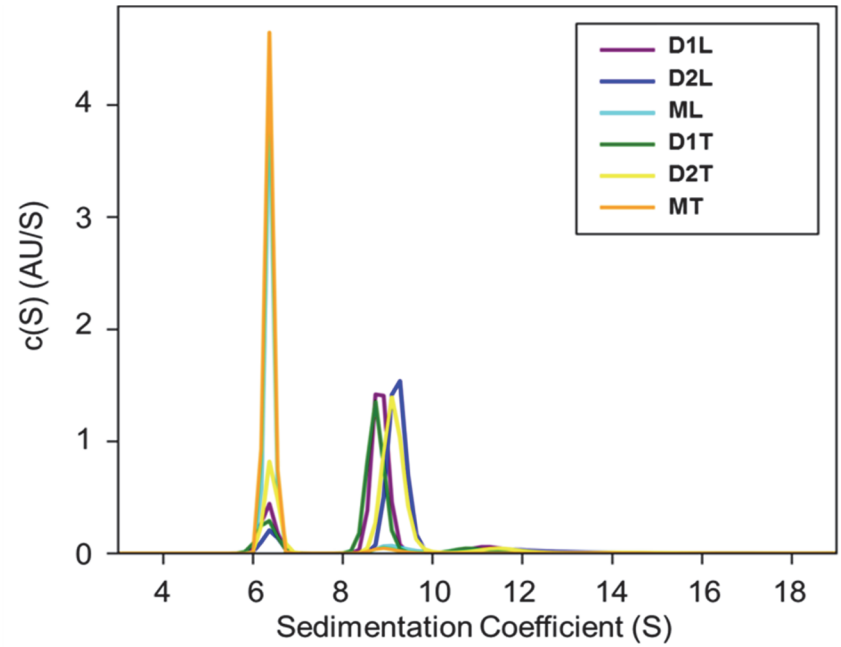

Fig. 41: Sedimentation coefficient distributions of monomer and stress induced dimer species analyzed by AUC. The x-axis shows the experimentally derived sedimentation coefficient; the y-axis shows the relative abundance of the species in signal units per sedimentation coefficient.

Tab. 17: Hydrodynamic data obtained by AUC analysis.

Sample	$s_{20,w}$	f/f_0
MT	6.52 S ± 0.01	1.52
D1T	9.08 S ± 0.08	1.77
D2T	9.39 S ± 0.10	1.66
ML	6.54 S ± 0.01	1.52
D1L	9.12 S ± 0.02	1.76
D2L	9.49 S ± 0.12	1.68

To get a deeper understanding of the dimeric structure small-angle X-ray scattering (SAXS) was applied. X-ray data collection was carried out in dilution series from 1.25 mg/mL, 2.5 mg/mL and 5.0 mg/mL to exclude interference caused by intermolecular repulsive or attractive interaction, using time-frame analyses to ensure the absence of radiation damage effects. The acquired scattering data were used to calculate the radii of gyration (R_G) by Guinier plotting. In addition, D_{max}, and ρ(r) were calculated with GNOM by indirect Fourier transformation of the scattering data. R_G is defined as the root mean square distance from each atom of the protein to the centroid and therefore describes size and dimensions of the molecule. The ρ(r) functions list the distribution of pairwise distances of each scattering center within the molecule which subsequently

includes D_{max} as the longest interatomic distance in the molecule. Figure 42A shows the raw data of the two investigated ML and MT samples. Both show very similar curves which indicates similar domain orientations of the monomer independent of possible stress-induced modifications. The dimer species significantly differ in their scattering profile from their corresponding monomer (Fig. 42B). Also, species 1 differs especially at lower scattering angles from the dimer 2 variants. D1T and D1L as well as D2T and D2L solely slightly differ from each other indicating comparable domain orientations. Data evaluation resulted in R_G values of 5.35 nm (ML), 5.38 nm (MT), 8.09 nm (D1L), 8.14 nm (D1T), 7.63 nm (D2L) and 7.60 nm (D2T). The calculated pair distribution functions describe D_{max} which amounts to 172.84 Å for ML, 174.11 Å for MT, 279.54 Å for D1L, 257.90 Å for D2L, 281.12 Å for D1T and 261.17 Å for D2T (exemplary ρ(r) functions are shown in Fig. 43).

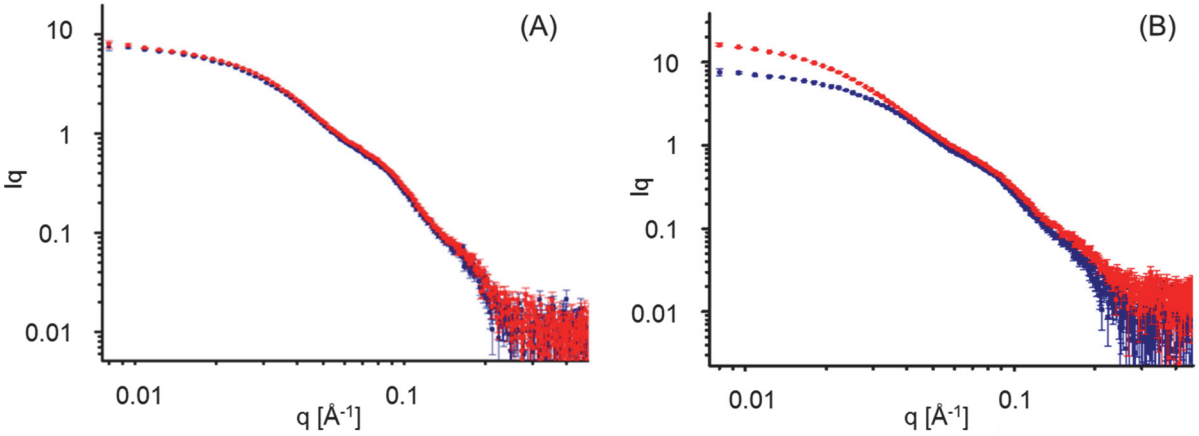

Fig. 42: Exemplary scattering raw data. In the left plot (A) a comparison of both monomer samples is shown (MT: red trace; ML: blue trace). The right plot illustrates the difference in scattering raw data of a monomer and a dimer sample (ML: blue trace; D2L: red trace). In both cases, the scattering intensity I is plotted in dependence of the scattering vector q.

The parameters derived from SAXS – summarized in Table 18 – support the observations from SEC and AUC analyses that dimer 1 species exhibit a more expanded overall shape than the dimer 2 variants whereas the temperature and light stressed dimer 1 and dimer 2 samples are supposed to have very similar size and shape.

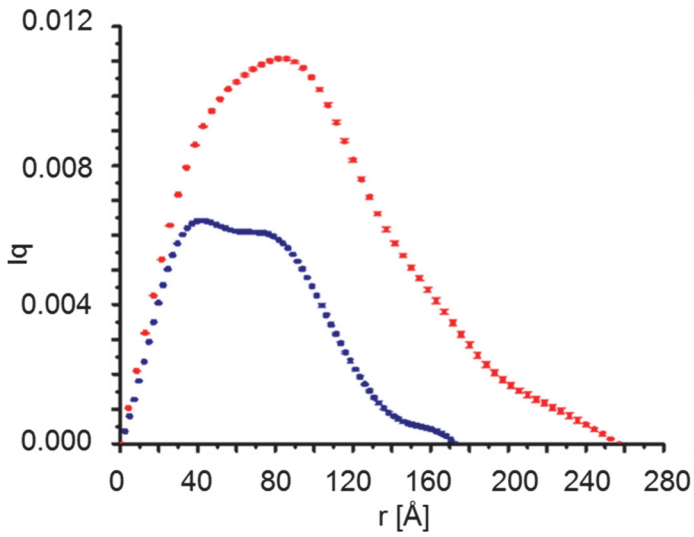

Fig. 43: Exemplary pair distribution function s of ML and D2L. The ρ(r) functions exemplary shown illustrate the pair-distribution function of a monomer and a dimer sample (ML: blue trace; D2L: red trace). The intersection with the x-axis marks D_{Max} of the variants.

Tab. 18: Summary of R_G and D_{max} values obtained by SAXS.

Parameter	MT	D1T	D2T	ML	D1L	D2L
R_G [nm]	5.38	8.14	7.60	5.35	8.09	7.63
D_{max} [Å]	174.11	281.12	261.17	172.84	279.54	257.90

Next high-resolution structural models were calculated from the hydrodynamic parameters that resulted from SAXS analysis. The molecular dynamics simulated all-atom model of the IgG1 trastuzumab (Brandt *et al.*, 2010; bpj_1831_mmc3) was used as a starting model. Due to the completeness of this structure, the applied energy minimization to the crystal structure and the high sequence homology – 91% identity in the heavy and 92 % in the light chain – this model was supposed to be suitable for the current study. The amino acid differences are restricted to the complementary determining regions CDR1 to CDR3 in the heavy and the light chains. These sequences were aligned within PyMol using the *mutagenesis* function to obtain a homology model with 100 % sequence identity to the IgG1 molecule of interest. Figure 44 displays the starting model with a magnified view of the mutated CDR sequences.

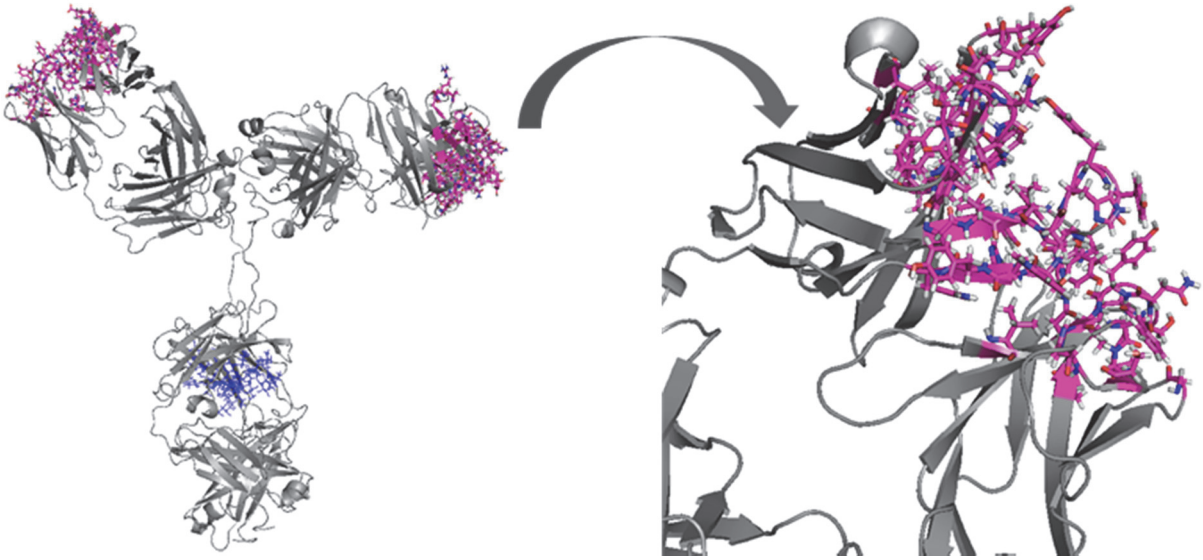

Fig. 44: Homology model of the investigated IgG1 molecule. Starting from trastuzumab as a template structure (Brandt *et al.*, 2010; PDB ID: bpj_1831_mmc3). The exchanged amino acids are located in the Fab domain and define the target interacting CDR sequences (stick representation colored in magenta). The wildtype framework is displayed in grey and glycans are colored in blue.

The initial homology model was not energy minimized upon mutation since a rigid body modeling approach was performed by using the informations revealed by SAXS. Nevertheless, mutation was necessary to adjust the molecular weight of the model structure to the IgG1 of interest.

Prior to subjecting the generated model to rigid body modeling calculations, the sequence section ^{223}Pro – ^{242}Gly of one heavy chain (hinge region) was cut out of the model to obtain two separated units – free Fab domain and Fc:Fab unit. The resulting domains were designated to be rigid, since the β-sheet rich domains form a tight and unflexible state, whereas the extended hinge of the Fc:Fab unit was defined as a flexible linker. During the calculations, the free Fab domain was iteratively approximated to the Fc:Fab counterpart which simultaneously exhibits predefined flexibility through the hinge region. For the approximation of the free Fab, a distance restriction of 66.5 Å between the $^{\alpha}$C-^{222}Glu of the Fab and the $^{\alpha}$C-^{243}Gly of the Fc-part was set to simulate the length of the missing hinge. Theoretical scattering data were calculated at every step of approximation and compared to the experimentally derived ones. For the analyzed ML and MT samples, 50 models each were computed and subsequently ranked by their χ^2-value. In addition, *ab-initio* bead models of the monomer samples were calculated directly from the scattering raw-data to compare the best-fit models with overall shape

of the molecule. Figure 45 displays the two modeled monomer samples ML and MT. The *ab-initio* bead models are shown in the background of the structures that fit well to the rigid-body modeling derived monomer structures.

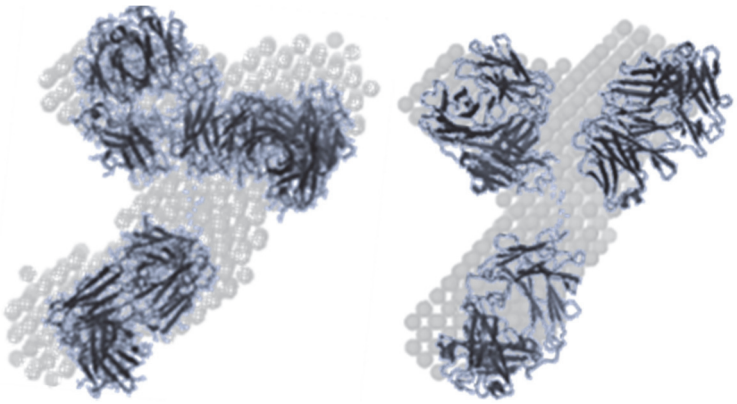

Fig. 45: Monomer structures of the differently stressed IgG1 molecules revealed by rigid-body modeling. The light stressed monomer (ML) is shown on the left, the temperature stressed one on the right (MT). *Ab-initio* bead model are displayed in the back to illustrate the goodness of fit of the all-atom model and the shape distribution directly derived by the scattering raw data.

Starting from these monomer structures. the different dimer variants were calculated by rigid-body modeling. For each dimer construct the monomer structure was duplicated and iteratively approximated to each other. In this approach, the monomer units were defined as rigid entities to restrict the degrees of freedom to the three-dimensional space where the approximation took place. After each step the theoretical scattering plots were calculated and compared to the experimental ones. The resulting dimer structures were finally ranked with regard to their χ^2-value. Figure 46 shows the best-fit models of the 90 calculated models including the *ab-initio* bead-models. Since Fab and Fc fragments have approximately the same masses and center of mass it was not feasible to distinguish the orientation of the single domains within the complexes.

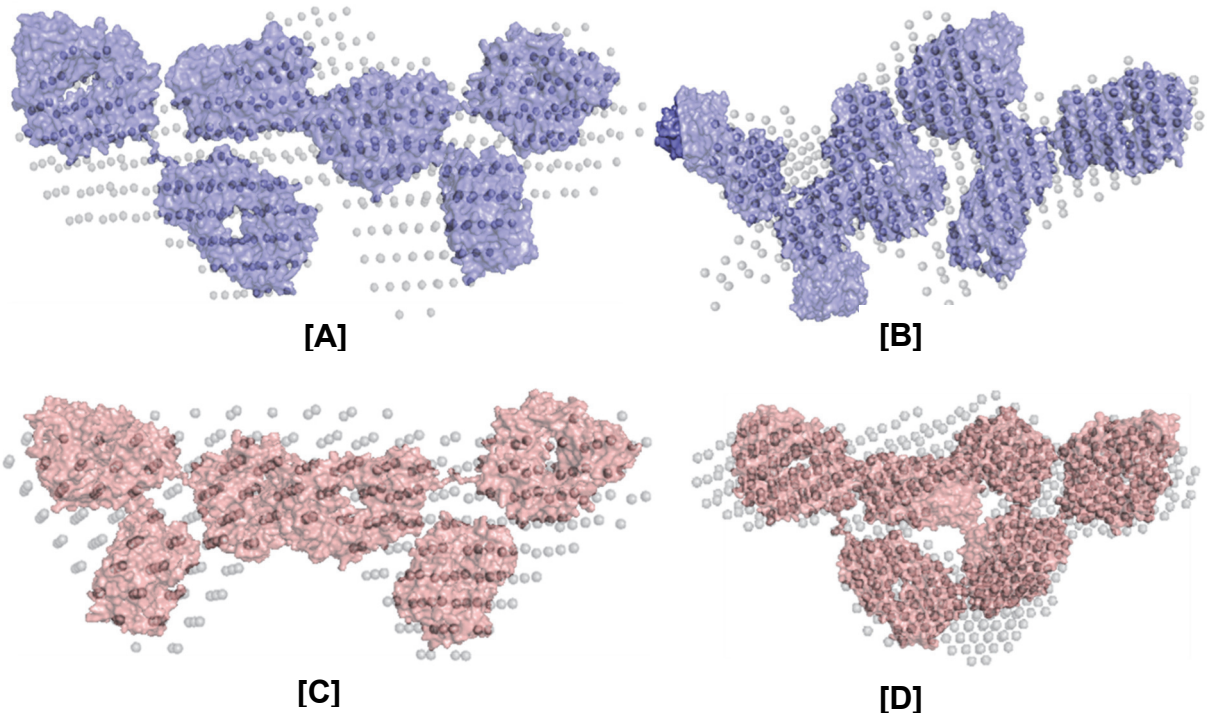

Fig. 46: Best-fit calculated models of the isolated dimer species obtained by rigid-body modeling. The upper row displays the temperature stress induced variants D1T [A] and D2T [B] and the lower row shows the light stress induced species D1L [C] and D2L [D]. The *ab-initio* bead models are displayed in the back of each model in a transparent manner.

The monomer and dimer models were cross validated by calculating the theoretical $s_{20,w}$ of each model using UltraScan Solution Modeler (US-SOMO). Therefore, bead-models were created of each all-atom model in advance and subsequently subjected to $s_{20,w}$ calculations [Brookes *et al.*, 2010]. Table 19 summarizes the parameter used for evaluation of the quality of the final models.

Tab. 19: Parameters used to assess accuracy of calculated models.

Sample	$S_{20,w}$ exp.	$S_{20,w}$ theor.	χ^2-value
ML	6.54	6.58	1.06
MT	6.52	6.59	1.05
D1L	9.12	9.15	1.41
D2L	9.49	9.46	1.57
D1T	9.08	9.12	1.43
D2T	9.39	9.40	1.09

The theoretical $S_{20,w}$ values calculated for the rigid body modeling derived monomer and dimer structures are in good agreement with the experimental ones. In addition, χ2-

value of the scattering raw data compared to the calculated ones implicate high accuracy of the models with the average structures of the variants present in solution.

4. 2. 3. Potency estimation of isolated size variants

In a next step, the potency of the isolated monomer and dimer fractions was determined by using the Pathhunter® cell-based bioassay and subsequent parallel line assay potency calculation [Lamerdin *et al.*, 2016].

The investigated IgG1 is a bivalent antibody. Hence, potency investigations can be useful for the determination of the orientation of the monomers within the dimer species and thus the global arrangement. The potency data summarized in Table 20 correspond relatively to the potency of an unstressed monomeric sample.

Tab. 20: Relative potency values of isolated fractions.

Sample	MT	D1T	D2T	ML	D1L	D2L
Rel. potency [%]	90	37	81	45	39	59

The potency assay revealed that the D1 samples of both sets have decreased potency than D2 fractions indicating a higher amount of blocked antibody/antigen interaction-sites. In the monomer samples it was noticed that ML is highly damaged by the applied stress conditions since it displayed not even half of the potency than the unstressed monomer.

4. 2. 4. Identification and localization of intermolecular interaction-sites

Size exclusion chromatography, analytical ultracentrifugation and small-angle X-ray scattering provide low-resolution structural informations, based on hydrodynamic properties of the molecule, from which it is possible to gain insight into the overall shape of the protein, but lack the information on accurate dimerization site localization. For this reason limited proteolysis by IdeS digestion was performed and subsequently analyzed by reversed phase LC-MS to get rough information on the position of the

interaction site. The protease cleaves the heavy chain right below the hinge disulfide bonds (...^{240}LLG ‖ GPS^{245}...) which results in Fc/2- and F(ab)$_2$ fragments.

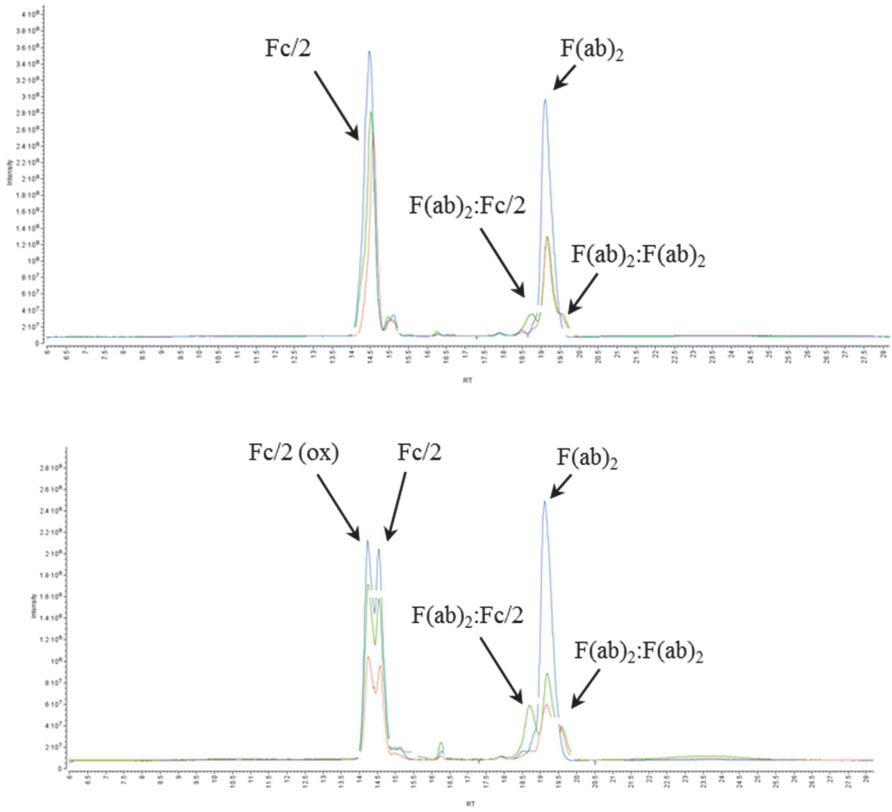

Fig. 47: Total ion chromatograms of IdeS digested monomer and dimer samples. The upper one displays the size variants isolated from the temperature stressed sample. The lower chromatogram shows the variants of the light stressed sample. Monomer samples are colored in blue, D1 variants in red and D2 species in green. The peak assignment corresponds to the observed masses of the separated fragments.

In the chromatograms of the digested temperature stressed samples, the major peaks observed correspond to Fc/2, F(ab)$_2$:Fc/2, F(ab)$_2$ and F(ab)$_2$:F(ab)$_2$ by mass whereas a significant high amounts of the Fc/2:F(ab)$_2$ fragment was solely detected in the D2T sample whereas this complex is almost absent in the D1T sample.

The light stressed size variants resulted in five major peaks by limited proteolysis. The associated fragments were identified by mass and revealed a splitting of the species into Fc/2 (oxidized), Fc/2, F(ab)$_2$:Fc/2, F(ab)$_2$ and F(ab)$_2$:F(ab)$_2$. D2L showed a remarkable high signal for F(ab)$_2$:Fc/2 which is almost absent in the D1L sample. Fc:Fc linked domains were not detected for the single light and temperature stressed dimer variants. These LC-MS measurments also demonstrated that the light stress resulted in very high levels of oxidized protein.

Since the LC-MS analysis of IdeS digested samples, potency estimation and quantification of covalently linked dimers of the light stressed fractions revealed that the stress condition was too harsh. The protein experinced a far too high level of damage and uncontrolled modifications. For this reason, the following investigations were solely performed with temperature stressed samples since this is the more relevant as this simulates the natural occurring ageing process.

Due to the fact that IdeS digestion resulted in a heterogeneous mixture of $F(ab)_2$:Fc/2 and $F(ab)_2$:$F(ab)_2$ fragments, which indicates differently linked dimer forms within the isolated fractions, the dimer variants were further processed to increase homogeneity. For this, a multi-step isolation process of the interacting domains including limited Lys-C digestion, SEC and Protein A affinity chromatography was applied to reduce heterogeneity. In a first step, the monomer and dimer samples were digested by limited Lys-C digestion that hydrolyses IgG1 molecules right above the hinge disulfide bonds (...^{222}SCDK ‖ THTC^{229}...) to create free Fab and Fc domains. In this way, the interacting domains within the dimer variants could be released (Fig. 48).

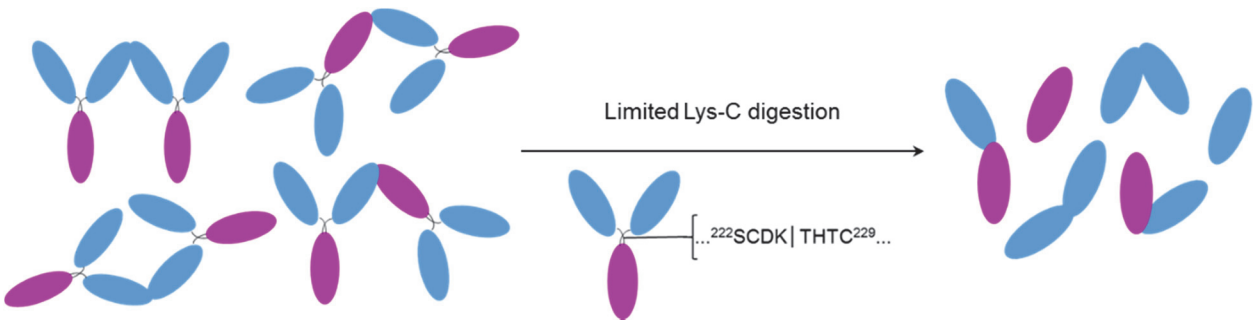

Fig. 48: Schematic illustration of limited Lys-C digested dimer aggregates. For the separation and isolation of free and interacting domains the monomer and dimer samples were subjected to limited Lys-C digestion. The IgG1 molecules were cleaved above the hinge region which resulted in free Fab and Fc fragments and the release of the interacting domains. Fab regions are indicated in light blue whereas Fc-parts are colored in violet.

Subsequently, the digested samples were subjected to SEC to separate Fc, Fab and interacting domains. The eluting fractions – Fab/Fc fragments from MT and interacting domains resulting from D1T and D2T digestion – were collected, buffer exchanged in drug substance buffer and concentrated. The elution order in size exclusion chromatography is illustrated in Figure 49.

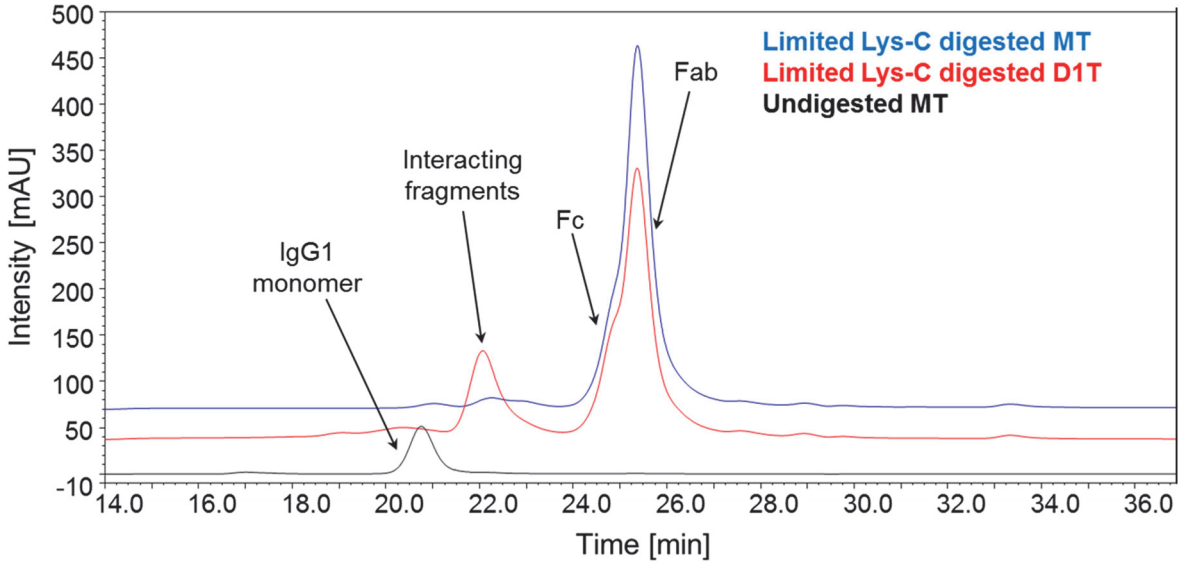

Fig. 49: SEC chromatogram of limited Lys-C digested samples. The chromatograms of the selected samples illustrate the size distribution of the resulting fragments. The unfractionated control sample (black) shows the elution-time of the undigested monomer. The blue trace illustrates the elution of the free Fc- and Fab- domains obtained by monomer digestion. The digested D1T dimer depicted in red shows an asymmetric peak of co-eluting Fc- and Fab-domains and a peak at approximately 100 kDa that corresponds to interacting domains.

In the next step, the resulting samples were injected onto a Protein A affinity column. Protein A has a strong affinity for the interface of C_H2-C_H3 in the Fc part of IgG1 molecules which allows the separation of the interacting domains by immobilizing all Fc containing domains. Fab:Fab interacting domains are collected from the flow through and the Fab:Fc interacting domains were eluted with a pH gradient and collected. This procedure was performed with the fractions derived from MT, D1T and D2T digestions. The collected fractions were buffer exchanged in drug substance buffer and concentrated. The final fractions were again subjected to SEC for purity and concentration estimation. Figure 50 schematically shows the final samples (A) obtained by this multi-step preparation as well as the size-exclusion chromatograms (B) of the re-injections.

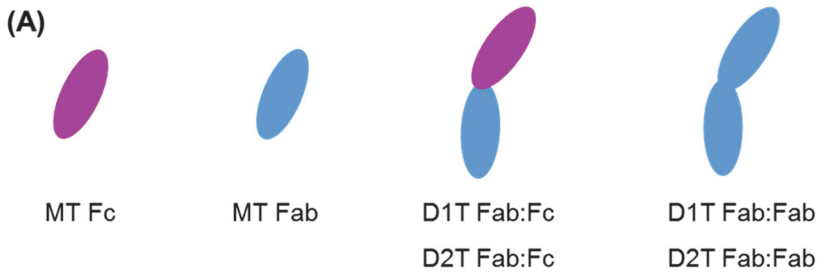

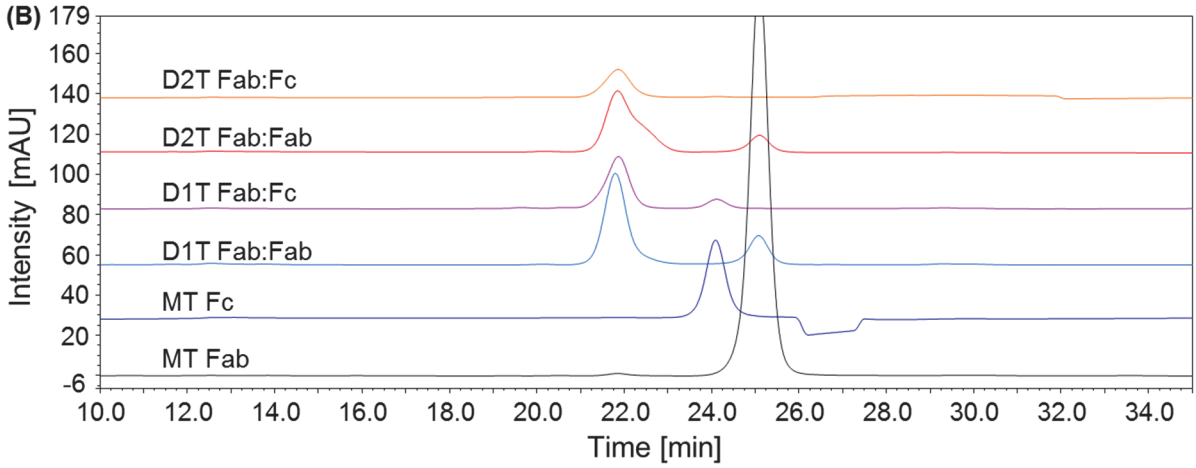

Fig. 50: Final Lys-C fragments derived from of the temperature stressed fractions. (A) Schematic illustration of the fragments derived by the digestion of monomer/dimer species and subsequent SEC and Protein A chromatography fractionation. The fragments are designated as described below the drawings. (B) SEC chromatograms of the re-injected final fragments for purity estimation. Interacting domains elute at approx. 22 minutes, Fc-fragments at approx. 24 min and free Fab domains at approx. 25 min. Single fragments within the complex samples are suggested to result from dissociation in the equilibrium-state.

The reinjections of the D1T Fab:Fc and D2T Fab:Fc samples just show free Fc fragments. This is attributable to the Protein A chromatography step in which all free Fab – resulting from complex dissociation – is removed. To verify the workflow the final fractions of the temperature-stressed samples were verified by exact mass determination using LC-MS.

These fractions were used to further investigate the interaction-sites within the different dimer samples by H/DX-MS. Exchange kinetics of the linked domains were compared to those of the free Fab or Fc, derived from the monomeric samples, respectively. Figure 51 summarizes the H/DX-MS comparison of the D1T Fab:Fab and MT Fab. In sum, 93.0 % of the light chain and 96.5 % of the heavy chain amino acids could be detected and taken into account for evaluation. Differences in exchange kinetics were detected solely in the V_H domain of the Fab fragment. Less uptake, indicating solvent protection, was observed for the sequence sections AA [21-35], AA [72-84] and AA [94-110]. Unexpectedly, one site within the heavy chain of D1T Fab:Fab showed more deuterium uptake, indicating increased solvent exposure, which was located in AA sequence [50-64].

For the light chain comparison of D1T Fab:Fab and MT Fab, AA [48-52] was identified to show more deuterium uptake in the complex sample (Fig. 51B).

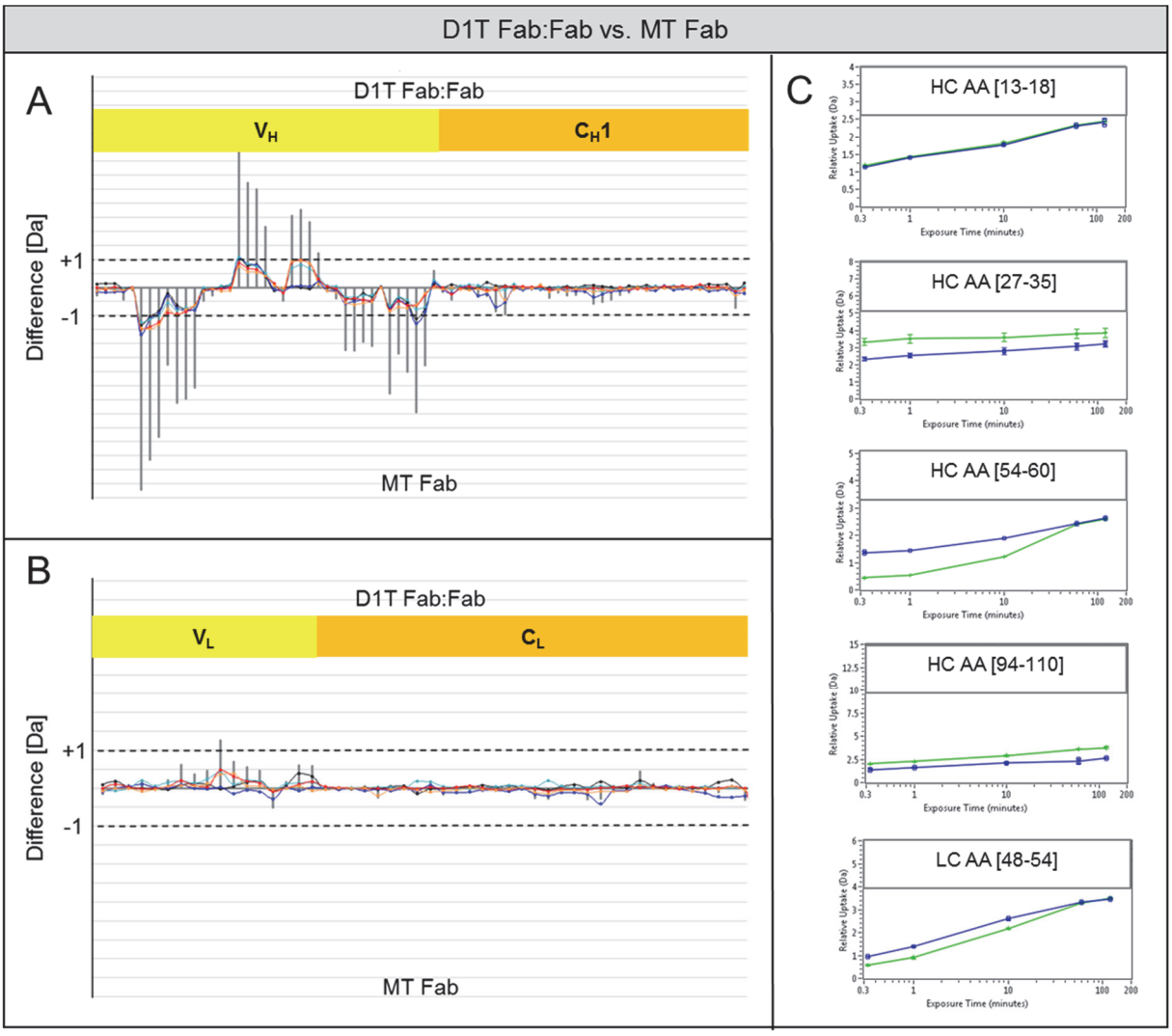

Fig. 51: H/DX-MS comparison of D1T Fab:Fab and MT Fab heavy (A) and light chain (B). The sum of difference plots show the sum of mass differences over all acquired deuteration time points for the identified heavy chain (A) and light chain (B) peptides from left to right (N- to C-terminus). Colored line data points indicate the single deuteration time-points (20 sec, 1 min, 10 min, 60 min, 120 min). The limits of significance (± 1 Da) for the summed up differences (grey bars) are marked as dashed lines. Locations of $V_H/C_H1/V_L$ and C_L are indicated as colored boxes. Exemplary uptake plots are shown in C with D1T Fab:Fab peptides in blue and MT Fab peptides in green. Single deuteration time points were measured in duplicates from which standard deviations were derived.

The H/DX-MS results were mapped onto the crystal structure of the IgG1 homology model (Fig. 52A). Differences in uptake kinetics are located in the variable domains of the heavy and the light chain including all of the heavy chain complementary determining regions. To illustrate the different uptake kinetics the time-course of raw spectra of an exemplary peptide HC AA [54-60] is shown in Figure 52B.

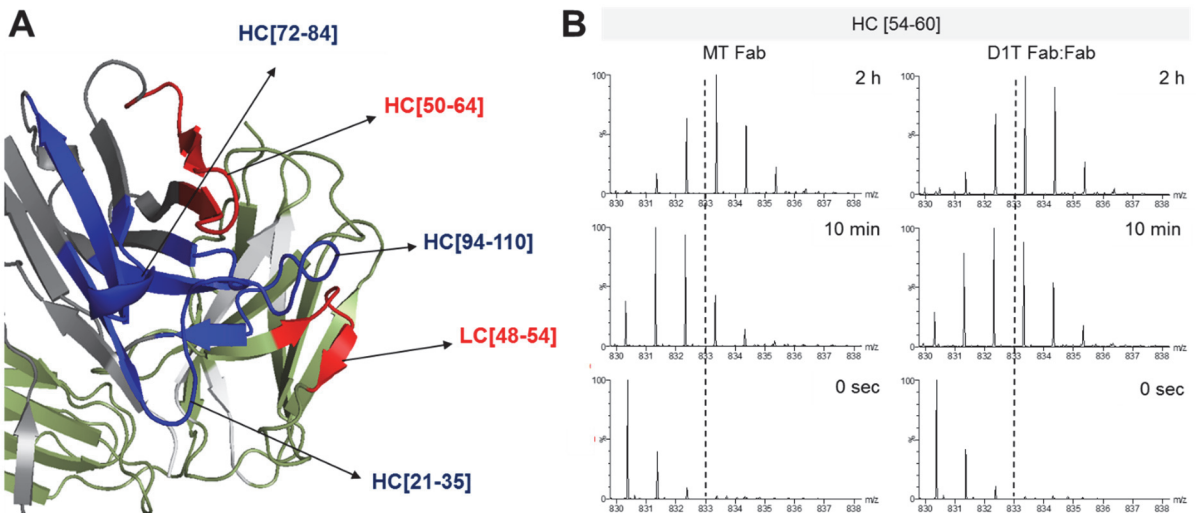

Fig. 52: Crystal structure for H/DX-MS comparison of D1T Fab:Fab and MT Fab. Crystal structure demonstrating the location of observed H/DX –MS results. Sequences showing less deuterium uptake in D1T Fab:Fab are colored in blue; more uptake in D1T Fab:Fab is colored in red. Not determined sequences are indicated in white. No differences detected for heavy chain peptides are marked in grey whereas for light chain peptides these are colored in green. Section B exemplary shows the different extent of *m/z* shift for peptide HC AA [54-60] for the deuteration time points 0 sec, 10 min and 2 h. A vertical dashed line is inserted to facilitate the comparison of the peak patterns.

For the clarification of interaction-sites within D1T Fab:Fc fragments, these complexes were compared by H/DX-MS on one hand with MT Fab and on the other hand with MT Fc in two separate experiments. The revealed deuterium uptake results for D1T Fab:Fc and MT Fab are summarized in Figure 53 for the heavy and light chain. In this experiment, deuteration time-points were decreased to five due to limited sample availability. Each point was measured in duplicates. In sum, 83.2 % of the heavy and 72.0 % of the light chain could be covered in this comparison. Decreased uptake kinetics were identified for the regions AA [19-35], AA [94-108], AA [132-151] and AA [180-188] in the heavy chain and for AA [196-214] in the light chain.

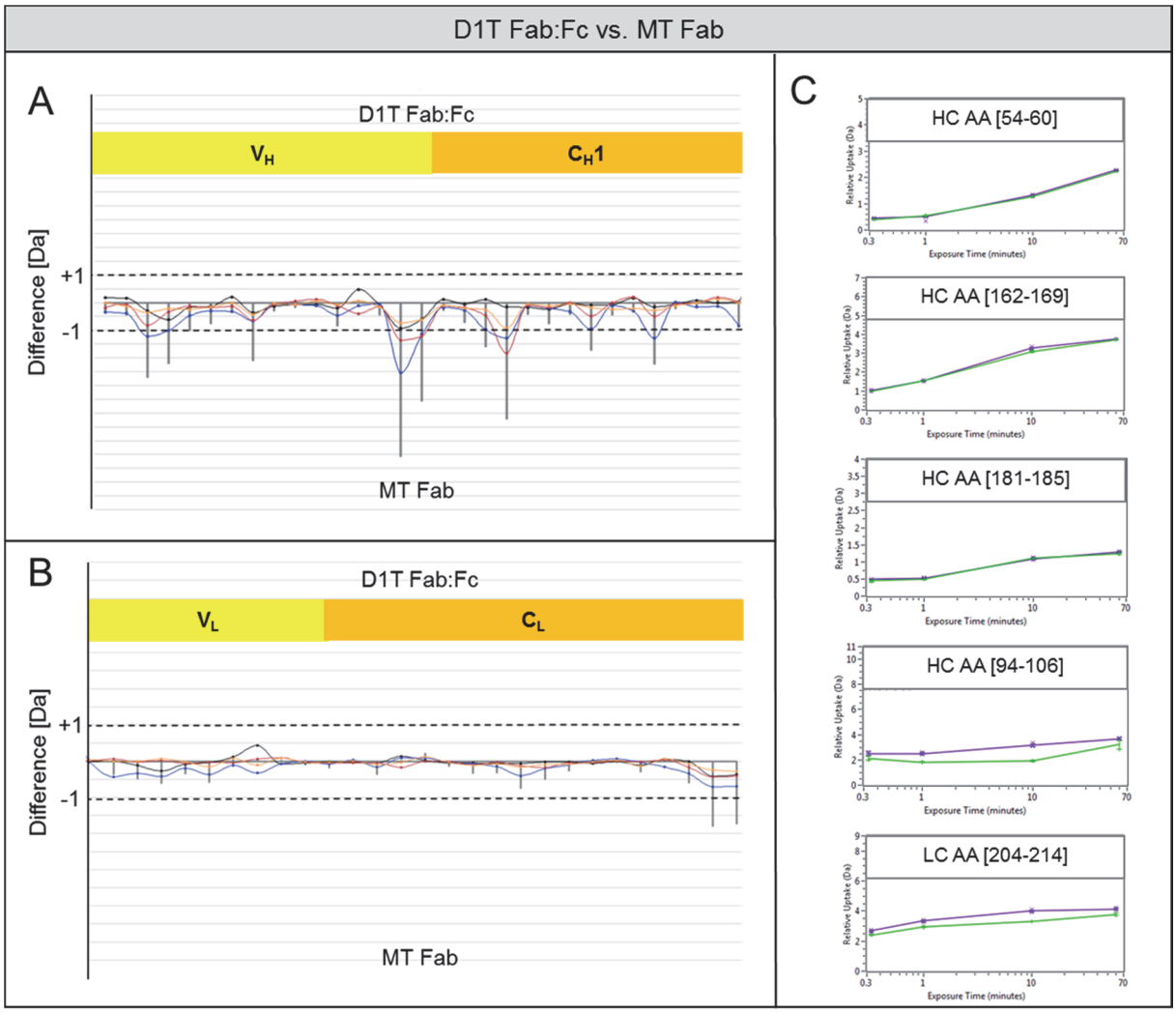

Fig. 53: H/DX-MS comparison of D1T Fab:Fc and MT Fab heavy and light chain. The sum of difference plots (A for the heavy chain and B for the light chain) show the sum of mass differences over all acquired deuteration time points for the identified heavy chain (A) and light chain (B) peptide from left to right (N- to C-terminus). Colored line data points indicate the single deuteration time points (20 sec, 1 min, 10 min, 60 min). The limits of significance (± 1 Da) for the summed up differences (grey bars) are marked as dashed lines. Locations of $V_H/C_H1/V_L$ and C_L are indicated as colored boxes. Exemplary uptake plots are shown in (C) with D1T Fab:Fc peptides in green and MT Fab peptides in blue. Single deuteration time points were measured in duplicates from which standard deviations were derived.

By illustrating the exchange results in the IgG1 model (Fig. 54A), it is obvious that solvent protection within D1T Fab:Fc differed from that of D1T Fab:Fab in a way that additional protected sequences were found in the C_H1 and C_L domains. Furthermore, no increased exchange kinetics were measured in this dimer variant. In line with the D1T Fab:Fab analysis also here the heavy chain CDR1 and CDR3 seem to play an important role in aggregation process.

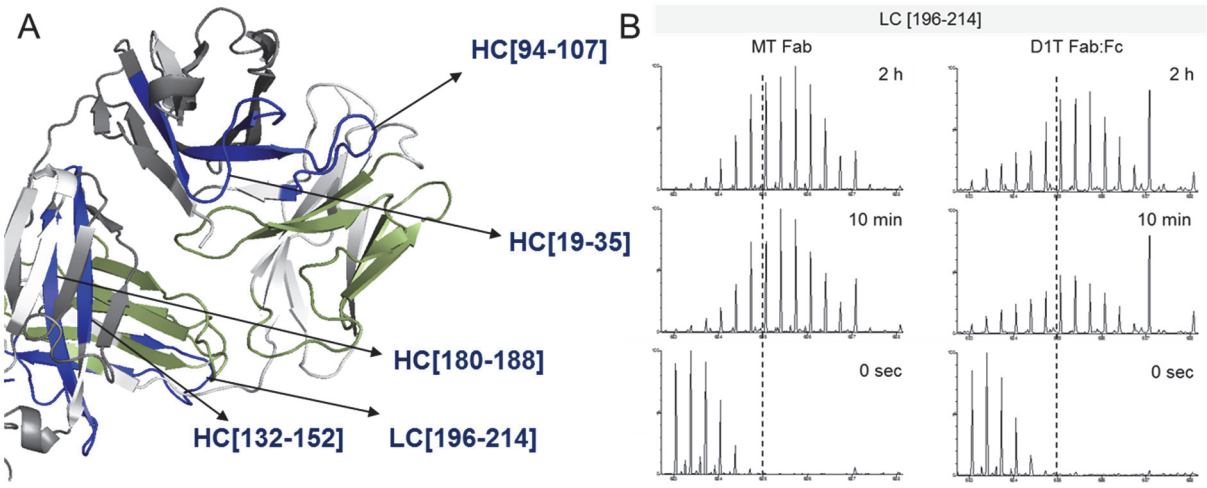

Fig. 54: H/DX-MS comparison of D1T Fab:Fc and MT Fab heavy and light chain. Crystal structure demonstrating the location of observed H/D exchange results (A). Less deuterium uptake in D1T Fab:Fc is colored in blue. Not determined sequences are indicated in white. No differences detected for heavy chain peptides are marked in grey whereas for light chain peptides these are colored in green. Time-course of exemplary raw spectra for peptide LC AA [196-214] are shown in (B) for the incubation time points 0 sec, 10 min and 2 h. A dashed vertical line is drawn to facilitate the comparison.

For D1T Fab:Fc versus MT Fc the H/DX-MS comparison revealed no significant differences in deuterium uptake. In sum, 83.4 % of the Fc sequence could be identified and evaluated regarding deuterium exchange kinetics. Figure 55 shows the H/D exchange results from which it can be seen that no peptide exceeds the limit of significance.

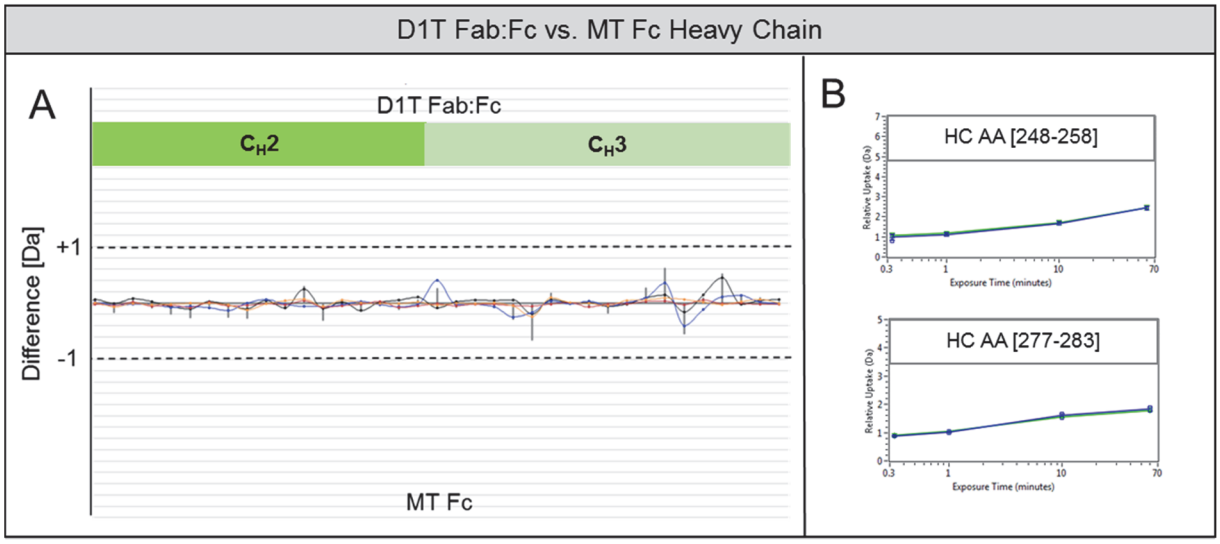

Fig. 55: H/DX-MS comparison of D1T Fab:Fc and MT Fc. The sum of difference plot (A) shows the sum of mass differences over all acquired deuteration time-points for each identified peptide from left to right (N- to C-terminus). Colored line data points indicate the single deuteration time points (20 sec, 1 min, 10 min, 60 min). The limits of significance (± 1 Da) for the summed up differences (grey bars) are marked as dashed lines. Locations of C_H,2 and C_H,3 are indicated as colored boxes. Exemplary uptake

plots are shown in (B) with D1T Fab:Fc peptides in green and MT Fab peptides in blue. Single deuteration time points were measured in duplicates from which standard deviations were derived.

In order to identify possible interaction sites within D2T, the limited Lys-C digested fractions were individually investigated by H/DX-MS analysis. The results for D2T Fab:Fab versus MT Fab are shown in Figure 56 for the heavy and light chain sequences (93.2 % of the heavy and 82.7 % of the light chain was covered).

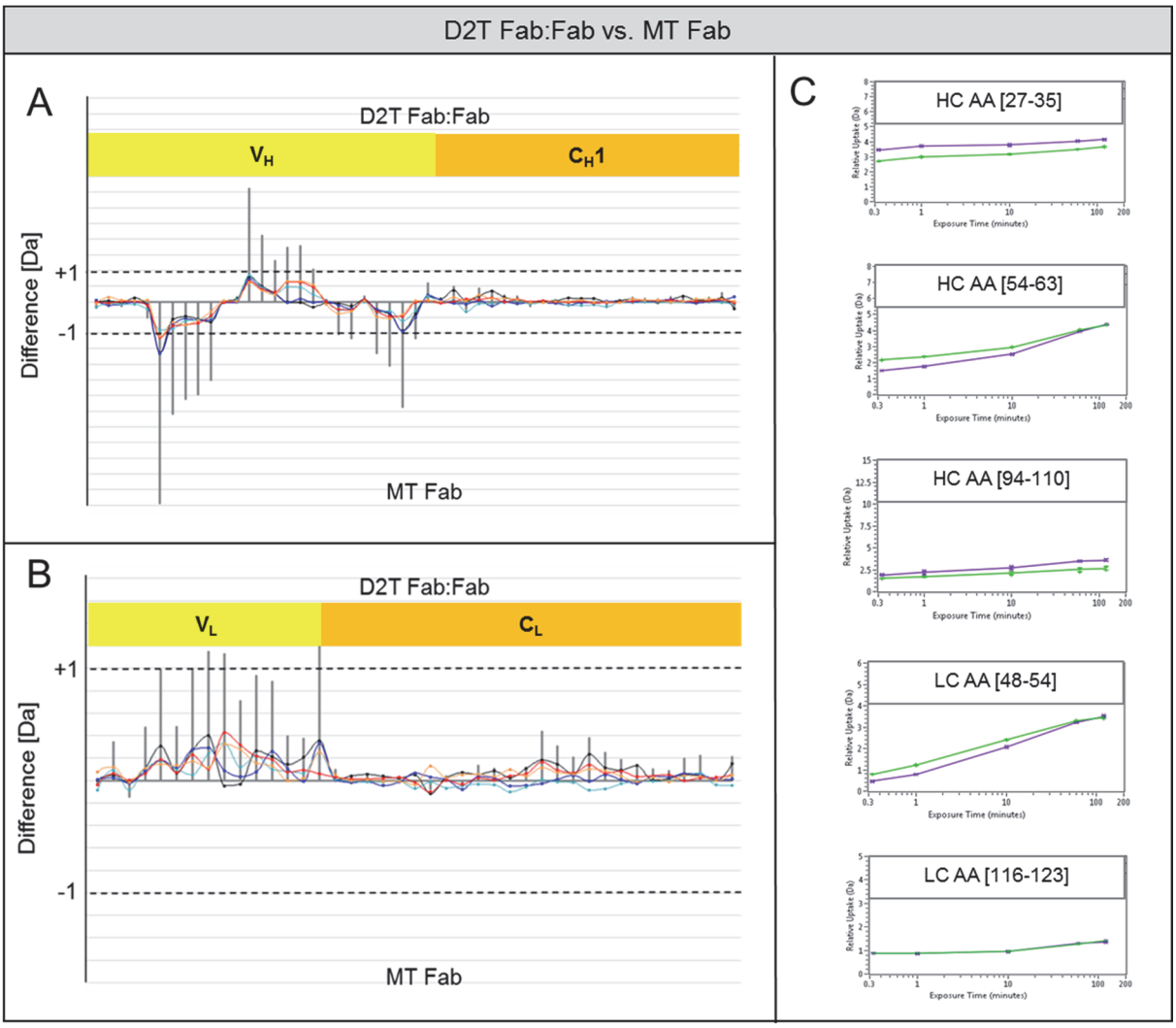

Fig. 56: H/DX-MS comparison of D2T Fab:Fab and MT Fab heavy and light chain. The sum of difference plots show the sum of mass differences over all acquired deuteration time points for the identified heavy chain (A) and light chain (B) peptide from left to right (N- to C-terminus). Colored line data points indicate the single deuteration time-points (20 sec, 1 min, 10 min, 60 min, 120 min). The limits of significance (± 1 Da) for the summed up differences (grey bars) are marked as dashed lines. Locations of $V_H/C_H1/V_L$ and C_L are indicated as colored boxes. Exemplary uptake plots are shown in (C) with D2T Fab:Fab peptides in green and MT Fab peptides in blue. Single deuteration time points were measured in duplicates from which standard deviations were derived.

D2T Fab:Fab revealed decreased exchange kinetics for the peptides AA [20-35], AA [72-80] and AA [85-110] in the heavy chain, but showed increased exchange kinetics for the sequences AA [49-62] in the heavy and AA [49-54] and AA [91-116] in the light chain. The specific sequences that showed differing exchange kinetics are mapped on the crystal structure of the IgG1 (Fig. 57A). Exemplary raw data are depicted in Figure 57B.

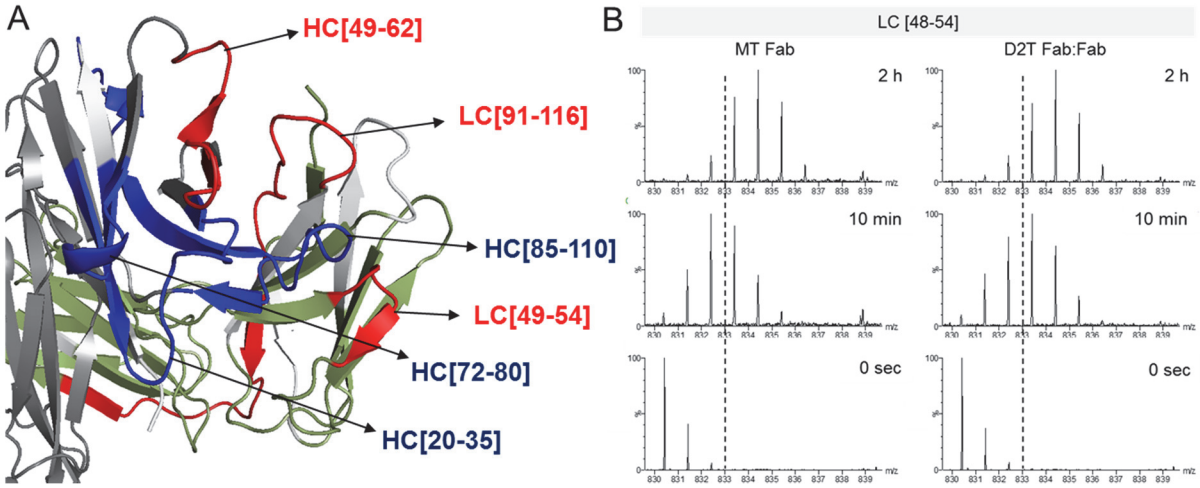

Fig. 57: Crystal structure for H/DX-MS comparison of D2T Fab:Fab and MT Fab. Crystal structure demonstrating the location of observed H/D exchange results (A). Less deuterium uptake in D2T Fab:Fab is colored in blue; more uptake in D2T Fab:Fab is colored in red. Not determined sequences are indicated in white. No differences detected for heavy chain peptides are marked in grey whereas for light chain peptides these are colored in green. Time-dependent *m/z* shift of peptide LC AA [48-54] is shown in (B). Comparison is facilitated by a vertical dashed line.

In addition, this variant showed decreased exchange rates in three CDR peptides of the heavy chains also increased rates in both chains of the Fab domain – including LC CDR3 and HC CDR2 – implicating increased solvent exposure and thus structural alteration in this region.

To investigate the isolated D2T Fab:Fc complex, this sample was measured head-to-head in two separate H/DX-MS analysis with either MT Fab or MT Fc. The D2T Fab:Fc versus MT Fab comparison resulted in deuterium uptake differences for the peptides AA [17-20], AA [27-54], AA [133-151] in the heavy and for AA [36-47] and AA [154-151] in the light chain. In all the listed sequences, the D2T Fab:Fc sample showed decreased uptake kinetics compared to these of MT Fab (Fig. 58). In sum, 92.7 % of the heavy and 84.2 % of the light chain could be identified and taken into account for data evaluation. The results displayed in Figure 58 are additionally marked in the homology model of

the IgG1 to illustrate the specific locations of the identified H/D exchange differences (Fig. 59 A).

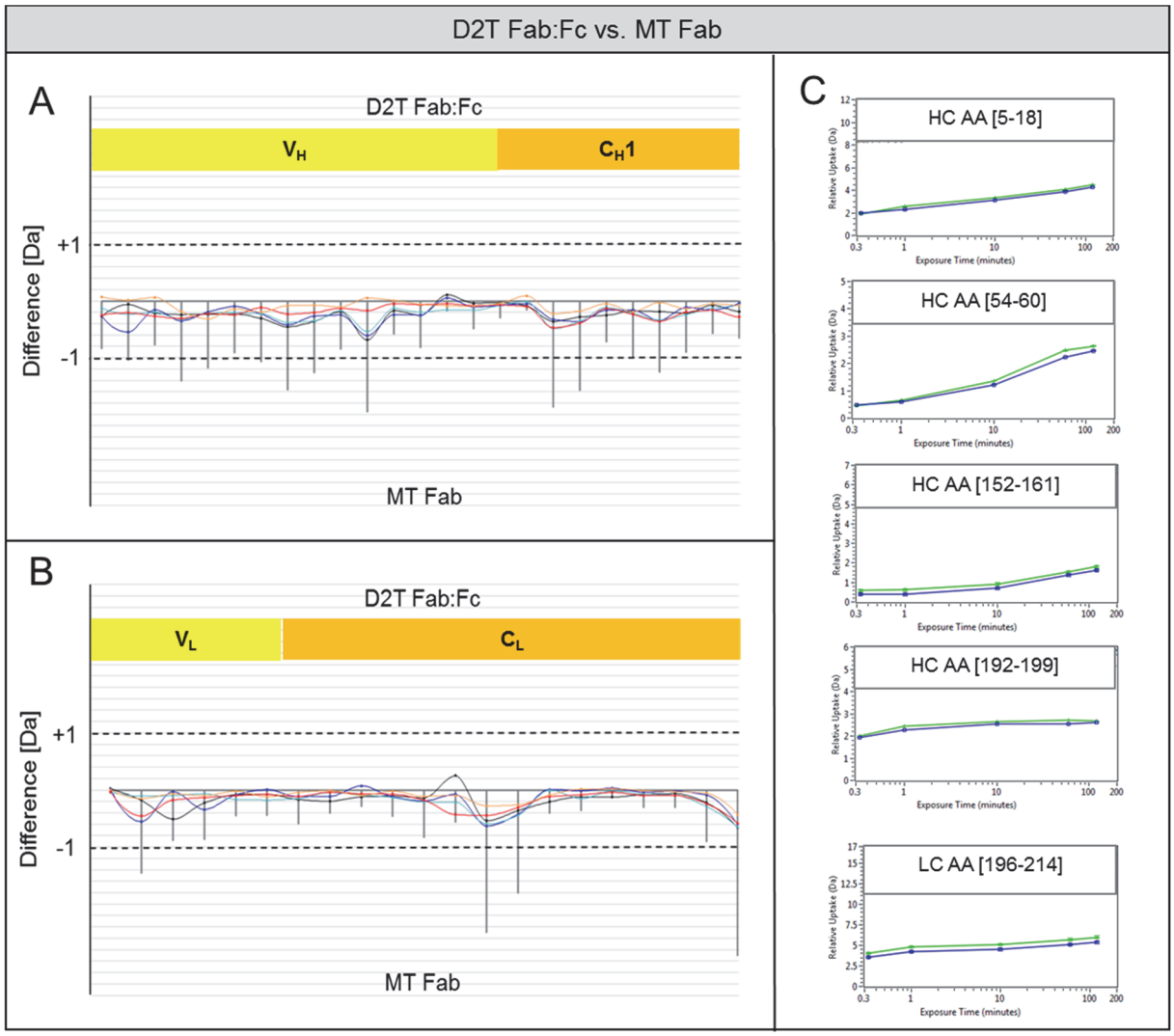

Fig. 58: H/DX-MS comparison of D2T Fab:Fc and MT Fab heavy and light chain. The sum of difference plot (A) shows the sum of mass differences over all acquired deuteration time points for the identified heavy chain (upper panel) and light chain (lower panel) peptide from left to right. Colored line data points indicate the single deuteration time points (20 sec, 1 min, 10 min, 60 min, 120 min). The limits of significance (± 1 Da) for the summed up differences (grey bars) are marked as dashed lines. Locations of $V_H/C_H1/V_L$ and C_L are indicated as colored boxes. Exemplary uptake plots are shown in (B) with D2T Fab:Fc peptides in blue and MT Fab peptides in green. Single deuteration time points were measured in duplicates from which standard deviations were derived. Section C shows compared raw spectra for the incubation points 0 sec, 10 min and 120 min illustrating the mass shift resulting from D_2O incubation.

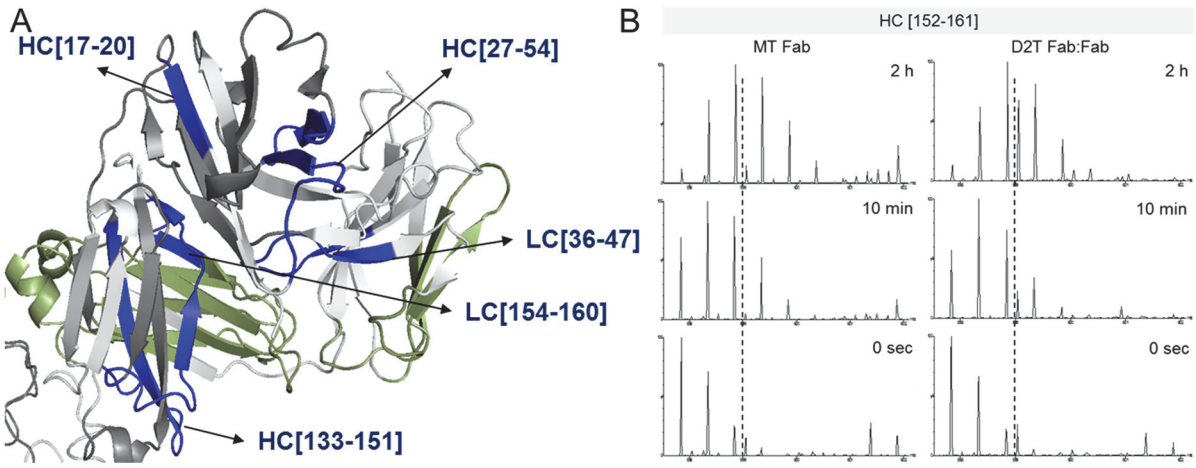

Fig. 59: Crystal structure for H/DX-MS comparison of D2T Fab:Fc and MT Fab. Crystal structure demonstrating the location of observed H/D exchange results (A). Less deuterium uptake in D2T Fab:Fc is colored in blue; more uptake in D2T Fab:Fc is colored in red. Not determined sequences are indicated in white. No differences detected for heavy chain peptides are marked in grey whereas for light chain peptides these are colored in green. Exemplary raw spectra for peptide HC AA [152-161] are shown in (B) with an inserted dashed line to facilitate the comparison.

For the D2T Fab:Fc versus MT Fc H/DX-MS comparison no significant differences were detected. In this measurement, 76.3 % of the Fc sequence could be identified and taken into account for H/D exchange comparison. Figure 60 summarizes the results of the measurement.

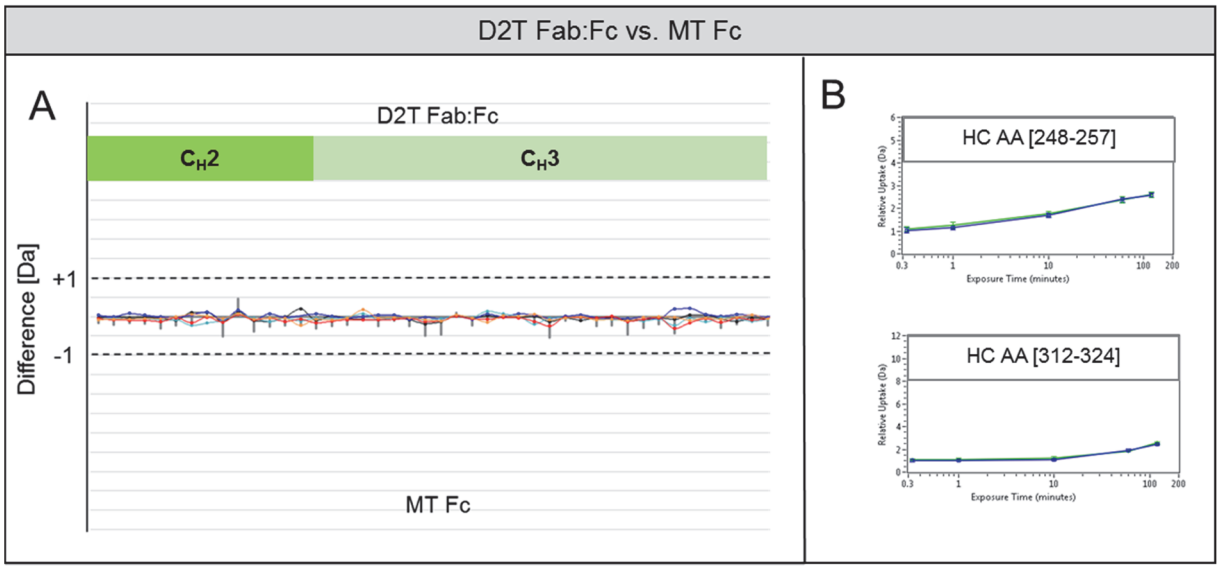

Fig. 60: H/DX-MS comparison of D2T Fab:Fc and MT Fc. The sum of difference plot (A) shows the sum of mass differences over all acquired deuteration time-points for the identified peptides from left to right (N- to C-terminus). Colored line data points indicate the single deuteration time-points (20 sec, 1 min, 10 min, 60 min, 120 min). The limits of significance (± 1 Da) for the summed up differences (grey bars) are marked as dashed lines. Locations of C_H2 and C_H3 are indicated as colored boxes. Exemplary uptake plots are shown in (B) with D2T Fab:Fc peptides in green and MT Fc peptides in blue. Single deuteration time-points were measured in duplicates from which standard deviations were derived.

From the results of the executed H/DX-MS comparisons it can be concluded that the CDR sequences of the IgG1 molecule play an essential role in the dimerization process and are directly or indirectly involved in intermolecular interactions.

A summary for the detected differences in deuterium uptake kinetics within the interacting domains of temperature stressed D1 and D2 samples compared to the free temperature stressed Fab and Fc fragments are listed in Table 21.

Tab. 21: Summary of differences revealed by H/DX-MS for temperature stress induced dimers.

Sample	D1 Fab:Fab	D2 Fab:Fab	D1 Fab:Fc	D2 Fab:Fc
Decreased H/D exchange kinetics in complex	HC[21-35] **CDR1** HC[72-84] HC[94-110] **CDR3**	HC[20-35] **CDR1** HC[72-110] **CDR3**	HC[19-35] **CDR1** HC[94-108] **CDR3** HC[132-151] HC[180-188] LC[196-214]	HC[17-20] HC[27-54] **CDR1** HC[133-151] HC[162-180] LC[36-47] **CDR1** LC[154-160]
Increased H/D exchange kinetics in complex	HC[50-64] **CDR2** LC[48-54]	HC[49-64] **CDR2** LC[49-54] LC[91-116] **CDR3**	-	-

By taking all the information obtained by potency investigation, AUC, SAXS, rigid body modeling, LC-MS and H/DX-MS together, it was possible to reveal the complex structure of the different temperature stressed dimer samples (Fig. 61).

From the potency data the dimer-antigen stoichiometry can be concluded which subsequently gives hints on the dimeric structures of the investigated variants. In the potency assays, D1T exhibited less potency compared to the D2T variant implicating that D2T neutralizes more antigen than D1T. The IgG1 under investigation is bivalent and dimer variants are consequently able to bind four antigen molecules. By comparing the potency data, it was suggested that in D1T more paratopes are blocked or sterically hindered than in D2T which in fact was also reflected by the LC-MS fragment analysis after IdeS digestion of the variants. Here, D2T showed significantly more $F(ab)_2$:Fc/2 fragments whereas these were nearly absent in D1T which almost exclusively resulted in $F(ab)_2$:$F(ab)_2$ fragments. From the obtained models it is obvious that the H/DX-MS data are in very good agreement with the interaction-sites of the calculated rigid body modeling structures which were based on the scattering data, although these solely describe the average global structure of the molecule in solution. Additional detected solvent protected areas within the Fab:Fc variants especially in the C_L and C_H1 segments

may result from close proximity and thus inductive effects of other domains or decreased flexibility within the dimer.

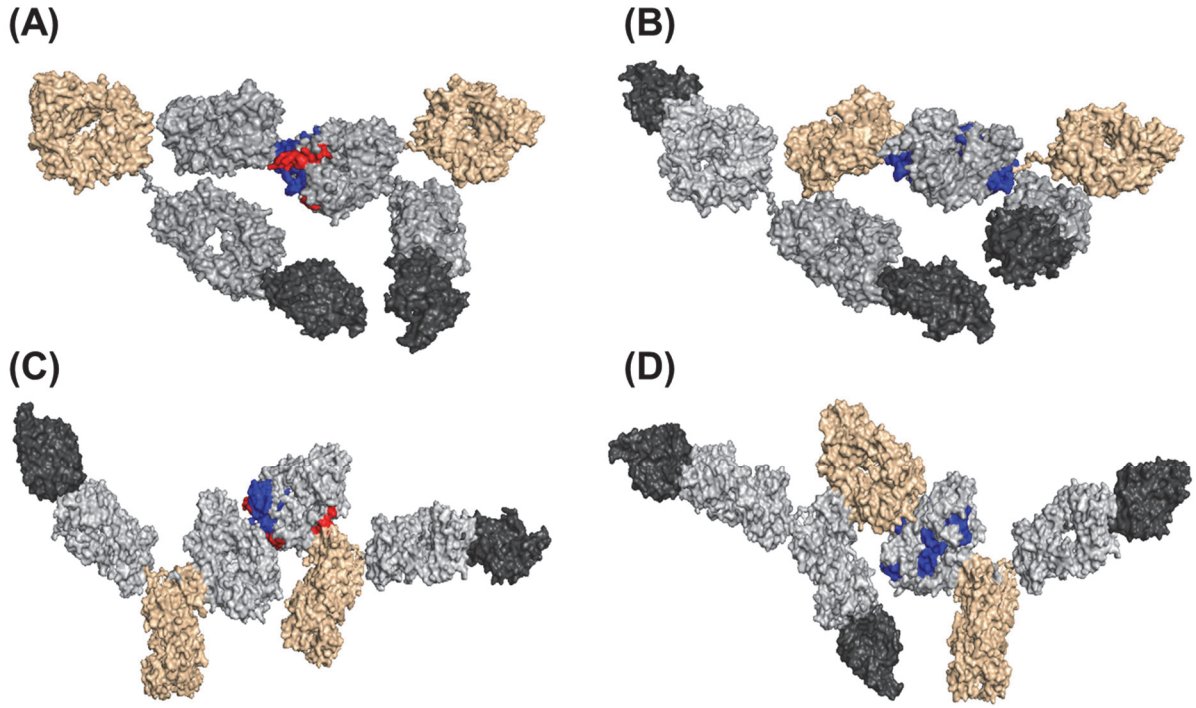

Fig. 61: Dimer models derived by rigid body modeling including color coded H/D exchange differences and docked antigen for temperature stress induced variants. The structures are proposed by combination of the different derived data sets. The antigen is docked to illustrate the differences in potency. Fab fragments are colored in grey; Fc fragments are colored in light orange and the antigen is depicted in dark grey. Differences in H/D exchange are colored in blue (less deuterium uptake in the dimer) and red (more uptake in the dimer). (A) D1T Fab:Fab interaction (B) D1T Fab:Fc interaction (C) D2T Fab:Fab interaction (D) D2T Fab:Fc interaction.

4. 2. 5. Analysis of post-translational modifications that trigger aggregation processes

After setting-up the different complex structures, it was furthermore important to unravel dimerization triggering factors of the IgG1 drug molecule. For this, reduced LC-MS/MS peptide mappings using Lys-C were performed. The resulting chromatograms of D1T Fab:Fab, D1T Fab:Fc, D2T Fab:Fab and D2T Fab:Fc were compared to those of MT Fab and MT Fc respectively and differences in peptide modifications were evaluated in a presence/absence search. Peptide modifications present in the dimer samples and absent in the monomeric counterpart were supposed to trigger the aggregation process.

Figure 62 shows the stacked chromatographic profiles obtained by nano-flow reversed phase separation. The main differences observed for D1T Fab:Fab and D2T Fab:Fab compared to MT Fab are highlighted with an orange box.

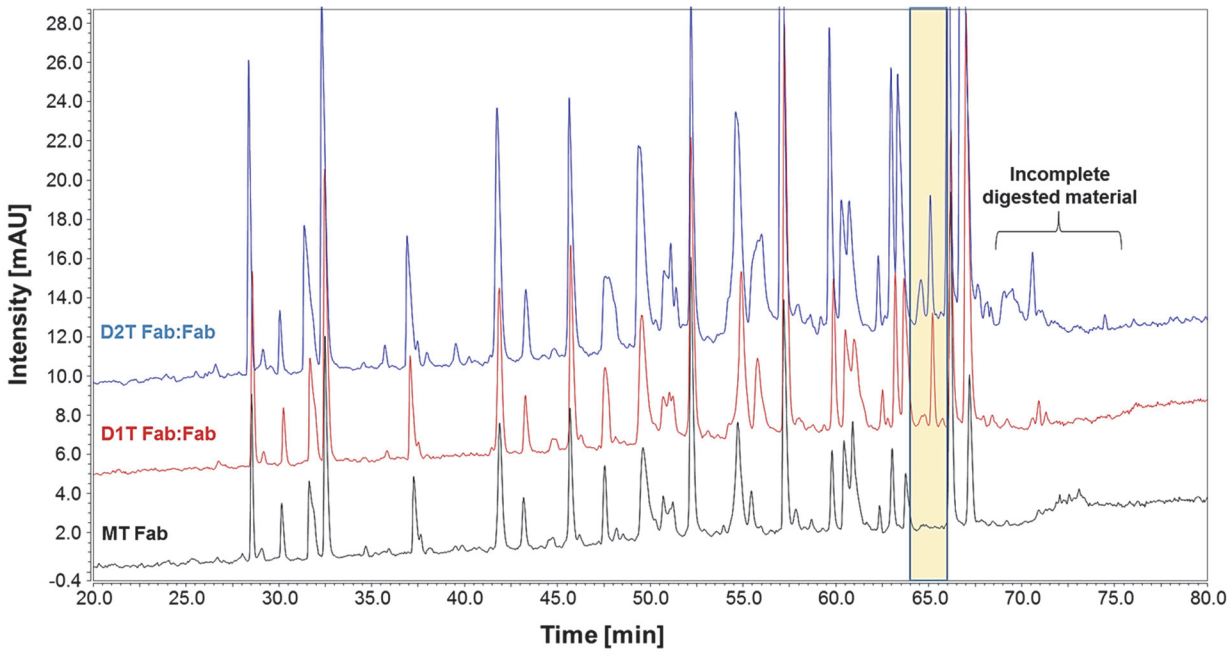

Fig. 62: Reduced Lys-C peptide mapping chromatograms of isolated interacting domains (Fab:Fab) of D1T and D2T and Fab of MT. Peptides obtained by Lys-C digestion under reducing conditions of the interacting Fab:Fab fragments of the temperature stressed dimer variants (D1T: red trace; D2T: blue trace; MT: black trace). The traces display the UV chromatograms obtained by LC-MS/MS analysis. The most remarkable differences are highlighted with an orange box.

A stacked overlay of the elution profiles of D1T Fab:Fc, D2T Fab:Fc, MT Fab and MT Fc is depicted in Figure 63. In this analysis, the dimer digests were compared to both Fab and Fc of the monomer to search for differing modifications.

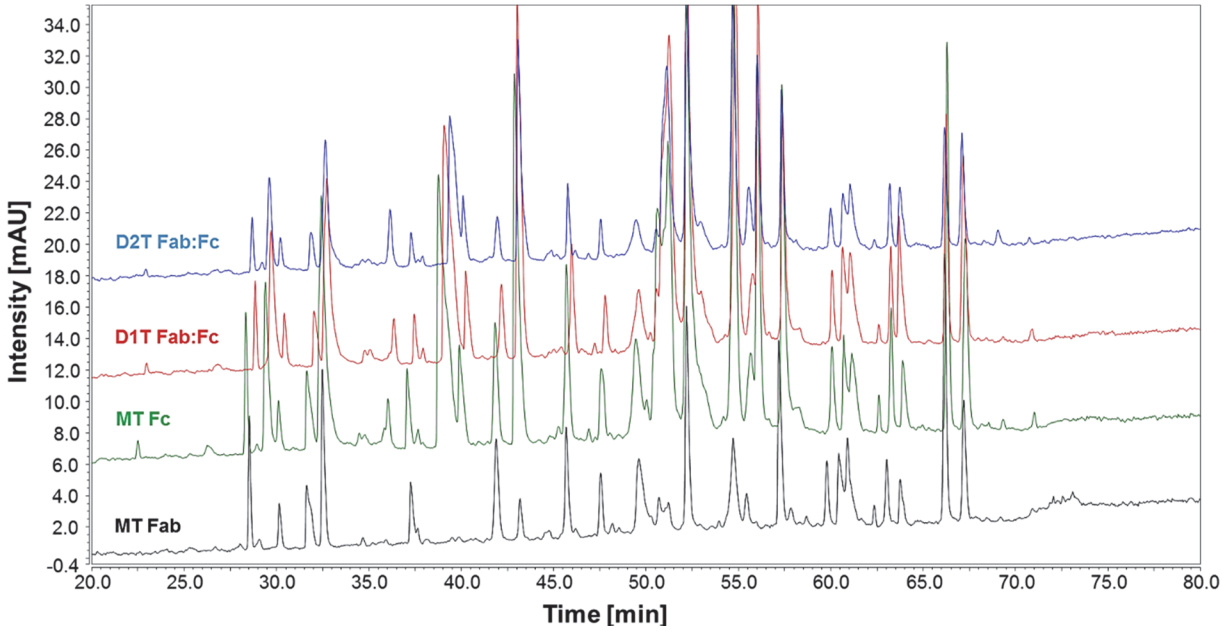

Fig. 63: Reduced Lys-C peptide mapping chromatograms of isolated interacting domains (Fab:Fc) of D1T and D2T and Fab and Fc of MT. Peptides obtained by Lys-C digestion under reducing conditions of the interacting Fab:Fc fragments of the temperature stressed dimer variants (D1T: red trace; D2T: blue trace; MT Fab: black trace; MT Fc: green trace). The traces display the UV-chromatograms obtained by LC-MS/MS analysis.

Peptides were identified by top five CID/HCD fragmentation within the mass spectrometer after full scan precursor mass determination. By analyzing the different peptide mappings, a comparison of quantities of the eluting peptides was performed.

No remarkable differences were obtained in the D1T Fab:Fc / MT Fab / MT Fc and D2T Fab:Fc / MT Fab / MT Fc comparisons. Some differences in peptide peak heights (Fig. 63) were observed but this is likely because of the variability in digestion efficiency and chromatography. For D1T Fab:Fab / D2T Fab:Fab / MT Fab the present/absent search revealed the modified peptides that are summarized in Table 22 and 23. The most remarkable differences obtained were isomerized variants of the peptide AA [44-65] as well as oxidized variants of the same peptide. Extracted ion chromatograms (EIC) illustrate the abundancies of the mentioned modified peptides in the different dimer samples and the MT Fab (Fig. 64, 65 & 66).

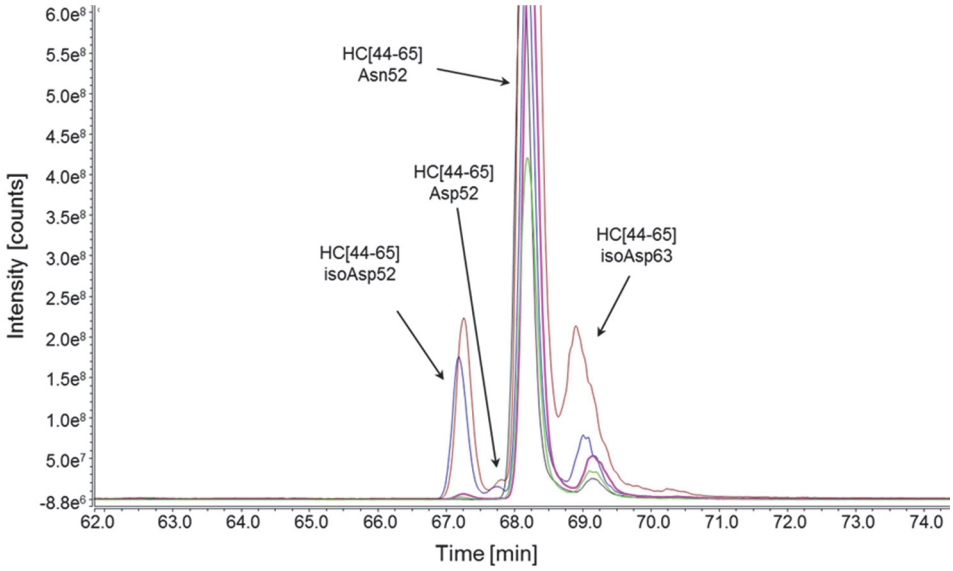

Fig. 64: Extracted ion chromatograms of isomerized and unmodified peptide AA [44-65]. The elution profile shows the EIC of *m/z* = 840.40 of the samples MT Fab (black), D1T Fab:Fab (blue), D1T Fab:Fc (pink), D2T Fab:Fab (brown) and D2T Fab:Fc (light green). HC AA [44-65] isoAsp52 is solely present in the D1T Fab:Fab and D2T Fab:Fab samples whereas it is almost absent in the other ones. Isomerization at position 63 is also drastically increased in D2T Fab:Fab and D1T Fab:Fab compared to the MT Fab sample.

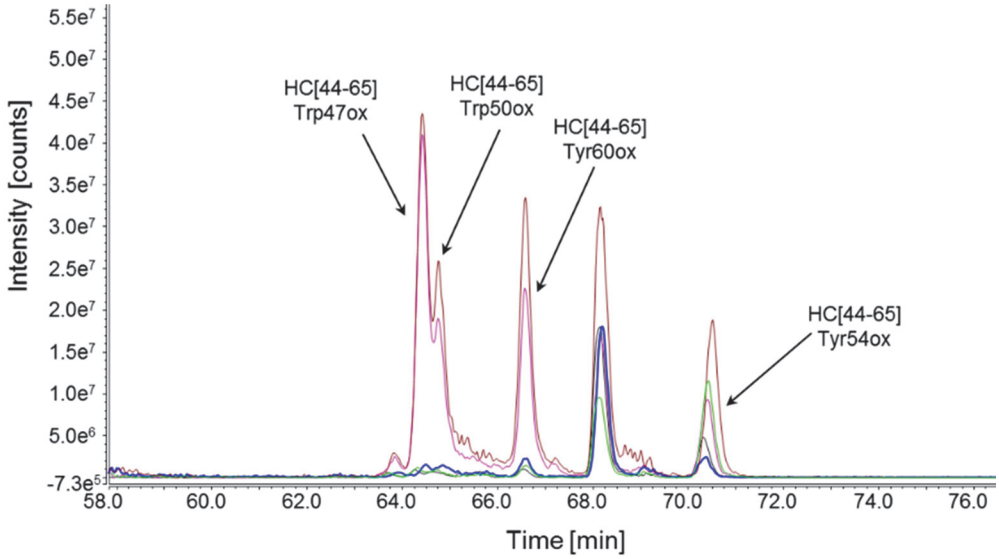

Fig. 65: Extracted ion chromatograms of the oxidized peptide AA [44-65]. The elution profile shows the EIC of *m/z* = 845.40 of the samples MT Fab (black), D1T Fab:Fab (pink), D1T Fab:Fc (blue), D2T Fab:Fab (brown) and D2T Fab:Fc (light green). Quantities of oxidized variants of HC AA [44-65] are drastically increased in the D1T Fab:Fab and D2T Fab:Fab samples whereas these are almost absent in the other ones.

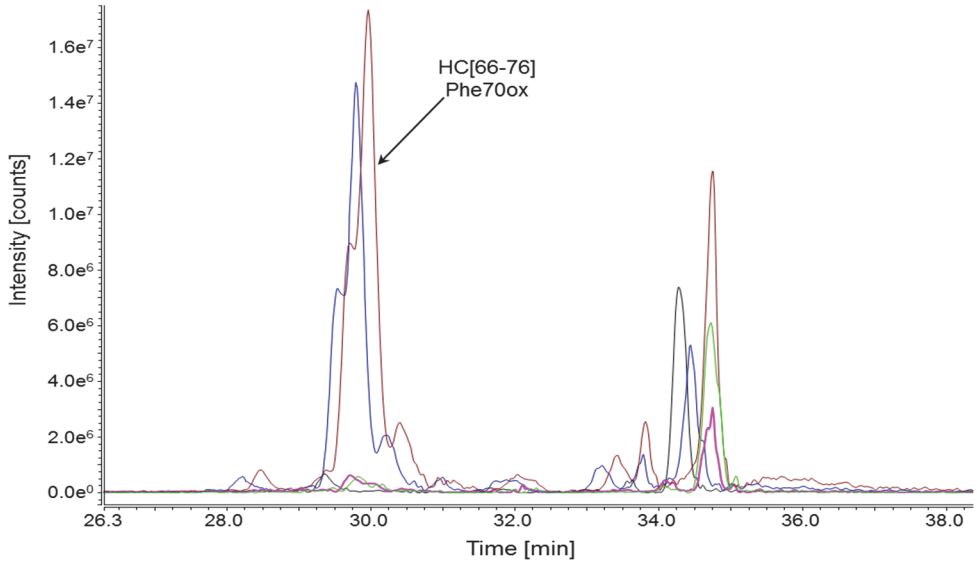

Fig. 66: Extracted ion chromatograms of oxidized peptide AA [66-76]. The elution profile shows the EIC of *m/z* = 458.58 of the samples MT Fab (black), D1T Fab:Fab (blue), D1T Fab:Fc (pink), D2T Fab:Fab (brown) and D2T Fab:Fc (light green). HC AA [44-65] Phe70ox is solely present in the D1T Fab:Fab and D2T Fab:Fab samples whereas it is almost absent in the other ones.

Tables 22 and 23 summarize the identified differences between D1T Fab:Fab / MT Fab and the comparison of D2T Fab:Fab / MT Fab. As can be seen, the differences are solely restricted to isomerization and oxidation in the Fab fragment

Tab. 22: Significantly increased post-translational modifications in D1T.

Peptide	Modification	Observed m/z-values	Neutral mass Unmodified peptide [Da]	Area rel. to unmodified Peptide [%] (D1T)	Area rel. to unmodified Peptide [%] (MT)
HC [1-43]	**Oxidation** [M34]; [N35]; [W36]	1140.31 912.50	4541.22	10.2	3.1
HC [44-65]	**Oxidation** [W47]; [W50]; [Y54]	1267.60 845.40	2517.19	19.2	0.0
HC [44-65]	**Dioxidation** [Y54]; [W47]	1275.60 850.73	2517.19	4.8	0.0
HC [44-65]	**Isomerization** [N52]	1260.09 840.40	2517.19	30.8	0.0
HC [44-65]	**Isomerization** [D63]	1260.09 840.40	2517.19	12.5	4.4
HC [66-76]	**Oxidation** [F70]	458.58	1356.72	6.8	0.0
HC [99-127]	**Oxidation** [W113]; [W108]	835.64	3322.54	2.8	0.3
HC [99-127]	**Dioxidation** [W108]	839.64	3322.54	1.5	0.0

Tab. 23: Significantly increased post-translational modifications in D2T.

Peptide	Modification	Observed m/z-values	Neutral mass Unmodified peptide [Da]	Area rel. to unmodified peptide [%] (D2T)	Area rel. to unmodified Peptide [%] (MT)
HC [1-43]	**Oxidation** [M34]; [N35]; [W36]	1140.31 912.50	4541.22	6.0	3.1
HC [44-65]	**Oxidation** [W47]; [W50]; [Y54]	1267.60 845.40	2517.19	12.3	0.0
HC [44-65]	**Dioxidation** [Y54]; [W47]	1275.60 850.73	2517.19	7.3	0.0
HC [44-65]	**Isomerization** [N52]	1260.09 840.40	2517.19	16.7	0.0
HC [44-65]	**Deamidation** [63]	1260.0893 840.40	2517.19	16.6	4.4
HC [66-76]	**Oxidation** [F70]	458.58	1356.72	5.6	0.0
HC [99-127]	**Oxidation** [W113]; [W108]	835.64	3322.54	6.4	0.3
HC [99-127]	**Dioxidation** [W108]	839.64	3323.54	2.1	0.0
HC [154-216]	**Deamidation** [Q181; Q202]	2239.11	6657.29	1.6	0.2
LC [108-126]	**Oxidation** [K126]	706.71	2118.13	2.3	0.8

Since aspartate and isoaspartate have the same mass and cannot be distinguished by CID/HCD fragmentation, isomerization at position Asn52 and Asp63 was unambiguously identified in a separate experiment using direct infusion and electron transfer dissociation (ETD) fragmentation. By using ETD fragmentation mainly c- and z-fragments are generated. In the case of isoaspartate containing peptides, the reporter fragments z-57 and c+57 are generated due to the insertion of one methylene group into the protein backbone. In this way, the presence and position of isoaspartate could be identified (Fig. 67, 68 & 69).

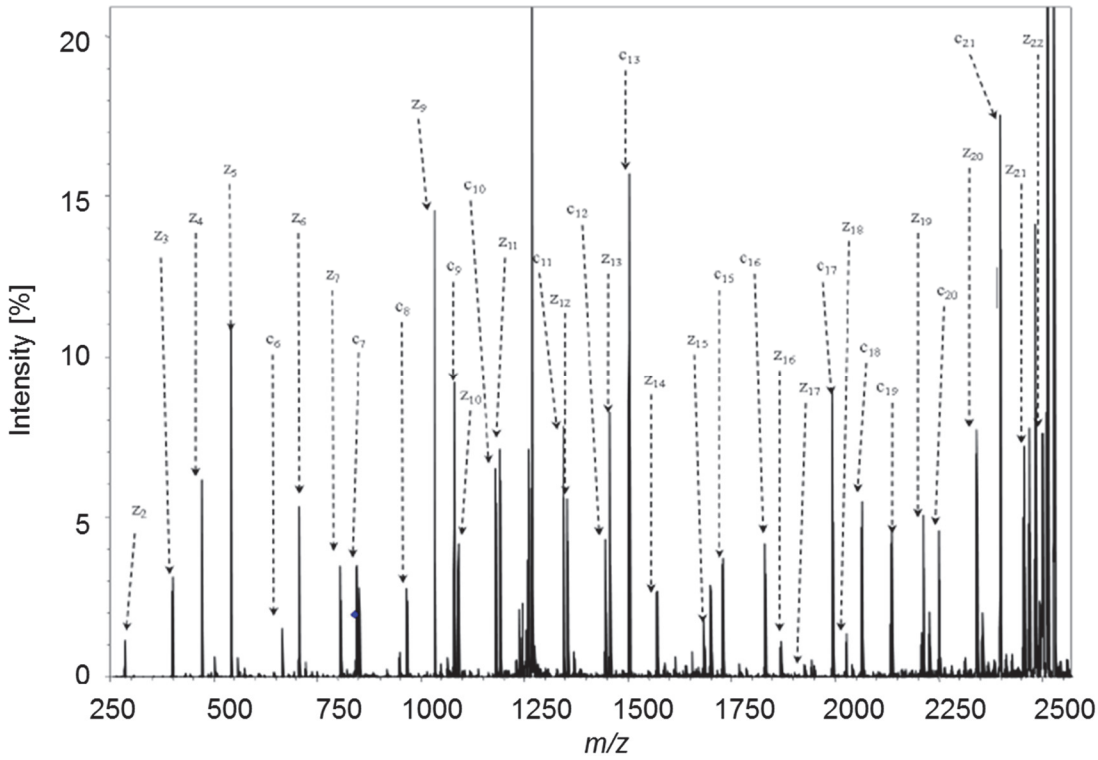

Fig. 67: MS/MS spectrum of AA [44-65] obtained by ETD fragmentation for N52 verification. The MS/MS spectrum of the precursor ($[M+3H]^{3+}$ with *m/z* = 840.1 verifies the sequence of the unmodified peptide.

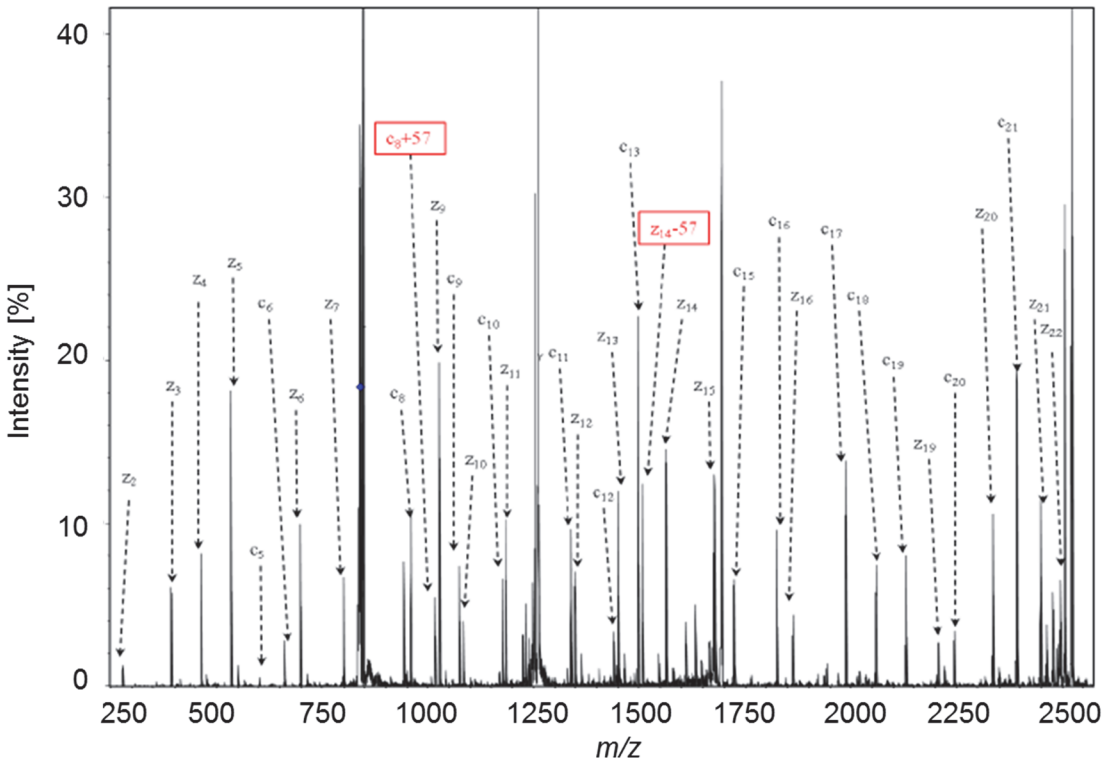

Fig. 68: MS/MS spectrum of AA [44-65] obtained by ETD fragmentation for isoAsp52 verification. The MS/MS spectrum of the precursor $[M+3H]^{3+}$ (m/z = 840.4) shows the reporter fragments $z1_4$-57 (*m/z* = 1505.7) und c_8+57 (*m/z* = 1015.5) for the verification of isomerization at position Asn52.

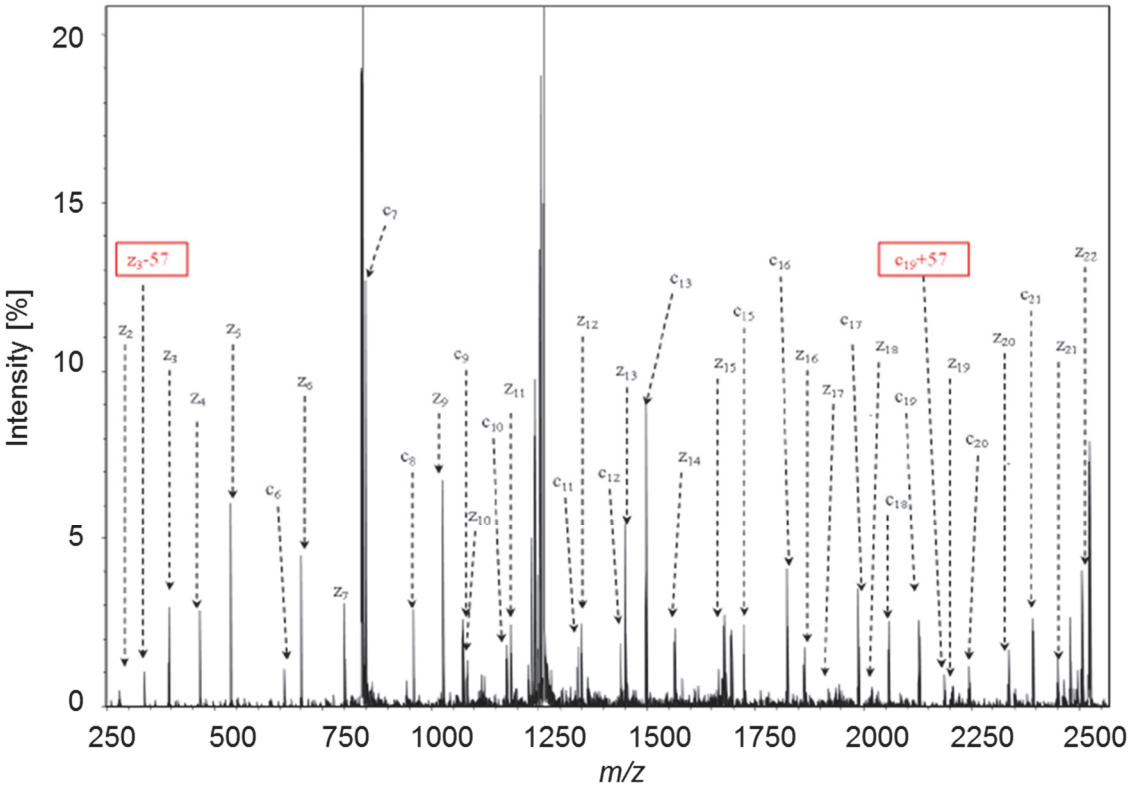

Fig. 69: MS/MS spectrum of AA [44-65] obtained by ETD fragmentation for isoAsp63 verification. The MS/MS spectrum of the precursor $[M+3H]^{3+}$ (m/z = 840.4) shows the reporter fragments z_3-57 (*m/z* = 335.2) and c_{19}+57 (*m/z* = 2184.0) for the verification of isomerization at position Asp63.

From H/DX-MS analysis and peptide mapping results can be seen that differences between the dimer and monomer samples are restricted to the Fab fragment. Furthermore, most of the modifications detected are in close proximity to each other and are located in / next to the sequences that were identified to be significant in H/DX-MS investigations. Figure 70 illustrates the location of identified modifications and H/D exchange results in the D1T Fab:Fab and D2T Fab:Fab samples. The colored residues mark the positions identified to show increased amounts of oxidation (Trp108, Trp113, Asn35, Met34, Trp36, Trp50, Trp47, Tyr54 and Phe70) as well as significantly increased amounts of isomerization (Asn52, Asp63). Red colored regions show increased exchange in H/DX-MS experiments whereas blue ones show decreased rates, suggesting these regions as intermolecular interaction sites within the Fab:Fab dimer variants.

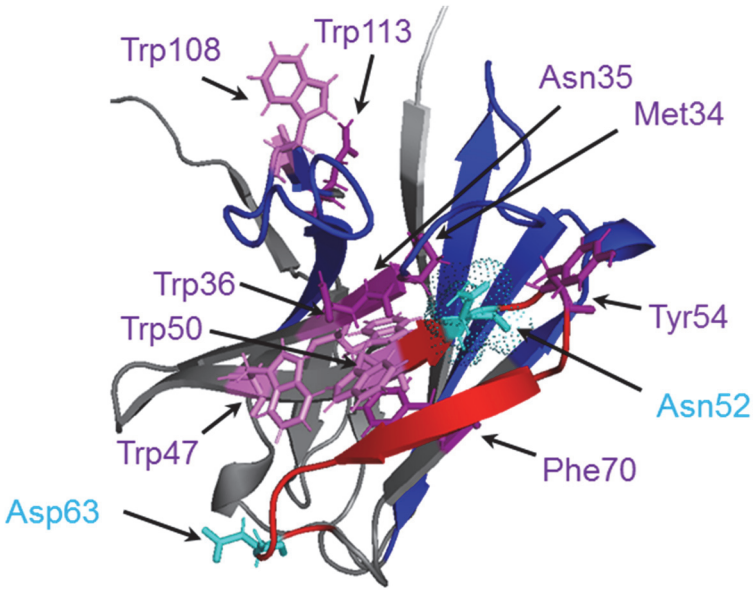

Fig. 70: Representation of the observed differences in D1T Fab:Fab and D2T Fab:Fab. The differences revealed by peptide mappings and H/DX-MS are mapped onto the crystal structure of the V_H domain of the analyzed IgG1. Residues with increased amounts of oxidation (Trp108, Trp113, Asn35, Met34, Trp36, Trp50, Trp47, Tyr54 and Phe70) are colored in purple. Highly isomerized residues (Asn52, Asp63) are colored in cyan. Sequences that showed decreased H/D exchange kinetics are colored in blue and those with increased kinetics in red.

4. 2. 6. *In silico* investigation of the conformational impact of isomerization in the CDR2

Reduced peptide mapping and H/DX-MS results suggested a direct correlation between isomerization at position [Asn52 HC] and the dimerization process of temperature-stressed dimer variants. Thus, isomerization at this specific position was investigated in more detail by molecular dynamics simulation.

In a first step, the Fab domain was isolated from the homology model (4. 2. 2.) and subsequently mutated at position Asn52 (Asn52isoAsp). To get insight into the probability of isomerization at this specific position the free energy of the conversion was computed using the AMBER package in a thermodynamic cycle. The results revealed that this conversion is an exergonic process with a Gibbs free energy ($\Delta\Delta G_{\mathrm{Asn} \rightarrow \mathrm{isoAsp}}$) of -55.0 kJ/mol. This value implicated that isomerization at Asn52 is energetically preferred and can occur spontaneously. Thus, isomerization does not need any unfolding event or catalysis prior conversion at position Asn52.

The isolated Fab domain was also subjected to molecular dynamics simulations to investigate the stability and local structural alterations in the Asn52 and isoAsp52 environment.

Interestingly, the resulting frames showed differences in amount and dynamics of hydrogen bonds between flanking amino acids and Asn52 or isoAsp52, respectively. For Asn52 four hydrogen bonds were found to be formed during 100 ns sampling between Asn52-OD1—Tyr54-N, Asn52-OD1—Thr55-N, Asn52-O—Gly56-N and Asn52-N—Glu57-O. Figure 71 illustrates the formation of hydrogen bonds which leads to a stabilizing effect within the heavy chain CDR2 of the Asn52 variant.

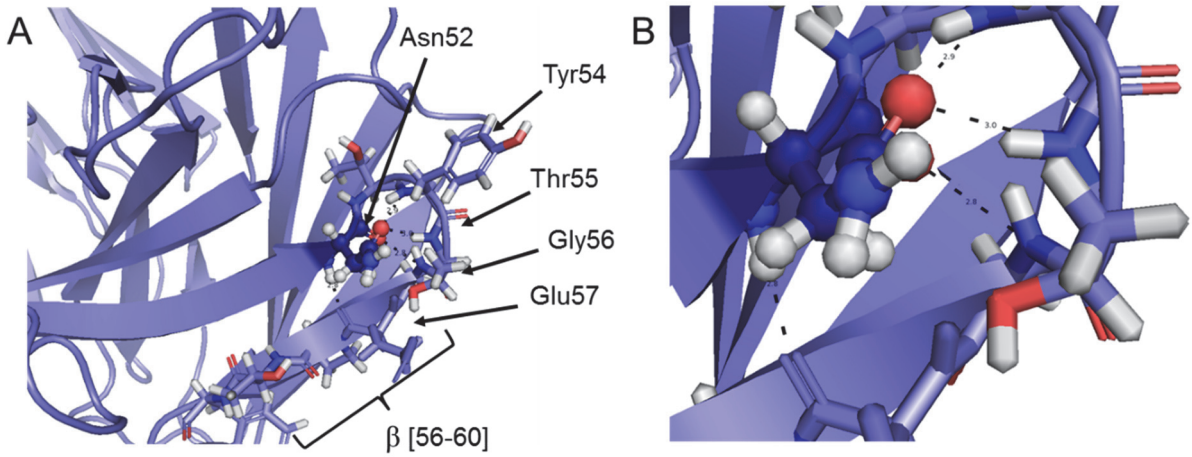

Fig. 71: Structural arrangement of the CDR2 in the Asn52 variant. (A) Stabilizing effect of the CDR2 due to hydrogen bond formation in the Asn52 variant. Asn52 interacts with the amide hydrogen in the protein backbone of Tyr54, Thr55, Gly56 and the oxygen of Glu57. Hydrogen bonds are depicted as dashed lines. Asn52 atoms are drawn as spheres for discrimination to highlight the specific position. (B) Zoomed view for better illustration of hydrogen bond formation.

The resulting hydrogen bonds showed remarkable stability and low dynamics which is reflected by the frequency of sampled donor-acceptor distances (Fig. 72A) as well as angles that were taken by the hydrogen acceptor and hydrogen acceptor pairs (Fig. 72B).

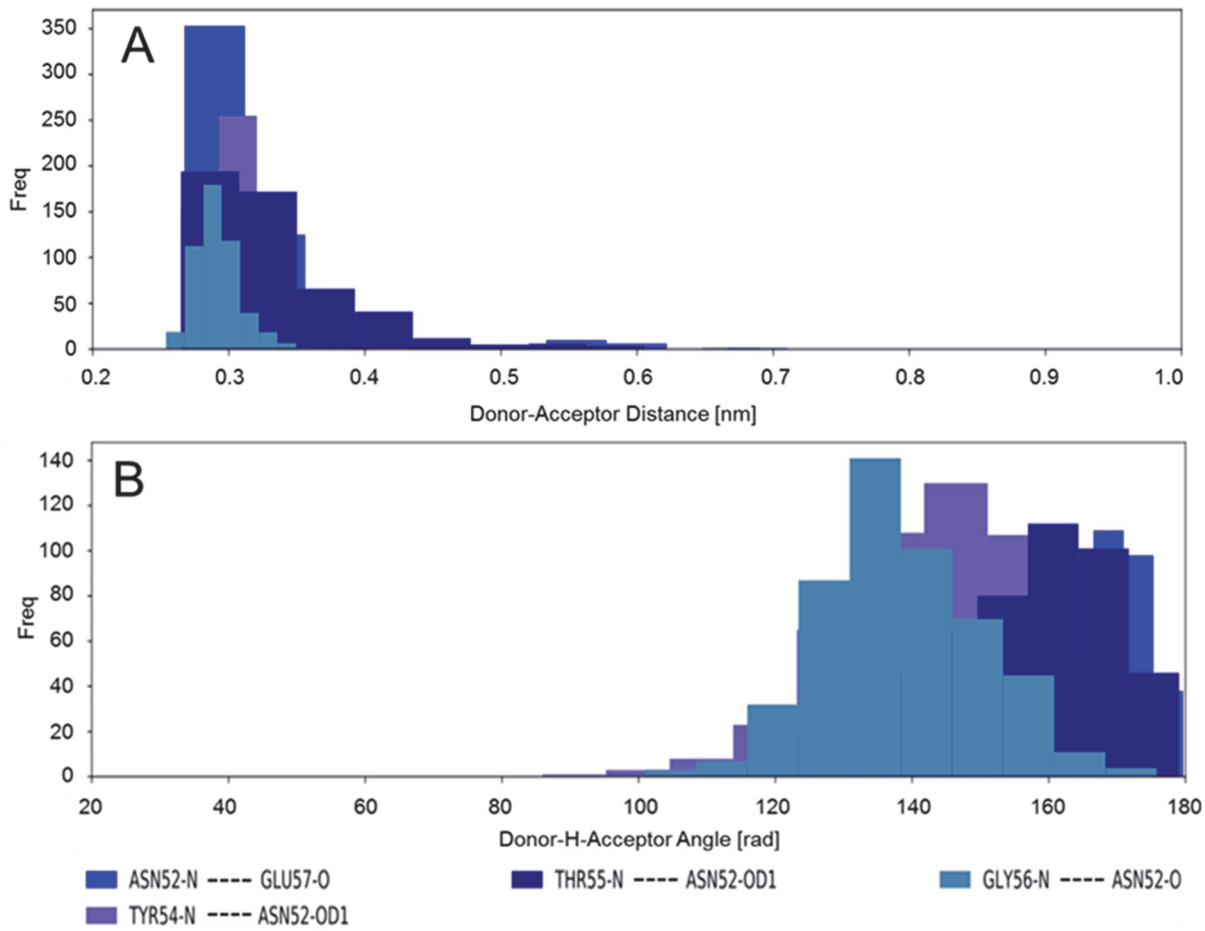

Fig. 72: Sampled hydrogen bond donor-acceptor distances and angles of Asn52. (A) Frequency of distances between hydrogen bond donor and acceptor (B) Frequency of different angels between hydrogen bond donor and acceptor. The color coding of investigated hydrogen bonds is depicted on the bottom.

In contrast to Asn52, the isoAsp52 variant forms only three hydrogen bonds. These are formed between the peptide bond oxygen of isoaspartate and the side-chain oxygen of Thr55, as well as the peptide bond nitrogen atoms of Thr55 and Gly56. Figure 73 shows the hydrogen bond geometry of the in the CDR2 located isoAsp52. Furthermore, the β-sheet AA [56-60] next to the CDR2 loop is disrupted due to isoaspartate formation which is likely caused by the insertion of the methylene group which in turn leads to a reorganization and disruption of β-sheet stabilizing hydrogen bonds.

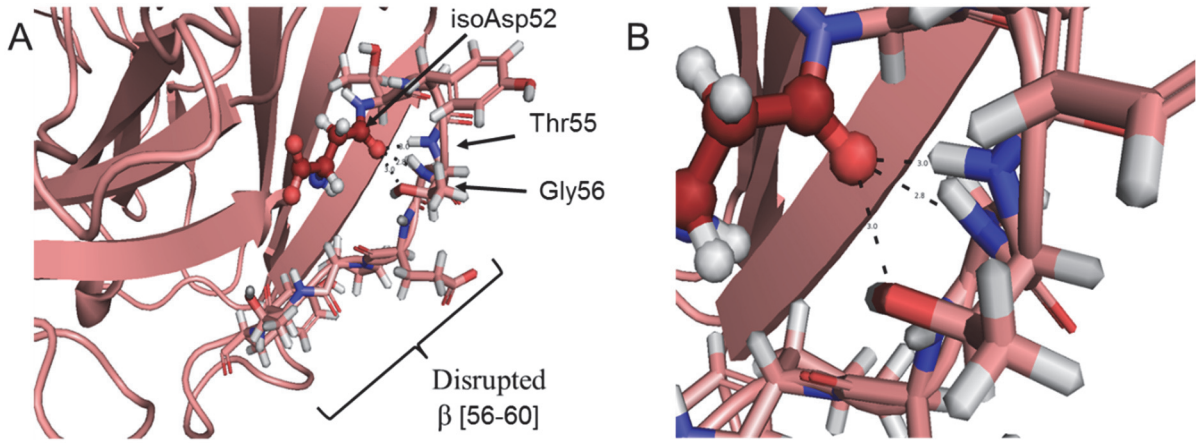

Fig. 73: Structural arrangement of the CDR2 in the isoAsp52 variant. (A) Hydrogen bonds formed in the presents of isoaspartate at position AA52 in the CDR2 region. IsoAsp52 interacts with Thr55 and Gly56. Hydrogen bonds are depicted as dashed lines. IsoAsp52 atoms are drawn as spheres for discrimination to highlight the specific position. (B) Zoomed view for improved illustration of hydrogen bond formation.

Hydrogen bonds formed in the presence of isoAsp showed increased dynamics and fluctuations compared to Asn52 which leads to increased instability of the CDR2 in this variant. This effect is suggested by the investigation of the wide range of acceptor-donor distances and angles that are taken by the three hydrogen bonds (Fig. 74).

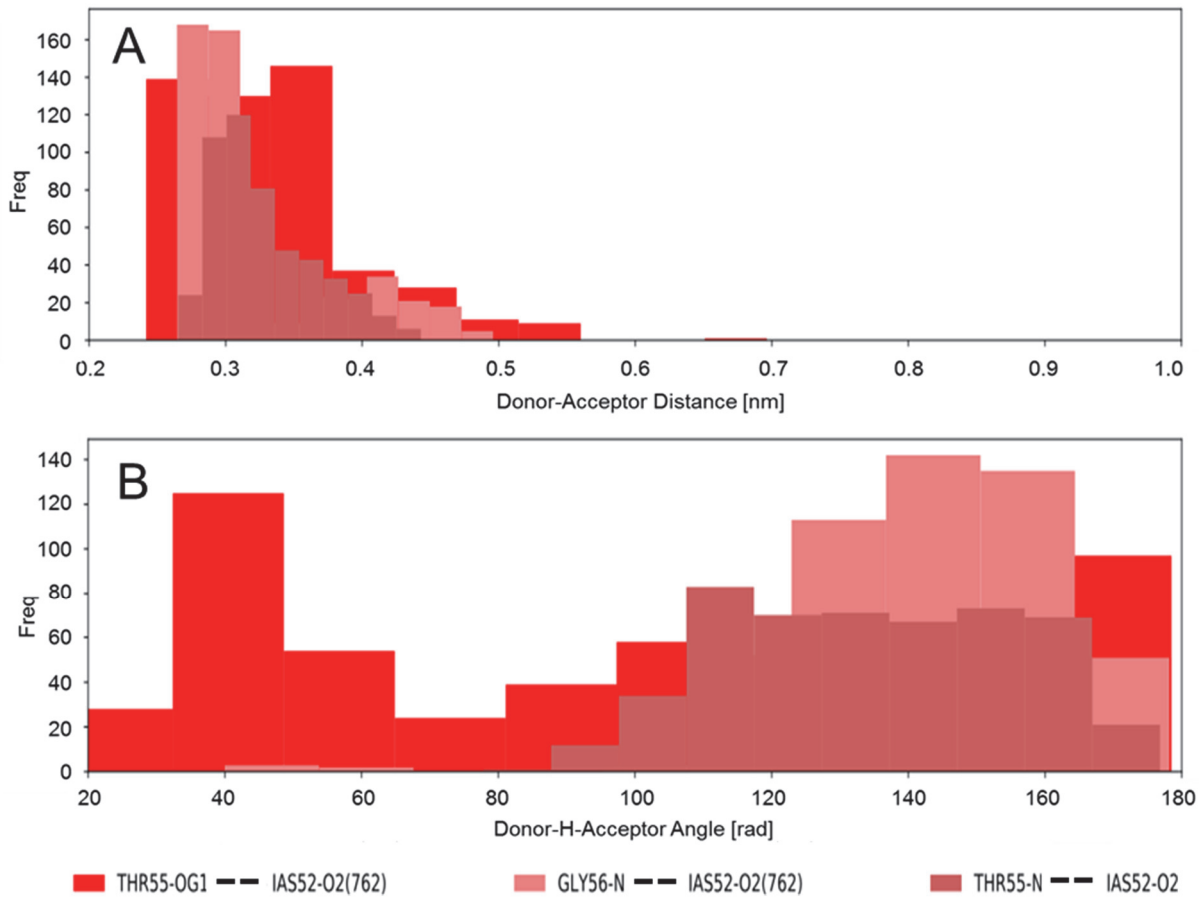

Fig. 74: Sampled hydrogen bond donor-acceptor distances and angels of isoAsp52. (A) Frequency of distances between hydrogen bond donor and acceptor (B) Frequency of different angles between hydrogen bond donor and acceptor. The color coding of investigated hydrogen bonds is depicted on the bottom.

4. 3. Discussion

4. 3. 1. Investigated IgG1 forms two predominant structural dimer variants

Structural characterization of different dimer species was performed on temperature- and light-stressed IgG1 samples. The isolated D1T/D2T species from the temperature stressed and D1L/D2L variants from the light stressed samples were sufficiently stable after isolation. Although the SEC reinjections of the isolated dimers showed low amounts of monomer subunits, resulting from transient aggregate dissociation, the dimer samples provided sufficient purity for detailed structural characterization using AUC, SAXS and rigid body modeling and thus global structural characterization.

In-line with previous studies that described dimerization of IgG1 as a complex process resulting in coexistence of different dimer species within an IgG1 sample [Plath *et al.*, 2016] or differently stressed IgG1 samples [Paul *et al.*, 2012], the obtained data revealed that D1 and D2 samples significantly differed in structural arrangement. The D1 species exhibit a more elongated structure than the D2 variants which are more compact in overall structure according to the acquired hydrodynamic data sets. These results reflect also the elution profile of the SEC from which the different species were isolated.

Rayner and co-workers presented theoretical sedimentation coefficients for monomers (6.26 – 6.66 S) and three trial IgG dimers exhibiting extrema in overall structure – face-to-face contact (10.2 S), extended tip-to-tip structure (8.6 S) and more compact $F(ab)_2$:$F(ab)_2$ double contact (9.4 S) [Rayner *et al.*, 2013]. The values presented here are in a similar order of magnitude. Sedimentation coefficients for the monomer samples fit very well into the previous presented range for IgGs. Concerning the parameters derived from the different dimer samples, the D1 samples are an intermediate between the elongated tip-to-tip model and the $F(ab)_2$:$F(ab)_2$ double contact model. Comparing the D2 sedimentation coefficients with the previously published theoretical values the D2 samples are like the $F(ab)_2$:$F(ab)_2$ double contact model.

To get a more detailed picture of the overall structures of the samples, acquired scattering data were used for rigid body modeling. Constructed homology models were fit to the scattering data of the temperature- and light-stressed monomer samples. For the obtained best-fit models, the theoretical $S_{20,w}$ values were calculated and compared

to the experimental derived ones. The deviations amounted to 0.04 S for ML and 0.07 S for MT which indicated good accuracy of the calculated models. These monomer models were subjected to rigid-body modeling using the acquired scattering data of the different dimer samples. Best-fit models were again used for calculation of the theoretical $S_{20,w}$ values. For the dimer models the deviations between experimental and theoretical data ranged from 0.01 to 0.04 S for D1L, D2L, D1T and D2T which suggests a good accuracy in terms of global structure of the calculated models although the AUC and SAXS data represent values of the average structural distribution of the molecules in solution of samples that had less than 100 % purity.

4. 3. 2. Analysis of intermolecular interaction-sites within dimeric variants

To understand the aggregation process of this IgG1 it was important to localize the specific intermolecular interaction-sites. Because of similar size and mass of Fab and Fc it was not feasible to distinguish between the fragments by low-resolution hydrodynamic parameters and thus orientation of them within the complex models. To get a more detailed picture of the interacting domains and domain orientation, limited proteolysis was performed and released/linked domains were analyzed. These investigations gave first insights into the complexity of IgG1 aggregation since no uniformity in domain distribution between linked and free fragments resulted which is consistent with the literature [Remmele *et al.*, 2006]. Instead, Fab:Fab and Fab:Fc connections were observed. In accord with previous studies performed on palivizumab [Iwura *et al*., 2014] and other IgG1 drug molecules [Plath *et al*., 2016; Paul *et al.,* 2012] especially the Fab domain seems to bear aggregation prone regions since no Fc:Fc complexes were found in all the investigated dimer variants - contrary to published data performed on epratuzumab [Remmele *et al.*, 2006]. This different aggregation behavior of the previously analyzed IgG drug molecules is very surprising since all of them are humanized IgGs sharing approximately 90% sequence identity [Wang *et al.,* 2009] with differences mainly condensed in the CDRs. Thus, the CDR regions might participate on intermolecular interactions. This was verified by H/DX-MS analysis of the isolated

linked fragments. The comparative measurements revealed differences solely in the Fab domains of the dimers and identify the CDR sequences to be main responsible in intermolecular interaction which is contrary to previous published work on another IgG1 [Iacob *et al.*, 2013] but would describe the reason for this IgG to be very sensitive to aggregation compared to other IgG1 molecules

The Fab:Fab complexes of the dimer variants isolated from temperature-stressed samples showed altered hydrogen deuterium exchange kinetics in all the heavy chain complementary determining regions whereas the CDR1 and CDR3 sections revealed decreased and the CDR2 region increased kinetics. The measurements of the Fab:Fc complexes of D1T and D2T evidenced that the HC CDR1 and the LC CDR1 in the case of D2T obviously participate in intermolecular interaction. In all the variants no H/D exchange difference could be identified which leads to the suggestion that the interaction-site in the Fc is either not site-directed and random or interaction with the Fc part occurs mainly via covalent interaction. In general, covalently bridged peptides cannot be detected and compared in head-to-head H/DX-MS experiments. Nevertheless, possible differences in the Fc-part would be less distinct than in the Fab since the Fc consists of two identical Fc/2 fragments. In the case one of both shows differences in H/D exchange kinetics this effect would be significantly smaller in the presence of one Fc/2 fragment that is not effected. This could in the worst case lead to non-detectable differences in H/D exchange in the Fc domain.

Detecting differences for interaction-site localization within IgG dimers is not feasible since the dimer consists of two identical monomeric units which in turn again consists of two identical heavy and two identical light chains. Giving site directed association, the majority of derived peptides would be exposed to deuterium in the same degree as in the monomer. Since differences in deuteration levels of one and the same peptide cannot be separated on the LC column or by drift-time, this subsequently lowers the effect in mass determination that would arise by different high exposure to the solvent. Thus, no differences compared to the monomer would be detected.

For this reason, partial digestion of the dimeric species was performed with subsequent removal of domains that are not involved in intermolecular interaction in order to gain sensitivity in H/DX-MS experiments.

4. 3. 3. The crucial role of the heavy chain CDRs in aggregation process

Although interaction-site analysis suggested highly complex aggregation mechanisms one post-translational modification was identified to directly correlate with dimerization. Peptide mappings of the interacting domains revealed several post-translational modifications in the Fab of the investigated Fab:Fab complexes that are exclusively present in the complex but not in the free Fab domain. Besides oxidation (Met34, Asn35, Trp36, Trp47, Trp50, Tyr54, Phe70, Trp113, Trp108 in the heavy chain and Lys126 in the light chain) isomerization of Asn52 and Asp63 to isoAsp52 or isoAsp63, respectively, were found in high abundancies in D1T Fab:Fab/D2T Fab:Fab but were almost absent in the monomeric Fab. The modification that showed the highest amount was isoAsp52 in the heavy chain CDR2, leading to the hypothesis that this interconversion triggers site-directed aggregation mechanisms. H/DX-MS investigations on D1T Fab:Fab and D2T Fab:Fab resulted in increased H/D exchange kinetics in HC[50-64] and HC[49-64], respectively, where isomerized Asn52 and Asp63 are positioned indicating structural alterations induced by isomerization in the CDR2. Since isoaspartate formation results in the insertion of one methylene group into the protein backbone [Aswad *et al.*, 2000] structural alterations of motifs flanking the altered amino acid may likely occur. This in turn led to the exposure of the residues that displayed increased oxidation rates and the exposure of aggregation prone regions for dimerization.

To investigate the impact of isomerization in the CDR2 in more detail molecular dynamics simulations of the Asn52 to isoAsp52 conversion was performed. The obtained data revealed that isoaspartate formation at this position is thermodynamically favored and can occur spontaneously. Asn52 is stabilized by four hydrogen bridges with the neighboring amino acids that show low fluctuations implicating high stability. In contrast, isoAsp52 lacks one hydrogen bridge and the remaining ones display a high range of sampled distances and angles which indicates increased fluctuations and thus destabilization of the neighboring motifs which is also reflected by the disruption of the C-terminal flanking β-sheet ranging from AA [56-60]. Although, isoAsp52 displays a lower amount of stabilizing hydrogen bonds it is thermodynamically favored since

additional stabilization occurs by the formation of hydrogen bonds with the surrounding bulk water. This suggestion is strengthened by the increased H/D exchange kinetics of HC [50-64]/HC [49-64]. The observed data are in-line with investigations that describe structural alterations due to isomerization in the CDR2 at position Asn54 of another IgG1 [Yan *et al.*, 2016]. But these data were not related to dimerization of the investigated IgG1.

Based on the results it can be concluded that the engineered CDR sequences are mainly responsible for site-directed dimerization. Spontaneous isomerization in the CDR leads to structural rearrangement of the flanking loops and disruption of secondary structural motifs. This in turn leads to the exposure of different residues that represent intermolecular interaction-sites within the dimer species. Dimerization again can afterwards result in an extended or more compact complex structure.

To prevent the described aggregation mechanism, the impact of distinct, modification-prone amino acids should be investigated in detail during the protein engineering step (e. g. *in silico*). During this early stage of development, amino acids that are found to induce or trigger aggregation can be exchanged by amino acids that are more stable, less prone to post-translational modifications and subsequent aggregation.

5. Phosphorylation caused structural rearrangement of c-Src kinase during activation

5. 1. Introduction

c-Src belongs to the family of non-receptor tyrosine kinases and is ubiquitously expressed in all tissues [Brown & Cooper, 1996]. It plays important roles in numerous signal transduction pathways ranging from cell proliferation to growth and survival. Deregulation of its activity is the main reason for c-Src to be involved in cancer emergence and progression [Broome & Hunter, 1996, Twamley-Stein *et al.*, 1993, Johnson *et al.*, 2000] and the formation of metastasis [Ellis *et al.*, 1990, Fincham *et al.*, 1995]. To understand the activation process of c-Src in detail, can therefore lead to avenues to cure Src-related cancer.

c-Src consists of a Unique domain, which is followed by the regulatory SH3- and SH2-domains and the kinase domain. When phosphorylated by C-terminal Src kinase (CSK), pY527 in c-Src is intramolecularly bound to the SH2-domain, which leads to a compact conformation in the inactive state of c-Src [Cooper *et al.*, 1986, Nada *et al.*, 1991, Okada & Nakagawa, 1988, Xu *et al*., 1997]. In contrast, in the activated state of c-Src, this site is dephosphorylated [Cowan-Jacob, 2005]. However, Y527-dephosphorylation might not be sufficient for full activation of c-Src [Lydon *et al*., 1992]. The kinase domain carries another phosphorylation-site within the activation loop at position Tyr416 which is located at the interface between the N- and the C-lobe. Upon autophosphorylation at this site, the kinase activity is increased [Smart *et al.*, 1981, Purchio, 1982, Kmiecik *et al*., 1987, Cooper & MacAuley, 1988, Reuter *et al*., 1990].

The compact, inactive conformation is mediated by the interaction between SH2-domain and pY527 as well as the binding of the SH3-domain to the SH2-domain-kinase-linker [Xu *et al*., 1999a]. Consequently, potential substrate binding sites on the SH2- and SH3-domains are blocked and within the active center, the αC-helix is tilted, leading to a conformation incompatible with the formation of an important salt bridge between K295

and E310 and thus, with enzymatic activity [Huse & Kuriyan, 2002]. In addition, the A-loop forms an α-helix, thereby sterically blocking the active center [Xu *et al.*, 1999a]. The activation process of c-Src is divided into three parts. (1) Substrate proteins are able to displace the pY527 and the linker from the SH2- and SH3-domains. Elimination of the SH2-pY527-interaction ("unlatching") leads to a conformational change in the kinase domain and (2) activating the enzyme in a process called "unclamping" [Xu *et al.*, 1999a]. In this conformation, the released C-terminal pY527 can be dephosphorylated, the αC-helix is tilted inwards the active center, forming the K295-E310-salt bridge and the A-loop becomes unstructured [Brown & Cooper, 1996, Cowan-Jacob *et al.*, 2005]. (3) In a step called "switching" Y416 in the A-loop is phosphorylated, which is thought to prevent the loop to re-interact with its former binding site and form a suitable platform for substrate binding. [Xu *et al*., 1999a, Roskoski, 2004, Cowan-Jacob *et al*., 2005]. In this active state, relative movement of the two lobes of the kinase domain enables the kinase to adopt an open and a closed conformation. While in the open conformation ATP can be bound and/or ADP released, the closed form is necessary for the active center to conformationally coordinate the substrates and to adopt a catalytically competent state [Huse & Kuriyan, 2002].

While the activation process is well understood for the first two steps of "unlatching" and "unclamping" [Xu *et al*., 1999a, Cowan-Jacob *et al*., 2005], the detailed mechanism of the last "switching" step still remains elusive. The question arises, what happens to the c-Src structure upon phosphorylation at Y416? Structures without any phosphorylation [Cowan-Jacob *et al*., 2005] and with phosphorylated Y416 [Breitenlechner *et al*., 2005] shed first light on this problem. However, firstly, *in vivo* c-Src is either phosphorylated at Y527 or at Y416 and no non-phosphorylated kinase, that would be comparable to the existing crystal structure, has ever been observed *in vivo* [Cowan-Jacob, 2005] and secondly, the pY416-phosphorylated kinase domain was crystallized without any regulatory domains, which is thought to interfere with its conformation [Breitenlechner *et al*., 2005]. In addition, key parts of the kinase, including the A-loop and pY416, were not resolved. MD-simulations indicate that the kinase domain would become more compact upon phosphorylation at

Y416 [Meng & Roux, 2014]. However, again only the kinase domain of c-Src was analyzed and the SH3- and the SH2-domains were left out.

Here, a detailed analysis of the influence of pY416 on c-Src kinase structural dynamics was performed. This was done by a combination of activity assays, MD-simulations, biochemical analyses and H/DX-MS to structurally elucidate how the last stage of c-Src activation is achieved. Furthermore, the full-length c-Src and its kinase domain was compared to separately determine the influence of the regulatory domains on the global kinase conformation.

5. 2. Results

5. 2. 1. Y416-phosphorylation increases the activity of c-Src

The influence of the inhibitory phosphorylation site Y527 in c-Src has been extensively studied [Roskoski, 2004]. In contrast, the influence of autophosphorylation on Y416 on c-Src activity, structure and dynamics still lacks detailed investigation. Y416 resides within the activation loop of c-Src, which is located in the C-terminal lobe of the kinase domain (Fig. 75 A).

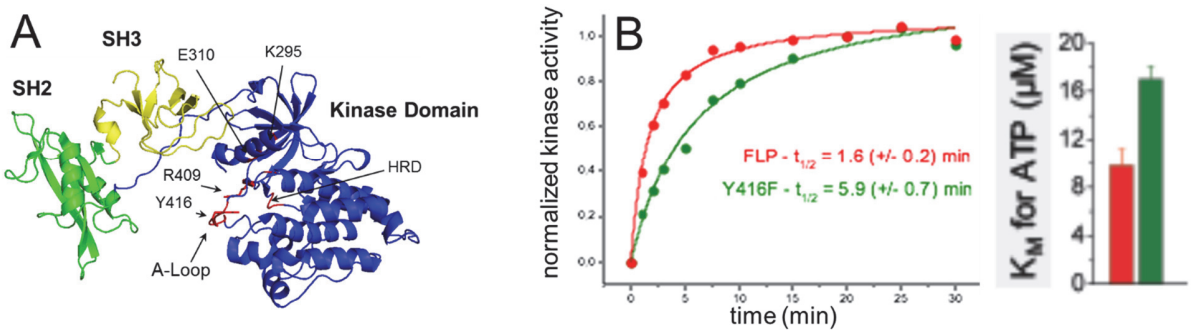

Fig. 75: Structural arrangement of c-Src (A) and phosphorylation dependent kinase activity (B). Y416-phosphorylation increases c-Src kinase activity. (A) Structure of c-Src kinase (PDB: 1Y57). Coloring from N- to C-terminus: SH3-domain in yellow, SH2-domain in green, linker and kinase domain in blue. Important elements involved in kinase activation are depicted in red: Y416, A-loop, KER-residues and HRD-motif. (B)Time-dependent substrate phosphorylation by c-Src full length in its phosphorylated state (FLP) and the non-auto-phosphorylatable mutant FLU-Y416F. Inset: K_M (ATP) for the two different constructs.

To determine how phosphorylation at Y416 influences c-Src *in vitro*, c-Src was purified from Baculovirus and subjected to autophosphorylation at position Y416. Mass spectrometric investigation using MS^E fragmentation confirmed the autophosphorylation at this specific site (Fig. 76).

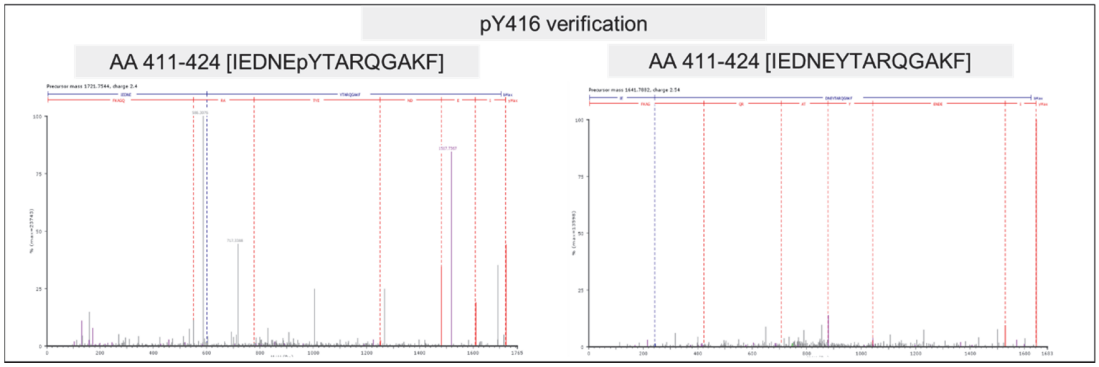

Fig. 76: Annotated MS/MS spectra of the phosphorylated and unphosphorylated peptide AA [411-424] obtained by protease digestion. MS/MS spectra resulted from fragmentation of the precursor AA [411-424] in the phosphorylated (M = 1721.75 Da; left) and dephosphorylated state (M = 1641.79 Da, right). The color code illustrates the b- and y-series in blue and red, respectively.

To assess whether phosphorylation at Y416 increases kinase activity of c-Src the autophosphorylated version was compared to a fully dephosphorylated version cSrcY416F, which lacks the tyrosine at position 416, in a kinase activity assay.

The measurements showed that due to phosphorylation the *in vitro* activity of c-Src is elevated almost 4-fold with an increase in $t_{1/2}$ of the reaction from 5.9 min to 1.6 min (Fig. 75 B). Furthermore, the phosphorylation-dependent affinity for ATP was determined. The results revealed that K_M decreased from 17.0 µM for the non-phosphosphorylatable c-SrcY416F to 9.8 µM for the phosphorylated c-Src (Fig. 75 B, inset).

5. 2. 2. Y416-phosphorylation traps c-Src in the active state

To analyze the impact of Y416-phosphorylation on the activity of c-Src in more detail the protein dynamics of the kinase at different stages during the activation process was performed. As an initial step, the full-length unphosphorylated c-Src at Y416 (FLU for Full Length Unphosphorylated) was subjected to full atomistic molecular dynamics (MD) simulations in microsecond time scales in the absence and presence of ATP (FLU & FLU/ATP), and in addition, with Y416 set-up in a phosphorylated state (FLP for Full-Length Phosphorylated).

Figure 77 shows the dynamics of the central active site regions, the K295-E310 ion-pair and the activation loop (A-loop), both of which are strongly involved in the conformational activation of c-Src (Ozkirimli *et al.*, 2006, Shukla *et al.*, 2014, Meng *et al.*, 2016).

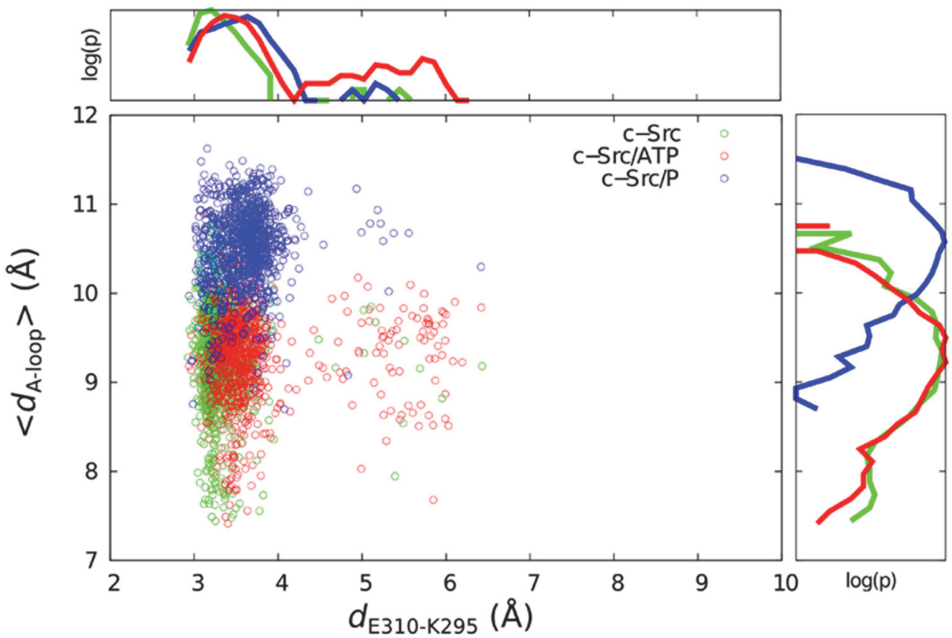

Fig. 77: A-loop and E310-K295 sampling of c-Src in different ligand states. Conformational sampling of the central E310-K295 (dE310-K295) and the extent of the A-loop (<dA-loop>). Log(p) is the logarithm of the probability distribution for a given reaction coordinate.

c-Src formed a stable ion-pairing between the K295-E310 residues and an A-loop with a relatively low extent in the unphosphorylated FLU state. In the ATP bound state (FLU/ATP), the A-loop dimension seemed to be unaffected. In contrast, the formation of the K295-E310 pair was strongly disturbed by the presence of ATP. Interestingly, upon phosphorylation of c-Src, simulated by the FLP state, the K295-E310 ion-pairing was restored and the A-loop resided in a more extended conformation. Nevertheless, the A-loop in the FLP state sampled more folded conformations compared to FLU. The simulations therefore suggest that ATP-binding is required to destabilize the K295-E310 ion-pair (Fig. 77), which further destabilizes the αC-helix, and allows E310 to interact more strongly with R409 (Fig. 78). The increased electrostatic interaction between E310 and R409 further weakened the interaction between R409 and Y416, allowing the tyrosine

residue to swing out from the A-loop. The more extended A-loop conformation would, thus be expected to increase the propensity of Y416 to become phosphorylated by interaction with another kinase yielding Y416-autophosphorylated c-Src (FLP).

By analyzing the FLP state via MD simulations, pY416 was found to strongly interact with a charged cluster of arginines: R385, R409, and R419 (Fig. 78). Interestingly, R385 is part of the HRD motif, which was also suggested to be involved in stabilizing the active state of the kinase [Kornev *et al*., 2006]. To structurally analyze the changes within this region in more detail, the solvent accessible surface area (SASA) of the HRD motif (H384, R385, D386) was calculated and key residues of the active center KER (K295, E310 and R409) were simulated in an additional 300 ns approach.

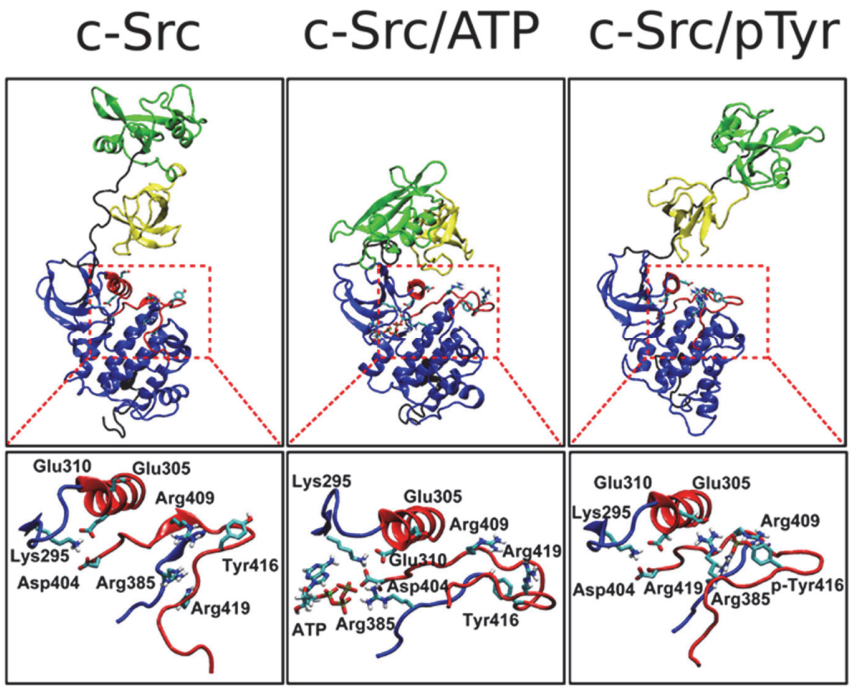

Fig. 78: Molecular dynamics simulations of c-Src in different ligand states. Snapshots of different c-Src states after 1 µs MD simulations. Zoom: Detailed picture of the interactions formed in the charged cluster of the active site αC-helix/A-loop regions during the different stated of activation.

The simulations showed that the KER residues and to a certain extent the HRD motif were less solvent accessible upon phosphorylation at Y416, suggesting a conformational consolidation of a more active state in the kinase domain (Figure 79A & B).

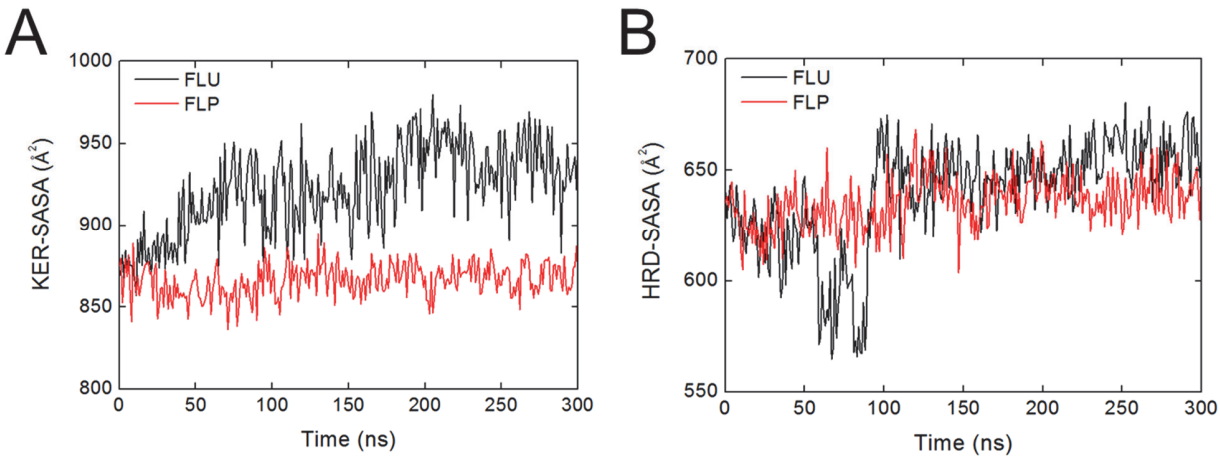

Fig. 79: Detailed analysis of the KER and HRD motif with regard to solvent accessible surface area. Solvent accessible surface area of the KER-residues (C) and the HRD-motif (D) during a 300 ns simulation of FLU (black traces) and FLP (red traces).

Similar effects for the active site region (KER) and even more pronounced for the HRD motif were observed when the isolated kinase domain was analyzed (Figure 80 A and B, KDU: Kinase Domain Unphosphorylated, KDP: Kinase Domain Phosphorylated).

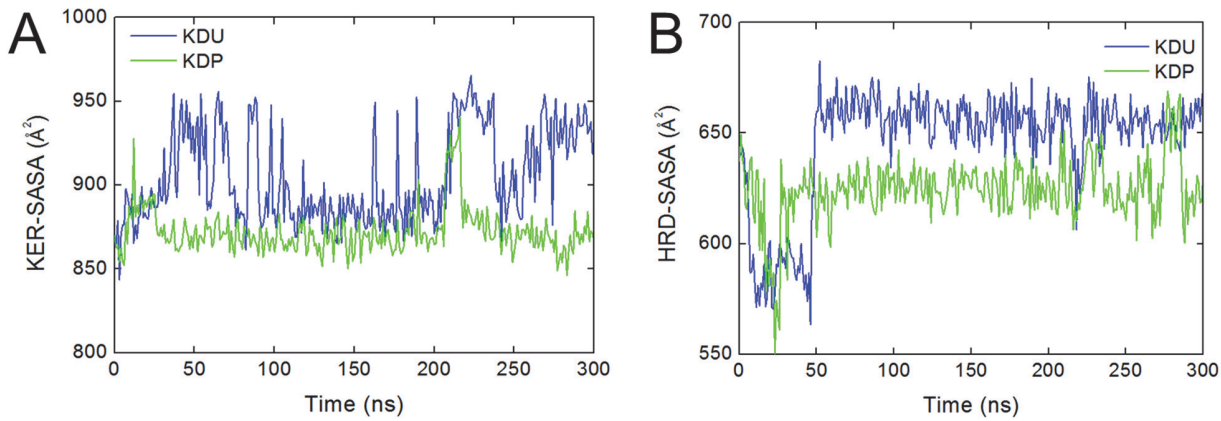

Fig. 80: Molecular dynamics simulations of the KER- and HRD motif of the unphosphorylated (KDU) and the phosphorylated (KDP) version of the kinase domain. Solvent accessible surface area of KER-residues (A) and the HRD-motif (B) during a 300 ns simulation of KDU (blue traces) and KDP (green traces).

Stabilization of the kinase domain was also suggested by a rotation of the αC-helix, which was observed upon Y416-phosphorylation in both the full-length c-Src and the kinase domain simulations (Fig. 81).

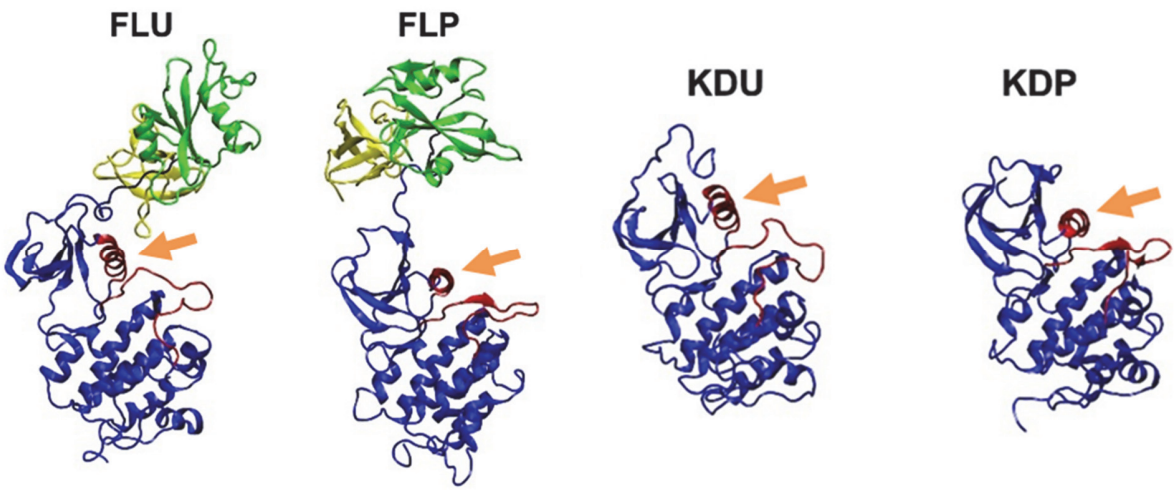

Fig. 81: Structural comparison of the different states of c-Src and the kinase domain. End-point structures of FLU, FLP, KDU and KDP at the final stage of the simulations. The αC-helix is marked by an orange arrow.

The simulations also showed that an ion-pair was formed between E305 of the αC-helix and R419 of the A-loop in the phosphorylated FLP state, which affected the dynamical flexibility of the αC-helix. This interaction was absent in the FLU and FLU/ATP simulations. In the ATP-bound state (FLU/ATP), however, E97 seemed to stabilize the αC-helix by forming an ion-pair with R409 of the A-loop that was most likely prevented in the FLP state due to strong interaction between R409 and pY416. Additionally, the E310-K295 ion-pair was found to be stabilized in the FLP state relative to the FLU/ATP state, which might result from the reduced interaction between E310 and R419.

To further investigate how phosphorylation of Y416 drives c-Src towards the active state, 0.5 µs metadynamics simulations were performed to probe its free energy landscape. Consistent with recent observations for the kinase domain only [Meng & Roux, 2014], the potential of mean force (PMF) was considerably altered in the FLP state, trapping c-Src kinase in the active conformation (Figure 82 A & B).

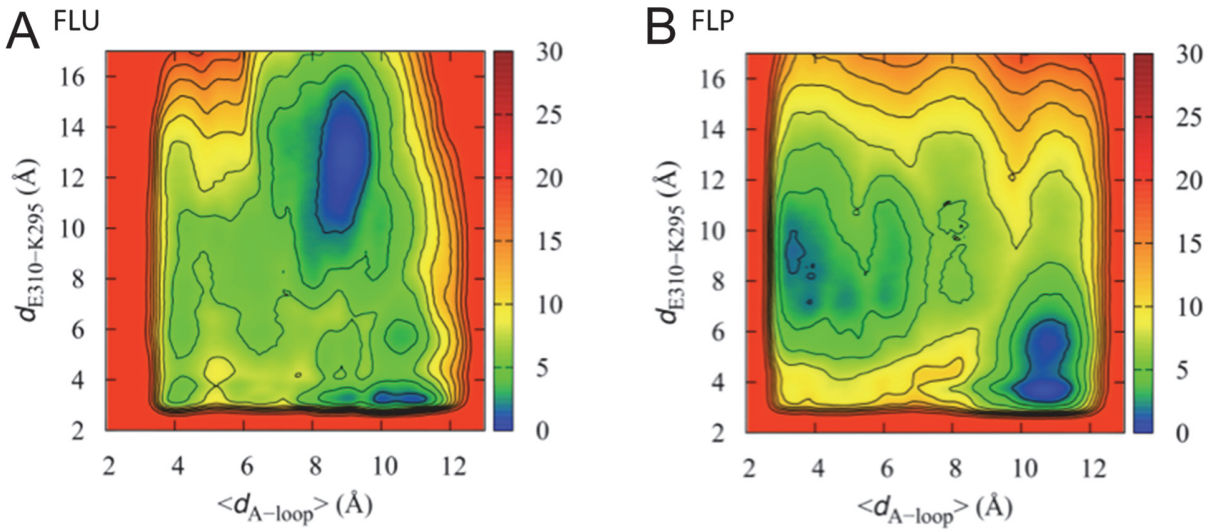

Fig. 82: Free energy landscape of FLU and FLP. Free energy landscape illustrating Δ*G* (in kcal mol^{-1}) for FLU (A) and FLP (B) obtained from 0.5 µs metadynamics simulations with reaction coordinates E310-K295 ($d_{E310-K295}$) and the extent of the A-loop (<d_{A-loop}>).

5. 2. 3. Intramolecular interactions in the kinase domain are strengthened upon Y416-phosphorylation

To gain more structural insights into the activation process, the two phosphorylated-states of c-Src were investigated by biophysical methods. In addition to unphosphorylated (FLU) and phosphorylated full-length c-Src (FLP) the truncated kinase domain in the unphosphorylated (KDU) and the phosphorylated form (KDP) was analyzed to shed light into the role of the regulatory domains.

First, the secondary structure elements were tracked by circular dichroism (CD). c-Src is a protein rich in alpha-helices as indicated by the minima at 207 nm and 222 nm in the CD-spectrum (Fig. 83 A). Upon phosphorylation at Y416 (FLP), c-Src showed subtle gain in its alpha-helical content. From high interest was to determine, whether this slight difference was due to structural transitions in the catalytic domain of the kinase. Upon phosphorylation (KDP), the kinase domain also showed a higher alpha-helical content as indicated by the minima at λ = 207 nm. Hence, the observed structural transitions seemed

to take place in the kinase domain of c-Src. To test for an increased stability, the thermal transitions of the four variants was determined. It was found that all c-Src constructs were similarly stable, independent of their phosphorylation status (Fig. 83 B). However, the results revealed that the unfolding cooperativity of KDP was increased compared to KDU. This is reflected in a larger temperature range of unfolding: the temperature range between 10 % and 90 % of unfolded protein decreased from 14.3 °C for KDU to 10.7 °C for KDP (Fig. 83 B, inset). Taken together, Y416-phosphorylation of c-Src did not globally alter the fold of the kinase, but increased the folding cooperativity in the kinase domain.

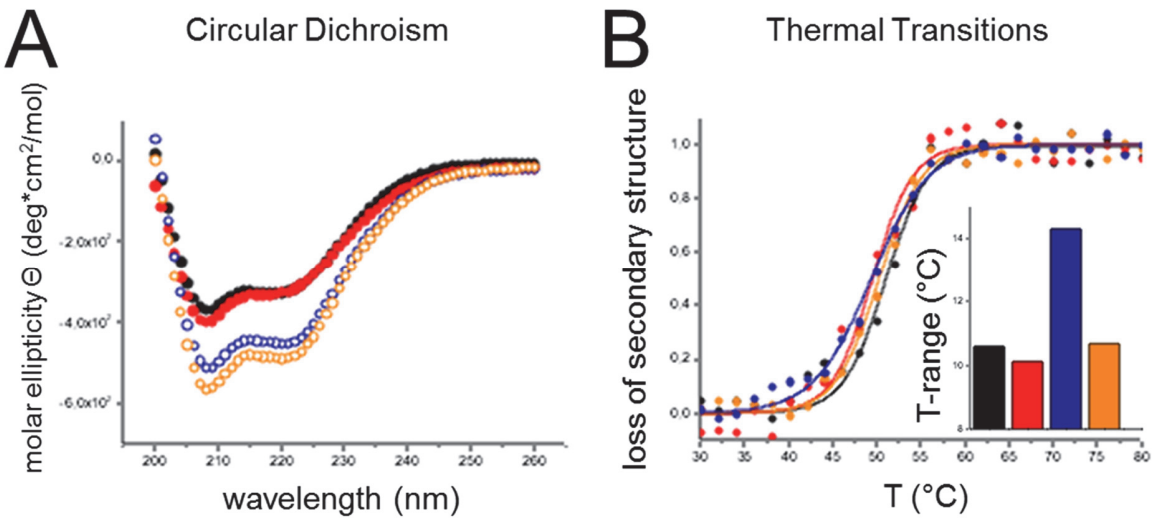

Fig. 83: Bioanalytical characterization of different c-Src constructs (CD-spectroscopy and T_M determination). c-Src full length in its unphosphorylated (FLU; black) and phosphorylated state (FLP; red) and the kinase domain of c-Src in its unphosphorylated (KDU; blue) and phosphorylated state (KDP; orange). (A) CD spectra of the different constructs indicating a high content of *α*-helices. (B) Stability and unfolding cooperativity measured by CD spectroscopy. Thermal transitions were recorded at 207 nm. Inset: shown are the temperature ranges spanning 10 % to 90 % of protein unfolding signal.

To gain more information on phosphorylation-dependent structural re-arrangements of the kinase, the surface-exposed hydrophobicity was determined of c-Src by measuring the binding of the fluorophore ANS to hydrophobic patches exposed on the protein surface. The FLU construct showed a strong fluorescence signal of 2.54 a.u. indicating that the kinase exposes hydrophobic surface area (Fig. 84 A). Upon Y416-phosphorylation, the fluorescence signal slightly decreased. Testing the unphosphorylated kinase domain

(KDU) showed much less exposed hydrophobic surface compared to the full-length construct and a fluorescence signal of 1.29 a.u. (Fig. 84 A). This indicates a significant contribution of the regulatory domains to the surface hydrophobicity in c-Src. Interestingly upon phosphorylation, the ANS fluorescence of the kinase domain (KDP) strongly decreased to a value of 0.94 a.u. This suggests that the conformational transitions causing a decrease in accessible hydrophobic area mainly take place within the kinase domain of c-Src. At the same time, structural alterations in the regulatory domains may compensate this effect in the full-length constructs by increased solvent accessibility of SH3 and SH2 due to phosphorylation.

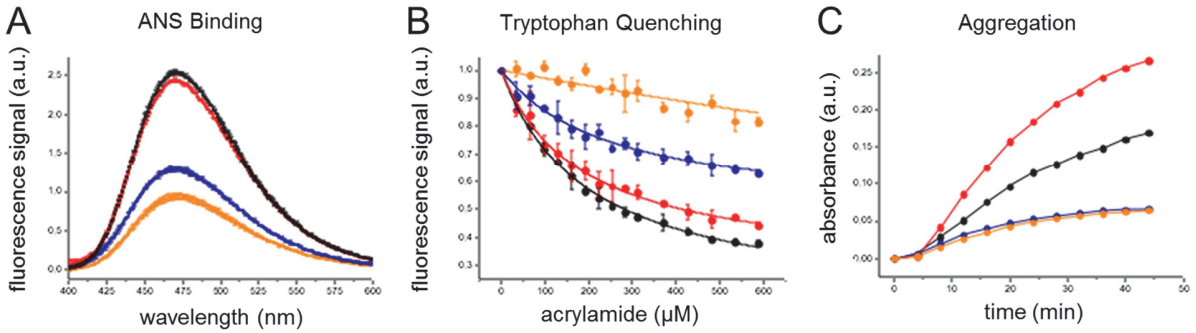

Fig. 84: Bioanalytical characterization of different c-Src constructs (ANS binding; Trp quenching; aggregation). (A) Analysis of ANS binding to hydrophobic protein patches. Fluorescence spectra after excitation at 380 nm were recorded and buffer corrected. (B) Tryptophan fluorescence emission quenching using acrylamide. Fluorescence signals at 328 nm were recorded after excitation at 295 nm. (C) Aggregation of c-Src constructs at 42 °C was analyzed by absorbance at 350 nm. (FLU: black; FLP: red; KDU: blue and KDP: orange).

Changes in conformation were further tested by assessing changes in accessibility of tryptophan residues. In Src kinase, the tryptophans are widely distributed across the protein and thus applying this method is able to track structural alterations of the whole protein. Lower molecular flexibility results in a decreased exposure of these hydrophobic residues and subsequently also to quenchers like acrylamide [Lakowicz, 1999]. With increasing acrylamide concentration, a decrease in tryptophan fluorescence was observed, which indicates that a significant fraction of the tryptophans was accessible for the quencher (Fig. 84 B). For the FLU and FLP constructs about 60 % of the initial fluorescence could be

quenched by acrylamide with the FLP state showing slightly less quenching capability. The kinase domain exhibited generally less tryptophan accessibility compared to the full-length kinase with KDU amounting to 30 %. Notably, phosphorylation of the kinase domain (KDP) resulted in a prevention of tryptophan quenching (Fig. 84 B), suggesting that the tryptophan residues were buried in this variant and are thus shielded from the titrated quencher.

An analysis of aggregation propensity revealed that the kinase domain was much less prone to aggregation than full-length c-Src and phosphorylation did not play a role in this context (Fig. 84 C). In contrast, the FLU construct readily aggregated and the phosphorylation (FLP) enhanced this effect (Fig. 84 C). These results indicate that phosphorylation of Y416 within the kinase domain globally rearranges the conformation of the full-length c-Src, which leads to higher aggregation propensity mediated by the regulatory domains since the kinase domain alone did not show this affect.

Taken together, the results point to the fact that phosphorylation of Y416 in c-Src does not significantly affect its secondary structure, but seems to strongly influence the dynamics and/or the tertiary structure of c-Src. While the kinase domain adopts a more rigid configuration upon phosphorylation, the regulatory domains seem to exhibit an increased conformational flexibility, thereby causing a higher aggregation propensity.

5. 2. 4. Y416 phosphorylation of c-Src globally alters its intramolecular interactions

Since the biophysical methods listed in Chapter 5. 2. 3. showed phosphorylation mediated structural alterations on global protein level hydrogen/deuterium exchange coupled to mass spectrometry (H/DX-MS) was applied to test for structural alterations on peptide level resolution.

Comparing the FLU and the FLP states, H/DX-MS revealed that Y416-phosphorylation of c-Src led to strongly decreased backbone proton exchange in the kinase domain and parts

of the SH2 domain (Fig. 85). In contrast, the SH3 and the unique domain were much more prone for proton exchange in the FLP state. In line with the biophysical analysis (Fig. 83 & 84), the H/DX-MS results indicated that the kinase domain undergoes a gain in conformational rigidity, whereas the regulatory domains seem to open up upon autophosphorylation in c-Src at position Y416. Notably all elements important for kinase activation underwent a decrease in solvent accessibility and decreased dynamics (Fig. 85): activation loop, KER- and HRD-motifs and the hydrophobic spine.

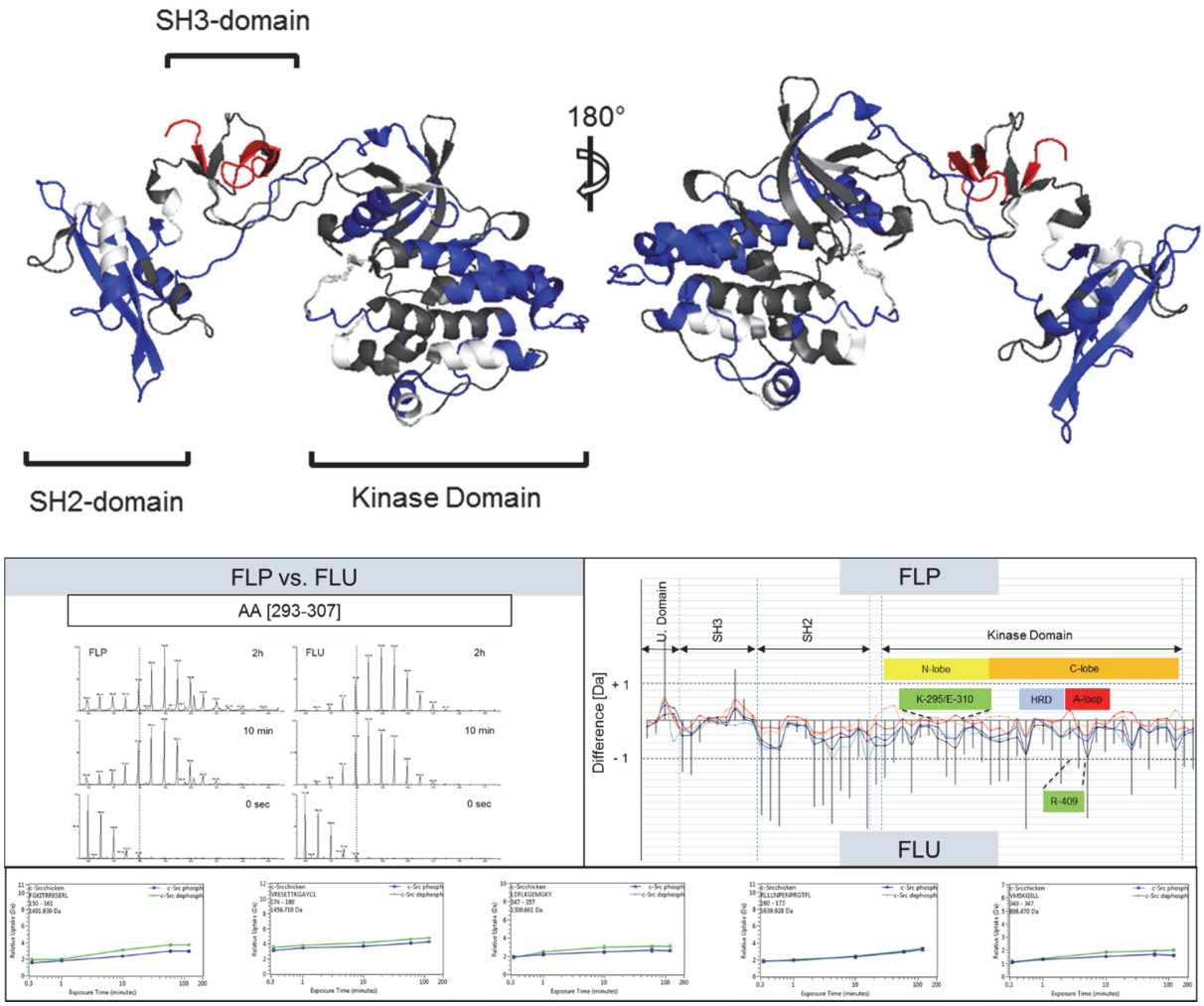

Fig. 85: H/DX-MS results for the comparison of exchange kinetics between FLU and FLP. On the top, the color-coded structure is shown. Red indicates more uptake and blue less uptake of the second-named in comparison to the first-named state. Regions showing no difference are marked in grey and not determined regions are shown in white. The middle panel shows the exemplary raw spectra acquired after 0 sec, 10 min and 120 min deuterium incubation of the peptide AA [293-307] of both states (left). The sum of differences plot is shown for the FLP and FLU state in the middle panel on the right. Colored lines

describe mass differences at each labeling time-point whereas the grey bars represent the sum of differences over all investigated labeling time-points. Elements important for kinase activation are highlighted. Active site KER-residues (K295, E310, R409), Activation Loop (D413 - R419) and HRD motif (H384, R385, D386). Exemplary uptake plots of the two different states are displayed on the bottom. The FLP state is illustrated in blue and the FLU state in green.

Consistent with the results on the FLU vs. FLP analysis, an H/DX-MS experiment using the catalytically inactive FLU-K295R mutant behaved very similar to FLU revealing no significant differences in deuterium uptake for identified peptides in the SH2 and kinase domain (Fig. 87). The mutation at position 295 was verified by MS/MS prior to H/DX-MS investigation (Fig. 86).

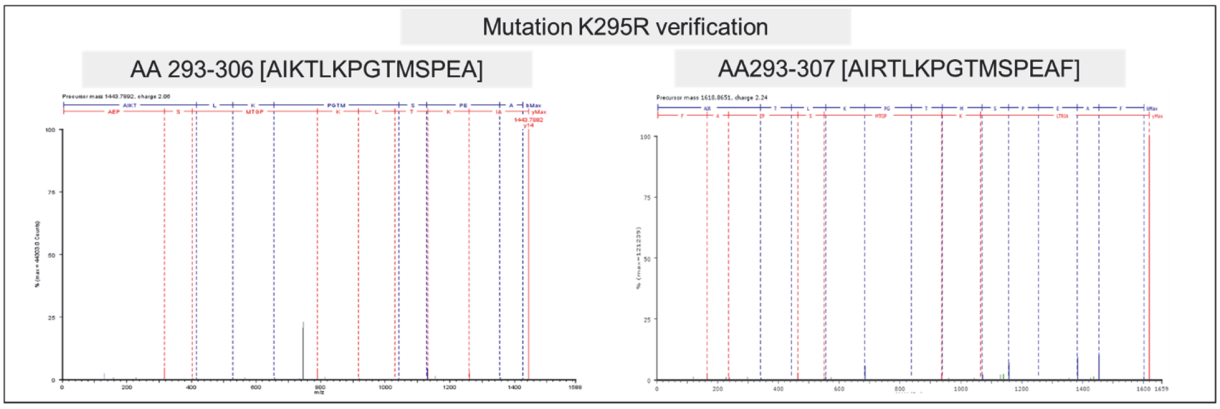

Fig. 86: Annotated MS/MS spectra of the mutated peptide AA [293-306] and unmutated peptide AA [293-307] obtained by protease digestion. MS/MS spectra resulted from fragmentation of the precursor AA [293-306] in the mutated version (M = 1443.7892 Da; left) and the unmutated peptide AA [293-307] (M = 1618.8651 Da, right). The color code illustrates the b- and y-series in blue and red, respectively.

This result indicates that FLU-K295R is unable to convert into the catalytically active state due to mutation at position K295.

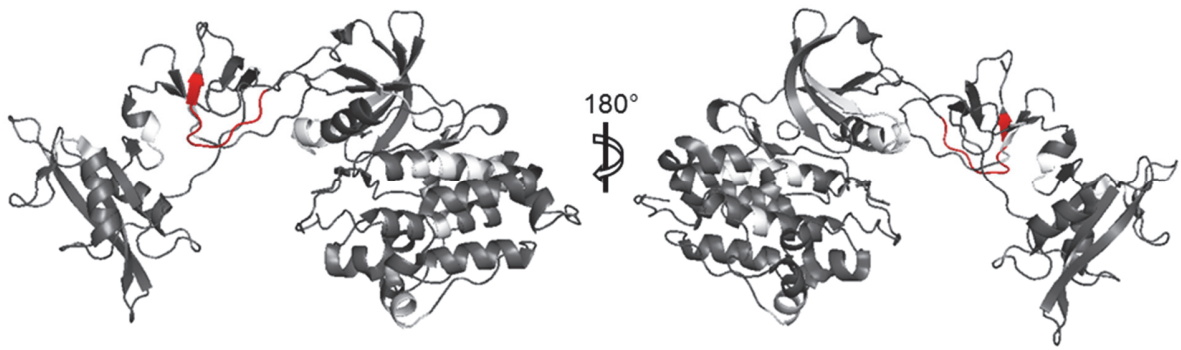

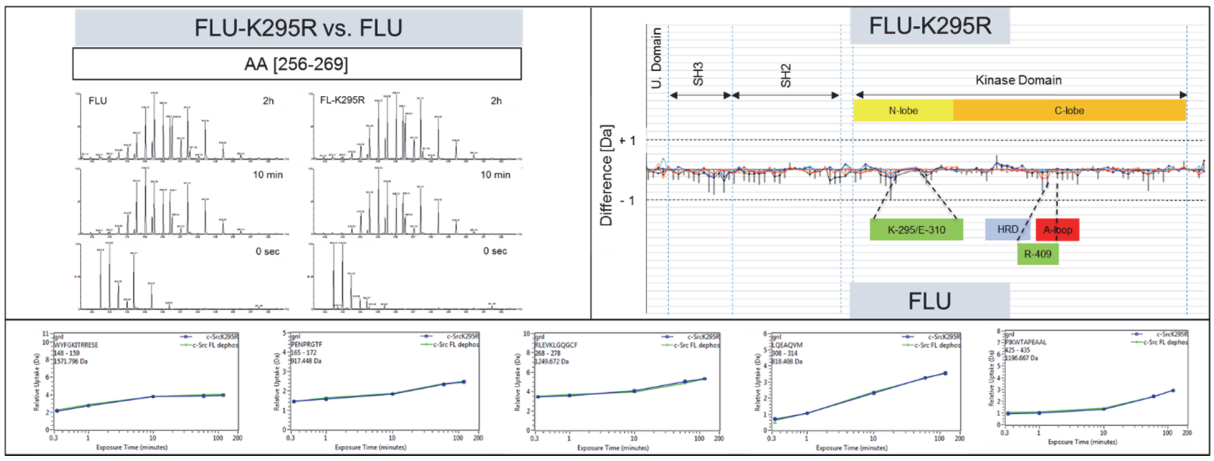

Fig. 87: H/DX-MS results for the comparison of exchange kinetics between FLU-K295R and FLU. On the top, the color-coded structure is shown. Red indicates more uptake of the second-named in comparison to the first-named state. Regions showing no difference are marked in grey and not determined regions are shown in white. The middle panel shows the exemplary raw spectra acquired after 0 sec, 10 min and 120 min deuterium incubation of the peptide AA [256-269] of both states (left). The sum of differences plot is shown for the FLU-K295R and FLU state in the middle panel on the right. Colored lines describe mass differences at each labeling time-point whereas the grey bars represent the sum of differences over all investigated labeling time-points. Exemplary uptake plots of the two different states are displayed on the bottom. The FLU-K295R state is illustrated in blue and the FLU state in green.

In line with the MD results, it was found that the presence of the regulatory domains led to stabilization of the KD by H/DX-MS. This was verified by comparing the FLP and the KDP construct (Fig. 88). Upon deletion of the regulatory domains in KDP, the N-lobe of the kinase domain exchanged more protons with the solvent. Since our thermal transition experiments suggested no significant loss of folding stability in this construct (Fig. 83 B), this result suggests a loss of intramolecular interaction in this region.

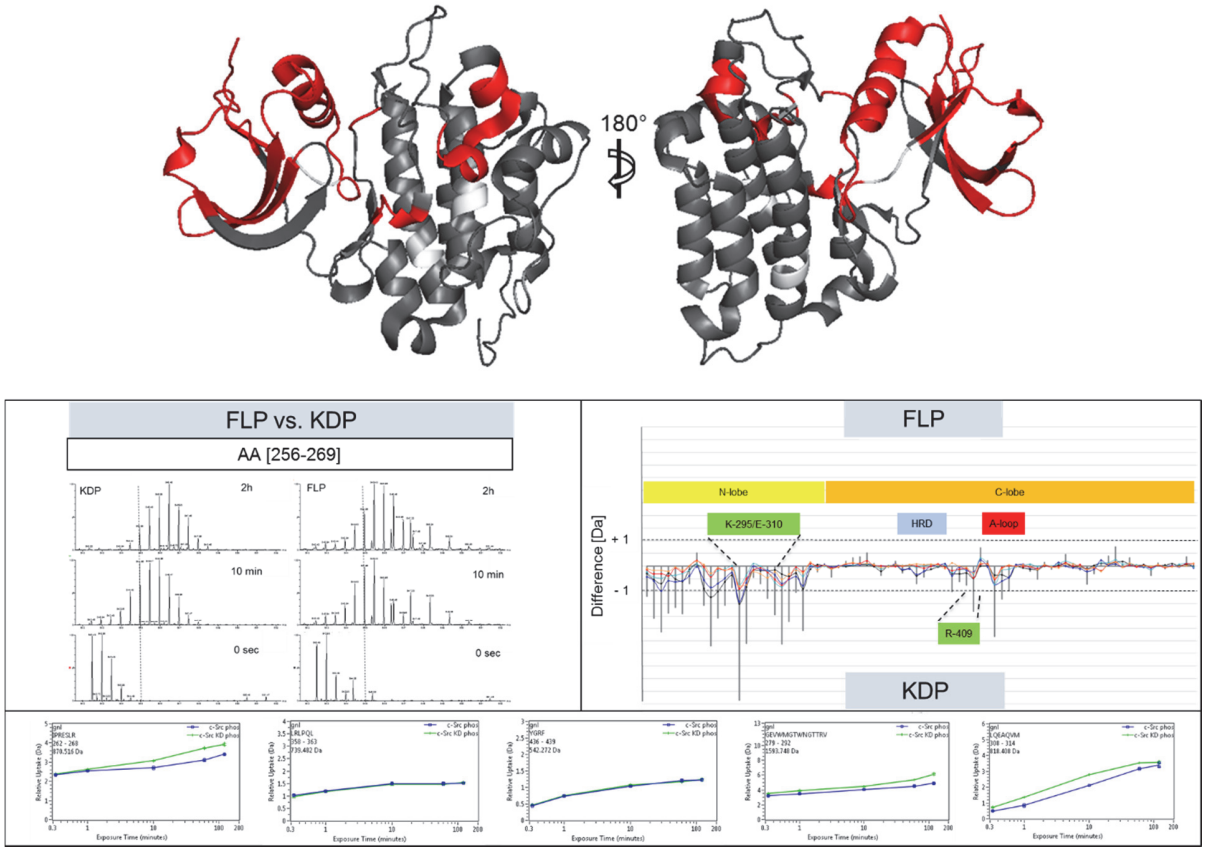

Fig. 88: H/DX-MS results for the comparison of exchange kinetics between FLP and KDP. On the top, the color-coded structure is shown. Red indicates more uptake of the second-named in comparison to the first-named state. Regions showing no difference are marked in grey and not determined regions are shown in white. The middle panel shows the exemplary raw spectra acquired after 0 sec, 10 min and 120 min deuterium incubation of the peptide AA [256-269] of both states (left). The sum of differences plot is shown for the FLP and KDP state in the middle panel on the right. Colored lines describe mass differences at each labeling time-point whereas the grey bars represent the sum of differences over all investigated labeling time-points. Exemplary uptake plots of the two different states are displayed on the bottom. The FLP state is illustrated in blue and the KDP state in green.

When comparing KDU vs. KDP by H/DX-MS, it was found that even in the absence of the regulatory domains proton exchange, although rather restricted to the active site, is strongly decreased when Y416 is phosphorylated (Fig. 89). This observation strengthened the results revealed by MD, which suggested decreased movement of the HRD and KER-motifs as well as decreased solvent accessible areas in the KDP when compared to the KDU construct (Fig. 80).

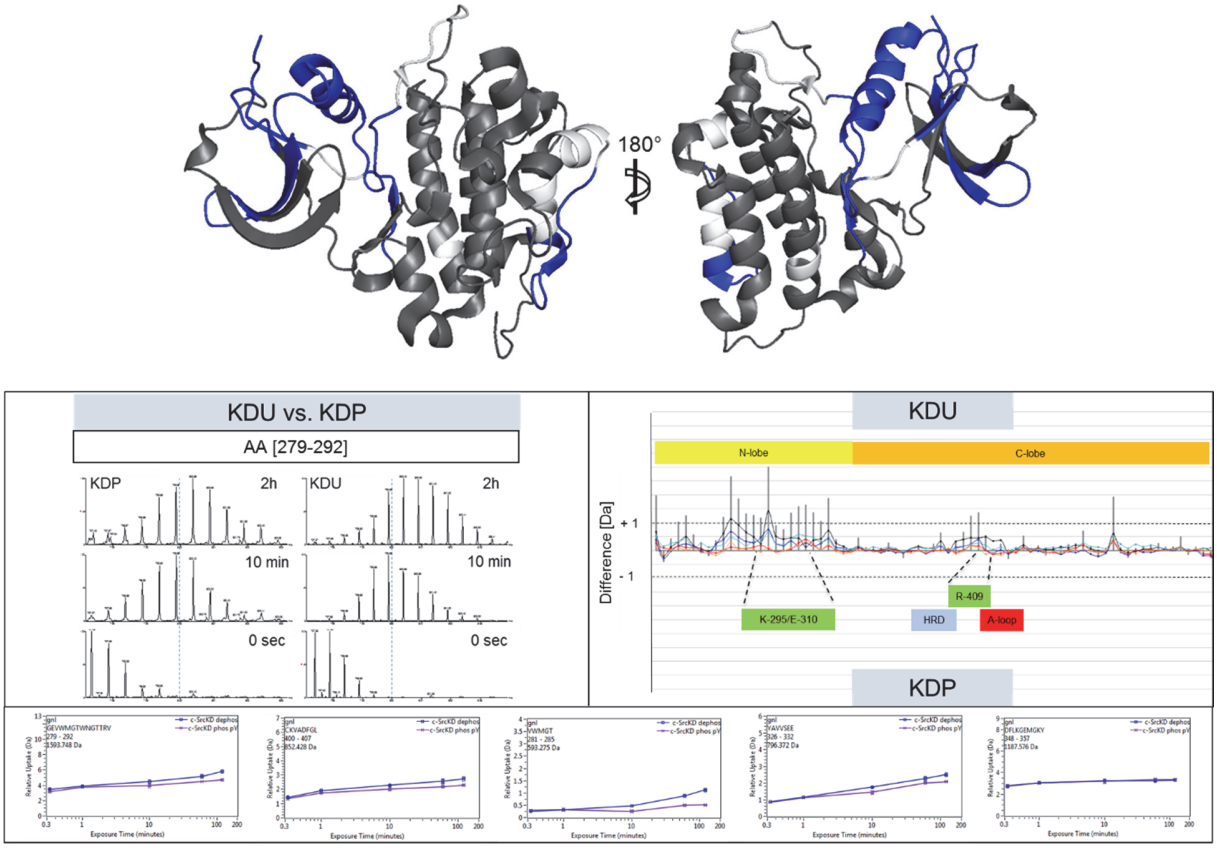

Fig. 89: H/DX-MS results for the comparison of exchange kinetics between KDU and KDP. On the top, the color-coded structure is shown. Red indicates more uptake of the second-named in comparison to the first-named state. Regions showing no difference are marked in grey and not determined regions are shown in white. The middle panel shows the exemplary raw spectra acquired after 0 sec, 10 min and 120 min deuterium incubation of the peptide AA [279-292] of both states (left). The sum of differences plot is shown for the KDU and KDP state in the middle panel on the right. Colored lines describe mass differences at each labeling time-point whereas the grey bars represent the sum of differences over all investigated labeling time-points. Exemplary uptake plots of the two different states are displayed on the bottom. The KDU state is illustrated in blue and the KDP state in violet.

To complete the picture on phosphorylation-dependent structural rearrangements of c-Src and to get an idea about the extent of these H/DX-MS effects, additionally, the FLU state was compared with the well described C-terminally phosphorylated FLU-pY527 state in a head-to-head H/DX-MS analysis. Prior to H/DX-MS analysis, full pY527 phosphorylation by CSK was confirmed by MS/MS. The fragments obtained from precursor AA [520-533] in the phosphorylated [M = 1690.71 Da] and the unphosphorylated [M = 1610.74 Da] state are shown in Figure 90.

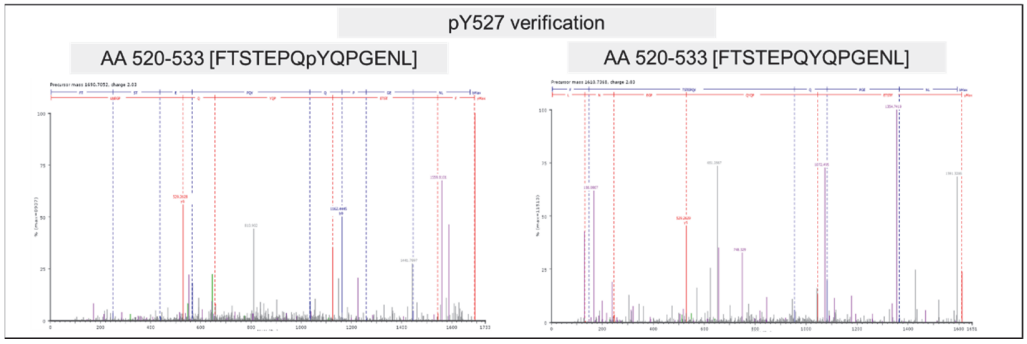

Fig. 90: Annotated MS/MS spectra of the phosphorylated and unphosphorylated peptide AA [520-533] obtained by protease digestion. MS/MS spectra resulted from fragmentation of the precursor AA [520-533] in the phosphorylated version (M = 1690.71 Da; left) and the unphosphorylated peptide (M = 1610.74 Da, right). The color code illustrates the b- and y-series in blue and red, respectively.

Very unexpectedly, only found minor alterations in the H/D exchange were revealed between these two states (Fig. 91). Some regions showed increased H/D exchange in the pY527 state, especially in the C-terminal and in the middle parts of the kinase domain and to some extent in the SH2- and SH3-domains. Furthermore, regions with less exchange were found that could be parts of described intramolecular interdomain interactions in the pY527 state. Decreased H/D exchange was mainly revealed for the SH2- and SH3-domains, which are thought to bind to the kinase linker and to the pY527 in the C-terminus, respectively. For technical reasons the phosphorylated C-terminus itself could not be resolved by H/DX-MS. Most notably, the magnitude of all these changes was on a much lower level as compared to the analysis of FLU vs. FLP (Fig. 85). This finding illustrates how the tertiary structure of a protein can dramatically change even without strong alterations of the H/D exchange profile. In addition, this observation suggests that the changes in the kinase dynamics upon Y416 phosphorylation on the other hand may be of considerable importance for the structure and function of c-Src.

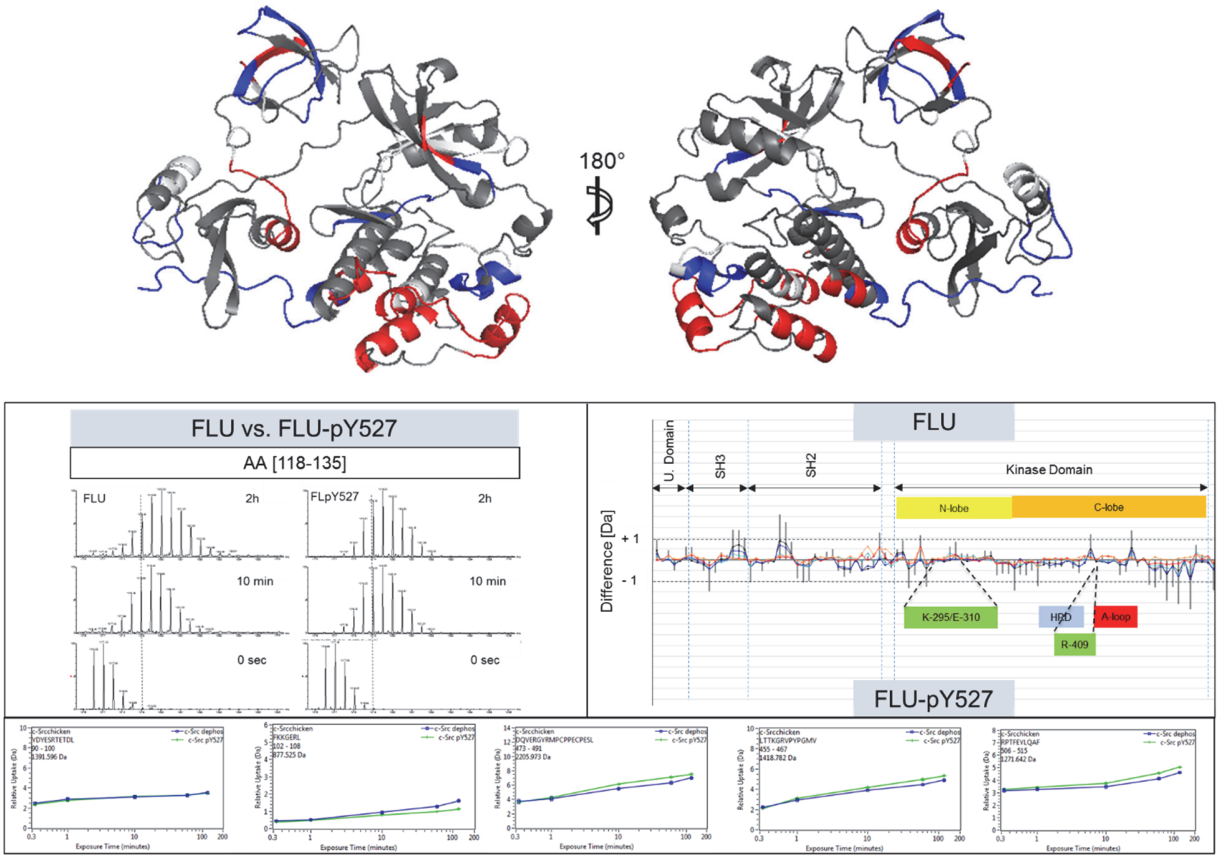

Fig. 91: H/DX-MS results for the comparison of exchange kinetics between FLU and FLU-pY527. On the top, the color-coded structure is shown (repressed form of c-Src; PDB: 2src). Red indicates more uptake of the second-named in comparison to the first-named state. Regions showing no difference are marked in grey and not determined regions are shown in white. The middle panel shows the exemplary raw spectra acquired after 0 sec, 10 min and 120 min deuterium incubation of the peptide AA [118-135] of both states (left). The sum of differences plot is shown for the FLU and FLU-pY527 state in the middle panel on the right. Colored lines describe mass differences at each labeling time-point whereas the grey bars represent the sum of differences over all investigated labeling time-points. Exemplary uptake plots of the two different states are displayed on the bottom. The FLU state is illustrated in blue and the FLU-pY527 state in green.

5. 2. 5. ATP differently affects the unphosphorylated and the pY416 state.

The MD simulations also suggested that ATP binding is important to open up the inactive conformation in the FLU state and enable the kinase to transition towards a phosphorylation competent state (Fig. 78). To verify these suggestions the influence of nucleotide binding to the unphosphorylated state (FLU) was examined by H/DX-MS. For

this, FLU was compared head-to-head to FLU in the presence of the non-hydrolyzable ATP analog AMP-PNP. The analysis revealed that the presence of nucleotide results in a decrease of H/D exchange kinetics of in the active site located N-lobe of the Src KD (Fig. 92).

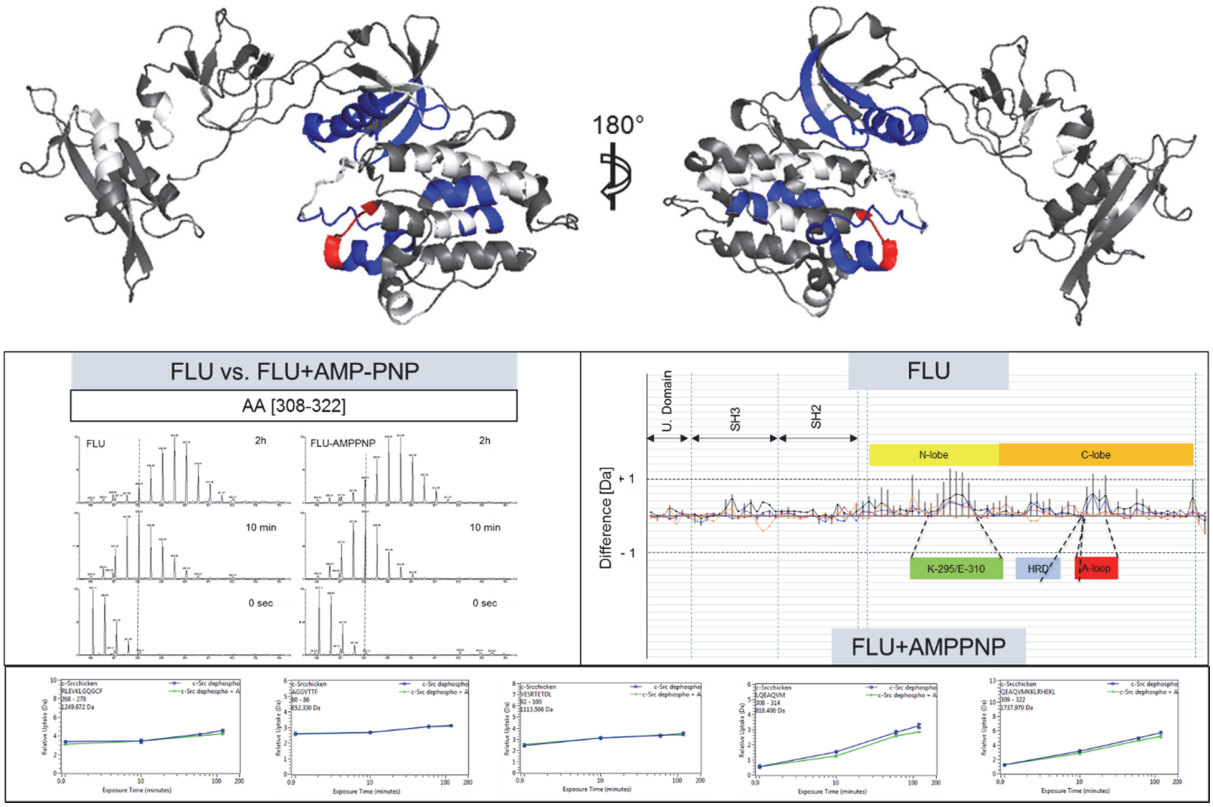

Fig. 92: H/DX-MS results for the comparison of exchange kinetics between FLU and FLU+AMP-PNP. On the top, the color-coded structure is shown. Red indicates more uptake of the second-named in comparison to the first-named state. Regions showing no difference are marked in grey and not determined regions are shown in white. The middle panel shows the exemplary raw spectra acquired after 0 sec, 10 min and 120 min deuterium incubation of the peptide AA [308-322] of both states (left). The sum of differences plot is shown for the FLU and FLU+AMP-PNP state in the middle panel on the right. Colored lines describe mass differences at each labeling time-point whereas the grey bars represent the sum of differences over all investigated labeling time-points. Exemplary uptake plots of the two different states are displayed on the bottom. The FLU state is illustrated in blue and the FLU+AMP-PNP state in green.

This finding supports the notion that strong binding of a nucleotide is important for triggering the conformational transition towards the active state. In stark contrast, the presence of AMP-PNP mainly increased the H/D exchange in the FLP construct (Fig. 93),

suggesting a strongly differing mechanism by which the kinase handles a nucleotide in the fully activated state.

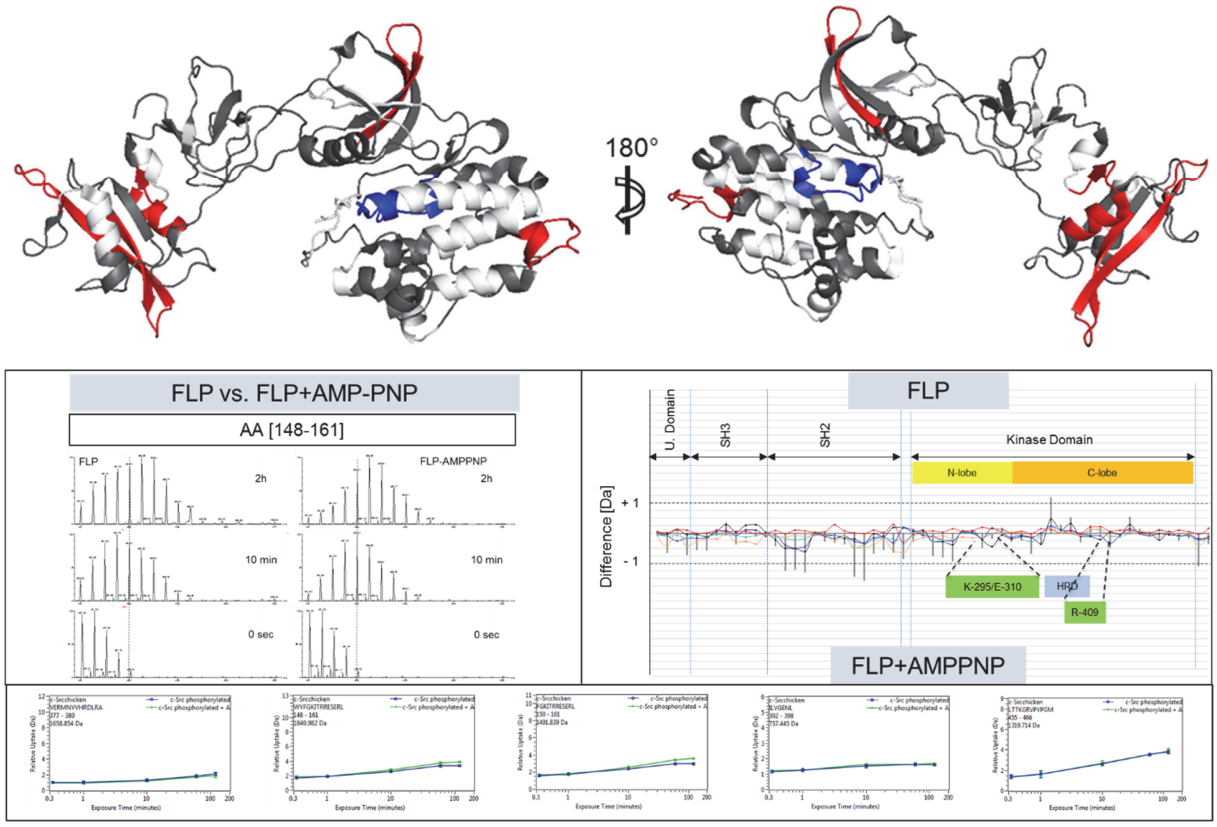

Fig. 93: H/DX-MS results for the comparison of exchange kinetics between FLP and FLU-pY527. On the top, the color-coded structure is shown. Red indicates more uptake of the second-named in comparison to the first-named state. Regions showing no difference are marked in grey and not determined regions are shown in white. The middle panel shows the exemplary raw spectra acquired after 0 sec, 10 min and 120 min deuterium incubation of the peptide AA [148-161] of both states (left). The sum of differences plot is shown for the FLP and FLP+AMP-PNP state in the middle panel on the right. Colored lines describe mass differences at each labeling time-point whereas the grey bars represent the sum of differences over all investigated labeling time-points. Exemplary uptake plots of the two different states are displayed on the bottom. The FLP state is illustrated in blue and the FLP+AMP-PNP state in green.

To get more insight into this phenomenon, the structures of FLU and FLP in the ATP bound state at the final stage of the MD simulations were analyzed (Fig. 94).

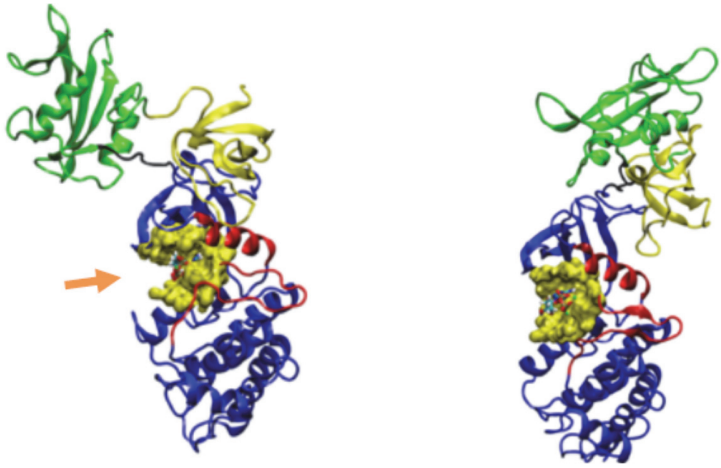

Fig. 94: The influence of nucleotide binding to different c-Src states. Structure of FLU/ATP (left) and FLP/ATP (right) at the final stage of MD simulations. The ATP binding cavity is shown as yellow surface marked by an arrow. The coloring from N- to C-terminus: SH3-domain in yellow, SH2-domain in green, linker and kinase domain in blue. Important elements involved in kinase activation are depicted in red: Y416, A-loop, KER-residues and HRD-motif.

Interestingly, great differences in the shape and size of the ATP binding cavity were determined. The binding site in FLP is more open than in FLU, suggesting that it is more available for ATP binding. This remarkable conformational shift upon Y416 phosphorylation in the FLP construct correlates with the differences observed in H/D exchange and might suggest a mechanism to explain the differences observed in H/D exchange.

5. 3. Discussion

The investigations show that autophosphorylation of c-Src kinase at Y416 leads to a 4-fold increase in kinase activity and a 2-fold lower K_M for ATP. In order to understand the underlying principles of this activation, MD simulations were performed in combination with bioanalytical experiments and H/DX-MS of the full-length and the kinase domain phosphorylation-variants.

This combinatorial approach revealed that in the activated FLP state the N-terminal domains show increased exchange, whereas the kinase domain gains rigidity. All previously identified activation elements show a decrease in H/D exchange. This holds true for (1) the activation loop (413-419), (2) the key active-center KER-residues (K295, E310 and R409), (3) the HRD motif (H384, R385, D386), which is thought to stabilize the active state of the kinase and (4) the hydrophobic spine (H384, F405, M314, L325), which retains the active conformation. These findings are supported by MD simulations, in which the HRD motif and the active site region including the KER-residues were found to decrease their solvent accessible surface area upon Y416-phosphorylation. In line with these results, previous studies have shown that H/D exchange of the HRD motif and the A-loop is increased upon binding of a kinase inhibitor (Tsutsui *et al*., 2016). CD experiments suggested that a structural loss in the regulatory domains is compensated by a structural gain in the kinase domain in the full-length constructs. An observed loss of folding cooperativity in the KDU construct further indicates that the regulatory domains are important for structural integrity of the KD. By testing the FLU vs. the KDU construct by H/DX-MS, it was shown that the presence of the regulatory domains in full-length c-Src, indeed, stabilizes intramolecular interactions within the kinase N-lobe. This finding supports previous studies suggesting that the regulatory domains affect the stability of the KD N-lobe (Breitenlechner *et al*., 2005, Fajer *et al*., 2016). Interestingly, Y416-phosphorylation in KDP leads to regain of integrity compared to KDU in the CD experiment pointing to a conformational shift towards a stabilized state of the kinase domain upon phosphorylation. This is in line with the H/DX-MS results with decreased

deuterium uptake upon phosphorylation in the KD constructs. Additionally, the H/DX-MS findings correlate with the ANS binding results, as the regions exchanging more protons upon phosphorylation (mainly the Unique- and the SH3-domains), include numerous hydrophobic residues and hence their exposure could well explain the observed differences in surface hydrophobicity between full-length c-Src and its kinase domain. Again, here a compensating effect of the two parts of c-Src was suggested: a loss of accessible hydrophobicity in the KD seemed to be compensated by a gain of hydrophobicity in the regulatory domains as phosphorylation of the KD leads to shielding of hydrophobic patches and to lower binding of ANS to the KDP construct when compared to KDU. In addition, decreased ANS binding to KDP could be interpreted to reflect at least a partial closure of a previously described allosteric ANS binding pocket in the KD of c-Src (Shukla *et al*., 2014. Peng *et al*., 2016). These results are further supported by tryptophan quenching experiments, showing that phosphorylation leads to decreased accessibility of tryptophan residues mainly in the kinase domain of c-Src. Furthermore, the increased H/D exchange in the regulatory domains correlates with the observed increased aggregation propensity of the FLU and the FLP construct in comparison to KDU and KDP. It seems that these domains represent the origin of the aggregation propensity and phosphorylation at Y416 leads to increased aggregation triggered by unblocking of further aggregation prone regions in the N-terminus.

Investigations on how binding of a nucleotide would influence the H/D exchange rates on the FLU and the FLP states, it was found stunning differences in how the two states of c-Src handle the ligand. AMP-PNP binding led to a decrease of deuterium uptake in the active center region of FLU. This supports the MD simulations performed on ATP bound FL states suggesting that binding of ATP enables the transition from the inactive to the active conformation by lowering the energy barrier between the two different states. In contrast, when FLP was analyzed in the presence of the nucleotide, increased exchange was found in the SH2 and parts of the KD N-lobe. Generally, changes in the H/D exchange profile of the FLP-KD were much less severe compared to the KD of FLU. This suggests a strongly altered behavior of the kinase during nucleotide binding in the unphosphorylated

compared to the phosphorylated state. A closer look at the endpoints of the MD simulation revealed that the binding site in FLP is more open than in FLU, suggesting that it is more readily available for ATP binding. Together with the results on H/D exchange in this region, this indicates that the active center tightly closes itself upon binding to ATP in the FLU state, which might enable the kinase to transition towards the phosphorylation competent state. In contrast, in the FLP state the ATP binding site gains a more open shape whose H/D exchange is not strongly altered in the presence of nucleotide. A decreased K_M of this construct in the kinase reaction indicates a higher affinity of this site for ATP. In FLP/ATP, the E310-K295 ion pair showed increased flickering compared to the FLU/ATP state. This may lead to a smaller repulsion of ATP by the presence of E310 near its binding site, which might explain the lower K_M for ATP in this state. In turn, ATP binding would concomitantly lead to E310 displacement and further destabilizes the E310-K295 ion pair. Previous studies suggested that Y416-phosphorylation may serve as a binding platform for the substrate, which may be stabilized by interaction of pY416 with the neighboring arginine R409 similar to a mechanism suggested for Lck (Cowan-Jacob, 2005, Yamaguchi *et al*., 1996). MD simulations indeed indicate an extended conformation of the phosphorylated A-loop region. In addition, the A-loop sampled more folded states in the FLP simulations, which were stabilized by interaction with the neighboring arginines R385, R409, and R419 in the FLP state. The H/DX-MS analysis consistently shows less H/D exchange in this region supporting these findings and underlining the importance of stabilizing interactions in the activated FLP state.

To explain the large shifts in the conformational dynamics of the kinase, the interaction of the central charged residues in different MD simulation states was analyzed in more detail. C-Src contains a remarkable number of charged residues (57 Glu and Asp residues and 53 Arg and Lys residues), which are likely to be electrostatically strongly coupled. The interaction of these charged clusters could easily be perturbed by the Y416-phosphorylation. In addition, the αC-helix of c-Src has a large dipole moment that is formed by E305/E310 and K315/K316/R318 at the two ends of the helix. This large dipole moment can be important in mediating long-range coupling effects in c-Src and is likely to

be sensitive to local charge perturbations, e.g. due to phosphorylation of Y416. It was found that c-Src mutants with a perturbed αC-helix dipole moment may affect the kinase activity (Boczek *et al.*, 2015, Luo *et al.*, 2017). In the MD simulations of the FLU and FLU/ATP states, K315/K316 form ion-pairs with D258 in the linker region, this interaction was found to be absent in the FLP state as the SH2-domain seems to move further away from the kinase domain. Interestingly, D258 also coordinates to R95 of the SH2-domain. In previous studies with R95 mutated to a tryptophan, spontaneous flickering between the active and inactive states was observed, suggesting that R95 is a key residue that may be involved in the kinase activation process (Boczek *et al.*, 2015).

Generally, combined electrostatic and conformational changes can trigger long-range coupling effects, as observed in the case of c-Src between the regulatory domains and the kinase domain. Similar long-range electrostatically-driven conformational coupling effects have recently been observed in other systems (Kaila *et al.,* 2014, Sharma et al., in press). The combined data from bioanalytical experiments and molecular simulations thus suggest that long-range a*ction-at-a-distance* effects might play a central role in the c-Src activation process.

Taken together, this study investigates previously hard-to-observe dynamic processes during the final activation step in c-Src. The combination of biochemical techniques, H/DX-MS and MD simulations applied here reveals how the dynamic structural landscape of the prototypical model kinase c-Src is shaped by the binding of nucleotide and Y416-phosphorylation. Kinases are an explicitly dynamic group of proteins whose activity is controlled by sophisticated conformational rearrangements and therefore are exceedingly well suited for the application of such analyses. Nonetheless, this study emphasizes the general power of this technical combination to understand dynamic conformational events in great detail.

6 Summary

In the first part of this work, the impact of disulfide scrambling within an IgG2 drug molecule was investigated regarding to the structure-function relationship of the observed disulfide isoforms. These isoforms could be isolated from the drug product in very high purities using a combination of redox enrichment and cation exchange chromatography. The isoforms were verified by mass spectrometric methods and subsequently analyzed with regard to their structure using a combinatorial approach consisting of AUC, DSF, SAXS, H/DX-MS and homology modeling. Since these data sets revealed major differences with regard to their global structure, the isoforms were analyzed with regard to their biological activity and IgG2/target complex formation. It was shown that due to the different structures and level of rigidity of the isoforms, these form differently stable complex geometries which had subsequently impact on the bioactivity as shown in potency bioassays. These data provide a detailed picture on the impact of complex formation and thus isoform ratio in the drug product - even while circulating in the patient´s blood - and the biological activity of the IgG2 product.

In the second part of this work, the dimeric structures as well as the dimerization pathways of an IgG1 drug product were investigated. After isolation of the major dimeric variants out of the drug product these were analyzed by a combination AUC, SAXS, H/DX-MS and homology modeling which revealed four major dimeric structures. As the main aggregation triggering factor, the isomerization at a specific position in the CDR2 was identified by MS/MS. By using a combination of H/DX-MS and MD simulation, this transition was shown to trigger structural alterations in the Fab domain leading to exposure of aggregation prone regions close to the isomerization position. The combination of various low- and high resolution techniques showed to be a powerful approach to unravel the complexity of aggregation and dimeric IgG1 structures as well as to identify the deep impact of a post-translational modification formed during storage on dimer formation.

In the third part of this work, a comprehensive investigation of the structural transitions within c-Src upon autophosphorylation on Tyr416 was performed by a combined approach using molecular dynamics simulations, various biophysical techniques and H/DX-MS. The combined data-sets revealed that Tyr416-phosphorylation leads to a significant increase in kinase activity and ATP-affinity. It was suggested that the activation process is coupled to large structural rearrangements. The kinase domain transitions to a more compact state, whereas the regulatory domains partly open up. MD-simulations of full length c-Src in the microsecond timescale revealed that long-range a*ction-at-a-distance* effects play a central role in the c-Src activation process and the binding of ATP facilitates this process which was in-line with observations done by H/DX-MS. This case study demonstrates the general power of the combination of bioanalytics, H/DX-MS and MD simulations to reveal the dynamics of protein conformational states.

7 Abbreviations

Å	Ångstrom
AA	Amino acid
ACN	Acetonitrile
ADCC	Antibody-dependent cellular cytotoxicity
A-loop	Activation loop
AMP-PNP	Non-hydrolyzable ATP analogon
ANS	1-Anilino-8-Naphthalene Sulfonate
AP	Aggregation peak
ATP	Adenosine tri-phosphate
AUC	Analytical ultracentrifugation
CD	Circular dichroism
CDC	Complement dependent cytotoxicity
CDR	Complement determining region
CH	Constant region heavy chain
CL	Constant region light chain
CRM	Charge residue model
CSK	C-terminal Src kinase
c-Src	Cellular Src kinase
D	Dimer
d	Day
Da	Dalton
D_{max}	Maximum distance
DP	Degradation peak
DSF	Differential scanning fluorimetry
DTT	Dithiothreitol

E_a	Activation energy
EDTA	Ethylenediamine-tetraecetic acid
EIC	Extracted io chromatogram
ER	Endoplasmatic reticulum
ESI	Electrospray ionization
ETD	Electron transfer dissociation
EX	Exchange model
FA	Formic acid
Fab	Fragment antigen binding
Fc	Fragment crystalizable
FcγR	Fc gamma receptor
FcRn	Neonatal Fc receptor
FL	Full-length
FLP	Phosphorylated full-length
FLU	Unphosphorylated full-length
G	Gibbs energy
Gua-HCl	Guanidinium hydrochloride
HC	Heavy chain
HCD	High collision dissociation
H/DX	Hydrogen/deuterium exchange
IAA	Iodactamide
IEM	Ion evaporation model
IgG	Immunoglobulin
IM	Ion-mobility
Iso	Isomerized
K	Equlibrium constant
KD	Kinase domain
kDa	Kilo dalton

KDP	Phosphorylated kinase domain
KDU	Unphosphorylated kinase domain
Kex	Exchange rate constant
kV	Kilo volt
λ	Wavelength
L	Light
LC	Light chain
Lys-C	Lysyl-endopeptidase
M	Monomer
mA	Milli ampere
mAU	Milli absorption unit
MALDI	Matrix-assisted laser desorption ionizatio
MD	Molecular dynamics
mM	Milli molar
μM	Micro molar
MP	Main peak
MS	Mass spectrometry
nm	Nano meter
ox	Oxidized
p	Phosphorylated
PAGE	Polyacrylamide gel electrophoresis
PBS	Phosphate buffered saline
PDB	Protein data bank
Pf	Protection factor
PDI	Protein disulfide isomerase
PMF	Potential mean force
R	Avogadro constant
R_G	Radius of gyration

Rpm	Rounds per minute
RT	Room temperature
SAXS	Small-angle X-ray scattering
SCX	Strong cation exchange
SEC	Size-exclusion chromatography
SH	Sequence homology domain
SoMo	Solution modeler
T	Temperature
TCEP	Tris(2-carboxyethyl)phosphin
TFA	Trifluoracetic acid
ToF	Time of flight
T_M	Melting temperature
TNF	Tumor necrosis factor
U	Voltage
V	Volt
V_H	Variable heavy chain
V_L	Variable light chain
w	Week
WCX	Weak cation exchange
WSTD	Working standard
UV	Ultra violet
v/v	Volume per volume

8 References

Abés, R. & Teillaud, J.-L. (2010). Impact of Glycosylation on Effector Functions of Therapeutic IgG. Pharmaceuticals, 3, 146-157.

Allen, M. J., Guo, A., Martinez, T., Han, M., Flynn, G. C., Wypych, J., Liu, Y. D., Shen, W. D., Dillon, T. M., Vezina, C. & Balland, A. (2009). Interchain Disulfide Bonding in Human IgG2 Antibodies Probed by Site-Directed Mutagenesis. Biochemistry, 48, 3755-3766.

Andya, J. D., Maa, Y. F., Costantino, H. R., Nguyen, P.-A., Dasovich, N., Sweeney, T. D., Hsu, C. C. & Shire, S. J. (1999). The effect of formulation excipients on protein stability and aerosol performance of spray-dried powders of a recombinant humanized anti-IgE monoclonal antibody. Pharm. Res., 16, 350-358.

Anfinsen, C. B. (1973). Principles that Govern the Folding of Protein Chains. Science, 181, 223-230.

Arnold, J. N., Wormald, M. R., Sim, R. B., Rudd, P. M. & Dwek, R. A. (2007). The Impact of Glycosylation on the Biological Function and Structure of Human Immunoglobulins. Annu. Rev. Immunol., 25, 21-50.

Arthur, K. K., Gabrielson, J. P., Hawkins, N., Anafi, D., Wypych, J., Nagi, A., Sullivan, J. K. & Bondarenko, P. V. (2012). In Vitro Stoichiometry of Complexes between the Soluble RANK Ligand and the Monoclonal Antibody Denosumab. Biochemistry, 51, 795−806.

Artimo, P., Jonnalagedda, M., Arnold, K., Baratin, D., Csardi, G., de Castro, E., Duvaud, S., Flegel, V., Fortier, A., Gasteiger, E., Grosdidier, A., Hernandez, C., Ioannidis, V., Kuznetsov, D., Liechti, R., Moretti, S., Mostaguir, K., Redaschi, N., Rossier, G., Xenarios, I. & Stockinger, H. (2012). ExPASy: SIB bioinformatics resource portal, Nucleic Acids Res., 40, 597-603.

Aswad, D.W., Paranandi, M.V. & Schurter, B. T. (2000). Isoaspartate in peptides and proteins: formation, significance, and analysis. J. Pharm. Biomed. Anal., 21, 1129-1136.

Ayoub, D., Jabs, W., Resemann, A., Evers, W., Evans, C., Main, L., Baessmann, C., Wagner-Rousset, E., Suckau, D. & Beck, A. (2013). Correct primary structure assessment

and extensive glyco-profiling of cetuximab by a combination of intact, middle-up, middle-down and bottom-up ESI and MALDI mass spectrometry techniques, mAbs, 5, 699–710.

Bai, Y., Milne, J. S., Mayne, L. & Englander, S. W. (1993). Primary Structure Effects on Peptide Group Hydrogen Exchange. Proteins, 17, 75-86.

Banerjee, S. & Mazumdar, S. (2011). Electrospray Ionization Mass Spectrometry: A Technique to Access the Information beyond the Molecular Weight of the Analyte, Intern. J. Anal. Chem., 2012, 1-40.

Bergman, L.W. & Kuehl, W. M. (1979). Formation of an intrachain disulfide bond on nascent immunoglobulin light chains. J. Biol. Chem., 254, 8869-8876.

Berkowitz, S. A., Engen, J. R., Mazzeo, J. R. & Jones, G. B. (2012). Analytical tools for characterizing biopharmaceuticals and the implications for biosimilars. Nature Rev., 11, 527-540.

Bieberich, E. (2014). Synthesis, processing, and function of N-glycans in N-glycoproteins. Adv. Neurobiol., 9, 47–70.

Bischoff, R. & Kolbe, H. V. (1994). Deamidation of asparagine and glutamine residues in proteins and peptides: structural determinants and analytical methodology. J. Chromatogr. B. Biomed. Appl., 662, 261-278.

Bobst, C. E., Abzalimov, R. R., Houde, D., Kloczewiak, M., Mhatre, R., Berkowitz, S. A. & Kaltashov, I. A. (2008). Detection and characterization of altered conformations of protein pharmaceuticals using complementary mass spectrometry-based approaches. Anal. Chem., 80, 7473–7481.

Boczek, E. E, Reefschläger L. G., Dehling, M., Struller, T. J., Häusler, E., Seidl, A., Kaila, V.R. & Buchner, J. (2015). Conformational processing of oncogenic v-Src kinase by the molecular chaperone Hsp90. Proc. Natl. Acad. Sci. USA., 112, 3189-3198.

Boyle, A. & L. & Woolfson, D. N. (2011). De novo designed peptides for biological applications. Chem. Soc. Rev., 40, 4295–4306.

Brandt, J., P., Patapoff, T. W. & Aragon, S. R. (2010). Construction, MD Simulation, and Hydrodynamic Validation of an All-Atom Model of a Monoclonal IgG Antibody. Biophys. Journ. 99, 905–913.

Brautigam, C. (2015). Calculations and Publication-Quality Illustrations for Analytical Ultracentrifugation Data. Methods Enzymol., 562, 109-133.

Breitenlechner, C. B., Kairies, N.A., Honold, K., Scheiblich, S., Koll, H., Greiter, E., Koch, S., Schäfer, W., Huber, R. & Engh, R.A. (2005). Crystal structures of active SRC kinase domain complexes. J. Mol. Biol., 353(2), 222-231.

Brookes, E., Demeler, B. & Rocco, M. (2010). The implementation of SOMO (SOlution MOdeller) in the UltraScan analytical ultracentrifugation data analysis suite: enhanced capabilities allow the reliable hydrodynamic modeling of virtually any kind of biomacromolecule. Eur. Biophys. J, 39, 423-435.

Brooks, C., Karplus, M. & Pettitt, B. (1990). Proteins: A Theoretical Perspective of Dynamics, Structure, and Thermodynamics.

Broome, M.A. & Hunter T. (1996). Requirement for c-Src catalytic activity and the SH3 domain in platelet-derived growth factor BB and epidermal growth factor mitogenic signaling. J. Biol. Chem., 271, 16798-806.

Brown, M.T. & Cooper, J.A. (1996). Regulation, substrates and functions of src. Biochim. Biophys. Acta, 1287, 121-149.

Buchner, G. S., Murphy, R. D., Buchete, N.-V. & Kubelka, J. (2011). Dynamics of protein folding: Probing the kinetic network of folding–unfolding transitions with experiment and theory. Biochimica et Biophysica Acta, 1814, 1001–1020.

Burkitt, W. & O´Connor, G. (2008). Assessment of the repeatability and reproducibility of hydrogen/deuterium exchange mass spectrometry measurements. Rapid Commun. Mass Spectrom., 22, 3893-3901.

Burkitt, W., Domann, P. & O'Connor, G. (2010). Conformational changes in oxidatively stressed monoclonal antibodies studied by hydrogen exchange mass spectrometry. Protein Science. 19, 826-835.

Busenlehner, L. S. & Armstrong, N. R. (2005). Insights into enzyme structure and dynamics elucidated by amide H/D exchange mass spectrometry. Arch. Biochem. and Biophys., 433, 34-46.

Castellano, M., Sepulveda, J. M., Garcia-Escobar, I., Rodriguez-Antolin, A., Sundlöv, A. & Cortes-Funes, H. (2011). The Role of RANK-Ligand Inhibition in Cancer: The Story of Denosumab. Oncologist, 16, 136-145.

D.A. Case, D.S. Cerutti, T.E. Cheatham, III, T.A. Darden, R.E. Duke, T.J. Giese, H. Gohlke, A.W. Goetz, D. Greene, N. Homeyer, S. Izadi, A. Kovalenko, T.S. Lee, S. LeGrand, P. Li, C. Lin, J. Liu, T. Luchko, R. Luo, D. Mermelstein, K.M. Merz, G. Monard, H. Nguyen, I. Omelyan, A. Onufriev, F. Pan, R. Qi, D.R. Roe, A. Roitberg, C. Sagui, C.L. Simmerling, W.M. Botello-Smith, J. Swails, R.C. Walker, J. Wang, R.M. Wolf, X. Wu, L. Xiao, D.M. York and P.A. Kollman (2017), AMBER 2017, University of California, San Francisco.

Cech, N. B. & Enke, C. G. (2001). Practical implications of some recent studies in electrospray ionization fundamentals. Mass Spectrom. Rev., 20, 362–387.

Chadd, H. E. & Chamow, S. M. (2001). Therapeutic antibody expression technology. Curr. Opin. Biotechnol., 12, 188-194.

Chauhan, R. & Sood, N. (2016). Biopharmaceuticals: New yet Natural. British Biotech. Journal, 14, 1-19.

Chennamsetty, N., Voynov, V., Kayser, V., Helk, B. & Trout, B. L. (2010). Prediction of Aggregation Prone Regions of Therapeutic Proteins. J. Phys. Chem. B., 114, 6614–6624.

Cholewinski, M., Lückel, B. & Horn, H. (1996). Degradation pathways, analytical characterization and formulation strategies of a peptide and a protein. Calcitonine and human growth hormone in comparison. Pharm. Acta Helv., 71, 405-419.

Clark, P. L. (2004). Protein folding in the cell: reshaping the folding funnel. TRENDS in Biochemical Sciences, 29, 527-534.

Coon, J. J., Shabanowitz, J., Hunt, D. F. & Syka, F. E. (2005). Electron transfer dissociation of peptide anions. J. Am. Soc. Mass Spectrom., 16, 880-882.

Cooper, J.A., Gould, K.L., Cartwright, C.A. & Hunter T. (1986). Tyr527 is phosphorylated in pp60c-src: implications for regulation. Science, 231, 1431-1434.

Cooper, J.A. & MacAuley, A. (1988). Potential positive and negative autoregulation of p60c-src by intermolecular autophosphorylation. Proc. Natl. Acad. Sci. USA., 85, 4232–4236.

Courtois, F., Agrawal, N. J., Lauer, T. M. & Trout, B. L. (2016) Rational design of therapeutic mAbs against aggregation through protein engineering and incorporation of glycosylation motifs applied to bevacizumab, mAbs, 8, 99-112.

Cowan-Jacob, S.W., Fendrich, G., Manley, P.W., Jahnke, W., Fabbro, D., Liebetanz, J. & Meyer, T. (2005). The crystal structure of a c-Src complex in an active conformation suggests possible steps in c-Src activation. Structure, 13, 861-871.

Crisp, S. J., Kullmann, D. M. & Vincent, A. (2016). Autoimmune synaptopathies. Nature Reviews Neuroscience, 17, 103-117.

Daub, C. D. & Cann, N. M. (2011). How are completely desolvated ions produced in electrospray ionization: insights from molecular dynamics simulations. Anal. Chem., 83, 8372-8376.

De Groot, A.S. & Scott, D.W. (2007). Immunogenicity of protein therapeutics. Trends Immunol., 28, 482-490.

Deperalta, G., Alvarez, M., Bechtel, C., Dong, K., McDonald, R. & Ling, V. (2013). Structural analysis of a therapeutic monoclonal antibody dimer by hydroxyl radical footprinting. mAbs, 5, 86-101.

Desmyter, A., Transue, T.R., Ghahroudi, M.A., Thi, M.H., Poortmans, F., Hamers, R., Muyldermans, S. & Wyns, L. (1996). Crystal structure of a camel single-domain V_H antibody fragment in complex with lysozyme. Nat. Struct. Biol., 3, 803-811.

Diamantis, N. & Banerji, U. (2016). Antibody-drug conjugates—an emerging class of cancer treatment, Br. J. Cancer, 114(4), 362-367.

Dillon, T. M., Ricci, M. S., Vezina, C., Flynn, G. C., Liu, Y. D., Rehder, D. S., Plant, M., Henkle, B., Li, Y., Deechongkit, S., Varnum, B., Wypych, J., Balland, A. & Bondarenko, P. V. (2008). Structural and Functional Characterization of Disulfide Isoforms of the Human IgG2 Subclass. J. Biol. Chem., 283, 16206-16215.

Dill, K. A., Ozkan, S. B., Shell, M. S. & Weikl, T. R. (2008). The protein folding problem. Annu. Rev. Biophys., 37, 289-316.

Dingermann, T. (2008). Recombinant therapeutic proteins: production platforms and challenges. Biotechnol. J., 3, 90-97.

Dinner, A.R., Sali, A., Smith, L. J., Dobson, C. M. & Karplus, M. (2000). Understanding protein folding via free-energy surfaces from theory and experiment, Trends Biochem. Sci., 25, 331–339.

Djira, G. D. 2010. Relative Potency Estimation in Parallel-Line Assays – Method Comparison and Some Extensions, Commun. Statistics – Theory and Methods, 39(7), 1180-1189.

Dolhofer, R., Siess, E. A. & Wieland, O. H. (1985). Nonenzymatic glycation of immunoglobulins leads to an impairment of immunoractivity, Biol. Chem. Hoppe-Seyler, 366, 361–366.

Ecker, D. M., Jones, S. D. & Levine, H. L. (2015). The therapeutic monoclonal antibody market. mAbs, 7, 9-14.

Edelman, G. M., Cunningham, B. A., Gall, W. E., Gottlieb, P. D., Rutishauser, U. & Waxdal, M. J. (1969). The covalent structure of an entire gammaG immunoglobulin molecule. Proc. Natl. Acad. Sci. USA 63, 78–85.

Ellis, C., Moran, M., McCormick, F. & Pawson, T. (1990). Phosphorylation of GAP and GAP-associated proteins by transforming and mitogenic tyrosine kinases. Nature, 343(6256), 377-381.

Engh, R.A. & Bossemeyer, D. (2002). Structural aspects of protein kinase control-role of conformational flexibility. Pharmacol. Ther., 93(2-3), 99-111.

Englander, S. W. (2006). Hydrogen exchange and mass spectrometry: A historical perspective. J. Am. Soc. Mass Spectrom., 17, 1481-1489.

Englander, S. W. & Kallenbach, N. R. (1983). Hydrogen exchange and structural dynamics of proteins and nucleic acids. Q. Rev. Biophys., 16, 521-655.

Fajer, M., Meng, Y. & Roux B. (2017). The Activation of c-Src Tyrosine Kinase: Conformational Transition Pathway and Free Energy Landscape. J. Phys. Chem. B., 121, 3352-3363.

Fang, J., Richardson, J., Du, Z. & Zhang, Z. (2016). Effect of Fc-Glycan Structure on the Conformational Stability of IgG Revealed by Hydrogen/Deuterium Exchange and Limited Proteolysis. Biochemistry, 55, 860-868.

Favero-Retto, M.P., Palmieri, L.C., Souza, T.A., Almeida, F.C. & Lima, L.M. (2013). Structural meta-analysis of regular human insulin in pharmaceutical formulations. Eur. J. Pharm. Biopharm., 85, 1112-1121.

Feige, M. J., Hendershot, L. M. & Buchner, J. (2009). How antibodies fold. Trends in Biochem. Scien., 35, 189-198.

Fenn, J. B., Rosell, J. & Meng, C. K. (1997). In Electrospray Ionization, How Much Pull Does an Ion Need to Escape Its Droplet Prison. J. Am. Soc. Mass Spectrom., 8, 1147-1157.

Feige, M. J., Nath, S., Catharino, S. R., Weinfurther, D., Steinbacher, S. & Buchner, J.(2009). Structure of the murine unglycosylated IgG1 Fc fragment. J. Mol. Biol., 21, 599-608.

Fincham, V.J, Wyke, J.A & Frame, M.C. (1995). v-Src-induced degradation of focal adhesion kinase during morphological transformation of chicken embryo fibroblasts. Oncogene, 10, 2247-52. Erratum in: Oncogene 1995, 11(10), 2185.

Franey, H., Brych, S. R., Kolvenbach, C. G. & Rajan, R. S. 2010. Increased aggregation propensity of IgG2 subclass over IgG1: Role of conformational changes and covalent character in isolated aggregates. Protein Science, 19, 1601-1615.

Gaussian 09, Revision A.1, Frisch, M. J.; Trucks, G. W.; Schlegel, H. B.; Scuseria, G. E.; Robb, M. A.; Cheeseman, J. R.; Scalmani, G.; Barone, V.; Mennucci, B.; Petersson, G. A.; Nakatsuji, H.; Caricato, M.; Li, X.; Hratchian, H. P.; Izmaylov, A. F.; Bloino, J.; Zheng, G.; Sonnenberg, J. L.; Hada, M.; Ehara, M.; Toyota, K.; Fukuda, R.; Hasegawa, J.; Ishida, M.; Nakajima, T.; Honda, Y.; Kitao, O.; Nakai, H.; Vreven, T.; Montgomery, Jr., J. A.; Peralta, J. E.; Ogliaro, F.; Bearpark, M.; Heyd, J. J.; Brothers, E.; Kudin, K. N.; Staroverov, V. N.; Kobayashi, R.; Normand, J.; Raghavachari, K.; Rendell, A.; Burant, J. C.; Iyengar, S. S.; Tomasi, J.; Cossi, M.; Rega, N.; Millam, J. M.; Klene, M.; Knox, J. E.; Cross, J. B.; Bakken, V.; Adamo, C.; Jaramillo, J.; Gomperts, R.; Stratmann, R. E.; Yazyev, O.; Austin, A. J.; Cammi, R.; Pomelli, C.; Ochterski, J. W.; Martin, R. L.; Morokuma, K.; Zakrzewski, V. G.; Voth, G. A.; Salvador, P.; Dannenberg, J. J.; Dapprich, S.; Daniels, A. D.; Farkas, Ö.; Foresman, J. B.; Ortiz, J. V.; Cioslowski, J.; Fox, D. J. Gaussian, Inc., Wallingford CT, 2009.

Geiger, T. & Clarke, S. (1987). Deamidation, isomerization, and racemization at asparaginyl and aspartyl residues in peptides. Succinimide-linked reactions that contribute to protein degradation. J. Biol. Chem., 262, 785–794.

Guilliams, M., Bruhns, P., Saeys, Y., Hammad, H. & Lambrecht, B. N. (2014). The function of Fcgamma receptors in dendritic cells and macrophages. Nat. Rev. Immunol., 14, 94–108.

Henzler-Wildmann, K. & Kern, D. (2007). *Dynamic personalities of proteins*, Nature, 450, 964-972.

Hardman, M. & Makarov, A. (2003). Interfacing the Orbitrap Mass Analyzer to an Electrospray Ion Source. Anal. Chem., 75, 1699-1705.

Higel, F., Seidl, A., Sörgel, F. & Friess, W. (2016). N-glycosylation heterogeneity and the influence on structure, function and pharmacokinetics of monoclonal antibodies and Fc fusion proteins. Europ. J. Pharm. and Biopharm, 100, 94–100.

Houde, D., Arndt, J., Domeier, W., Berkowitz, S. & Engen, J. R. (2009). Characterization of IgG1 Conformation and Conformational Dynamics by Hydrogen/Deuterium Exchange Mass Spectrometry. Anal. Chem., 81, 2644–2651.

Hogarth, P.M. & Pietersz, G. A. (2012). Fc receptor-targeted therapies for the treatment of inflammation, cancer and beyond. Nat. Rev. Drug Discov., 11, 311–331.

Hotzel, I., Theil, F.P., Bernstein, L.J., Prabhu, S., Deng, R., Quintana, L., Lutman, J., Sibia, R., Chan, P., Bumbaca, D. et al. (2012). A strategy for risk mitigation of antibodies with fast clearance. mAbs, 4, 753–760.

Hu, Q., Noll, R. J., Li, H., Makarov, A., Hardman, M. & Cooks, R. G. (2005). The Orbitrap: A new mass spectrometer. J. Mass Spectrom., 40, 430–443.

Humphrey, W., Dalke, A. & Schulten, K. (1996). VMD: visual molecular dynamics. J. Mol. Graph., 14, 33–38, 27–28.

Huse, M. & Kuriyan J. (2002). The conformational plasticity of protein kinases. Cell, 109(3), 275-82.

Hvidt, A. (1964). A discussion of the pH dependence of the hydrogen deuterium exchange of proteins, C. R. Trav. Lab. Carlsberg, 34, 299-317.

Hvidt, A. & Nielsen, S. O. (1966). Hydrogen exchange in proteins. Adv. Protein Chem., 21, 287-386.

Iacob, R. A., Bou-Assaf, G. M., Makowski, L., Engen, J. R., Berkowitz, S. A. & Houde, D. (2013). Investigating Monoclonal Antibody Aggregation Using a Combination of H/DX-MS and Other Biophysical Measurements. J. Pharm. Sciences, 12, 4315-4329.

Irani, V., A. Guy, J., Andrew, D., Beeson, J. G., Ramsland, P. A. & Richards, J. S. (2015). Molecular properties of human IgG subclasses and their implications for designing therapeutic monoclonal antibodies against infectious diseases. Molecular Immun., 67, 171-182.

Iwura, T., Fukuda, J., Yamazaki, K., Kanamaru, S. & Arisaka, F. (2014). Intermolecular interactions and conformation of antibody dimers present in IgG1 biopharmaceuticals. J. Biochem., 155, 63-71.

Jaswal, S. S. (2013). Biological insights from hydrogen exchange mass spectrometry. Biochimica et Biophysica Acta, 1834, 1188-1201.

Jefferis, R. (2009). Glycosylation as a strategy to improve antibody-based therapeutics. Nature Reviews, 8, 226-234.

Johnson, I. S. (1983). Human insulin from recombinant DNA technology. Science, 219, 632-637.

Johnson, D., Agochiya, M., Samejima, K., Earnshaw, W., Frame, M. & Wyke, J. (2000). Regulation of both apoptosis and cell survival by the v-Src oncoprotein. Cell Death Differ, 7, 685-696.

Jonsson, A. P. (2001). Mass spectrometry for protein and peptide characterization, Cell. Mol. Life Sci., 58, 868–884.

Joubert, M. K., Luo, Q., Nashed-Samuel, Y., Wypych, J. & Narhi, L. O. (2011). Classification and Characterization of Therapeutic Antibody Aggregates. J. Biol. Chem., 286, 25118–25133.

Kaila, V.R.I., Wikström, M. & Hummer, G. (2014). Electrostatics, hydration, and proton transfer dynamics in the membrane domain of respiratory complex I. Proc. Natl. Acad. Sci. U S A, 111, 6988-6993.

Kaltashov, I. A., Bobst, C. E., Abzalimov, R. R., Wang, G., Baykal, B. & Wang, S. (2012). Advances and challenges in analytical characterization of biotechnology products: mass spectrometry-based approaches to study properties and behavior of protein therapeutics. Biotechnol. Adv., 30, 210-222.

Karplus, M. (2011). Behind the folding funnel diagram. Nat. Chem. Biol., 7, 401-404.

Katta, V. & Chait, B. T. (1991). Conformational Changes in Proteins Probed by Hydrogen-exchange Electrospray-ionization Mass Spectrometry. Rap. Comm. Mass Spectrom., 5, 214-217.

Kebarle, P. & Verkerk, U. H. (2009). Electrospray: From Ions in Solutions to Ions in the Gas Phase, What We Know Now. Mass Spectrom. Rev., 28, 898-917.

Kebarle, P. & Verkerk, U.H. (2009). Electrospray: from ions in solution to ions in the gas phase, what we know now. Mass Spectrom. Rev., 28, 898-917.

Kebarle, P. & Tang, L. (1993). From ions in solution to ions in the gas phase: the mechanism of electrospray mass spectrometry. Anal. Chem., 65, 972–986.

Kim. K. S., Fuchs, J. A. & Woodard, C. K. (1993). Hydrogen Exchange identifies Native-State Motional Domains important in Protein Folding. Biochemistry, 32, 9600-9608.

Kmiecik, T.E. & Shalloway, D. (1987). Activation and suppression of pp60c-src transforming ability by mutation of its primary sites of tyrosine phosphorylation. Cell, 49(1), 65-73.

Konermann, L. & Pan, X. T. Y. (2008). Protein structure and dynamics studied by mass spectrometry: H/D exchange, hydroxyl radical labeling, and related approaches. J. Mass Spectrom., 43, 1021-1036.

Konermann, L., Ahadi, E., Rodriguez, A. D. & Vahidi, S. (2012). Unraveling the Mechanism of Electrospray Ionization, Anal. Chem., 85, 2-9.

Korndoerfer, I.P., Schlehuber, S. & Skerra, A. (2003). Structural mechanism of specific ligand recognition by a lipocalin tailored for the complexation of digoxigenin. J. Mol. Biol., 330, 385-396.

Kornev, A.P., Haste, N.M., Taylor, S.S. & Ten Eyck L.F. (2006). Surface comparison of active and inactive protein kinases identifies a conserved activation mechanism. Proc. Natl. Acad. Sci. USA, 103, 17783-17788.

Kurogochi, M., Mori, M., Osumi, K., Tojino, M., Sugawara, S., Takashima, S., Hirose, Y., Tsukimura, W., Mizuno, M., Amano, J., Matsuda, A., Tomita, M., Takayanagi, A., Shoda, S. & Shirai, T. (2015). Glycoengineered Monoclonal Antibodies with Homogeneous Glycan (M3, G0, G2 and A2) Using Chemoenzymatic Approach Have Different Affinities for FcγRIIIa and Variable Antibody-Dependent Cellular Cytotoxicity Activities. PLoS One, 7, 1-24.

Kyi, C. & Postow, M. A. 2014. Checkpoint blocking antibodies in cancer immunotherapy. FEBS letters, 588 (2), 368-376.

Labrijn, A. F., Aalberse, R. C. & Schuurman, J. (2008). When binding is enough: nonactivating antibody formats. Curr. Opinion in Immun., 20, 479-485.

Lakowicz, J.R. (Ed.) (1999). Principles in Fluorescence Spectroscopy (Plenum Press, New York) p. 724.

Lamerdin, J., Daino-Laizure, H., Neil, W. C., & Saharia, A. 2016. [White Paper] Accelerating Biosimilar & Biobetter Drug Development: Ready-to-Use, Cell-Based Assays for Potency and Lot Release Testing, DiscoverX.

Li, G., Zhang, X. & Cui, Q. (2003). Free Energy Perturbation Calculations with Combined QM/MM Potentials Complications, Simplifications, and Applications to Redox Potential Calculations, J. Phys. Chem. B., 107, 8643-8653.

Li, W., Prabakaran, P., Chen, W., Zhu, Z., Feng, Y. & Dimitrov, D. S. (2016). Antibody Aggregation: Insights from Sequence and Structure. Antibodies, 5, 19-28.

Li, S., Schoneich, C. & Borchardt, R. T. (1995). Chemical Instability of Protein Pharmaceuticals: Mechanisms of Oxidation and Strategies for Stabilization. Biotechnol. Bioeng., 48, 490-500.

Lightle, S., Aykent, S., Lacher, N., Mitaksov, V., Wells, K., Zobel, K. & Oliphant, T. (2010). Mutations within a human IgG2 antibody form distinct and homogeneous disulfide isomers but do not affect Fc gamma receptor or C1q binding. Protein Science, 19, 753-762.

Lilie, H., Rudolph, R. & Buchner, J. (1995). Association of antibody chains at different stages of folding: prolyl isomerization occurs after formation of quaternary structure. J. Mol. Biol., 248, 190-201.

Liu, H., Bulseco, G.-G. & Sun, J. (2006). Effect of posttranslational modifications on the thermal stability of a recombinant monoclonal antibody. Immunology Letters, 106, 144–153.

Liu, L. (2015). Antibody Glycosylation and Its Impact on the Pharmacokinetics and Pharmacodynamics of Monoclonal Antibodies and Fc-fusion Proteins. J. Pharm. Sci., 6, 1866-1884.

Liu, Y. D., Goetze, A. M., Bass, R. B. & Flynn, G. C. (2011). N-terminal Glutamate to Pyroglutamate Conversion in Vivo for Human IgG2 Antibodies. J. Biol. Chem., 286, 11211-11217.

Liu, Y. D., Chaen, X., Zhang-van Enk, J., Plant, M., Dillon, T. M. & Flynn, G. C. (2008). Human IgG2 Antibody Disulfide Rearrangement in Vivo. J. Biol. Chem., 283, 29266-29272.

Liu, H. & May, K. (2012). Disulfide bond strictures of IgG molecules: Structural variations, chemical modifications and possible impacts to stability and biological function. mAbs, 4, 17-23.

Liu, Y. D., Chou, R. Y.-T., Dillon, T. M., Poppe, L., Spahr, C., Shi, S. D. H & Flynn, G. C. (2014). Protected hinge in the immunoglobulin G2-A_2 disulfide isoform. Protein Science, 23, 1753-1764.

Luo, Q., Joubert, M. K., Stevenson, R., Ketchem, R. R., Narhi, L. O. & Wypych, J. (2011). Chemical modifications in therapeutic protein aggregates generated under different stress conditions. J. Biol. Chem., 286, 25134–25144.

Lydon, N.B., Gay, B., Mett, H., Murray, B., Liebetanz, J., Gutzwiller, A., Piwnica-Worms, H., Roberts, T.M. & McGlynn, E. (1992). Purification and biochemical characterization of non-myristoylated recombinant pp60c-src kinase. Biochem. J., 287, 985-993.

MacKerell, A. D. *et al.* (1998). All-Atom Empirical Potential for Molecular Modeling and Dynamics Studies of Proteins. J. Phys. Chem., B 102, 3586-3616.

Maier, C. S. & Deinzer, M. L. (2005). Protein Conformations, Interactions, and H/D Exchange, Methods in Enzymology. 402, 312-360.

Makarov, A. (2000). Electrostatic axially harmonic orbital trapping: A high-performance technique of mass analysis. Anal. Chem., 72, 1156-1162.

Manning, M.C., Patel, K. & Borchardt, R. T. (1989). Stability of Protein Pharmaceuticals. Pharmaceut. Res., 6, 903-918.

McAllister, R.G. & Konermann, L. (2015). Challenges in the Interpretation of Protein H/D Exchange Data: A Molecular Dynamics Simulation Perspective, Biochemistry, 54, 2683-2692.

Martinez, T., Guo, A., Allen, M. J., Han, M., Pace, D., Jones, J., Gillespie, R., Ketchem, R. R., Zhang, Y. & Balland, A. (2008). Disulfide Connectivity of Human Immunoglobulin G2 Structural Isoforms. Biochemistry, 47, 7496-7508.

Meng, Y. & Roux, B. (2014). Locking the active conformation of c-Src kinase through the phosphorylation of the activation loop. J. Mol. Biol., 426, 423-435.

Meng, Y., Shukla, D., Pande, V.S. & Roux, B. (2016). Transition path theory analysis of c-Src kinase activation. Proc. Natl. Acad. Sci. U S A., 113, 9193-9198.

Molday, R. S., Englander, S. W. & Kallen, R. G. (1972). Primary structure effects on peptide group hydrogen exchange. Biochemistry, 18, 150-158.

Moore, J. M. R., Patapoff, T. W. & Cromwell, M. E. M. (1999). Kinetics and Thermodynamics of Dimer Formation and Dissociation for a Recombinant Humanized Monoclonal Antibody to Vascular Endothelial Growth Factor. Biochemistry, 38, 13960-13967.

Morgan, C. R. & Engen, J. R. (2009). Investigating solution-phase protein structure and dynamics by hydrogen exchange mass spectrometry. Curr. Protoc. Protein Sci. Chapter: Unit–17, 617.

Nada, S., Okada, M., MacAuley, A., Cooper, J.A. & Nakagawa, H. (1991). Cloning of a complementary DNA for a protein-tyrosine kinase that specifically phosphorylates a negative regulatory site of p60c-src. Nature, 351, 69-72.

Narhi, L. O., Schmit, J., Bechtold-Peters, K. & Sharma, D. (2012). Classification of Protein Aggregates. J. Pharm. Sci., 101, 493-498.

National Center for Biotechnology Information (NCBI). Bethesda (MD): National Library of Medicine (US), National Center for Biotechnology Information; [1988] – [cited 2017 May 20]. Available from: https://www.ncbi.nlm.nih.gov/

Neglia, C. I., Cohen, H. J., Garber, A. R., Ellis, P. D., Thorpe, S. R. & Baynes, J. W. (1983). ^{13}C NMR investigation of non-enzymatic glucosylation of protein. Model studies using RNase A. J. Biol. Chem., 258, 14279-14283.

Niwa, R. & Satoh, M. (2015). The Current Status and Prospects of Antibody Engineering for Therapeutic Use: Focus on Glycoengineering Technology. J. Pharm. Sci., 104, 930–941.

Okada, M. & Nakagawa, H. (1988). Identification of a novel protein tyrosine kinase that phosphorylates pp60c-src and regulates its activity in neonatal rat brain. Biochem. Biophys. Res. Commun., 154, 796-802.

Ozkirimli, E. & Post, C.B. (2006). Src kinase activation: A switched electrostatic network. Protein Sci., 15, 1051-1062.

Paul, R., Graff-Meyer, A., Stahlberg, H., Lauer, M. E., Rufer, A. C., Beck, H., Briguet, A., Schnaible, V., Buckel, T. & Boeckle, S. (2012). Structure and Function of Purified Monoclonal Antibody Dimers Induced by Different Stress Conditions. Pharm. Res., 29, 2047-2059.

Peng, L., Oganesyan, V., Damschroder, M. M., Wu, H. & Dall'Acqua, W. F. 2011. Structural and Functional Characterization of an Agonistic Anti-Human EphA2 Monoclonal Antibody. Journ. Mol. Biol., 413 (2), 390-405.

Peng, L.X., Lawrenz, M., Shukla, D., Tang, G.W., Pande, V.S. & Altman, R.B. (2016). Application of new informatics tools for identifying allosteric lead ligands of the c-Src kinase. bioRxiv preprint.

Pepinsky, R.B., Silvian, L., Berkowitz, S.A., Farrington, G., Lugovskoy, A., Walus, L., Eldredge, J., Capili, A., Mi, S., Graff, C. & Garber, E. (2010). Improving the solubility of anti-LINGO-1 monoclonal antibody Li33 by isotype switching and targeted mutagenesis. Protein Science, 19, 954-966.

Perico, N., Purtell, J., Dillon, T. M. & Ricci, M. S. (2009). Conformational Implications of an Inversed pH-Dependent Antibody Aggregation. J. Pharm. Science, 98, 3031-3042.

Perkins, S. J., Okemefuna, A. I., Nan, R., Li, K. & Bonner, A. (2009). Constrained solution scattering modeling of human antibodies and complement proteins reveals novel biological insights. J. R. Soc., Interface, 6, 679-696.

Petruk, A. A., Defelipe, L. A., Limardo, R. G. R, Bucci, H., Marti, M. A. & Turjanski, A. G. (2013). Molecular Dynamics Simulations Provide Atomistic Insight into Hydrogen Exchange Mass Spectrometry Experiments. J. Chem. Theory Comput., 9, 658-669.

Phillips, J. C. *et al*. (2005). Scalable molecular dynamics with NAMD. J. Comput. Chem., 26, 1781–1802.

Philo, J. S. & Arakawa, T. (2009). Mechanisms of Protein Aggregation. Current Pharm. Biotech., 10, 348-351.

Pinada, C., Hernandez, G. C. Jacobs, I. A., Alvarez, D. F. & Carini, C. (2016). Assessing the Immunogenicity of Biopharmaceuticals. BioDrugs, 30, 195–206.

Pincetic, A., Bournazos, S., DiLillo, D. J., Maamary, J., Wang, T. T., Dahan, R., Fiebiger, B. M., Ravetch, J. V. (2014). Type I and type II Fc receptors regulate innate andadaptive immunity. Nat. Immunol., 15, 707-716.

Plath, F., Ringler, P., Graff-Meyer, A., Stahlberg, H., Lauer, M. E., Rufer, A. C., Graewert, M. A., Svergun, D., Gellermann, G., Finkler, C., Stracke, J. O., Koulov, A., & Schnaible, V. (2016). Characterization of mAb dimers reveals predominant dimer forms common in therapeutic mAbs, mAbs, 8, 928-940.

Plumb, R. S., Johnson, K. A., Rainville, P., Smith, B. W., Wilson, I. D., Castro-Perez, J. M. & Nicholson, J. K. (2006). UPLC/MS^{E}; a new approach for generating molecular fragment information for biomarker structure elucidation, Rapid Comm. Mass Spec., 20, 1989-1994.

Purchio, A.F. (1982). Evidence the pp60src, the product of the Rous sarcoma virus src gene, undergoes autophosphorylation. Journal of Virology, 41, 1-7.

Quan, L. & Liu, M. (2013). The Generating Function of CID, ETD and CID/ETD Pairs of Tandem Mass Spectra: Applications to Database Search. Mol. Cell Proteomics, 9, 2840-2852.

Ratanji, K. D., Derrick, J. P., Dearman, R. J. & Kimber, I. (2014). Immunogenicity of therapeutic proteins: Influence of aggregation. J. Immunotoxicol, 11, 99-109.

Rayner, L. E., Hui, G. K., Gor, J., Heenan, R. K., Dalby, P. A. & Perkins, S. J. (2015). The Solution Structures of two Human IgG1 Antibodies show Conformational stability and Accommodate their C1q and FcγR Ligands. J. Biol. Chem., 290, 8420–8438.

Rayner, L. E., Kadkhodayi-Kholghi, N., Heenan, R. K., Gor, J., Dalby, P. A. & Perkins, S. J. (2013). The Solution Structure of Rabbit IgG Accounts for Its Interactions with the Fc Receptor and Complement C1q and Its Conformational Stability. J. Mol. Biol., 425, 506-523.

Remmele, R. L., Callahan, W. J., Krishnan, S., Zhou, L., Bondarenko, P. V., Nichols, A. C., Kleemann, G. R., Pipes, G. D., Park, S., Fodor, S., Kras, E. & Brems, D. N. (2005). Active Dimer of Epratuzumab Provides Insight into the Complex Nature of an Antibody Aggregate. J. Pharm. Science, 95, 126-145.

Reuter, C., Findik, D. & Presek, P. (1990). Characterization of purified pp60c-src protein tyrosine kinase from human platelets. European Journal of Biochemistry, 190, 343–350.

Rink, R., Arkema-Meter, A., Baudoin, I., Post, E., Kuipers, A., Nelemans, S. A., Akanbi, M. H. J. & Moll, G. N. (2010). To protect peptide pharmaceuticals against peptidases, J. Pharm. and Toxicol. Methods, 61, 210–218.

Roopenian, D. C. & Akilesh, S. (2007). FcRn: the neonatal Fc receptor comes of age. Nat. Rev. Immunol., 7, 715-725.

Rosenberg, A. S. (2006). Effects of Protein Aggregates: An Immunologic Perspective. The AAPS Journal, 8, 3.

Roskoski, R. Jr. (2004). Src protein-tyrosine kinase structure and regulation. Biochem. Biophys. Res. Commun., 324, 1155-64.

Roskoski R Jr. (2015). Src protein-tyrosine kinase structure, mechanism, and small molecule inhibitors. Pharmacol Res., 94, 9-25.

Sang, P.,Yang, Q., Du, X., Yang, N., Yang, L.-Q., Ji, X. L., Fu, Y.-X., Meng, Z.-H. & Liu, S. Q. (2016). Effect of the Solvent Temperatures on Dynamics of Serine Protease Proteinase K, Int. J. Mol. Sci., 17, 254.

Schieferdecker, A., Voigt, M., Riecken, K., Braig, F., Schinke, T., Loges, S., Bokemeyer, C., Fehse, B & Binder, M. 2014. Denosumab mimics the natural decoy receptor osteoprotegerin by interacting with its major binding site on RANKL. Oncotarget, 5, 6647-6653.

Schroeder, H. W. Jr & Cavacini, L. (2010). Structure and Function of Immunoglobulins. J. Allergy Clin. Immunol, 125, 41-52.

Schuck, P.(2000). Size-distribution analysis of macromolecules by sedimentation velocity ultracentrifugation and lamm equation modeling. Biophy. J., 78, 1606-1619.

Schuck, P. (2003). On the analysis of protein self-association by sedimentation velocity analytical ultracentrifugation. Anal. Biochem, 320, 104-124.

Schroeder, H. W. Jr. & Cavacini, L. (2010). Structure and function of immunoglobulins. J. Allergy Clin. Immunol. 125, S41–S552.

Scigelova, M & Makarov, A. (2006). Orbitrap Mass Analyzer - Overview and Applications in Proteomics. Practical Proteomics, 1-2, 16-21.

Seeliger, M.A., Young, M., Henderson, M.N., Pellicena, P., King, D.S., Falick, A.M., Kuriyan, J. (2005). High yield bacterial expression of active c-Abl and c-Src tyrosine kinases. Protein Science, 14, 3135-3139.

Sekhon, S. B. (2010). Biopharmaceuticals: an overview. Thai J. Pharm. Sci., 34, 1-19.

Sharma, V., Belevich, G., Gamiz-Hernandez, A.P., Róg, T., Vattulainen, I., Verkhovskaya, M., Wikström, M., Hummer, G. & Kaila, V.R.I. Redox-Induced Activation of the Proton Pump in the Respiratory Complex I, submitted.

Shields, R. L., Namenuk, A. K., Hong, K., Meng, Y. G., Rae J., Briggs, J., Xie, D., Lai, J., Stadlen, A., Li, B., Fox, J. A. & Presta, L. G. (2001). High Resolution Mapping of the Binding Site on Human IgG1 for FcγRI, FcγRII, FcγRIII, and FcRn and Design of IgG1 Variants with Improved Binding to the FcγR. J. Biol. Chem., 276, 6591-6604.

Shimizu, T., Fukuda, H., Murayama, S., Izumiyama, N. & Shirasawa, T. (2002). Isoaspartate Formation at Position 23 of Amyloid Beta Peptide Enhanced Fibril Formation

and Deposited Onto Senile Plaques and Vascular Amyloids in Alzheimer's Disease. J. Neurosci. Res., 70, 451-461.

Shukla, D., Meng, Y., Roux, B. & Pande, V.S. (2014). Activation Pathway of Src Kinase Reveals Intermediate States as Targets for Drug Design. Nature communications, 5
Singh, S.K. (2001). Impact of product-related factors on immunogenicity of biotherapeutics. J. Pharm. Sci., 100, 354-387.

Smart, J.E., Oppermann, H., Czernilofsky, A.P., Purchio, A.F., Erikson, R.L. & Bishop, J.M. (1981). Characterization of sites for tyrosine phosphorylation in the transforming protein of Rous sarcoma virus (pp60v-src) and its normal cellular homologue (pp60c-src). Proc. Natl. Acad. Sci. U S A., 78, 6013-6017.

Sobott, F., Watt, S. J., Smith, J., Edelmann, M. J., Kramer, H. B. & Kessler, B. M. (2009). Comparison of CID versus ETD Based MS/MS Fragmentation for the Analysis of Protein Ubiquitination. J. Am. Soc. Mass Spectrom., 20, 1652–1659.

Sousa Da Silva, A. W. & Vranke, W. F. (2012). ACPYPE - AnteChamber PYthon Parser interfacE. BMC Research Notes, 5, 367 ff.

Tarentino, A. L., Gomez, C. M. & Plummer, T. H. Jr. (1985). Deglycosylation of Asparagine-Linked Glycans by Peptide:N-Glycosidase F. Biochemistry, 24, 4665-4671.

Thévenon-Emeric, G., Kozlowski, J., Zhang, Z. & Smith, D. L. (1992). Determination of Amide Hydrogen Exchange Rates in Peptides by Mass Spectrometry. Anal. Cham. 1992, 64, 2456-2458.

Thies, M. J., Mayer, J., Augustine, J. G., Frederick, C. A., Lilie, H. & Buchner, J. (1999). Folding and association of the antibody domain CH3: prolyl isomerization preceeds dimerization. J. Mol. Biol., 293, 67-79.

Thoman, M., Schlothauer, T., Dashivets, T., Malik, S., Avenal, C., Bulau, P., Rüger, P. & Reusch, D. (2015). *In Vitro* Glycoengineering of IgG1 and Its Effect on Fc Receptor Binding and ADCC Activity. PloS, 10, 1-16.

Tian, X., Vestergaard, B., Thorolfsson, M., Yang, Z., Rasmussen, H. B. & Langkilde, A. E. (2014). In-depth analysis of subclass-specific conformational preferences of IgG antibodies. IUCrJ, 2, 9-18.

Tsutsui, Y., Deredge, D., Wintrode, P.L. & Hays, F.A. (2016). Imatinib binding to human c-Src is coupled to inter-domain allostery and suggests a novel kinase inhibition strategy. Sci. Rep., 6, 30832-30843.

Twamley-Stein, G.M., Pepperkok, R., Ansorge, W. & Courtneidge, S.A. (1993). The Src family tyrosine kinases are required for platelet-derived growth factor-mediated signal transduction in NIH 3T3 cells. Proc. Natl. Acad. Sci. U S A., 90, 7696-7700.

Van Beers, M. M, Sauerborn, M., Gilli, F., Brinks, V., Schellekens, H. & Jiskoot, W. (2010). Aggregated recombinant human interferon Beta induces antibodies but no memory in immune-tolerant transgenic mice. Pharm Res., 27, 1812-1824.

Vanhove, M., Usherwood, Y. K. & Hendershot, L. M. (2001). Unassembled Ig heavy chains do not cycle from BiP in vivo but require light chains to trigger their release. Immunity, 15, 105-114.

Vidarsson, G., Dekkers, G. & Rispens, T. (2014). IgG Subclasses and Allotypes: From Structure to Effector Functions. Front Immunol**.,** 5, 520-537.

Walters, T., Ricciuti, A., Mayne, L. & Englander, S. W. (2012). Minimizing Back Exchange In the Hydrogen Exchange Mass Spectrometry Experiment. J. Am. Soc. Mass Spectrom., 23, 2132–2139.

Walsh, G. (2010). Biopharmaceutical benchmarks. Nat. Biotechnol., 28, 917-924.

Wang, T., Liu, Y. D., Cai, B., Huang, G. & Flynn, G. C. (2015). Investigation of antibody disulfide reduction and re-oxidation and impact to biological activities. J. Pharm. and Biomed. Anal., 102, 519-528.

Wang, X., Das, T.K., Singh, S.K. & Kumar, S. (2009). Potential aggregation prone regions in biotherapeutics: A survey of commercial monoclonal antibodies. mAbs, 1, 254–267.

Wei, H., Ahn, J., Yu, Y.Q., Tymiak, A., Engen, J.R. & Chen, G. (2012). Using Hydrogen/Deuterium Exchange Mass Spectrometry to Study Conformational Changes in Granulocyte Colony Stimulating Factor upon PEGylation. J. Am. Soc. Mass Spectrom., 23, 498-504.

Weis, D. D. & Engen, J. R. (2006). Semi-Automated Data Processing of Hydrogen Exchange Mass Spectra Using HX-Express, J. Am. Soc. Mass Spectrom., 17, 1700-1703.

Wilm, M. (2011). Principles of Electrospray Ionization, Molecular & Cellular Proteomics. 10, 1–8.

Wilson, C., Agafonov, R.V., Hoemberger, M., Kutter, S., Zorba, A., Halpin, J., Buosi,, V., Otten, R., Waterman, D., Theobald, D.L. & Kern, D. (2015). Kinase dynamics. Using ancient protein kinases to unravel a modern cancer drug's mechanism. Science, 347, 882-886.

Woutersen, S., Pfister, R., Hamm, P. Mu, ., Kosov, D. S. & Stock, G. (2002). Peptide conformational heterogeneity revealed from nonlinear vibrational spectroscopy and molecular-dynamics simulations. J. Chem. Phys., 117, 6833 – 6840.

Wright, H. T. (1991). Nonenzymatic deamidation of asparaginyl and glutaminyl residues in proteins, Critical Reviews in Biochemistry and Molecular Biology, 26, 1–52.

Wright, H. T. (1991). Sequence and structure determinants of the nonenzymatic deamidation of asparagine and glutamine residues in proteins. Protein Eng., 4, 283-294.

Wu, S.J., Luo, J., O'Neil, K.T., Kang, J., Lacy, E.R., Canziani, G., Baker, A., Huang, M., Tang, Q.M., Raju, T.S. et al. (2010). Structure-based engineering of a monoclonal antibody for improved solubility. Protein Eng. Des. Sel., 23, 643–651.

Wysocki, V. H., Resing, K. A., Zhang, Q. & Cheng, G. (2005). Mass Spectrometry of Peptides and Proteins. Methods, 35, 211–222.

Wypych, J., Li, M., Guo, A., Zhang, Z., Martinez, T., Allen, M. J., Fodor, S., Kelner, D. N., Flynn, G. C., Liu, Y. D., Bondarenko, P., Ricci, M. S., Dillon, T. M. & Balland, A. (2008). Human IgG2 Antibodies Display Disulfide-mediated Structural Isoforms. Journ. Biol. Chem., 283, 16194-16205.

Xu, W., Doshi, A., Lei, M., Eck, M.J. & Harrison, S.C. (1999). Crystal structures of c-Src reveal features of its autoinhibitory mechanism. Mol. Cell., 3, 629-638.

Xu, W., Harrison, S. C. & Eck, M. J. (1997). Three-dimensional structure of the tyrosine kinase c-Src. Nature, 385, 595-602.

Xuguang, Y., Watson, J., Shing Ho, P. & Deinzer, M. L. (2004). Mass Spectrometric Approaches Using Electrospray Ionization Charge States and Hydrogen-Deuterium Exchange for Determining Protein Structures and Their Conformational Changes. Mol. & Cell. Prot., 3, 10-23.

Yamaguchi, H. & Hendrickson, W.A. (1996). Structural basis for activation of human lymphocyte kinase Lck upon tyrosine phosphorylation. Nature, 384, 484-489.

Yan, Y., Wei, H., Fu, Y., Jusuf, S., Zeng, M., Ludwig, R., Krystek, S. R. Jr., Chen, G., Tao, L. & Das, T. K. (2016). Isomerization and Oxidation in the Complementarity-Determining Regions of a Monoclonal Antibody: A Study of the Modification-Structure-Function Correlations by Hydrogen-Deuterium Exchange Mass Spectrometry. Anal. Chem., 88, 2041-2050.

Yang, J., Wang, S., Liu, J., & Raghani, A. (2007). Determination of tryptophan oxidation of monoclonal antibody by reversed phase high performance liquid chromatography, J. of Chromat. A, 1156, 174–182.

Yang, L.-Q., Sang, P., Tao, Y., Fu, Y.-X., Zhang, K.-Q., Xie, Y.-H. & Liu, S.-Q. (2014). Protein dynamics and motions in relation to their functions: several case studies and the underlying mechanisms, J. Biomol. Struc. and Dynamics, 32, 372-393

Yang, L.-Q., Ji, X.-L. & Liu, S.-Q. (2013). The free energy landscape of protein folding and dynamics: a global view, J. Biomol. Struc. and Dynamics, 31, 982-992.

Yang, S., Banavali, N.K. & Roux, B. (2009). Mapping the conformational transition in Src activation by cumulating the information from multiple molecular dynamics trajectories. Proc. Natl. Acad. Sci. U S A, 106, 3776-3781.

Zhang, A., Hu, P., MacGregor, P., Xue, Y., Fan, H., Suchecki, P., Olszewski, L. & Liu, A. (2014). Understanding the Conformational Impact of Chemical Modifications on

Monoclonal Antibodies with Diverse Sequence Variation Using Hydrogen/Deuterium Exchange Mass Spectrometry and Structural Modeling. Anal. Chem., 86, 3468-3475.

Zhang, A., Fang, J., Chou, R. Y.-T., Bondarenko, P. V. & Zhang, Z. (2015). Conformational Difference in Human IgG2 Disulfide Isoforms Revealed by Hydrogen/Deuterium Exchange Mass Spectrometry. Biochemistry, 54, 1956-1962.

Zhang, B., Harder, A. G., Connelly, H. M., Maheu, L. L. & Cockrill, S. L. (2010). Determination of Fab-Hinge Disulfide Connectivity in Structural Isoforms of a Recombinant Human Immunoglobulin G2 Antibody. Anal. Chem., 82, 1090-1099.

Zhong, X. & Wright, J. F. (2013). Biological Insights into Therapeutic Protein Modifications throughout Trafficking and Their Biopharmaceutical Applications. Internat. J. Cell Biol., 2013, 1-19.

Zhang, Z., & Smith, D. L. (1993). Determination of amide hydrogen exchange by mass spectrometry: A new tool for protein structure elucidation. Protein Science, 2, 522–531.

Zubarev, R. A. & Makarov, A. (2013). Orbitrap is the newest addition to the family of high-resolution mass spectrometry analyzers. With its revolutionarily new, miniature design, Orbitrap combines high speed with excellent quantification properties, ranking favorably in many analytical applications. Anal. Chem., 85, 5288-5296.

9 ACKNOWLEDGEMENTS

This thesis was prepared at the Technische Universität München, Department Chemie, Lehrstuhl Biotechnologie under supervision of Prof. Dr. Johannes Buchner in cooperation with the Sandoz Biopharmaceuticals AG.

I would like to thank Prof. Dr. Johannes Buchner for offering me the scientific tasks, for giving me the opportunity to prepare my PhD thesis under his supervision, reviewing the manuscripts and for giving me exceptional advice and support during the years.

I want to thank Dr. Andreas Seidl and Dr. Otmar Hainzl for taking over the supervision from company side and for giving me the opportunity to gain lots of experience in the biopharmaceutical industry. Thanks for all the support and advices I experienced over the last years.

A big thanks also goes to Dr. Fabian Higel and his PKP team for countless scientific advices, reviewing of manuscripts/presentations and meanwhile for being a great and competent line-manager.

I also want to thank my collaboration partners Dr. E. Boczek and Prof. Dr. V. Kaila for giving me the opportunity to work with them on the c-Src kinase topic. Thanks a lot for the uncomplicated and interesting collaboration.

Special thanks also goes to Dr. Ralf Stehle for introducing me to SAXS and the corresponding data evaluation methodologies and Florian Kandzia for performing MD simulations. Thanks for the support, all your time and your patience also during stressful times.

I also want to thank all the colleagues in BPCI and BPCII under supervision of Dr. Otmar Hainzl and Dr. Alexander Bepperling for introducing me to several helpful methodologies (AUC, SPR, DSF), performing analysis and offering measurement time.

Furthermore, I want to thank Dr. Luis Borlido and Dr. Roky Bamert for the support on the IgG2 topic.

A big thanks also goes to Dr. Florian Wolschin and all the people in his PCC department for giving me the opportunity to work on the instruments, for numerous scientific advices from the people working in the department and the support I experienced from all sides. Especially I want to name Urs Hanke who spent a lot of time to introduce me to H/DX-MS.

Last but not least, a big thanks goes to my family and friends for all the “non-scientific” support during my studies and my PhD thesis. Really helped a lot to get through the past years.

DECLARATION

I, Marco Dehling, hereby declare that this thesis was prepared independently using only the references and resources stated here. This work has not been presented to any examination board yet.

Hiermit erkläre ich, Marco Dehling, dass ich die vorliegende Arbeit selbständig verfasst und nur die angegebenen Quellen und Hilfsmittel verwendet habe. Die Arbeit wurde bisher keiner Prüfungskommission vorgelegt.

_____

Marco Dehling
München, 29.November 2017